EHD Augmentation of Convective Boiling within a Transparent Heat Exchanger

Gerard Joseph McGranaghan
BSc, BA BAI

Department of Mechanical and Manufacturing Engineering
Parsons Building
Trinity College
Dublin 2
Ireland

A thesis submitted to the University of Dublin in partial fulfilment of the requirements for the degree of Ph.D.

Declaration

I declare that I am the author of this thesis and that all work described herein is my own, unless otherwise referenced. Furthermore, this work has not been submitted, in whole or part, to any other university or college for any degree or qualification.

I authorize the library of Trinity College, Dublin to lend or copy this thesis.

_____

Gerard Joseph McGranaghan

April 2013

Summary

This work investigated the influence of electrohydrodynamic forces on the two-phase flow patterns of HFE7000 refrigerant under convective boiling conditions. A flow loop was constructed which featured two novel transparent heat exchanger designs which facilitated visualisation of the flow field under EHD and diabatic conditions. In both designs, a sapphire tube was employed which allowed heat transfer and optical access to the boiling refrigerant. A stainless steel rod within the sapphire tube formed a high voltage electrode, while a thin layer of Indium Tin Oxide (ITO), deposited on the tube exterior provided an optically transparent though electrically conductive transparent ground. High-speed video imaging was combined with thermal-hydraulic measurements to relate flow patterns with voltage.

In Test Section A, the sapphire tube was surrounded by an acrylic channel through which heated water flowed, forming a transparent concentric heat exchanger. Heat transfer coefficients were calculated using thermocouples embedded in the sapphire tube wall and along the water side, and pressure drop was measured across the test section. A high speed camera recorded imagery along the test section length.

In the first study, experiments were carried out at a refrigerant mass flux (G) of 100 kg/m^{2}s, inlet qualities from 0-45%, heat input ($Q^{//}$) of 12.4 kW/m^2 and EHD voltage levels between 0 to 8 kV at 60Hz AC. It was found that at a constant heat flux of 12.4 kW/m^2, EHD increased the heat transfer coefficients but with lower superheat temperatures. At 2% inlet quality an EHD voltage of 8 kV altered the flow regime from a stratified flow with nucleate boiling to a complex mixed flow with oscillating bubbles and liquid jets, resulting in improved heat transfer. It was also found that as quality increased, EHD voltages precipitated a flow regime change from stratified to annular, resulting in improved heat transfer.

In the second study of tests at a constant water inlet temperature, the flow regime was seen to fall into three types dependent on EHD voltage. A base case was performed at 0 kV and voltage was increased in 1 kV increments. The first regime was of a stratified wavy flow with nucleate boiling, interspersed with occasional slugs which wet the top of the tube. The evaporation of this layer at the top provided lower thermal resistance

and high heat transfer. As voltage was increased to 1 and 2 kV, bubble size increased and oscillations became apparent. Heat transfer rose by about 13% during this phase.

As the voltage rose to between 3 to 6 kV, a new flow regime where occurred where liquid was extracted from the lower layer towards the electrode. Bubble diameter and oscillation increased further. At 6 kV the flow alternated between oscillatory entrained bubble flow and a flow of waves of cresting bubbles and liquid. These cresting events caused wetting of the top of the tube. EHD forces seemed to contribute to the upward movement and cresting of the large bubbles. This regime accounted for around 55% of the total heat transfer enhancement.

At 7 kV another change appeared where liquid jets were produced and the flow began to alternate between the oscillating bubble and thin film regimes. In-tube flow was highly mixed, featuring droplets both from liquid jets and from bursting of the elongated bubbles. The top wall was highly wetted by the bubble bursting and cresting and this regime contributed 37% of the total heat transfer enhancement.

Finally a third series of tests were conducted on Test Section B. This used an identical sapphire tube to Test Section A, but instead of water heating, the ITO coating on the tube exterior was thicker which permitted direct electrical heating. Thermocouples imbedded in the tube wall permitted local temperature measurements. On investigating the local heat transfer coefficients and flow patterns, it was found that EHD enhancement was higher at lower qualities and this was strongly linked to the higher liquid levels. EHD enhancement was also improved at higher qualities, but to a lesser level. The amount of liquid in proximity to the central electrode, and thus subject to higher EHD forces was central to high heat transfer enhancement. The magnitudes and profiles of the thermal measurements differed significantly from the water heated test section. This was mainly due to the upper temperature in the water heated section being limited, while the temperatures in the ohmically heated section had no such upper bound.

Dedication

To Pirzada Ashgar Ahmed Khan

Acknowledgements

Firstly I want to express my sincere thanks and admiration to my supervisor Dr. Tony Robinson for all his guidance, patience, enthusiasm, understanding, and never ending stream of ideas. I am continually amazed by his profound knowledge of heat transfer, his ability to define the nub of a problem, and his optimism and ingenuity in finding alternative solutions whenever a plan didn't work out. Working with him has been rewarding and a privilege.

I would like to thank Gerry Byrne in the Thermo lab for all his assistance with my ever-expanding test rig and his problem solving ability. Thanks are due to Mick Reilly and the Mechanical Workshop staff, Alex, Gabriel, JJ and Sean for their high quality work and for allowing me to work as one of them. I wish to also acknowledge the other departmental staff who contributed in various ways including Dr. Darina Murray and Dr. Tim Persoons. I am pleased to thank the intelligent and diligent visiting students from INSA Lyon, Aurelie Michel, Thomas Lebreton and Elodie Decourchelle who assisted so much with the design and experimental phases.

It would be a great slight if I wasn't to mention my office mates, Alan, Brian, Rayhaan, Seamus and Tom, and also Stephen, Jessica and Karl. Without all their constant distractions, coffee, tea, poker, and lunchtime movies, I feel I might have been finished this thesis sooner, but it would not have been as much fun. Despite our different tastes in taste, and views on the volume it should be played, I hope we remain friends for life.

I cannot forget to acknowledge Dr. Roger West and the late Professor Simon Perry when I worked in the Civil Engineering Department. Both were highly supportive of my earlier studies with the Open University which got me to where I am today. Likewise I received much support from my friends and colleagues in Civil Engineering, Chris, Dave, Eoin, George, Mick, Martin and Kevin. Thanks to you all.

I want to thank the Canadian contingent including Dr. Chan Ching, Dr. Jim Cotton, and Dr. Hossam Sadek. Not only did they host me for a very enjoyable and informative month when I worked on the EHD rig in McMaster University, they remained in correspondence when I was back in Ireland. My thanks also go to Dr. Roger Kempers for his valuable assistance in thermometry.

My gratitude is also due to a seasoned Mechanical Engineer, Mr. Tom Weymes whose gimlet eye scrutinised the thesis draft. I also want to thank most sincerely Dr. Michael Maguire for his tireless encouragement, patience, and assistance in the structure of the thesis, but most significantly, his unwavering friendship.

Finally, I want to thank my siblings, Anna, Emma, Breege, Mary and Matthew for supporting my lengthy endeavour in many minor but personally significant ways. And most of all I have to thank my parents, Patsy and Matt, for their continual and subtle encouragement this past forty something years. As a child, I was never drawn away from reading, be it a Beano comic or the World Book encyclopaedia. Thanks for recognising my appetite for knowledge.

Table of Contents

List of Figures

List of Tables

Nomenclature

Latin Symbols

Symbol	Name	Units
A	Cross-sectional area	m^2
a	Exponent in Dittus Boelter correlation	-
B	Magnetic induction	T
b	Exponent in Dittus Boelter correlation	-
$_C$	Convective	
C_1	Coefficient in Dittus Boelter correlation	-
$_{cb}$	Convective boiling	
c_p	Specific heat capacity	J/kg.K
$_{crit}$	Critical	
D	Diffusion coefficient	-
d_e	Electrode diameter	m
D_h	Hydraulic diameter of the tube	m
D_i	Inner diameter of the water jacket	m
d_i	Inner diameter of the sapphire tube	m
d_o	Outer diameter of the sapphire tube	m
dP	Pressure differential	Pa
dT	Temperature differential	K
E	Electric field strength	V/m
E	Convective enhancement factor, Chen correlation	-
$_{eB}$	Electrical body (relating to force)	
f	Friction factor	-
f_{eB}	Electric body force per unit volume	N/m^3
$_{FZ}$	Forster Zuber	
g	Acceleration due to gravity	m/s^2
G	Mass flux	$kg/m^2.s$

H	Magnetic field intensity	A/m
h	Enthalpy	J/kg
h	Heat transfer coefficient	$W/m^2.K$
h_{lv}	Latent heat of vaporization	kJ/kg
HTC	Heat transfer coefficient	$W/m^2.K$
I_o	Current from the EHD electrode	A
J	Electric current density	A/m^2
j	Superficial velocity	m/s
k	Thermal conductivity	W/m.K
K	Parameter in Taitel and Dukler map	-
L	Length	m
M	Molecular weight	g/mol
$\dot{m}$	Mass flow rate	kg/s
$_{nb}$	Nucleate boiling	
$_{ONB}$	Onset of nucleate boiling	
P	Power	W
Q	Heat	W
q	Heating power	W
q'	Heat flux referred to the inner surface of the sapphire tube	W/m^2
q"	Heat flux	W/m^2
q'''_{eB}	Electrical energy generation	J
R	Thermal resistance	K/W
S	Surface area	m^2
S	Nucleate boiling suppression factor (Gungor and Winterton)	-
$_{strat}$	Stratified	
T	Parameter in Taitel and Dukler map	-
T	Temperature	ºC
$_{tp}$	Two phase	
u	Velocity	m/s
V_e	Applied high-voltage	V
x	Working fluid vapour quality	-
x/L	Lengthwise position on the axis of the sapphire tube	-
ΔP	Pressure drop along the tube	Pa
ΔT	Temperature difference	K, °C

Dimensionless Numbers

Bi	Biot Number	$Bi = \frac{hL}{k}$
E_{hd}	EHD Number	$E_{hd} = \frac{I_0 L^3}{\rho_0 \nu^2 \mu_c A}$
Fr	Froude Number	$Fr = \frac{u^2}{gD_h}$
M_d	Masuda Number	$M_d = \frac{\varepsilon_0 E_0^2 T_0 \left(\partial \varepsilon_s / \partial T\right)_\rho L^2}{2\rho_0 \nu^2}$
Nu	Nusselt Number	$Nu = \frac{hL}{k}$
Pr	Prandtl Number	$\mathrm{Pr} = \frac{c_p \mu}{k}$
Re	Reynolds Number	$\mathrm{Re} = \frac{VL}{\nu}$

Greek Symbols

α	Void fraction	-
α	Heat transfer coefficient	W/m^2K
β	Coefficient of thermal expansion	1/K
δ	Thickness of stratified liquid layer	m
ε	Dielectric permittivity	N/V^3
ε_0	Dielectric permittivity of free space	N/V^2
ε_s	Dielectric constant	-
θ	Angle of wetted or dry perimeter	radians
λ	Gas phase parameter, Baker flow map	-
μ	Dynamic viscosity	kg/m.s
μ_c	Ion mobility	m^2/Vs
ρ	Density	kg/m^3
ρ_{el}	Charge density	C/m^3
σ	Surface Tension	Dyn/cm
σ_e	Electrical conductivity	S/m
υ	Kinematic viscosity	m^2/s
ψ	Liquid phase parameter, Baker flow map	-

Chapter 1: Introduction

1.1 Motivations for Two-Phase Heat Transfer Augmentation

Boiling and condensation in heat exchangers have long been associated with large scale steam raising plant and condensers as found in power stations or other industrial or chemical plants. Early designs were often based on trial and error or well winnowed experience and empiricism. However, beginning in the 1950's, the deployment of nuclear energy in the power generation field spurred a new era of investigation into two-phase flow phenomena motivated by safety-critical issues such as determination of critical heat flux and burnout. This led to development of tools to predict the fluid behaviour occurring during in-tube boiling. More recently, two-phase flow heat exchangers are experiencing a renewal of interest driven by the cooling demands of high power density electronics, space applications, and by the resurgence of renewable energy conversion methods such as heat pumps and waste heat recovery. Novel heat transfer enhancement methods are now being investigated in order to extract the maximum gains possible, be it higher heat transfer, increased efficiency, smaller device size, or even a means of "active" control of heat exchanger performance. Electrohydrodynamics is one such enhancement technique.

1.1.1: Heat exchanger basics

According to Shah [1] heat exchangers can be divided into various classifications depending on construction, contact nature, fluid type and other factors, including whether single phase or two-phase. Basic single phase heat exchangers typically consist of one fluid stream passing through a tube, whose outer surface is in contact with the other fluid stream. Heat transfer is dependent on fluid type, velocity, temperature difference, geometry, thermal conductivity of tube material and fluid media, as well as on many other parameters. Enhancement of heat transfer in single phase heat exchangers may be achieved by disturbance of the thermal boundary layer

using cavities and corrugations which cause turbulence and promoting mixing, or by extending heat transfer surface areas by means of fins. Though such features provide an incremental gain in heat transfer, they can suffer an associated pressure drop due to increased fluid friction and turbulence.

Likewise in two-phase flow, passive techniques such as surface irregularities, grooves, spirals, and re-entrant cavities serve to disturb the thermal boundary layer and to promote bubble nucleation and mixing, thus improving the heat transfer coefficient (HTC). However, two-phase heat transfer in the boiling phase, in conjunction with these enhanced surfaces, can achieve gains of up to 100 times that of single-phase [2], but without the severe pressure drop. In boiling heat transfer, such passive features are used to create preferential nucleation sites for bubbles to develop.

1.1.2: Active Heat Transfer Augmentation

Heat transfer augmentation can also be provided by "active" techniques. As an example, in horizontal stratified flow, only the lower part of the tube may be wetted, so heat transfer into the fluid is via the tube wall to the liquid and the tube wall to the vapour. The difference in heat transfer coefficient between vapour and liquid is around an order of magnitude, so any method of redistributing the liquid to areas of the tube normally in contact with vapour would increase the overall heat transfer capability of the unit. These active techniques attempt to increase the wetted area by using an external stimulus, such as rotation of the tube, tube wiping, or ultrasonic vibration to provide the thermal boundary layer disturbance. Another "active" method utilises an electric field to create internal electrostatic forces within the fluid. These forces again disturb the fluid flow and thermal conditions within the heat exchanger, leading to high heat transfer gains under certain conditions, but again with a low pressure drop penalty. This latter method is better known as "Electrohydrodynamics" commonly abbreviated to EHD, and is the focus of this thesis.

1.1 Enhancement of Heat Transfer by Electrohydrodynamics

The augmentation of heat transfer by electrohydrodynamics has a number of advantages over other active methods, as it requires no moving parts. As the current flow through a dielectric medium is low, it uses little additional electrical energy [3]. By varying factors such as voltage, waveform and frequency or duty cycle, "tuning" can be easily implemented to provide optimal efficiency across a range of loads. The method may even be beneficial in low gravity environments where EHD can provide a volumetric body force [3].

While many studies of EHD augmented boiling in traditional metallic type test sections have been performed to date, visualisation studies of the precise effect of the EHD forces within a working heat exchanger are very few. Most researchers utilised heated metallic test sections which preclude visualisation. However, others such as Cotton *et al*. and Sadek *et al*. [4-12] employed a transparent tube at the exit area of horizontal tube test section to view flow regimes. However, this window was outside the diabatic area of the actual heat exchanger. Consideration was given to the use of radiation or x-ray scanning in order to penetrate the traditional metallic heat exchanger test sections so as to ascertain the exact flow patterns under EHD forces, but the challenges presented would be considerable in terms of costs, restrictive operating protocols and safety. Ohta [13] created a non-EHD transparent heat exchanger by depositing a thin transparent gold film onto a glass tube to effect ohmic heating of the tube wall. However, if such a technique were to be applied to a device incorporating electrohydrodynamics, compatibility of the EHD electrical circuit and the heating circuit could be an issue. In addition, the liquid/vapour stratification that occurs in terrestrial horizontal flows could give rise to dryout or burnout of the thin heater film.

This work described in this thesis attempted to overcome these difficulties by designing a transparent test section which would (a), permit optical access to the entire flow field, and yet function as a practical heat exchanger by allowing adequate heat transfer, and

(b).facilitate provision of the necessary electrode and grounding enabling electrohydrodynamic forces to be applied.

1.2: Objectives of the Research

The goal of the research was to experimentally investigate two phase flow boiling under EHD conditions in order to elucidate the precise mechanisms by which the EHD forces affect the flow regime and consequently, how these in turn affect the heat transfer coefficient and the pressure drop.

More specifically, the first phase objective was to construct a test rig with instrumented test section capable of convective boiling of a test fluid. A means with which to apply Electrohydrodynamic forces to this fluid while boiling also had to be included. In order to visualise the effect of electrohydrodynamics on boiling two-phase flow of the test fluid, the heated test section had to be transparent.

The second phase objective was investigative research in order to elicit the influence of high voltage AC on the flow patterns and flow regimes in boiling two phase flow at various inlet qualities and at different heat input conditions. Pressure drop and its relation to flow pattern was also investigated.

To these ends a novel two-phase flow test facility incorporating fully instrumented and completely transparent heat exchanger test sections was designed, built and commissioned. High speed imaging was used to correlate thermal/hydraulic measurements with the flow regime visible at various stages along the test section.

1.3: Outline of Thesis

This thesis consists of five chapters structured as follows. Chapter 1 briefly introduces the thesis and highlights the motivation and rationale behind the investigation.

Chapter Two is divided into three sub-sections. The first sub-section introduces the background theories of two-phase flow, followed by a discussion on flow patterns and

flow mapping, and predictive methods for flow pattern transitions, heat transfer calculations, and pressure drop calculations. The second sub-section similarly begins with an outline of the basics of electrohydrodynamics, and then provides more detail on advanced EHD theory with specific relevance to the present study. The final subsection comprises a literature review reporting the major studies in combined two-phase flow with EHD, leading up to the present state of the art and highlighting the gap in convective boiling flow patterns which the research aimed to address through visualisation.

Chapter 3 describes the novel two-phase flow test rig. It explains the rig hardware with its various flow loops, materials and methods of construction, and gives a complete description of the two types of transparent test section utilised, with their associated instrumentation and ancillary equipment. It also describes the commissioning and validation of the rig through a series of energy balances and an error analysis. In addition, the experimental methods, rig operation, rig calculations, and data reduction are detailed.

Chapter 4 is split into three sub-sections. The first sub-section provides details of a series of two-phase flow tests with EHD carried out at a constant heat input on the water heat test section. An initial test was performed at 2% inlet quality without EHD to act as a field-free baseline case. Subsequent tests were then performed with increasing voltage levels of 4 and 8 kV. This format was then repeated with increased inlet qualities of 15, 30 and 45%. Wall thermocouple variations and wall temperature superheat along with overall heat transfer coefficients were obtained and examined in conjunction with high speed video and imagery captured from inside the tube at various locations along the test section. The pressure drop was also examined and related to the high speed videos and images. The results show that while the average heat transfer coefficient improves with applied voltage over the entire range of qualities tested, the level of enhancement tends to decrease with increased inlet quality.

The second subsection of Chapter 4 describes a series of EHD tests on two-phase flow from the water heated test section. Again the inlet quality was maintained at 2% but the heating condition was a constant heat source water inlet temperature. The purpose of this test was two-fold: firstly to elucidate the nature of the flow regime changes with

voltage increased at finer 1 kV increments, and secondly, to better compare the enhancement and penalty associated with EHD. Again, a field-free base case was established and voltage was subsequently increased in 1 kV steps up to 10 kV. Wall temperature data, heat transfer coefficient, and pressure drop were analysed and related to the in-tube flow phenomena captured by the high-speed video along the transparent test section. This chapter showed that heat transfer augmentation at 10kV could be up to 1.5 times the field free case, the trend following an "S" shaped curve with voltage.

The final subsection of Chapter 4 presents experimental results from the ohmically heated second test section. Inlet quality was set to 3% and voltage increased from 0 to 10 kV in 1 kV intervals. This new test section and heating method allowed measurement of the local heat transfer coefficients along the tube allowing pairing of the local heat transfer to particular flow regime patterns. The results show for the conditions tested, that the application of EHD substantially increases the heat transfer coefficient at all measurement locations on the test section. Near the entrance, the top surface heat transfer enhancement reached over 7.2 fold and this decreased monotonically to 2.4 fold at the exit region. The bottom enhancement was more uniform along the heat exchanger ranging between approximately 3 to 4 fold at the highest applied voltage tested.

Chapter 5 presents the conclusions of the thesis and also contains recommendations for future study.

1.4: Thesis Contributions

This thesis contributed to improved knowledge of the specific mechanisms by which EHD forces induce flow regime changes in a two phase flow. The thesis utilised a very novel test section featuring a coated sapphire tube that was completely transparent yet permitted heat transfer so as to allow boiling and an electrical conduit to allow EHD influence. This is the first known apparatus of its type where these demanding technical challenges were overcome.

It was found that EHD augmentation of the heat transfer coefficient was greatest at lowest qualities. This was common in all three test regimes. It was shown that the availability of liquid in close proximity to the electrode, and thus available for redistribution, was a dominant factor in this enhancement. Fluid redistribution by EHD forces served to re-wet dry areas of the tube, and also to disturb the stratified liquid layer, both increasing heat transfer. In addition, EHD forces greatly affected nucleated bubble behaviour within the liquid layer causing oscillation and climbing of bubbles which served to increase wetting. Higher EHD forces were also found to create liquid jets which contributed to rewetting and liquid re-distribution.

In addition, the heat transfer gains from EHD were also found to outweigh the associated penalties by at least 15 times. And finally, for a given amount of heat input, EHD was found to improve heat transfer at lower superheat temperatures.

The following journal articles are also a direct result of this research;

G J McGranaghan, A J Robinson, "EHD Augmentation of the Heat Transfer Rates for Convective Boiling of HFE7000", *Heat Transfer Engineering* (accepted)

G J McGranaghan, A J Robinson, "The Mechanisms of Heat Transfer during AC Electrohydrodynamically Enhanced Convective Boiling", *Experimental Thermal Fluid Science* (submitted)

G J McGranaghan, A J Robinson, "The Influence of Inlet Quality and Applied Voltage on EHD Enhanced Convective Boiling", *Experimental Thermal Fluid Science* (in preparation)

Chapter 2: Electrohydrodynamically Augmented Two-Phase Flow

Two-phase flow boiling is not an easily modelled phenomenon due to the many factors involved, such as liquid velocity, vapour velocity, wall friction, interfacial shear, nucleation, buoyancy and vapour generation. Furthermore, coupling two-phase flow boiling with EHD serves to make an already non-trivial scenario more complex. Therefore this chapter attempts to provide a step by step introduction to both topics before merging them. This section details the basic definitions of two-phase flow and describes the basic forces. It progresses to methods of heat transfer, pressure drop and void fraction prediction, finishing in an overview of the state of the art. The subject of electrohydrodynamics or EHD is then introduced so as to familiarise the reader with the basic terms and concepts. The topic is then developed with specific reference to EHD pertaining to two-phase flows of dielectric fluids. Finally, a review of experimentation and research that couples two-phase flow with electrohydrodynamics will be given to convey the scope of the major historical research and to summarise the current state of the art, highlighting the need which the current study addresses.

2.1: Two Phase Flow

Two–phase flow describes the phenomena arising when solid/liquid, solid/gas or liquid/gas phases occur together in the same channel or tube. For heat transfer applications, liquid/vapour is the most common occurrence, and as it is the subject of this research, any subsequent mention of two-phase flow in the text will automatically refer to this liquid/vapour condition. As well as the forces of inertia, viscosity and pressure found in single phase flow, two-phase flow has the added complexities of interfacial forces between the phases, the interference of phase streams, and the tendency of the liquid to adhere to the tube wall surface. During any flow boiling process, sub-cooled or saturated liquid will enter at one end, and at the outlet, a mixture

of liquid and vapour or superheated vapour will exit depending on the amount of heat added in the heat exchanger. As the fluid changes from liquid to vapour, the two-phase mixture undergoes various morphologies or flow regimes, all of which strongly influence the heat-transfer characteristics. The flow regime is also affected by the mass flow rate and quality, *x*, of the fluid, as well as the angle of inclination of the flow. In the case of a two-phase flow heat exchanger, the local HTC is dependent on the local flow regime and on whether evaporation or condensation is occurring.

For convective boiling applications, maximum liquid wetting of the heated surface is desirable. Thus perturbations to the flow pattern which cause fluid mixing (thereby disturbing the thermal boundary layer), or surface wetting are beneficial. In condensation, wetting of the wall is also important but high HTCs are promoted by minimisation of the liquid condensate layer thickness. In order to better understand the important terms relating to two-phase flow, consider the simple two-phase flow model shown in Figure 1.

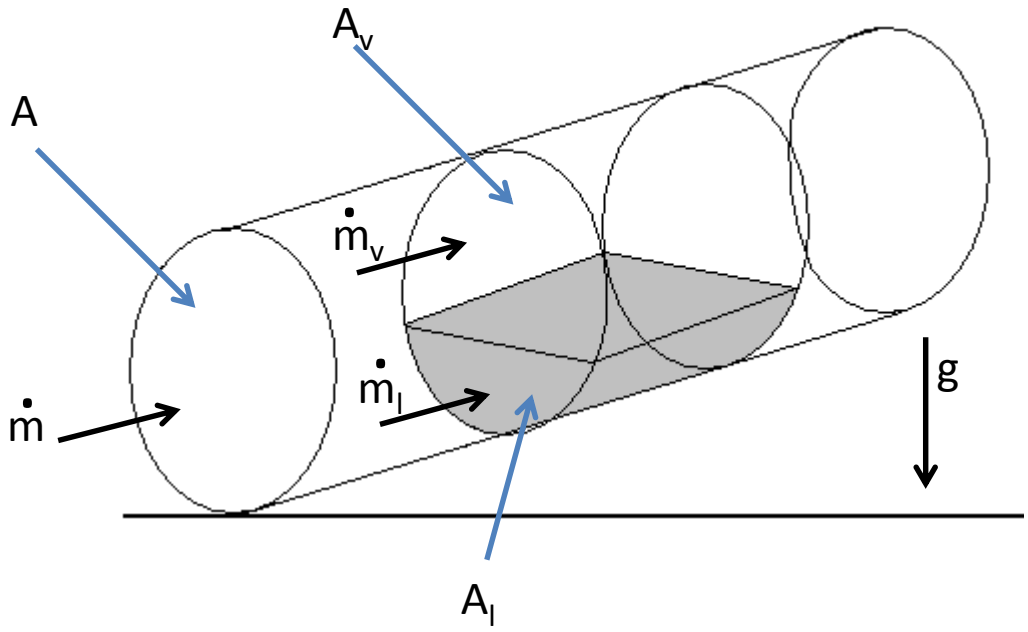

Figure 1: Idealised model of two-phase flow in an inclined tube, adapted from Carey [14]

The total mass flow rate through the tube is the sum of the liquid and gas mass flow rates respectively.

$$\dot{m} = \dot{m}_v + \dot{m}_l \tag{1}$$

The quality or dryness fraction (ratio of vapour flow to total flow) x, is given by

$$x = \frac{\dot{m}_v}{\dot{m}} \tag{2}$$

For a tube of cross sectional area A, the mass velocity (mass flux) G is defined as

$$G = \frac{\dot{m}}{A} \tag{3}$$

There the total cross sectional area, A must equal the sum of cross sectional areas occupied by the vapour and liquid phases such that

$$A = A_v + A_l \tag{4}$$

The void fraction α, is defined as the ratio of the gas flow cross sectional area A_v to the total cross sectional area

$$\alpha = \frac{A_v}{A} \tag{5}$$

The superficial liquid and gas fluxes j_l and j_v are defined as the liquid and vapour velocities if they were to flow alone along the entire cross section.

$$j_l = \frac{G(1-x)}{\rho_l} \tag{6}$$

and

$$j_v = \frac{Gx}{\rho_v} \tag{7}$$

The Reynolds numbers for vapour and liquid phases are given by

$$\mathrm{Re}_v = \frac{GD_h}{\mu_v}\frac{x}{\alpha} \tag{8}$$

and

$$\mathrm{Re}_l = \frac{GD_h}{\mu_l}\frac{1-x}{1-\alpha} \tag{9}$$

Another relevant dimensionless number is the Froude number which is the ratio of inertia forces to gravitational forces

$$Fr = \frac{u^2}{gD_h} \tag{10}$$

For the liquid phase this is expressed as

$$Fr_l = \frac{G^2}{\rho_l^2 gD_h} \tag{11}$$

2.1.1: Upward Vertical Flow

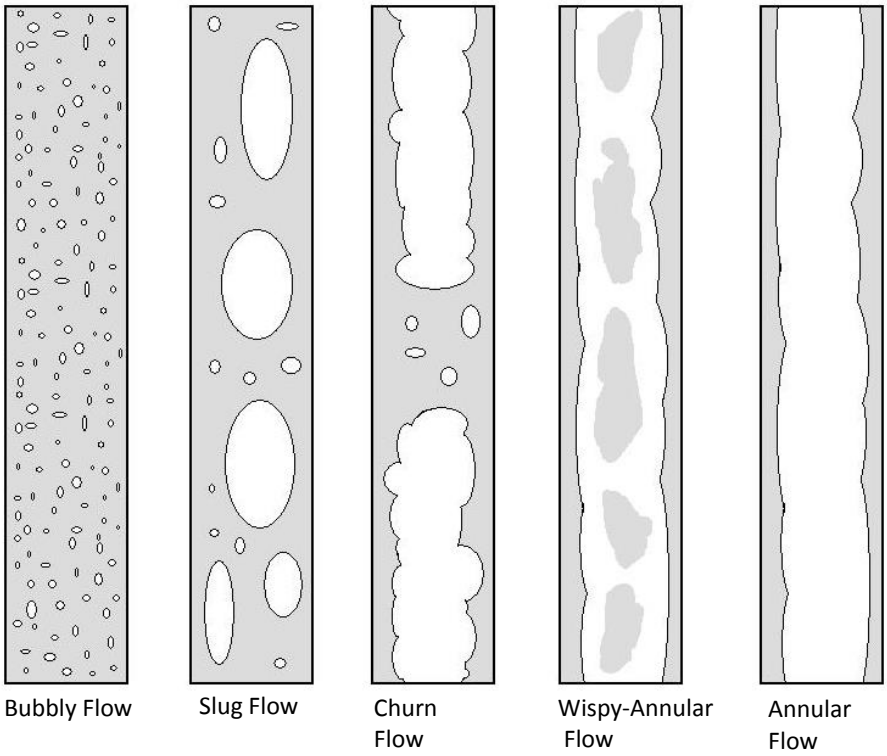

Figure 2: Flow regimes in vertical upward co-current gas/liquid flow

Although the current study deals with horizontal flow, vertical flow will be introduced as many of the flow patterns are subsequently found in a modified form in horizontal flow. Figure 2 details flow regimes as found in co-current vertical upward vapour/liquid flow. "Bubbly flow" usually occurs at low qualities and consists of small discrete bubbles dispersed within the liquid phase, the mean bubble diameter being much smaller than the channel diameter. As the quality increases, individual bubbles coalesce into slugs that almost fill the cross sectional of the channel or tube. This is usually referred to as "slug flow". At higher vapour qualities, the vapour phase dominates the central area of the flow channel with the liquid remaining at the wall forming an annular flow film.

At intermediate qualities however, two additional regimes occur. For flows with high vapour and liquid flow rates, annular flow occurs, but with additional entrained "wisps" of liquid in the vapour core. This is referred to as "wispy annular flow".

At intermediate quality, but with a lower liquid flow rate, an unstable region occurs where the imposed pressure gradient and gravity are similar in magnitude to the vapour shear on the liquid vapour interface. Although the mean velocity of the flow remains positive, the liquid experiences alternate positive and negative motion as gravity and liquid/vapour forces interact, thus producing an irregular interface. This is referred to as “churn flow”.

2.1.2: Horizontal Flow

Figure 3 depicts the typical horizontal two-phase flow regimes. A similarity in pattern with vertical flow regimes is clear, except that the influence of gravity acts at 90° to the fluid flow. The denser liquid settles to the lower parts of the tube because of gravitational forces, while buoyancy causes the bubbles or slugs to migrate to the top of the tube.

As with vertical flow, “bubbly flow” is associated with lower qualities. In horizontal flow however the bubbles concentrate mainly along the top of the tube. With higher liquid velocity, shear forces may promote more even distribution of bubbles within the tube.

As the quality increases, coalescence leads to an increase in bubble size resulting in large oblong bullet shaped plugs, hence the title “plug flow”. These tend towards the top of the tube due to buoyancy forces.

With higher qualities combined with low flow rates, gravity and buoyancy provide a separation effect and “stratified flow” occurs where the liquid and vapour are separated by a smooth interface.

As flow rate and quality increase further in the stratified regime, the vapour/liquid boundary develops ripples caused by shear from the higher velocity vapour. These ripples then result in “wavy flow”: the waves may begin to climb up the tube sides, and the liquid layer on the bottom may be subject to thinning.

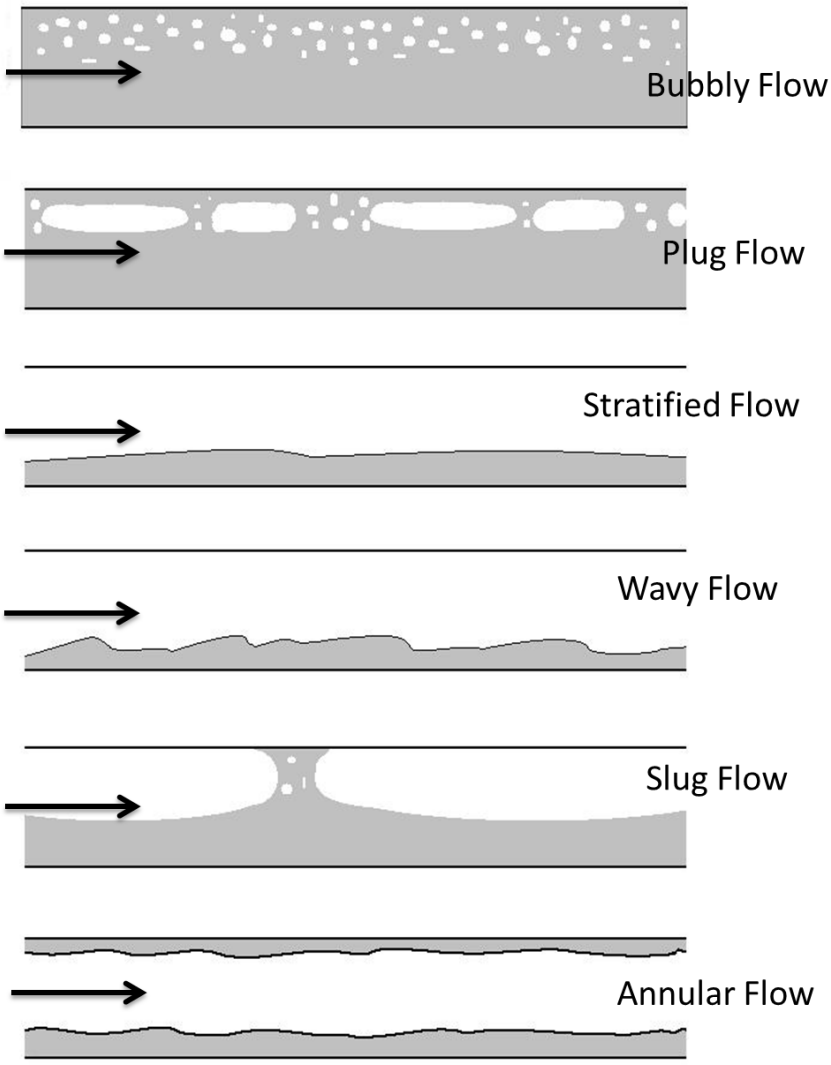

Figure 3: Flow regimes as observed in horizontal co-current gas liquid flow.

With higher liquid flow rates, the amplitude of the waves grows so large that the crests make contact with the upper surface of the tube or channel, forming a bridging effect. This forms large slugs similar to that found in vertical flow, and hence this is also known as “slug flow”.

“Annular flow” is the next stage as the liquid and vapour core velocity increases still further; the more dense liquid remains at the outer circumference while the much faster vapour travels in the centre. Droplets of liquid may be suspended in the vapour core as a mist. This is similar to annular flow as found in a vertical tube; however, the liquid film is not as evenly distributed, being thicker at the bottom of the tube due to gravity. Often the liquid film is wavy due to disturbance by the vapour core, and if dryout occurs at the top of the tube, the flow is then re-classified as stratified wavy.

2.1.3: Single Phase Heat Transfer Correlations

Single phase heat transfer correlations can generally be divided into two areas, laminar flow and turbulent flow. In the fully developed laminar flow region of a tube flow, the expression for a constant heat flux has been shown to reduce to

$$Nu_D = \frac{hD}{k} = 4.36 \tag{12}$$

while for a constant wall temperature again this reduces to a constant

$$Nu_D = \frac{hD}{k} = 3.66 \tag{13}$$

For turbulent correlations, the calculations are more involved but again have been reduced to a form known as the Colburn equation

$$Nu_D = 0.023 \mathrm{Re}_D^{.8} \mathrm{Pr}^{.33} \tag{14}$$

This is then modified to become the more preferred Dittus-Boelter equation

$$Nu_D = 0.023 \mathrm{Re}_D^{.8} \mathrm{Pr}^{n} \tag{15}$$

where n=0.4 for heating and 0.3 for cooling. A further modification of the Dittus-Boelter equation to take account of property variations is the Sieder-Tate correlation

$$Nu_D = 0.027 \mathrm{Re}_D^{.8} \mathrm{Pr}^{.33} \left(\frac{\mu}{\mu_s} \right)^{0.14} \tag{16}$$

While the above forms are simple to use, more accuracy can be achieved via the more complex correlation attributed to Petukhov

$$Nu_D = \frac{\left(f/8\right)\mathrm{Re}_D\,\mathrm{Pr}}{1.07 + 12.7\left(f/8\right)^{0.5}\left(\mathrm{Pr}^{2/3} - 1\right)} \tag{17}$$

To accommodate smaller Reynolds numbers Gnielinski modified this form to become

$$Nu_D = \frac{\left(f/8\right)\left(\mathrm{Re}_D - 1000\right)\mathrm{Pr}}{1 + 12.7\left(f/8\right)^{0.5}\left(\mathrm{Pr}^{2/3} - 1\right)} \tag{18}$$

All the correlations in this single phase subsection, as well as their range of validity and calculation details for the friction factor "f", can be found in more detail in common heat transfer textbooks such as that of Bejan, Holman, and Incropera [15-17].

2.1.4: Two Phase Flow Mapping

In contrast to correlations for single phase heat transfer, where the basic form is dependent totally on liquid properties, the development of a "generalised" two-phase heat transfer correlation is more complex due to the liquid and vapour phases, and also due to the interaction of both phases in the various types of flow regime found. Figure 4 illustrates qualitatively the variation in heat transfer coefficient with flow regime in convective boiling along a horizontal tube under a moderate tube superheat. The heat transfer coefficient increases in the early stages as nucleate boiling becomes more dominant. As the amount of vapour increases, annular flow begins to take over and causes a further increase in heat transfer. However, as vapour amount increases further, dryout begins to occur on the tube wall and this causes a sharp decrease in heat transfer coefficient.

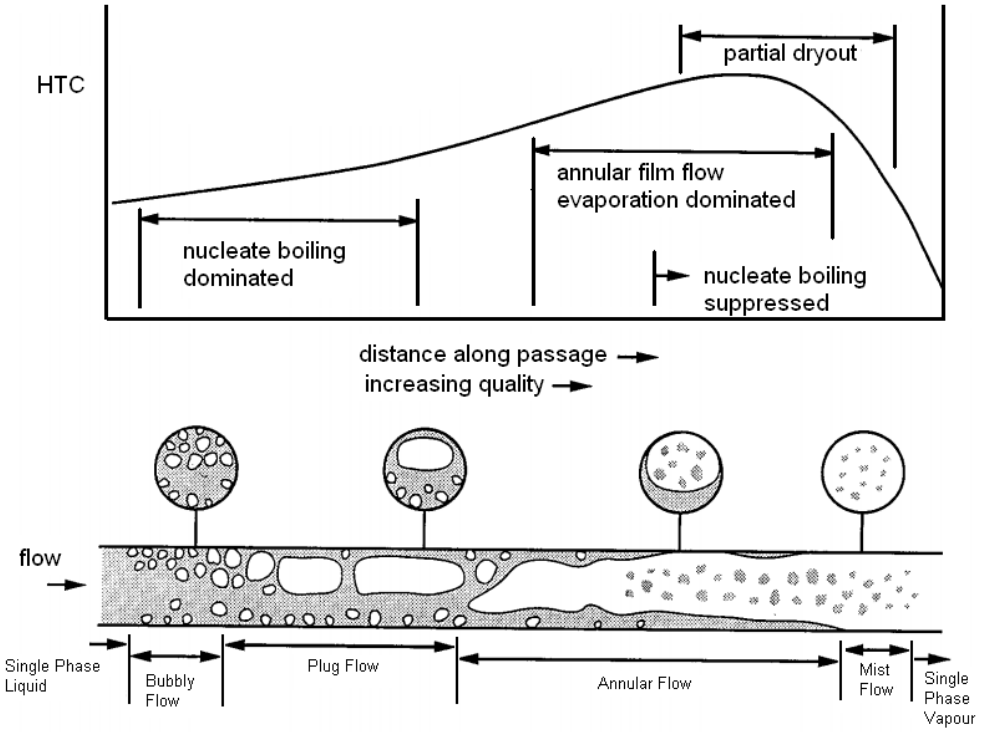

Figure 4: Variation of convective boiling heat transfer coefficient with flow regime, adapted from Kreith and Boehm [18]

According to Taitel [19], no less than 11 parameters can affect the flow pattern through a tube. These are shown in Table 1.

Table 1: Parameters which Influence Flow Pattern

	Parameter	Symbol	Unit
1	Liquid superficial velocity	j_l	m/s
2	Gas superficial velocity	j_v	m/s
3	Liquid density	ρ_L	kg/m^3
4	Gas density	ρ_G	kg/m^3
5	Liquid viscosity	μ_L	kg/s m
6	Gas viscosity	μ_G	kg/s m
7	Pipe diameter	D	m
8	Acceleration due to gravity	g	m/s
9	Surface tension	σ	kg/s^2
10	Pipe roughness	ε	m
11	Pipe inclination	β	°

Therefore, construction of heat transfer predictions must take into account, not only the parameters found in single-phase relations, such as geometric terms and dimensionless property characteristics like Reynolds and Prandtl numbers, but must also somehow account for the extra vapour properties, and include how the liquid and vapour are interacting. Hence studies revolve around precise determination of these flow regimes by varying flow rates, inlet quality and heat input. Thus flow regime mapping began as an aid to predict the flow regimes for given conditions where, once the flow regime was first determined, an applicable correlation could then be applied.

While certain elementary correlations have been put forward for two-phase flow, their derivation may not take account of the many flow regime factors discussed above. A more complete discussion of these correlations will be given in subsection 2.1.5: Two Phase Heat Transfer Correlations.

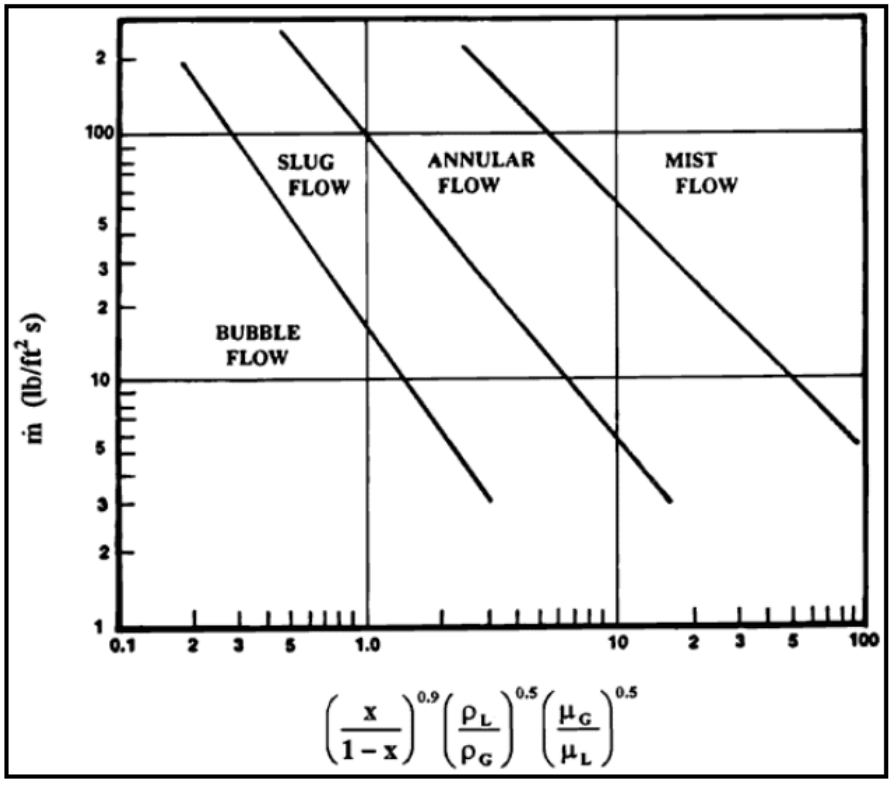

Figure 5: Vertical tube flow pattern map by Fair [20]

Two of the early maps for vertical flow were devised by Fair (Figure 5) in 1960 and Hewitt and Roberts (Figure 6) in 1969 [21]. The Fair map is used by first calculating the value of the x-axis and then the mass flux on the y-axis. The intersection of both

determines if the point is in the bubbly, slug, annular or mist flow regime. The Hewitt and Roberts map relates the superficial momentums of liquid and vapour phases. The flow regimes were determined by visual observation along a transparent tube, and the boundary lines between regimes demarcate the middle of a transition between those regimes.

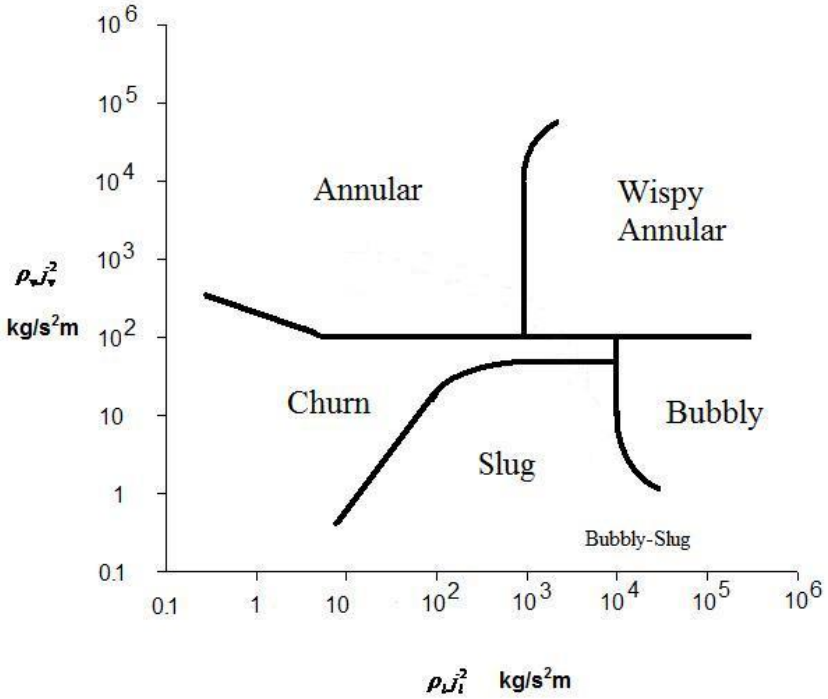

Figure 6: Flow regime map proposed by Hewitt and Roberts [21]

A horizontal two-phase flow map was produced by Baker [20] in 1954 for use in the oil industry. The mass velocities of both liquid and vapour are first calculated. Then Baker introduces a gas-phase parameter λ, and a liquid-phase parameter, Ψ, which are calculated using;

$$\lambda = \left(\frac{\rho_G}{\rho_{air}} \frac{\rho_L}{\rho_{water}} \right)^{0.5} \tag{19}$$

$$\psi = \left(\frac{\sigma_{water}}{\sigma} \right) \left[\left(\frac{\mu_L}{\mu_{water}} \right) \left(\frac{\rho_{water}}{\rho_L} \right)^2 \right]^{0.3333} \tag{20}$$

The values of the x and y axes are then calculated to determine the flow regime. The Baker map is shown in Figure 7.

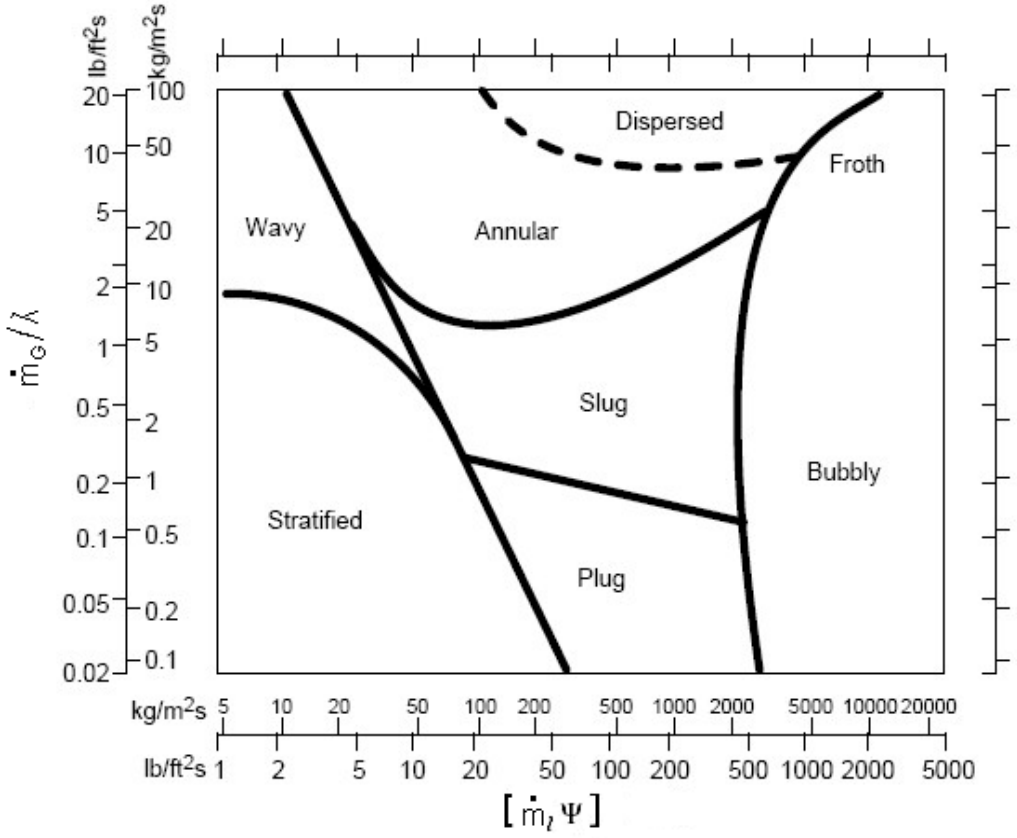

Figure 7: Baker flow map for horizontal tubes

From these flow maps, research focused on the delineation of the boundaries between flow regimes. Various analytical expressions for the transitions between these regimes have been obtained by various researchers and are now summarised.

In 1962, Radovcich and Moissis [22] proposed that bubble collision frequency could determine the transition from bubbly flow to slug flow at void fractions (α) greater than 0.3. Taitel and Dukler [23] later analysed this thesis further and proposed the relation

$$\frac{j_l}{j_v} = 2.34 - 1.07 \frac{[g(\rho_l - \rho_v)]^{.25}}{j_v \rho_l^{.5}} \tag{21}$$

which would predict the conditions for transition from bubbly to slug flow. Increases in quality can result in the transition from slug flow to churn flow. Due to the

buoyancy of the bubble slug, it moves upwards at a higher velocity than the two–phase flow average velocity, while the liquid actually moves downward. With further increases in quality and resultant void fraction, the plug bubble size increases and a Helmholtz type of instability arises precipitating the breakdown of the large plug bubbles and giving rise to churn flow. This transition was predicted to occur at conditions presented in a relation proposed by Porteus [24]

$$\frac{j_l}{j_v} = 0.105\frac{[gD(\rho_l - \rho_v)]^{0.5}}{j_v \rho_l^{.5}} - 1 \tag{22}$$

where D is the tube diameter. However Taitel and Dukler [23] argued that for

$$(j_l + j_v)/(gD)^{0.5} > 50 \tag{23}$$

the slug to churn transition occurs when

$$j_l / j_v = 0.16. \tag{24}$$

The transition from churn flow to annular flow arises when the shear stress of the vapour core combined with the imposed pressure gradient balances the gravity force on the liquid film. Wallis [25] postulated that based on theoretical models, this occurred approximately when

$$\left[\frac{j^2{}_v \rho_v^{.}}{[gD(\rho_l - \rho_v)]}\right]^{0.5} = 0.9 \tag{25}$$

Taitel and Dukler [23] proposed a more involved correlation to predict the transition from churn to annular flow

$$\left[\frac{j_v \rho_v^{0.5}}{[g(\rho_l - \rho_v)\sigma]^{0.25}}\right] = 3.09\left[\frac{(1 + 20X + X^2)^{0.5} - X}{1 + 20X + X^2)^{0.5}}\right] \tag{26}$$

where X (the Martinelli parameter) is defined as

$$X = \left[\frac{(dP/dz)_l}{dP/dz)_v} \right]^{0.5} \tag{27}$$

Here dP/dz is the frictional pressure gradient for the liquid and vapour phases as if they were flowing alone in the pipe, and methods of calculation are listed in Carey [14].

Taitel and Dukler developed the horizontal map shown in Figure 8, based on an analysis of flow transition mechanisms combined with empirical choice of specific parameters. The three part map uses the Martinelli parameter X, the gas Froude number Fr_G and the parameters T and K. The gas Froude number is defined as

$$Fr_g = \frac{\dot{m}_g}{\left[\rho_g \left(\rho_l - \rho_g\right) d_i g\right]^{0.5}} \tag{28}$$

Taitel and Dukler define T as the parameter

$$T = \left[\frac{\left|\left(dp/dz\right)_l\right|}{g\left(\rho_l - \rho_g\right)} \right]^{0.50} \tag{29}$$

where g in both cases is the acceleration due to gravity =9.81 m/s^2.
The parameter K is defined as

$$K = Fr_g \, \mathrm{Re}_l^{0.5} \tag{30}$$

The pressure gradient of the flow for phase k (where k is either *l* or *g*) is given by

$$(dp/dz)_k = -\frac{2 f_k \dot{m}_k^2}{\rho_k d_i} \tag{31}$$

where f_k , is the friction factor, which depends on the flow Reynolds number. If Re_k<2000, then the laminar flow friction factor is used

$$f_k = \frac{16}{\mathrm{Re}_k} \tag{32}$$

If Re_k>2000, then the turbulent flow friction factor is used

$$f_k = \frac{0.0079}{\mathrm{Re}_k^{0.25}} \tag{33}$$

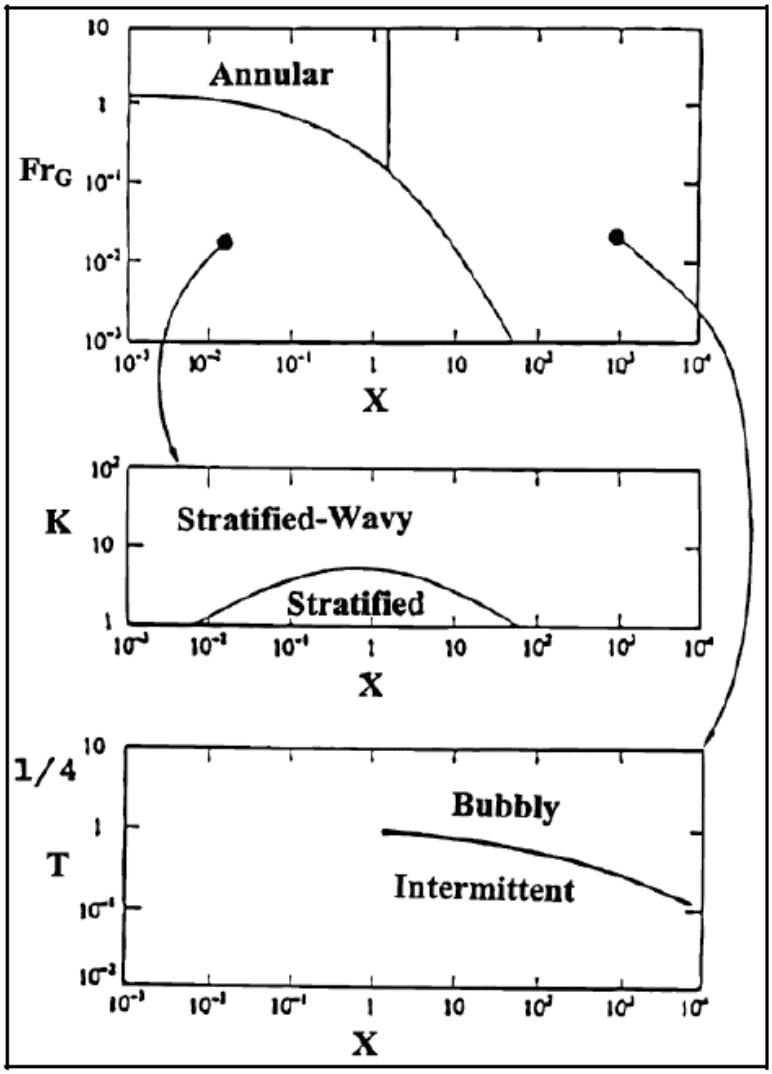

Figure 8: Taitel and Dukler Two-phase Flow Pattern Map, from [20]

To use the map, the Martinelli parameter X and Fr_g are found and plotted on the top graph. If the point falls in the annular region, then the flow is annular. If the point falls in the lower left area, then K must be calculated. Then using K and X in the middle graph, confirms if the flow regime is either stratified wavy or fully stratified. If the co-ordinates of X and Fr_g lie in the right zone of the top graph, then T must be calculated.

Again, using T and X in the lower graph, the flow regime can be confirmed as either bubbly or intermittent flow. Although the Taitel and Dukler map is more complex to calculate, it does attempt to incorporate in the final calculation the flow characteristics found at various regimes.

Hashizume [26] in 1983 presented a flow map based on a modified form of the Baker map. This is shown in Figure 9. Hashizume found that the boundaries between the original Baker map and his modified map differed considerably due to the dissimilarity in surface tension properties of the refrigerant liquid and vapour from those of water and air as used by Baker.

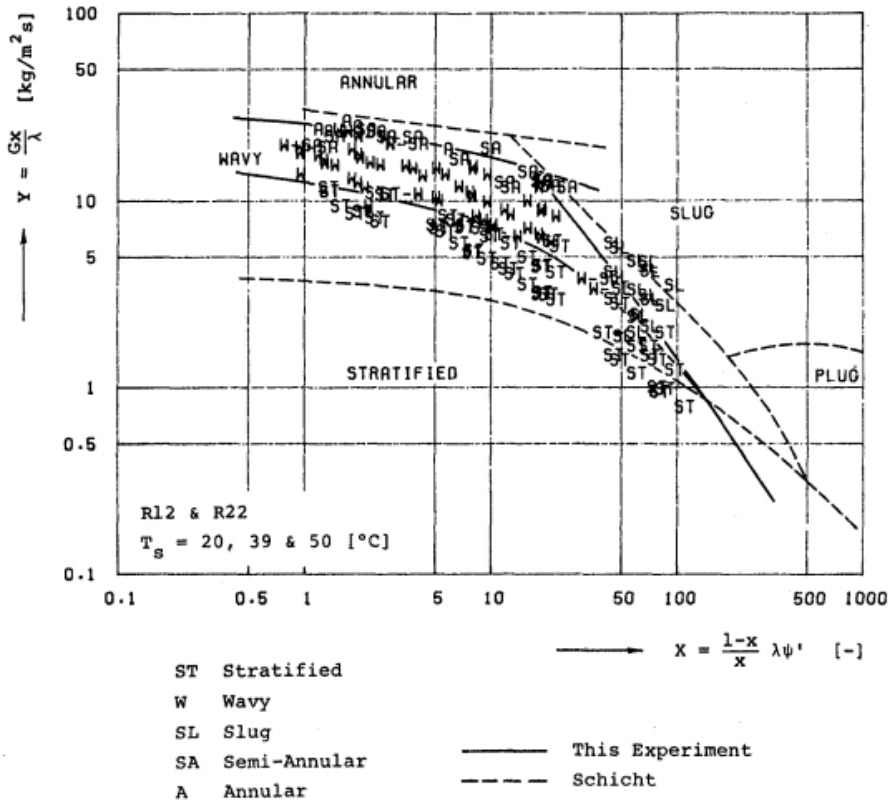

Figure 9: Hashizume two-phase flow map[26]

Steiner in 1993 produced a modification of the Taitel and Dukler map, the form of which is shown in Figure 10. The logarithmic axes have been replaced by linear axes of quality and mass flux, simplifying the use of the map although it is now fluid specific.

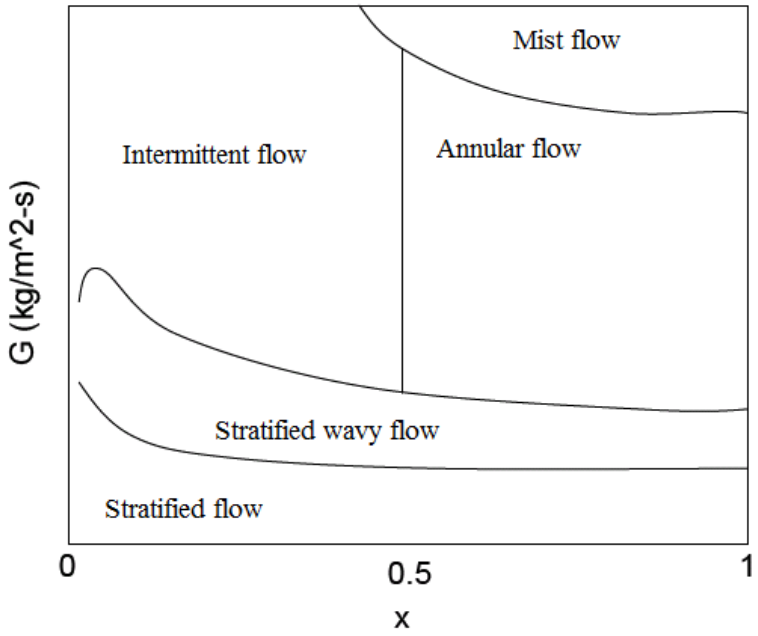

Figure 10: Flow map form as proposed by Steiner

Despite the attempt by Taitel and Dukler to integrate realistic fluid conditions into their model, Kattan, Thome and Favrat [27] found that the Taitel and Dukler model only achieved a 50% success rate in identification in a range of flow patterns studied. In addition, they found that a threshold between two regimes defined by the liquid Froude number (Eq.(28)) could be off by significant amounts compared to the experimental observations. Consequently, Kattan *et al*. [28-30] published a modified version of the Steiner map, itself a development of the Taitel and Dukler map, which is shown in Figure 11.

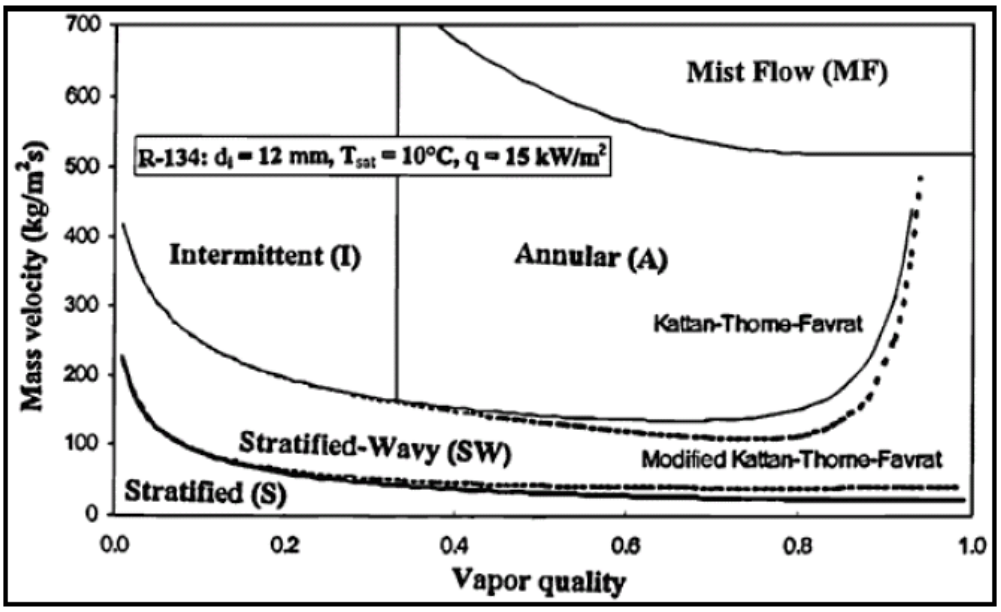

Figure 11: Flow map of Kattan, Thome and Favrat [28], sourced from [28]

The Kattan *et al*. map plots vapour quality on the x axis and mass velocity on the y, with curves and lines to delineate the boundaries between regimes. The Kattan *et al*. map places plug and slug flows in the Intermittent (I) classification, where the tube wall is assumed to remain constantly wetted due to the large waves which ensure a film of liquid on the top of the tube. Due to the axes being linear as in the Steiner map, interpretation is simpler than other log-log map formats. In addition, the Kattan *et al*. map avoids the use of iterative calculations by incorporating the Steiner modified version of the Rouhani-Axelsson drift flux model [30, 31] used to calculate the cross-sectional void fraction, ε. Complete equations for the curves defining the transitions between regimes can be found in the Wolverine Heat Transfer Engineering Data book III [20] and also in the publications of Kattan *et al*. [28-30].

Another illustration of the Kattan et al map is shown in Figure 12. In this figure, the inset pictures help to illustrate the various flow regimes of intermittent, stratified, stratified-wavy, annular, and mist.

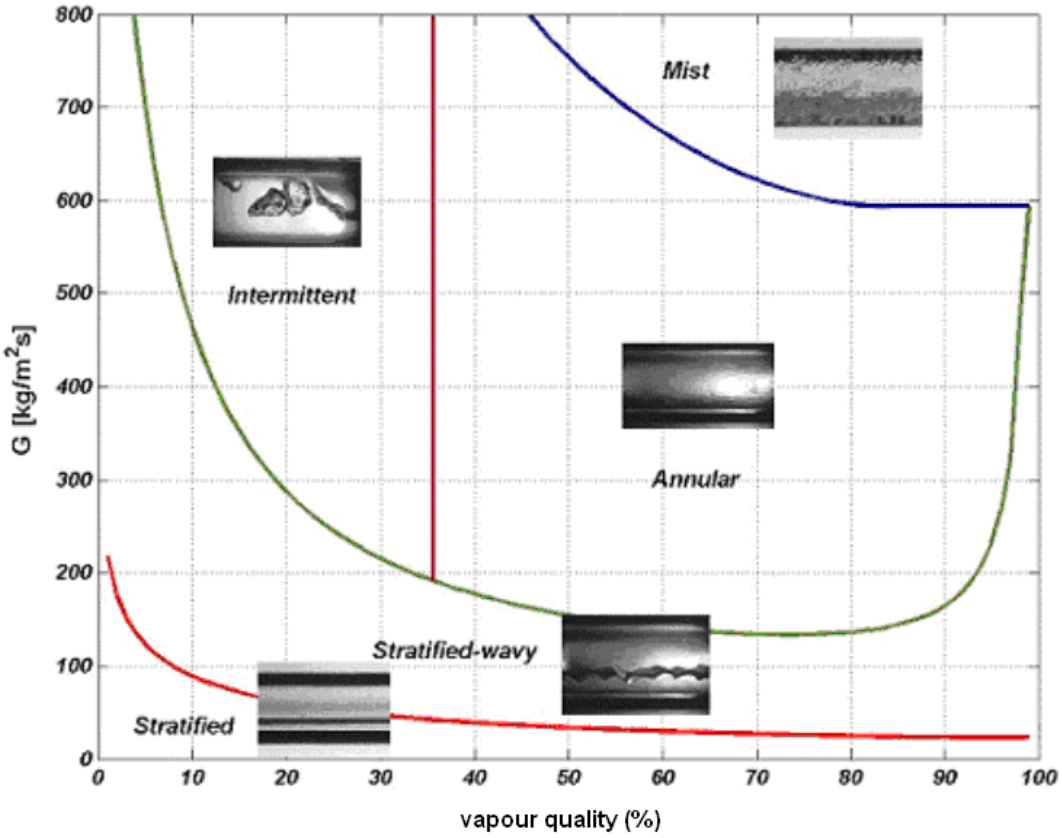

Figure 12: Typical two-phase flow patterns dependent on mass flux and quality overlaid on a Kattan *et al*. type flow map [20]

The final flow map to be discussed is a follow-on from the Kattan *et al*. map. Wojtan, Ursenbacher and Thome [31] found that the flow regime during evaporation is highly influenced by nucleate boiling, evaporation of liquid, and acceleration of the flow as a result of this phase change. Consequently, Wojtan *et al*. revisited the map of Kattan *et al*., using improved observation techniques, and proposed that the stratified wavy region be divided into three regions, slug, slug and stratified wavy, and stratified wavy. The newer Wojtan *et al*. map is shown in Figure 13. In this map, I is intermittent, S is stratified, SW is stratified wavy, and A is annular. The dashed lines D and M indicate revised boundaries of the transition to dryout and mist flow regions.

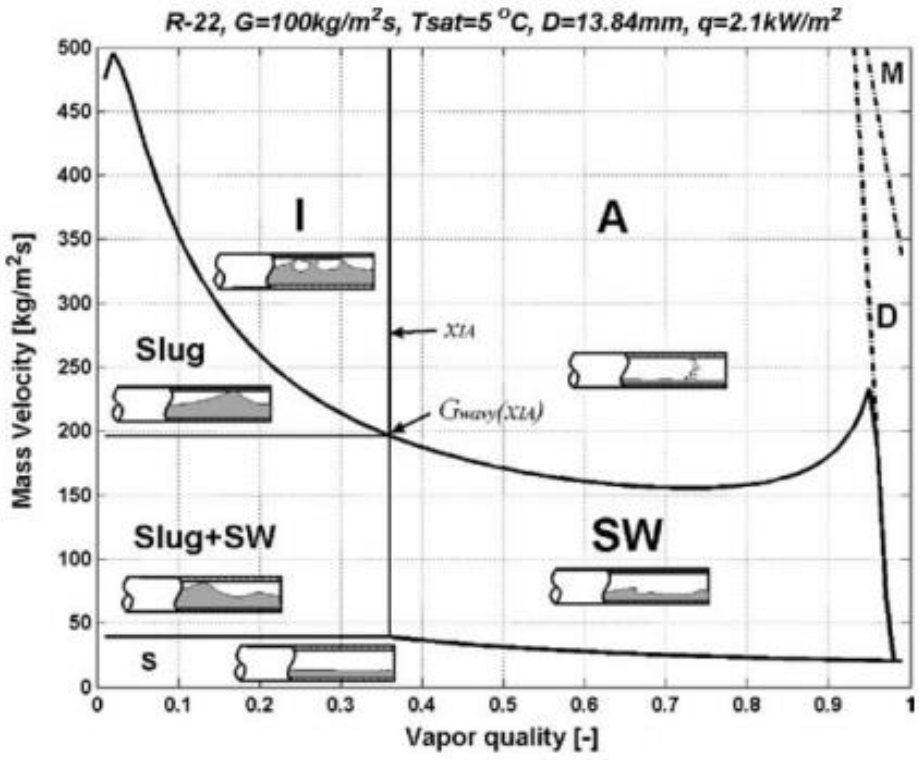

Figure 13: Flow map of Wojtan, Ursenbacher and Thome, image from [31]

Another modification was made to the transition curve between stratified and stratified wavy below vapour qualities of x_{IA}, where the intermittent to annular transition takes place, thus accuracy below G_{wavy} is improved.

2.1.5: Two Phase Heat Transfer Correlations

Earlier methods of horizontal flow prediction in plain tubes were extensions of those derived from vertical upward flows. One of the earliest developed and widely used was the Chen correlation from 1966 [32]. Chen proposed a superpositional correlation for vertical channels that calculated the nucleate boiling contribution based on the Forster-Zuber pool boiling equation and then added the convective non-boiling contribution based on the Dittus Boelter equation (15). The final form is

$$\alpha_{tp} = \alpha_{FZ} S + \alpha_L F \tag{34}$$

where

$$\alpha_{FZ} = 0.00122\left[\frac{k_L^{0.79} c_{pL}^{0.45} \rho_L^{0.49}}{\sigma^{0.5} \mu_L^{0.29} h_{LG}^{0.24} \rho_G^{0.24}}\right] \Delta T_{sat}^{0.24} \Delta p_{sat}^{0.75} \quad (35)$$

and

$$\alpha_L = 0.023 \,\mathrm{Re}_D^{4/5}\, \mathrm{Pr}^{2/5} \left(\frac{k_L}{d_i}\right) \quad (36)$$

S is a nucleate boiling suppression factor, intended to take account of a steeper temperature gradient occurring in the liquid near the wall under forced convection conditions, which would lessen nucleation from that found in pool boiling. The other factor, F, is a two-phase multiplier which is used to augment the single phase contribution given by the Dittus-Boelter correlation. Details of both factors can be found in [20]. The difference between the inner tube wall and the liquid saturation temperature is

$$\Delta T_{sat} = (T_{wall} - T_{sat}) \quad (37)$$

Likewise the pressure difference, Δp_{sat} is obtained from the vapour pressure of the fluid at that wall temperature, giving

$$\Delta p_{sat} = (p_{wall} - p_{sat}) \quad (38)$$

This correlation is applicable for qualities $0.01<x<0.71$ as long as the heated wall does not dry out. Iteration is necessary if the heat flux is specified as T_{wall} and p_{wall} are often not known.

The Shah correlation [33] developed in 1982, provided a graphical alternative to the Chen correlation and can be used in horizontal as well as vertical channels. The chart from his original paper is reproduced in Figure 14.

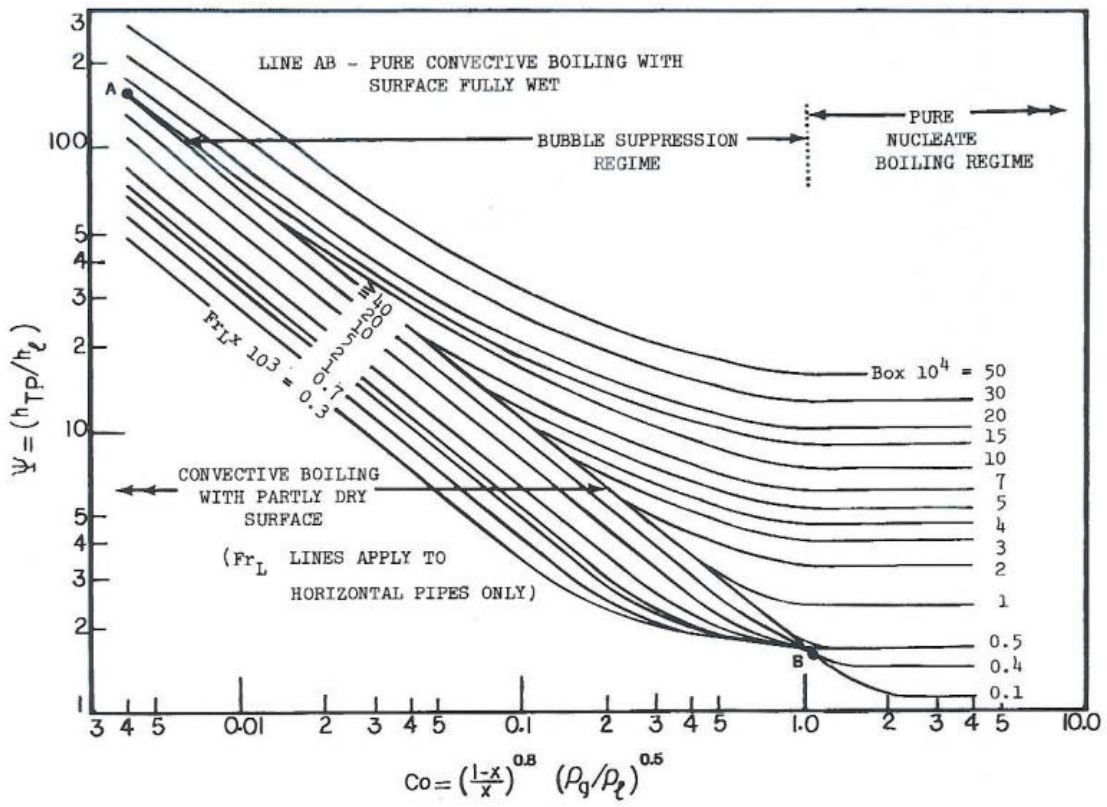

Figure 14: Chart of Shah correlation, image from [33]

To use the chart, one first had to calculate the dimensionless parameters C_0, the boiling number Bo and the Froude number Fr_L. For a vertical tube, the parameter C_0 was then plotted on the x-axis and drawn vertically upward until it intersected the Bo line, whereupon a horizontal line was then drawn leftwards to intersect the y axis. Fr, being applicable to vertical tubes, was neglected. For horizontal tubes, a line was plotted from C_0 as before but only to the intersection of the Fr number. Then a horizontal line was extended to the right to intersect the line A-B. From here another vertical line was extended to reach the Bo line and another horizontal line extended leftwards to read off the augmented heat transfer. Full details of the dimensionless parameters are given in Shah [33] and Collier [34].

The Chen correlation was revisited by Gungor and Winterton [35] in 1986 who proposed a modified form after studying over 3690 data points for water, ethylene glycol and various refrigerants, for both vertical upward and downward flows and horizontal flows.

The basic equation became

$$\alpha_{TP} = E\alpha_f + S\alpha_{nb} \tag{39}$$

where α_f was calculated using the Dittus-Boelter equation but using the local liquid fraction of the flow i.e., G(1-*x*). This convective component was then multiplied by the new convection enhancement factor E

$$E = \left[1 + 24.000Bo^{1.6} + 1.37\left(\frac{1}{X_{tt}}\right)^{0.86}\right] \tag{40}$$

where X_{tt} is the Martinelli parameter as seen before, but in this case calculated as

$$X = \left[\frac{(dP/dz)_l}{dP/dz)_v}\right]^{0.5} = \left(\frac{1-x}{x}\right)^{0.9}\left(\frac{\rho_g}{\rho_f}\right)^{0.5}\left(\frac{\mu_f}{\mu_g}\right)^{0.1} \tag{41}$$

The nucleate boiling component was based on the reduced pressure correlation derived by Cooper [36]. This expression gives the heat transfer coefficient in W/m^{2}K.

$$\alpha_{nb} = 55p_r^{0.12}(-0.4343\ln p_r)^{-0.55}M^{-0.5}q^{0.67} \tag{42}$$

where M is the molecular weight, q is the heat flux in W/m^2 and p_r is the reduced pressure which is the ratio of the saturation pressure p_{sat} to the critical pressure p_{crit}. Gungor and Winterton proposed an empirically derived boiling suppression factor S

$$S = \left[1 + 0.00000115E^2\,\mathrm{Re}_f^{1.17}\right]^{-1} \tag{43}$$

with Re_f also based on G(1-*x*).

When compared with their database, the Gungor and Winterton method gave a mean deviation of ±21.4% compared with ±57.7% given by the Chen correlation and ±21.9% given by the Shah correlation. This provides a good independent verification of the Shah correlation given that it was developed using a different database.

In 1992, Steiner and Taborek [20, 34, 37] provided a mechanistic model which would take into account the principles of pool and convective boiling terms. They proposed combining both convective and nucleate boiling contributions using a power law of the form

$$h_{tp} = \left[(h_{nb})^n + (h_C)^n \right]^{\frac{1}{n}} \tag{44}$$

Steiner and Taborek proposed that the following limits should apply to evaporation in vertical tubes: For heat fluxes below the threshold for the onset of nucleate boiling ($q'' < q''_{ONB}$), the nucleate boiling contribution should not be included, only the convective contribution.

For very large heat fluxes, the dominative term should be nucleate boiling.

When the inlet quality is zero, the two-phase heat transfer coefficient, h_{tp}, should equal the single-phase liquid convective heat transfer coefficient when heat flux is less than the heat flux for the onset of nucleate boiling ($q'' < q''_{ONB}$), but, h_{tp} should correspond to that plus h_{nb} when $q'' > q''_{ONB}$.

When x = 1.0, h_{tp} should equal the vapour-phase convective coefficient (the forced convection coefficient when the total flow is vapour only).

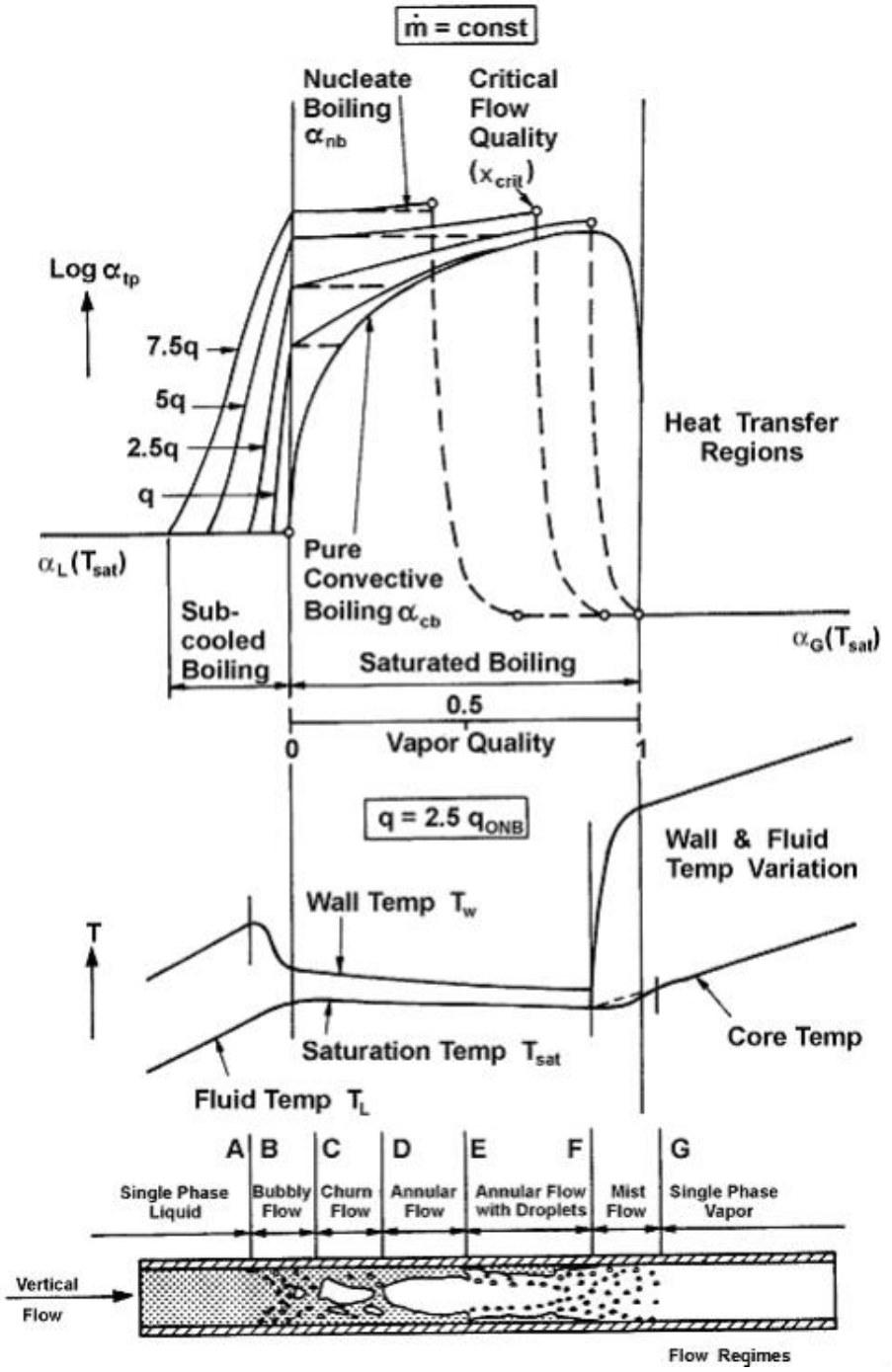

Figure 15: Steiner-Taborek description of boiling processes in a vertical tube

The Steiner-Taborek depiction of flow boiling in a vertical tube is shown in Figure 15 and the regions A-G are described in the following text.

Region A-B

Before point A, only single-phase convection to the subcooled liquid occurs. Between A-B, only liquid phase convection occurs if $q<q_{ONB}$, while subcooled boiling occurs if

$q>q_{ONB}$. During subcooled boiling, the growth and collapse of bubbles near the wall increases heat transfer.

Region B-C_D

Only convective evaporation occurs when $q<q_{ONB}$, as indicated by the "pure convective boiling" curve. Both nucleate and convective boiling contributions are present and can be superimposed when $q>q_{ONB}$. The nucleate boiling coefficient at the particular heat flux is shown by horizontal dashed lines while the solid curves are the superimposed contribution of nucleate and convective boiling that together constitute h_{tp}. The flow pattern as shown in the bottom diagram transits through both bubbly flow and churn flow regimes.

Region D-E-F

When $q<q_{ONB}$, the process continues along the pure convective boiling curve up to the onset of dryout at high vapour qualities approaching x=1.0. The annular flow regime constituting a thin turbulent annular liquid layer on the tube wall and a central vapour core, is reached when $q>q_{ONB}$, and continues up to the point where the critical vapour quality x_{crit} is reached, after which the annular film dries out.

Region F-G

The liquid film at x_{crit} is subject to instability from interfacial shear and adhesion forces. The heat transfer mechanisms also change in the mist flow regime, where heat transfer is now by vapour-phase convection, by evaporation of entrained liquid droplets within the superheated vapour, by droplets impinging onto the tube wall, and by radiation.

Based on the power-law type equation (62), Steiner and Taborek now proposed the correlation

$$h_{tp} = \left[(h_{nb,o} F_{nb})^3 + (h_{Lt} F_{tp})^3 \right]^{\frac{1}{3}} \tag{45}$$

where

$h_{nb,o}$ is the local nucleate pool boiling coefficient at a reference heat flux q_0 at the reduced pressure p_r equal to 0.1

F_{nb} is the nucleate boiling correction factor (not a suppression factor, as this is an asymptotic model)
h_{Lt} is the local liquid-phase forced convection coefficient based on the total flow as liquid (as opposed to liquid fraction of flow shown in earlier methods) derived from the Gnielinski correlation instead of the Dittus-Boelter correlation.
F_{tp} is the two-phase multiplier accounting for the higher velocity of liquid in a two-phase flow – a flow regime which gives higher heat transfer enhancement as opposed to a lower-velocity single-phase flow.

A more complete description of the Steiner-Taborek model including full details of the terms relating to equation (63) is provided in Collier and Thome [34].

While the correlations of Chen [32], Shah [33], Gungor and Winterton [38] were vertical flow correlations, modifications of these models were developed in order to fit flow in horizontal tubes. One simple modification was made by Shah to his vertical tube correlation presented earlier, where he set a threshold delineating stratified and non-stratified flow based on the liquid Froude number. Below the threshold Fr_L=0.4, the normal vertical correlation is applied. Above that threshold, a modified N term is introduced to take account of the stratification. Gungor and Winterton also utilised the liquid Froude number based threshold, but set the value of Fr_L=0.05, and in addition modified both their convective enhancement and boiling suppression (E and S) terms.

However, while the methods offer simple calculation and perform well in the annular flow regime, certain limitations were noted [20] when these correlations are used for other flow regimes;
They only predict stratified and non-stratified flows and accommodate neither other flow regimes nor the transition from unstratified to stratified flow.
Plotting the predicted HTC values versus quality (x) often do not reflect actual experimental values or trends.
They do not take into account the region near dryout. They hence can both under-predict heat transfer before this region and over-predict heat transfer after the onset of dryout - in some cases by up to 300%.
They mistakenly attempt to model annular flow by using the Dittus-Boelter equation, a tubular flow correlation, instead of using a film flow approach.

Consequently, a more phenomenological approach proposed by Kattan, Thome and Favrat [28-30] was developed related to their flow map described earlier. Cotton [4], reviewing various two-phase correlations, also favours this approach over previous methods as it includes mechanisms to account for the effects of local two-phase flow patterns, flow stratification and partial dryout. This phenomenological study was greatly facilitated by use of visualisation tools such as high-speed cameras and laser equipment in order to properly define flow regimes and their boundaries. Optical methods were also utilised by Kattan *et al.* to measure liquid/vapour transitions passing a particular point of the tube, and this was then related to void fraction and used in their calculations of flow regimes.

The Kattan, Thome and Favrat map represents simplified two-phase flow structures of fully stratified, stratified-wavy, and annular flow regimes, based on the flow map seen in Figure 11. The simplified structures are shown in Figure 16. The two upper drawings depict stratified flow, while the lower three show the transition from annular to stratified flow.

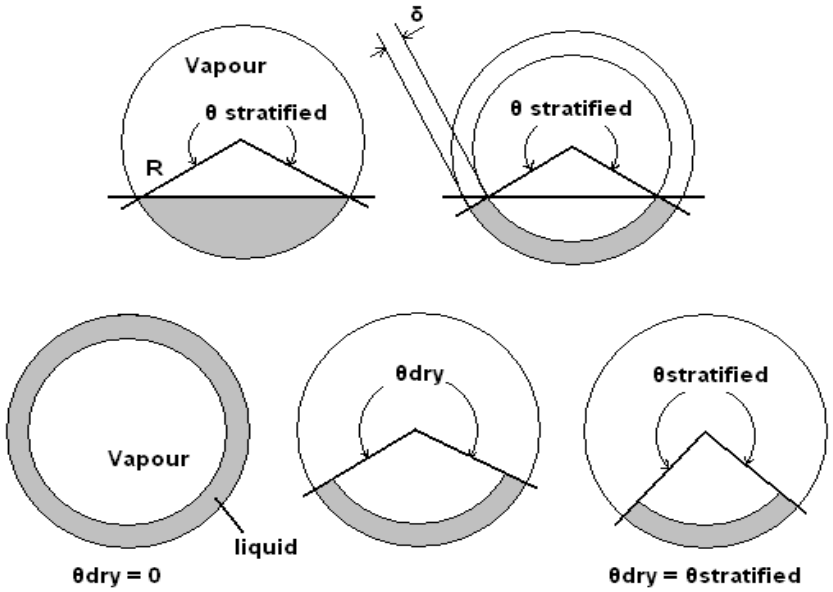

Figure 16: Simplified flow structures proposed in Kattan Thome Favrat Model, adapted from [20, 30]

The new geometrical parameters account for liquid and vapour areas, stratified and dry angles θ, and liquid film thickness δ. Methods for the measurement of the parameters

and the subsequent flow regime calculations are detailed by Kattan *et al*. in [28-30]. The general equation for the flow boiling coefficient in a horizontal tube is given by

$$\alpha_{tp} = \frac{d_i \theta_{dry} \alpha_{vapour} + (2\pi - \theta)\alpha_{wet}}{2\pi d_i} \tag{46}$$

The dry perimeter of the tube is given by the dry angle θ_{dry} and the corresponding heat transfer is given by α_{vapour}. α_{wet} denotes the heat transfer coefficient on the wetted perimeter and this is made up of an asymptotic expression combining nucleate boiling and convective boiling and using an exponent of three giving:

$$\alpha_{wet} = \left[{\alpha_{nb}}^3 + {\alpha_{cb}}^3 \right]^{\frac{1}{3}} \tag{47}$$

A reduced pressure correlation, put forward by Cooper and used to determine α_{nb} , is

$$\alpha_{nb} = 55 p_r^{0.12} \left[-\log_{10} p_r \right]^{-0.55} M^{-0.5} q^{0.67} \tag{48}$$

M is the liquid molar weight, p_r is the reduced pressure, and q is the heat flux at the wall in W/m^2K. The convective boiling heat transfer coefficient of the annular film of liquid is given by

$$\alpha_{cb} = 0.0133 \left[\frac{4\dot{m}(1-x)\delta}{(1-\varepsilon)\mu_L} \right]^{0.69} \left[\frac{c_{pL}\mu_L}{k_L} \right]^{0.4} \frac{k_L}{\delta} \tag{49}$$

The first term in brackets is the liquid Reynolds number calculated on the mean velocity of the liquid which is a function of the vapour quality, *x*, the void fraction ε, and the annular film thickness δ.

Normal tubular flow is assumed in the vapour at the dry wall and the Dittus-Boelter equation is used

$$\alpha_{vapour} = 0.023 \left[\frac{\dot{m} x d_i}{\varepsilon \mu_G} \right]^{0.8} \left[\frac{c_{pG}\mu_G}{k_G} \right]^{0.4} \frac{k_G}{d_i} \tag{50}$$

Methods are also given to calculate the dry angle, θ_{dry}, which can vary depending on flow.

$$\theta_{dry} = (2\pi - \theta_{\max})\frac{(x - x_{\max})}{(1 - x_{\max})} + \theta_{\max} \tag{51}$$

or

$$\theta_{dry} = (\theta_{strat})\frac{(G_{high} - G)}{(G_{high} - G_{low})} + \theta_{\max} \tag{52}$$

The procedure for selection of θ_{dry} along with details of G_{high} and G_{low} are described in more detail in Collier and Kattan *et al*. [20, 30]. The vapour void fraction is calculated from the Steiner [20] modification to the Rouhani-Axelson [39] drift flux model.

$$\varepsilon = \frac{x}{\rho_G}\left\{[1 + 0.12(1-x)]\left(\frac{x}{\rho_G} + \frac{1-x}{\rho_L}\right) + \frac{1.18}{\dot{m}}\left[\frac{g\sigma(\rho_L - \rho_G)}{\rho_L^2}\right]^{0.25}(1-x)\right\}^{-1} \tag{53}$$

The film thickness of the annular liquid layer is found by taking the cross-sectional area taken up by the liquid phase and equating it to the area of a truncated annular ring. The liquid thickness, δ, is assumed small compared to the tube radius, r_i.

$$\delta = \frac{A_L}{r_i(2\pi - \theta_{dry})} = \frac{A(1-\varepsilon)}{r_i(2\pi - \theta_{dry})} = \frac{\pi d_i(1-\varepsilon)}{2(2\pi - \theta_{dry})} \tag{54}$$

The cross-sectional area taken up by the liquid layer is solved from the void fraction using

$$A_L = A(1-\varepsilon) \tag{55}$$

For the fully stratified regime this can be solved iteratively from the relation

$$A_L = 0.5r_i^2[(2\pi - \theta_{strat}) - \sin(2\pi - \theta_{strat})] \tag{56}$$

In 2005, Wojtan *et al*. [31, 40] updated the Kattan *et al*. [28-30] map to improve accuracy in the stratified wavy zone. This zone was subdivided into three new flow

patterns identified as slug, slug/stratified wavy and stratified wavy zones. These improvements enabled the map to be used at vapour qualities below 0.15 [40]. Based on their experimental results, the annular zone was also modified by the inclusion of a boiling suppression factor. Wojtan *et al*. also included new methods for both a mist zone and a dryout region, but these will not be covered in the present study. Their observations of the new regimes in the stratified zone also led to the following changes.

Slug Regime

The high frequency slugs were thought to create a constant thin film of liquid on the upper tube perimeter. As the entire tube perimeter is always wet, $\theta_{dry} = 0$.

Stratified-Wavy regime

Wojtan *et al*. dropped the linear interpolation used in the previous calculation of θ_{dry} in favour of a quadratic method to account for the wetting of the tube sidewalls by the waves, thus:

$$\theta_{dry} = \theta_{strat}\left[\frac{G_{high} - G}{G_{high} - G_{low}}\right]^{0.61} \tag{57}$$

Slug/Stratified-Wavy Regime

In this regime, slugs that cause complete wetting and waves that only wet the sides of the tube were observed. As quality increases however, the slug frequency decreases and smaller amplitude waves dominate. The slugs disappear completely when the vapour quality reaches the Intermittent-Annular regime, ($x = x_{IA}$). To provide a smooth transition in heat transfer coefficient at the boundaries, a further modification of equation (58) is proposed when $x < x_{IA}$.

$$\theta_{dry} = \theta_{strat}\left(\frac{x}{x_{IA}}\right)\left[\frac{G_{high} - G}{G_{high} - G_{low}}\right]^{0.61} \tag{58}$$

Instead of Equation (54), the film thickness δ, is now calculated using

$$\delta = \frac{d_i}{2} - \left[\left(\frac{d_i}{2}\right)^2 - \frac{2A_L}{2\pi - \theta_{dry}}\right]^{0.5} \tag{59}$$

However, when the above expression returns a value for the liquid thickness of $\delta > d_i/2$, δ must be set equal to $d_i/2$ to satisfy geometric constraints. θ_{strat} is no longer calculated iteratively, but the void fraction from Eq.(53) is now utilised in the expression developed by Biberg [41]:

$$\theta_{strat} = 2\pi - 2\left\{\begin{array}{l}\pi(1-\varepsilon)+\left(\frac{3\pi}{2}\right)^{\frac{1}{3}}\left[1-2(1-\varepsilon)+(1-\varepsilon)^{1/3}-\varepsilon^{1/3}\right] \\ -\frac{1}{200}(1-\varepsilon)\varepsilon[1-2(1-\varepsilon)]\left[1+4\left((1-\varepsilon)^2+\varepsilon^2\right)\right]\end{array}\right\} \tag{60}$$

Equation (47) is also modified slightly: a fixed value of 0.8 is used as a boiling suppression factor, S, to reduce the nucleate boiling contribution so that equation (47) now becomes

$$\alpha_{wet} = \left[S\alpha_{nb}{}^3 + \alpha_{cb}{}^3\right]^{\frac{1}{3}} \tag{61}$$

The modifications resulted in more accurate predictions of the experimental points, especially with higher heat fluxes. Incipient dryout was also better predicted, and the heat transfer coefficients were more accurate in the dryout and mist flow regimes. An illustration of a simulation performed according to the completed model [20] is given in Figure 17 and shows how the predicted heat transfer coefficients transit smoothly across the flow regime boundaries without steps.

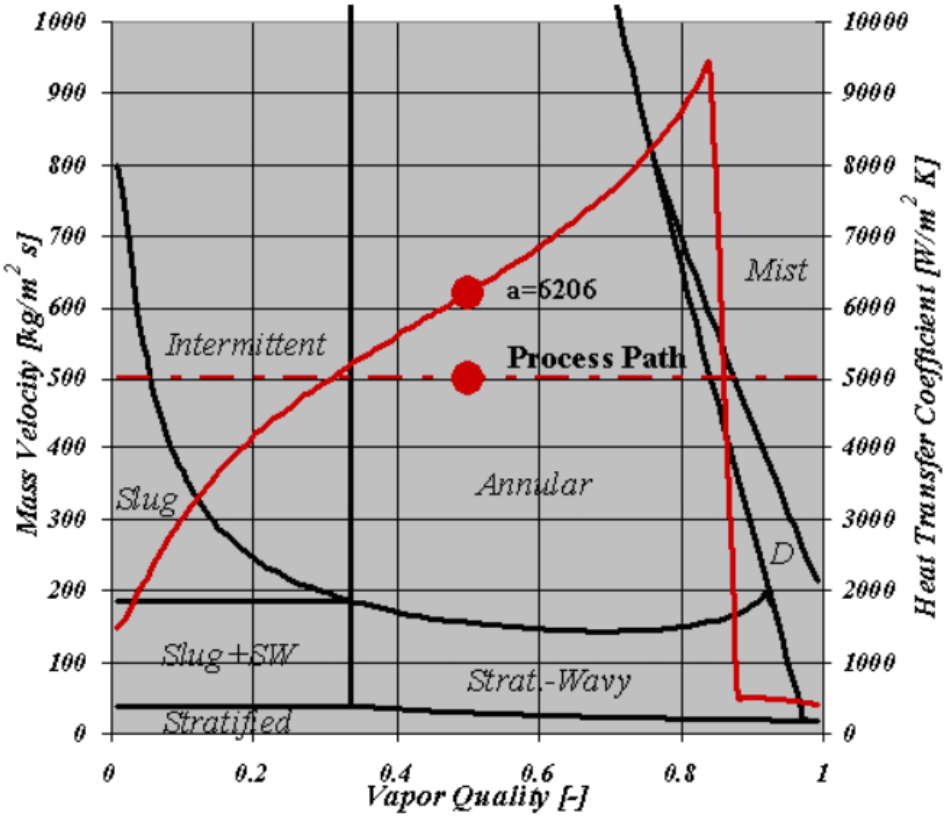

Figure 17: Simulation of Wojtan *et al*. model showing heat transfer coefficient predictions and smooth transition between flow regime boundaries , image from [20]

2.2: Electrohydrodynamics

Electrohydrodynamics or EHD refers to hydrodynamic systems subject to an electric field [42]. The liquids are usually good electrical insulators such as purified water, oils, alcohols or as in this study, refrigerants. The currents are weak, but the electrical forces generated can be high and may form a significant term in the Navier-Stokes equation. These resultant force interactions can result in flow structure changes that can be exploited for mixing, electrically induced pumping and enhancement of heat transfer. During the latter case, the complex electrostatic forces are found in tandem with another complex phenomenon, that of two-phase thermal flow. However, the purpose of this section is to review the basic theory of electrohydrodynamics, and the next section will then address the confluence of two-phase flow with electrohydrodynamics as applied to heat transfer augmentation.

2.2.1: The Governing Equations of Electrohydrodynamics

The conservation equations for mass, momentum and energy for a laminar flow under the action of an electric field can be expressed by the following three equations [43, 44] as

(i) Mass Conservation

$$\frac{\partial \rho}{\partial t} + \rho \nabla \cdot \bar{u} = 0 \tag{62}$$

(ii) Momentum Conservation

$$\rho \frac{\partial \bar{u}}{\partial t} + \rho(\bar{u} \cdot \nabla)\bar{u} = -\rho \bar{g} \beta (T - T_0) - \nabla P + \bar{f}_{eB} + \mu \nabla^2 \bar{u} \tag{63}$$

(iii) Energy Conservation

$$\rho C_p \frac{\partial T}{\partial t} + \rho C_p \bar{u} \cdot \nabla T = k \nabla^2 T + q_{eB}''' \tag{64}$$

where u is the velocity, β is the coefficient of thermal expansion of the fluid, k is the thermal conductivity , C_p is the specific heat, ρ is the density, f_{eB} is the body force per unit volume, and $q_{eB}^{'''}$ is the energy generation rate per unit volume due to a magnetic or electric field.

Maxwell's Equations, which govern electrostatic behaviour for a linear Ohmic dielectric, are also valid and are summarised by

(i) The Poisson equations,

$$\nabla \cdot (\varepsilon \bar{E}) = \rho_{ei} \tag{65}$$

and

$$\nabla \times \bar{E} = 0 \tag{66}$$

(ii) Conservation of Charge

$$\nabla \cdot \bar{J}_j + \frac{\partial p_j}{\partial t} = 0 \tag{67}$$

(iii) Charge Transport Equation for Positive and Negative Charge Species

$$\bar{J}_j = \rho_j \bar{u} - D_j \bar{\nabla} \rho_j \pm \mu_j \rho_j \bar{E} \tag{68}$$

Definition of Electric Potential

$$\bar{E} = -\nabla V \tag{69}$$

where ρ_e, σ_e, and D represent the charge density, electrical conductivity and diffusion coefficients respectively. Chu [45] developed the expressions for additional body forces created by the presence of an electric or magnetic field in 1959. The total force $\bar{f}_{eB}$ is given by

$$\bar{f}_{eB} = \bar{f}_1 + \bar{f}_2 - \bar{f}_3 - \bar{f}_4 + \bar{f}_5 \tag{70}$$

$$\bar{f}_{eB} = \rho_{ei}\bar{E} + J_x B - \frac{1}{2}E^2\nabla\varepsilon - \frac{1}{2}H^2\nabla\mu + \nabla\left[\frac{1}{2}\rho E^2\left(\frac{\partial\varepsilon}{\partial\rho}\right)_T + \frac{1}{2}\rho H^2\left(\frac{\partial\mu}{\partial\rho}\right)_T\right] \quad (71)$$

where

$\bar{f}_1$ = force per unit volume due to space charge

$\bar{f}_2$ = force per unit volume due to the charge particle motion

$\bar{f}_3$ = force per unit volume due to dielectric property changes

$\bar{f}_4$ = force per unit volume due to the fluid permeability changes

$\bar{f}_5$ = force per unit volume due to the electrostriction and magnetostriction effects

and the terms B and H refer to the magnetic induction and magnetic excitation respectively. Chu [45] also obtained the energy generation term due to an electromagnetic field

$$q'''_{eB} = q'''_1 + q'''_2 + q'''_3 \quad (72)$$

$$q'''_{eB} = \left(\bar{J} - \rho_{ei}\bar{u}\right)(\bar{E} + \bar{u} + \bar{B}) + \nabla[(\bar{E} + \bar{u} + \bar{B}) \times (\bar{H} - \bar{u} \times \bar{D})] \quad (73)$$

where

q'''_1 = heat generation due to flow of charged particles such as Ohmic heating

q'''_2 = energy due to polarisation, such as electromagnetic hysteresis losses

q'''_3 = energy due to the displacement current and time varying magnetic fields, such as energy storage in an electromagnetic field

2.2.2: The Electrohydrodynamic Body Force

During electrohydrodynamic processes, the high-voltage low-current phenomena allow the magnetic field generated by the current flux to be neglected [4, 9, 44]. Jones [46] found that electric field dependent thermal conductivity and viscosity could also be neglected. This leads therefore to a simplification of Equation (71) in the form

$$f_e = \rho_e \overline{E} - \frac{1}{2} E^2 \nabla \varepsilon + \frac{1}{2} \nabla \left[\rho E^2 \left(\frac{\delta \varepsilon}{\delta \rho} \right)_T \right] \tag{74}$$

and

$$q_e''' = \sigma_e E^2 \tag{75}$$

In addition, the last term (75), pertaining to heat generation within the fluid, was also found by Seyed-Yagoobi and Bryan [47], Cotton [4] and Sadek [9] to be negligible due to the low current flow because of the low conductivity (10^{-10}-10^{-16} ohms^{-1}m^{-1}) of dielectric fluids.

In equation (74) the three right hand terms represent the electrophoretic, dielectrophoretic and electrostrictive components of the EHD body force. A representation of the various terms is given in Figure 18.

The first term is the electrophoretic force or Coulomb force (fig 10(a)) which quantifies the force acting on the net free charge in the fluid. The Coulomb force is the force that exists between two electrically charged bodies where it is proportional to the product of their charges divided by the square of the distance, *d*, between them. The second term represents the dielectrophoretic force on the dielectric fluid due to spatial gradient on the permittivity, and can occur in single phase (fig 10(b)), where it is usually weaker than the free charge in a single phase flow. However, in a two-phase flow, due to the difference in permittivity of the two phases, the polarisation force may dominate significantly, causing a liquid and vapour redistribution or "extraction" (fig 10(c)) or causing the migration of bubbles or droplets (fig 10(d)). This dielectrophoretic force is believed by Cotton to be the most dominant during flow boiling [5].

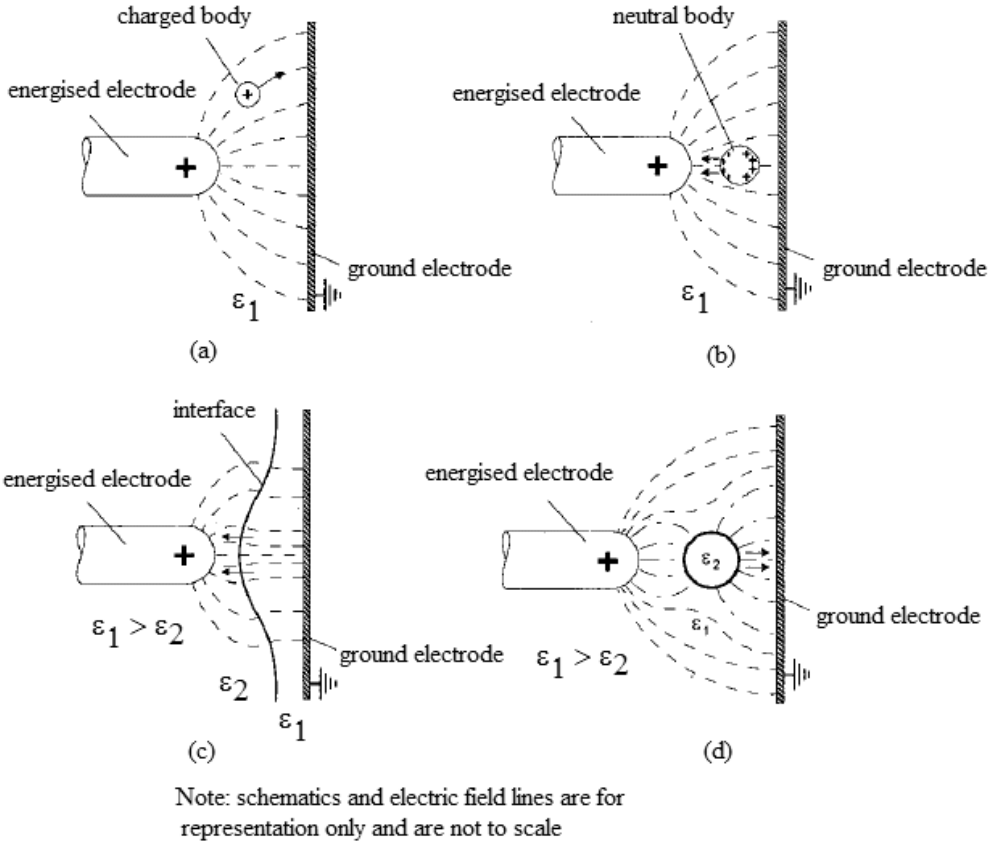

Figure 18: Electric body force density components on a (a) charged body (b) neutral molecule (c) interface (d) bubble or droplet. Figure adapted from Bryan [48]

The last term is the electrostrictive force which arises due to inhomogeneity in the electric field strength and variation in dielectric constant with temperature and density. It is often regarded as a "pressure" rather than as a force, and its significance is generally considered low in two-phase heat transfer situations. However this is a matter of some debate among researchers [49].

Dimensional analysis can also be applied [50] to the equations of EHD in two-phase flow. Two such numbers used are the EHD number E_{hd} and Masuda number M_d.

$$E_{hd} = \frac{I_0 L^3}{\rho_0 \nu^2 \mu_c A} \tag{76}$$

where I_o is the current, L is the length, ρ_0 is the liquid density, ν is the kinematic viscosity, μ_c is the ion mobility and A is the area.

$$M_d = \frac{\varepsilon_0 E_0^2 T_0 \left(\partial \varepsilon_s / \partial T\right)_\rho L^2}{2\rho_0 v^2} \tag{77}$$

where ε_0 is the dielectric constant of vacuum, E_0 is the electric field strength, T_0 is the temperature and ε_s is the dielectric constant.

Both E_{hd} and M_d numbers are analogous to buoyancy-driven flow, and both can be likened to the Grashof number in application. They are used to predict the influence of electrostatic forces and dielectric forces on the heat transfer augmentation when related to the liquid Reynolds number. When $E_{hd}/Re^2 \approx 1$ and or $M_d/Re^2 \approx 1$, the combined effects of EHD and forced convection must be considered. If $E_{hd}/Re^2 << 1$ or $M_d/Re^2 <<1$ then electric convection effects may be neglected. Conversely, when $E_{hd}/Re^2 >> 1$ or $M_d/Re^2 >> 1$, forced convection effects may be neglected. When the ratios E_{hd}/Re^2 and M_d/Re^2 are greater than 0.1, it is expected that EHD will begin to significantly influence the flow of liquid. Cotton describes the relationship of both numbers in graphical format [5] in Figure 19 and Figure 20.

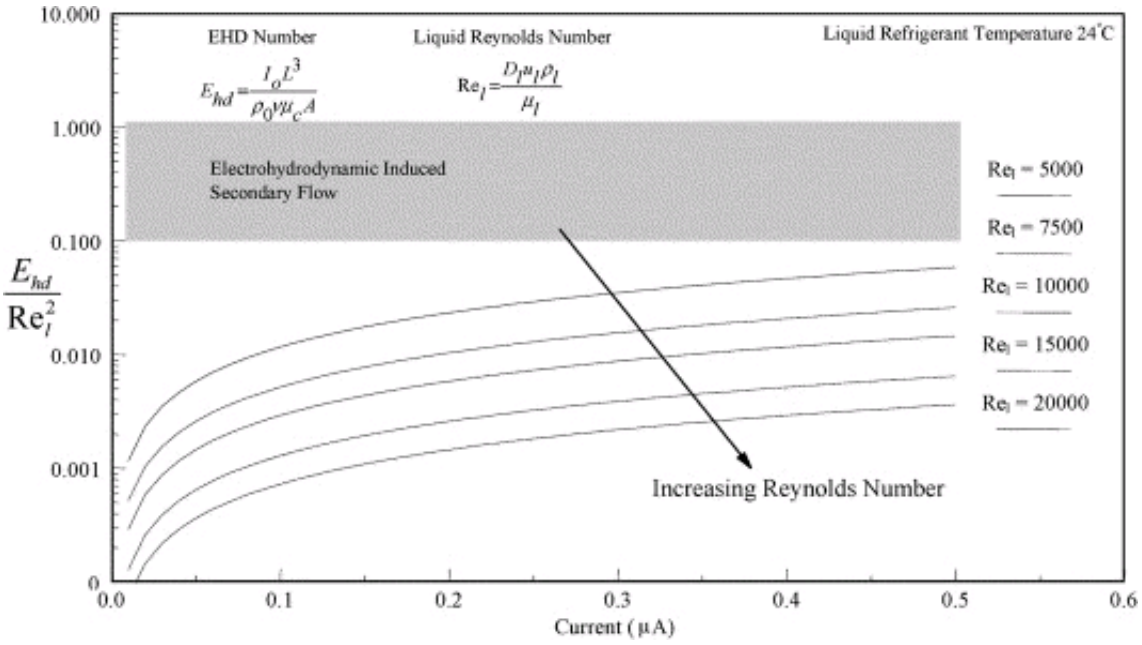

Figure 19: The relationship between EHD number and Reynolds number ratio as a function of current for R134a, image from [5]

The grey zone in Figure 19 depicts the region of electrically induced flow and forced convection. For these test conditions, Cotton found it unlikely for E_{hd} to have an effect on phase redistribution.

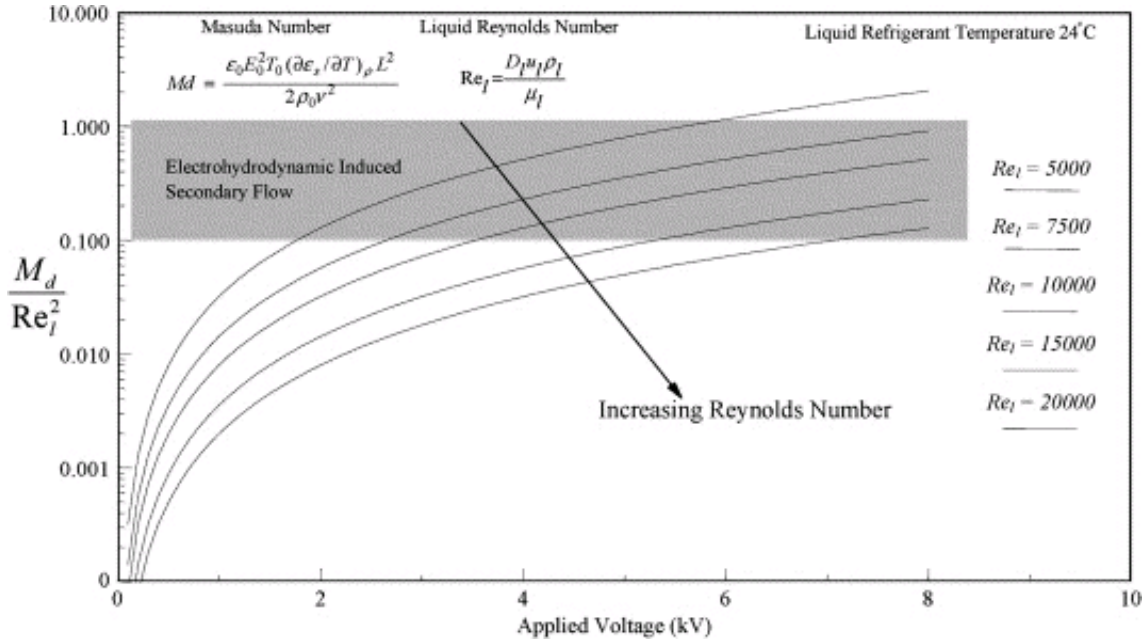

Figure 20: The relationship between the Masuda number and Reynolds number ratio as a function of applied voltage for R134a, image from [5]

In Figure 20, $M_d \approx \mathrm{Re}^2$, indicating that dielectric forces are significant and that dielectric and electrostrictive forces increase with applied voltage, and decrease with Reynolds number. According to Cotton [5], the dimensional analysis also suggests that for high Reynolds numbers (>20,000) and low voltages (2 kV) the flow condition will be determined primarily by forced convection and that flow redistribution due to electrohydrodynamic forces becomes unlikely.

2.3: Relevant Studies in EHD Augmented Two-Phase flow

The EHD phenomenon has been known for over ninety years [51] and its effect has relatively recently been investigated for use in two-phase heat transfer enhancement. Several general review papers have been published that cover the last thirty years of research by Jones [46] in 1978, Allen and Karayiannis [52] in 1995 and most recently by Laohalertdecha *et al*. [53] in 2007. As well as evaporation, which is the focus of this thesis, EHD augmentation of heat transfer is studied in pool boiling and condensation processes. Evaporation processes can be further narrowed down by type, whether forced convection within a tube or across a flat plate, and again by whether the study involved visualisation of the phenomena or not. According to Seyed-Yagoobi and Bryan [47], the EHD enhancement effect depends on many factors such as

- heat flux
- quality of the fluid
- mass flux
- voltage
- fluid saturation temperature
- fluid type
- tube and electrode design

Table 2 shows a brief outline of some studies in EHD augmented boiling. Of the seventeen studies listed, seven have involved visualisation of the EHD augmented boiling phenomenon. However, most of these are of pool boiling or of the shell side in a tube bundle, and not of actual in-tube convective boiling. Cotton and Sadek [4-12, 54] did attempt to address this visualisation gap by utilising transparent sections of tube before and after the EHD test section, but these sections were not in the diabatic section of the heat exchanger and thus the combined effects of EHD with the boiling phenomenon could not be visualised. Consequently Cotton *et al*. used a combination of flow patterns leaving the test section in conjunction with thermocouple measurements of the tube wall superheats in order to infer the flow conditions within the diabatic test section.

Table 2: Studies of EHD Augmented Boiling Heat Transfer

Researcher	Fluid	h_{EHD}/h_0 (max)	V (kV)	Test Section	Visualisation
Bryan and Seyed-Yagoobi [48]	R-134a	~4	15	Horizontal Cu tube	No
Cheung *et al*. [55]	R-134a	5.1	15	Tube bundle in pool	Yes
Chen [56]	R-11	~1.35	15	Pool boiling	Yes
Cotton [4-8]	R-134a	3	8	In-tube convective boiling	Yes
Di Marco *et al*.	R-113, Vertrel XF	6.4	15	Pool	Yes
Feng and Seyed-Yagoobi [57]	R-134a	~4.5	15	In tube boiling	No
Grassi *et al*. [58]	FC-72		22	Vertical annulus, modified electrode	
Jia-Xiang [59]	R-11	~1.1-1.2	15	Pool boiling	Yes
Karayiannis [60]	R-123 and R-11	9.3	25	Tube bundle	No
Karayiannis *et al*. [61]	R-114	4	27	Review	
Kawahira *et al*. [62]	R-11	6.6	30	Tube in pool	Yes
Liu *et al*. [63]	R-123	2.1	16	Vertical tube	No
Neve and Yan [64]	R-114	3.4	30	Horizontal enhanced tube	No
Ogata [65]	R-11+2% ethanol	8.5	25	Tube in pool	Yes
Salehi, Ohadi, Dessiatoun	R-134a	~10	3	Vertical channels	No
Watson [66]	n-hexane	2.6	7	Pool	No
Yamashita and Yabe [67]	R-123	6	18	Falling film evaporator	No

Chang and Watson [44] published a graph of the Nukiyama type pool boiling curve shown in Figure 21, where the EHD enhanced boiling curve exhibited improved characteristics over the non-EHD results. This is supported by Allen and Karayiannis [52] who noted that EHD can increase the value of q'_{crit}, (critical heat flux) thus delaying the onset of tube wall dryout or burnout, and that the EHD effect can be applied to the enhancement and control of condensation and boiling of many fluids. In addition, Allen *et al*. [52] and Karayiannis *et al*. [61] demonstrated that in boilers the EHD effect can eliminate effects brought on by transitional and film boiling, namely boiling hysteresis and decreases in the boiling HTC. Eames and Sabir [51]also supported the observations of Allen and Karayiannis [52] that EHD had two further advantages: it (i) allowed heat transfer rates to be controlled by varying the voltage
(ii) provided a force in lieu of gravity for dislodging boiling bubbles from the heated surface
The latter factor could be important for microgravity and downward facing heater orientations and is being investigated by Di Marco [3].

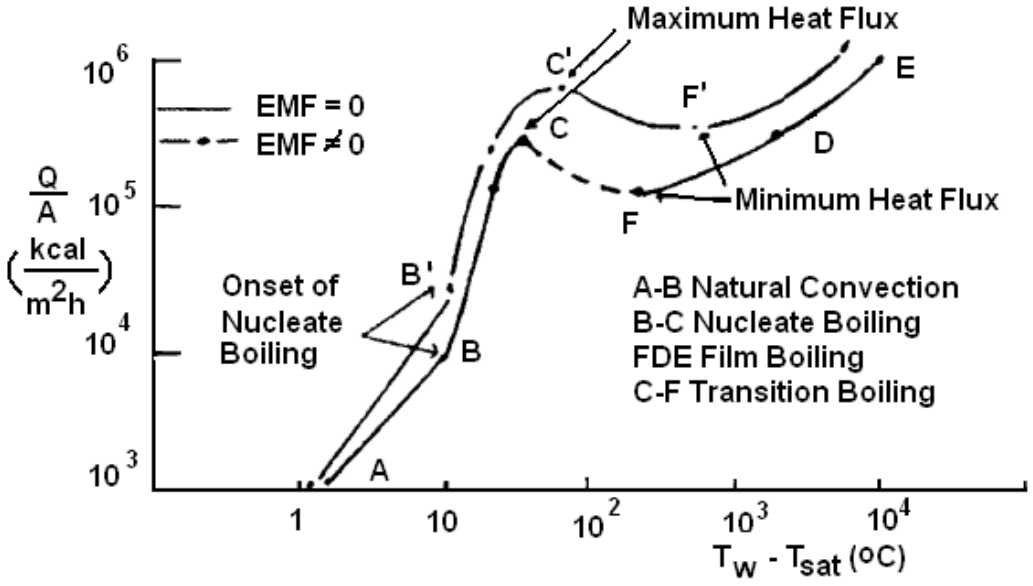

Figure 21: Chang and Watson illustration of EHD augmentation of Nukiyama curve in pool boiling, adapted from [44]

Oh [68] reported that in two-phase flow boiling, EHD affects the heat transfer via several phenomena which cause film destabilization at the vapour-liquid interface, and according to Eames and Sabir [51], these include the following factors,

- movement of vapour bubbles at the heated surface due to Maxwell Stress[65]

- spreading of the vapour bubble base
- increasing bubble number and turbulence
- increased wetting ability by reduction of surface tension

2.3.1: Electric Field Effects

2.3.1.1: EHD Effects on Bubbles

Bubble growth rate was investigated by Cheng and Chaddock [69] who suggested two mechanisms by which an electric field affects bubbles during nucleate boiling. They found that the electric field causes elongation of bubbles, making them spheroidal instead of spherical. For a given size of bubble, this increase in surface area allows more effective heat transfer from the surrounding liquid. In addition, the narrow bubble has a reduced area of contact with the heating surface and hence a lower surface tension which gives rise to a smaller bubble departure size. Conversely, Ogata and Yabe [70], noting vigorous bubble activity, re-growth and an elongation of the bubble shape, found that bubble contact area increased along the heated surface, and suggested this to be a factor in the improved heat transfer.

A numerical study was performed by Zu and Yan [37] of the EHD effects on bubble deformation under pseudo-nucleate boiling conditions. Fluent was used to solve the electric field and body forces, and results were claimed to agree well with actual EHD effects. The simulations also show the bubble being elongated in the axial direction and indicate the presence of vortices around the bubble, which may also account for enhancement of heat transfer.

Cheung *et al*. [55] have carried out a series of experiments and have demonstrated that combined electro-convection and improved nucleate boiling dynamics have contributed to the augmented HTCs. The studies were carried out in pool boiling on enhanced finned tubes, but the observation of the bubble dynamics may well be applicable to bubble dynamics in flow boiling and evaporation. Cheung *et al*. [55] observed that under a moderate voltage (0-10 kV), liquid convection increased although nucleation sites and bubble generation lessened. However the convection outweighed the nucleation resulting in a net increase. At higher voltages, it was noticed that columns

of vapour were formed from coalescing bubbles. They behaved in a variety of patterns highly dependent on the particular tube and electrode geometry, but the net destabilisation brought about by the formation and destruction of the columns caused greater mixing and higher HTCs. They do caution that a decrease in heat transfer may occur at 9 kV and over as the vapour comes to envelope the tube fins thereby preventing wetting. However at still higher voltages they postulate that the heat transfer rises once more as the bubbles are broken down into smaller diameters by the electric field and jet out of the regions. This is supported by Ogata and Yabe and also by Cooper 1990 who noticed this effect at 5-8 kV for R-114. Di Marco[3] also notes that early bubble detachment is promoted by EHD, the most significant reasons being the alteration in bubble shape and the increase in internal pressure.

2.3.1.2: EHD Effects in Convective Flow

Fluids with a higher specific dielectric constant, ε_s, will tend to move from areas of weak electric field to areas to higher electric field. Therefore, vapour with lower values of ε_s (typically ε_{svap}=1) will move to regions of weaker field, while liquids with higher values (,$\varepsilon_{s\ HFE7000}$=7.4) will be forced towards highly intense areas of electric field. The phenomenon of liquids being drawn to such high regions of electric field is known as "liquid extraction". This liquid extraction can be responsible for redistribution of fluid and this can coupled with the movement of the vapour at the same time to create a highly mixed and complex fluid condition.

In an analysis of electrode position in relation to liquid level, Cotton *et al*. [6, 7] performed simulations and tests on stratified and annular flow configurations. The electrodes were positioned concentrically, offset 2.73mm above, and offset 2.73mm below. They showed numerically that in a stratified flow the region of highest field strength occurred when the electrode was above the stratified liquid layer. This gives rise to large forces at the liquid/vapour interface and therefore causes large phase migration. In a submerged electrode however the electric field was found to be highest in the vicinity of the electrode but decreased with vertical elevation. The electric field strengths at the higher liquid/vapour interface were found to be negligible. Therefore the vertical EHD forces were also expected to be small. An exception to this was found when the liquid level was lower than the electrode. In annular flows, Cotton also

numerically predicted larger field strengths near the electrode. These are expected to induce large extraction forces opposing gravity, thus drawing liquid from the lower levels into the core. However, the same forces may also be responsible for extraction of the liquid layer from the top of the tube, and consequently encourage the formation of dryout. The numerical results were verified by experiments where the higher offset electrode (2.73mm above the liquid layer) gave an enhancement of 60% at 2 kV compared to an enhancement of 85% at 8 kV with the concentric electrode.

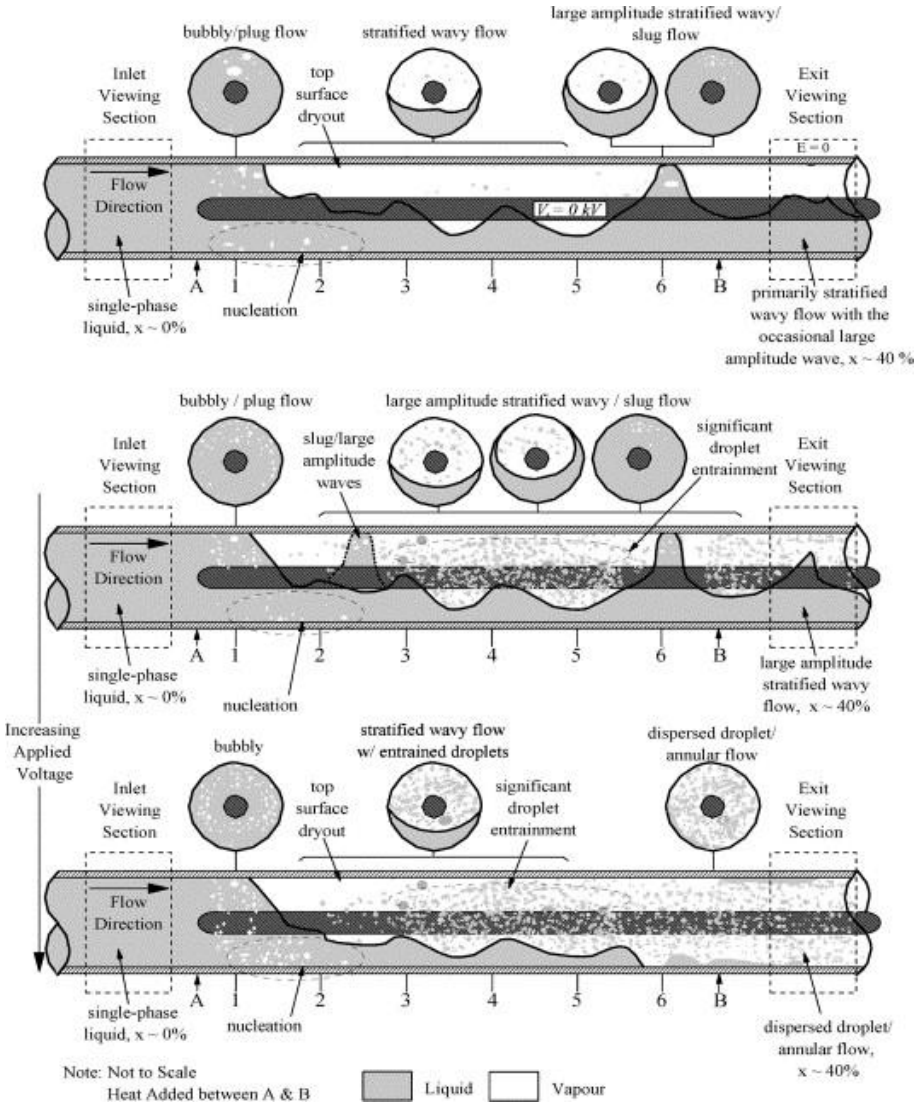

Figure 22: Flow pattern reconstructions proposed by Cotton for increasing DC voltage levels (G = 100 kg/m^2 s, q''=10 kW/m^2, and x_{in} = 0%), image from [5]

Although the test section employed was metallic, using a combination of tube wall temperature measurements and a viewing window at the test section outlet, Cotton [5] was able to infer the type of flow regime that may exist inside the tube. The proposed

flow patterns thought to exist inside the metallic tube test section under increasing DC voltages are seen in Figure 22. The single phase liquid enters from the left and nucleation begins from point A onwards. The first image at the top is in the field free condition, while the subsequent lower photos are under the influence of increasing EHD level. As quality and thus void fraction increase, a stratified wavy/slug flow is generated. With the application of EHD voltage however, two main changes in flow are postulated to occur; (i) increasing voltage increases the incidence of slugs, (ii) liquid is drawn into the vapour core in the form of entrained droplets.

Cotton [8] noted a special case at frequencies of 60Hz which he referred to as "oscillatory entrained droplet EHD two-phase flow". In this case, an annular flow regime is clearly visible but additionally with droplets as large as 2mm diameter oscillating at 120Hz within the vapour core. Cotton ascribes the phenomenon to the continuous construction and destruction of two separate flow regimes, namely stratified flow and intermittent annular or entrained droplet flow. A 300 percent enhancement of the overall Nusselt number is associated with this special case. Based on his results, Cotton [5] developed another flow map (shown in Figure 23) similar in form to the Steiner and Kattan *et al*. map, but adding the effects of EHD coupled with two-phase flow. The map is based on an annular channel using R134a under a DC voltage of 8 kV and indicates the change in flow regime transition under EHD.

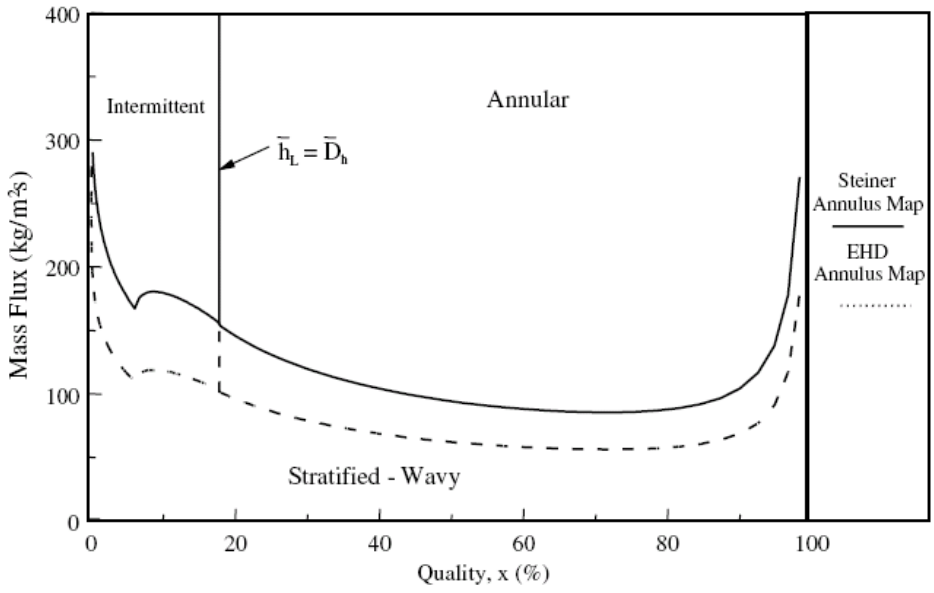

Figure 23: Flow map proposed by Cotton *et al* [5]

In a later study on condensing flows, Sadek *et al*. [11] also investigated the effect of high voltage frequency on two-phase flow regimes. Sadek utilised a concentric electrode layout and voltages in the range 0 to 8 kV and square-waves at frequencies between 4Hz to 1kHz. He found that at lower frequencies ($4Hz \leq f \leq 10Hz$) the liquid could respond to the forces before the AC wave completed its cycle. Therefore, an increase in frequency in this range resulted in increased extraction from the liquid layer and redistribution to the top of the tube. In the intermediate range of frequencies ($10Hz < f < 100Hz$) the time period of the wave was less than the time necessary for the liquid extraction cycle, however liquid interaction with the electrode was high. An increase in the frequency in this region was found not to affect the flow above the electrode, but to cause higher intensity liquid/vapour interactions below the electrode. Increasing the frequency further ($100Hz \leq f$) meant the fluid could not respond quickly enough to the rapidly varying voltage cycle, therefore liquid vapour interactions decreased.

With regard to electrical polarity Jones [46], Cooper [71] and Cheung [72] all reported zero or a negligible effect of polarity on heat transfer enhancement. However, Paschkewitz [73] did find that, depending on the electrode material, negative polarity did give lower enhancement on a polyalphaolefin fluid. Liu *et al*. [63] in a test of convective boiling of R-123 in a downward tube, noted a better performance for positive polarity high voltages compared to negative polarity. Therefore, the effect of polarity, fluid type and electrode and ground material cannot be neglected in EHD related heat transfer enhancement.

Gidwani et al, [74] in a condensative study of EHD in condensation also found that EHD was more effective in stratified wavy and stratified flow patterns. This was due to the dominance of the EHD forces over the momentum flux resulting in higher fluid extraction and crossed motions within the tube. They noted lower EHD enhancement and lower pressure drops as quality increased.

Ng also studied the mechanisms of EHD two phase flow structures [75]. He showed that at lower qualities, liquid is extracted from the lower stratum and attracted to the central electrode due to the EHD body force. Then, once the electrode is surrounded by the liquid, twisted liquid cones are formed which emanate radially from the surface of the electrode to the tube wall surfaces. Using pulsed width control of the DC EHD

voltage, Ng found that the twisted cones were a transitory feature, the development of which are shown in the illustration in Figure 24.

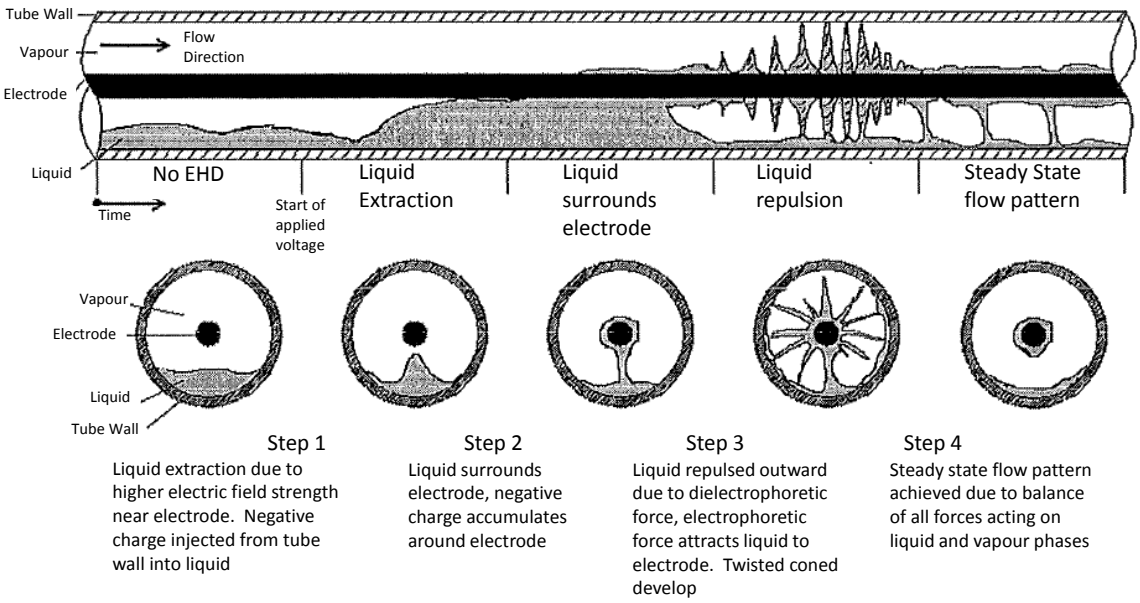

Figure 24: Illustrative representation of the various steps in the development and decay of the twisted liquid cone structures, image adapted from Ng [75]

Although EHD is predominantly employed for its enhancement role, a number of researchers noticed that the EHD effect could, in certain conditions, inhibit the convective heat transfer coefficient. Feng and Seyed-Yagoobi [57] found that a transition from EHD enhancement to EHD suppression occurred near the annular-to-mist transition region. This is supported by Bryan and Seyed-Yagoobi [48] who also performed experiments with R134a and observed a similar suppression with EHD at certain conditions, noting that the EHD force could effectively strip the liquid layer from the tube wall, thus reducing the heat transfer. EHD boiling suppression was also observed by Ogata and Yabe [65], and Kawahira *et al*. [62].

2.3.1.3: Other studies

Salehi *et al*. [76] carried out experiments by boiling R134a in a subcompact heat exchanger at vertical upward, vertical downward and horizontal flow conditions. They found that at low Reynolds numbers (Re =500) EHD enhanced the HTC – more so in downward flow, noting a decrease in EHD power consumption with higher vapour

quality. It is interesting to note that Salehi *et al*. also included an enhanced surface heat exchanger in their study and found up to a 10-fold increase in heat transfer with a corrugated surface in the downward flow orientation. Neve and Yan [64] also found good results and an enhancement of the EHD effect as compared to smooth surfaces. Neve and Yan propose that the geometry features of the enhanced surfaces create sharper field contour gradients and resultant greater field distortion as the main factor behind the enhancement. Similar findings have been made by Grassi *et al*. [58] who found that in a study of upward vertical flow, a Reynolds number of 600 with EHD gave similar heat transfer to an equivalent Reynolds number of 20,000 without EHD. Grassi *et al*. used a modified electrode with sharp points to create charge build up at the tips. This concentration of charge leads to ion injection into the fluid, causing jets of the cold liquid layer to mix with the warm layer at the tube surface. Minimal pressure drop is associated with the heat transfer improvements.

As EHD enhancement is due to the redistribution of liquid around the tube, it may be expected that greater liquid/vapour interaction and the presence of liquid at previously dry areas would account for greater friction and hence lead to a pressure drop penalty. Most researchers have encountered pressure penalties: however Yabe *et al*. [77] reported that pressure drop in EHD was insignificant. Bryan and Seyed-Yagoobi [78] published findings which countered Yabe, proposing that it was due to the presence of the introduced electrode and that to have a more realistic comparison, pressure drop should be compared to a tube with no electrode. Bryan and Seyed-Yagoobi [78] also proposed a linkage between EHD pressure and momentum flux as an indicator of enhancement and pressure drop. Bryan *et al*. calculated the radial EHD pressure and related it to the axial momentum flux. The EHD field was approximated for both a homogenous liquid/vapour condition and an annular flow condition; however the transition points were based on non-EHD conditions, a limitation acknowledged by the authors. More recent experimental investigations (albeit in condensation conditions) by Sadek *et al*. [12] have shown a pressure drop factor of 1.5 with a HTC enhancement of up to 3.2, indicating that pressure drop is not negligible in all cases. Sadek utilised temperature measurements from the tube surface to indicate that flow regime transition from stratified to annular flow caused the improved heat transfer and higher pressure drop. Feng and Seyed-Yagoobi [79] have since put forward a turbulence based model

of EHD analysis in annular flow conditions in order to relate pressure drop and heat transfer enhancement.

2.4: Summary

This chapter set out to give an understanding and introduction to the fields of two-phase flow, describing the basic theories and terms and then introducing the gradual progress with relation to flow regimes, flow mapping and also in two-phase flow heat transfer prediction and pressure drop correlations. This was followed by an introduction to the essential basics of Electrohydrodynamics. It then converged both two-phase flow and EHD in a literature review relating specifically to heat transfer augmentation. The literature review established that the precise mechanisms by which EHD forces affect two-phase convective boiling are not yet fully understood, and the development of a transparent test section would greatly assist in elucidating the enhancement mechanisms during in-tube diabatic processes.

Chapter 3: Experimental Facility and Methodology

The aims of the experimental facility or test rig are two-fold:
(i) to perform thermal hydraulic measurements (temperature, flow, heat input, pressure drop) of heat exchangers in convective flow boiling mode, with and without the application of high-voltage electric fields from a concentric electrode
(ii) to observe the ensuing flow regimes through the transparent test section and relate them with the physical measurements results obtained in (i), in order to assess the effect of EHD on two phase flow heat transfer augmentation.

3.1: Experimental Facility: The Test Rig

Figure 25 shows a schematic of the test rig. The rig consists of a primary loop containing the working fluid and an instrumented transparent test section for measurement and observation. There are three secondary water loops: two of these provide indirect heating of the working fluid via heat exchangers, and the third contains chilled water to condense the working fluid.

The test fluid, refrigerant HFE7000, is circulated in a closed stainless steel circuit forming the primary loop. HFE7000 (methylperfluoropropylether), manufactured by 3M Corp, is a new-generation heat transfer fluid with a low global warming potential intended to replace traditional CFC type refrigerants. An important factor in its selection was its boiling temperature of 35°C at 1 bar, meaning the rig can operate at a low pressure differential to atmosphere, thus obviating the need for high pressure sealing arrangements. A summary of the properties of HFE7000 is given in Table 3.

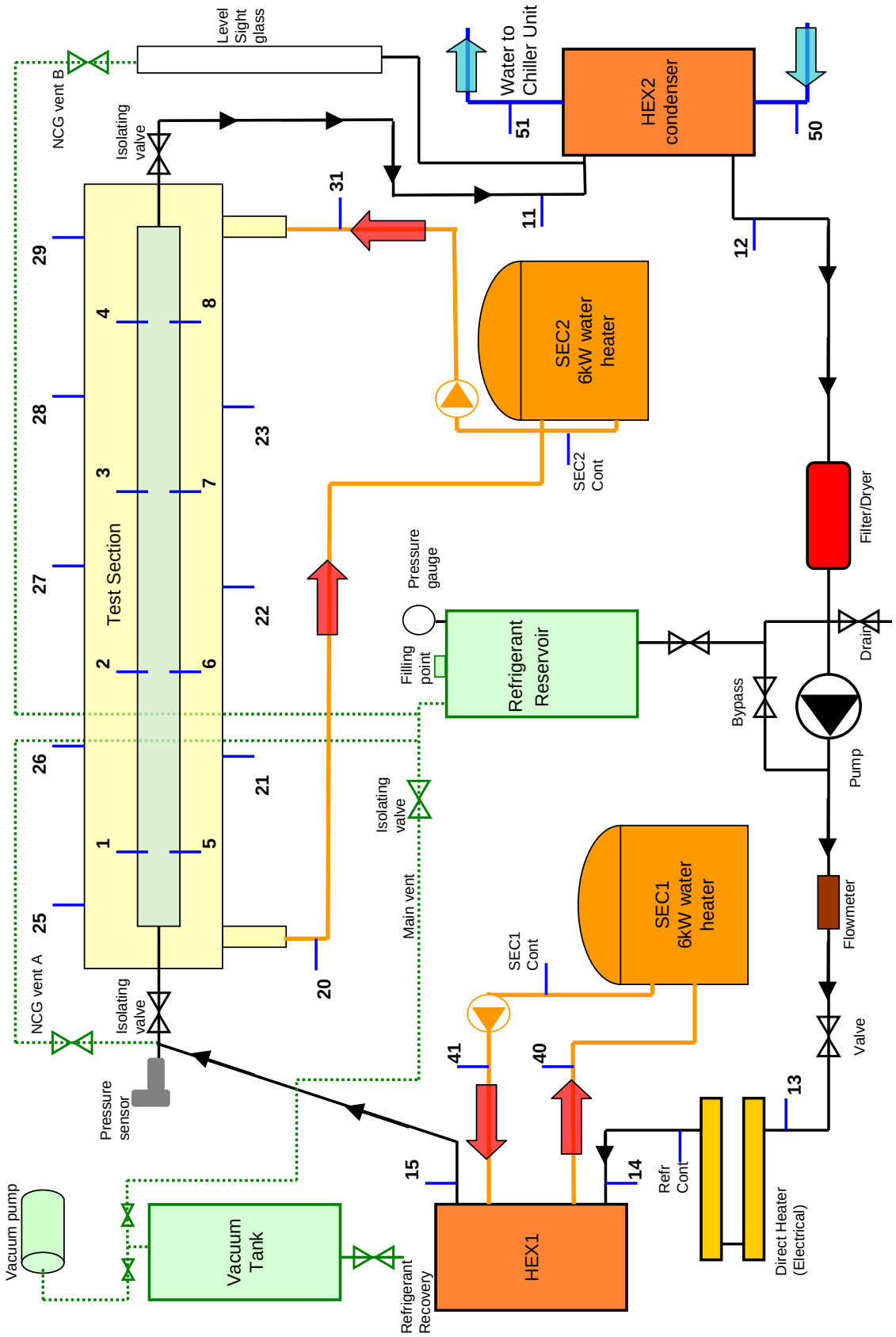

Figure 25: Schematic of flow loop

Table 3: Properties of HFE7000 (from 3M Corp)

Molecular Weight	200	g/mol
Freeze Point	-122.5	°C
Boiling Point	34	°C
Liquid Density	1400	kg/m^3
Kinematic Viscosity	0.32	cSt
Kinematic Viscosity @-80°C	2	cSt
Kinematic Viscosity @-120°C	17	cSt
Coefficient of Expansion	0.00219	K^{-1}
Critical Density	553	kg/m^3
Critical Pressure	2.48	MPa
Critical Temperature	165	°C
Dielectric Constant	7.4	-
Dielectric Strength	~40	kV
Latent Heat of Vapourisation	142	kJ/kg
Solubility of water in fluid	~60	ppmw
Solubility of air in fluid	~35	vol %
Specific Heat	1300	J/kg K
Surface Tension	12.4	dynes/cm
Thermal Conductivity	0.075	W/m K
Vapor Pressure	64.6	kPa
Volume Resistivity	$10x10^7$	ohm-cm

The main components in this primary loop are the pump, electrical heater, hot water heat exchanger, test section, condenser, and pressure control vessel. Two secondary heating circuits and one cooling circuit are used for heating/boiling and condensation of the working fluid respectively. All joints in the primary loop are Swagelok or welded fittings except for several unavoidable threaded joints which were sealed with epoxy adhesive as recommended by Tuma [80]. The main sapphire tube test section sealing gland was fabricated in-house and tested satisfactorily to 4 bar, comfortably in excess of the normal rig operating pressures of 0.9-1.1 bar. All piping and associated equipment are contained within a framework constructed of modular aluminium profile bar (Bosch Rexroth) which allows for flexibility and modification.

3.1.1: The Primary Loop

In the primary loop, the working fluid is circulated by a closed gear pump (Micropump Type GN-N23) magnetically coupled to a 3-phase variable speed motor. The motor is controlled by an electronic Motor Controller (Siemens) permitting variable speed control. The pump circuit also features a bypass, and a refrigerant filter/dryer cartridge (Carly DCY164) is in the suction line. The fluid then passes through a turbine flowmeter (Titan Instruments Type 945), which measures flow between 0.14-3.2 l/min (0.2-4.5 litres/min water) and is accurate to within ±3%. It then passes through a manually operated flow control valve and enters an electrical direct contact heater (DIR 1) which heats the working fluid to just below its saturation temperature.

This direct heater comprises 2 heating units in series, (see Figure 26) each unit consisting of one 400W cartridge heater, 12.7mm in diameter and 360mm long, concentrically located within a stainless steel tube 340mm long and of 25.4mm outer diameter, thus forming an annular chamber. The heaters are sealed at one end by means of a welded end-cap and at the other by a removable seal plate into which an O-ring seal is fitted. DIR1 can be controlled by an Omega CNi 3253 PID controller, giving a fixed outlet temperature, or by a Variac, giving constant power input.

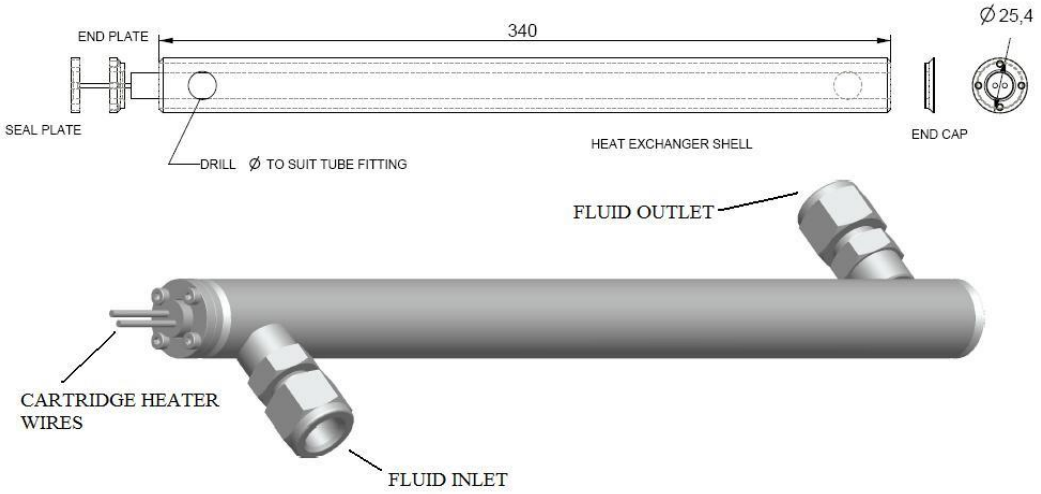

Figure 26: One of two heater units which together comprise DIR1

It is important that only single-phase flow occurs in this heat exchanger i.e. that T_{sat} (approx 35°C) in DIR1 is not exceeded due to the risk of local dryout and "hot spots" forming on the cartridge heater surface. The constant heat flux of the cartridge coupled

with a vapour barrier may cause high temperatures to occur on the heater and cause degradation of the fluid (maximum heat flux of 18W/cm^2 specified by 3M [54]) or burnout of the heater.

The amount of heat transferred from the direct heater is calculated from the energy change across the heater, using the flowmeter and working fluid inlet and outlet temperatures logged by two calibrated type T thermocouples, and is given by the expression

$$Q_{DIR} = \dot{m}_{REF} c_{pREF} (T_{14} - T_{13}) \tag{78}$$

An electrical connection is provided so that a cross check can also be performed by measuring voltage and current used by the electrical heaters.

$$Q_{DIR} = VI \tag{79}$$

Subsequent to DIR1, the fluid then enters HEX1, a compact plate heat exchanger of up to 36kW capacity, where hot water is circulated from SEC1 (described in Section 3.1.2). A fluid-fluid heat exchanger is employed so as to avoid burnout which may be associated with electrical heaters in the presence of a two-phase flow. The temperature and flow rate of SEC1 is controlled to regulate the exit quality of the working fluid. The heat input raises the working fluid to T_{sat} , causing evaporation and forming a two-phase mixture of liquid and vapour. A 0-10 bar electronic pressure transmitter (Bourdon Sedeme type E7-13) measures the fluid pressure (P1) at the exit of HEX1. During single–phase flow conditions, the heat transferred to the working fluid can be calculated from

$$Q_{HEX1} = \dot{m}_{REF} c_{pREF} (T_{15} - T_{14}) \tag{80}$$

However, for two-phase conditions, the above equation cannot be used as it does not take account of the latent heat transfer. The procedure for calculation of energy transferred and hence quality is described later in this chapter.

Upon leaving HEX1, the two-phase working fluid passes through a flexible stainless steel pipe which connects it to the test section. As there is an elevation change from HEX1 to the test section level, another pressure transmitter (Omega PX4201) records the pressure (P2) entering the test section. This pressure reading allows a correction of the quality to be re-calculated as the two-phase fluid enters the test-section. After station P2, just before the test section, the fluid passes through a developing length of the same diameter (8mm) to permit the flow to stabilise before entering the test section. In the first embodiment, the test section consists of a sapphire tube surrounded by a transparent Perspex water shell to form a concentric counter current heat exchanger, and is described in more detail in 3.1.2. This counter-current shell is supplied with heated water from SEC2, allowing the quality of the working fluid, and hence the flow regime, to be varied along the test section. In the second test section, which will be discussed later, heat is supplied from a conductive layer around the sapphire tube.

3.1.2: The Secondary Water Loops

The secondary water loops were designated Secondary 1 and Secondary 2 or SEC1 and SEC2. The heat input from SEC1 to HEX1 governs working fluid quality entering the test section, while SEC2, an identical heating loop, is used to supply heat to the fluid in the test section. The SEC1 circuit consists of an insulated copper water tank of 50L capacity into which are fitted two 3 kV electrical heating elements. The water outlet temperature is controlled to a desired set point by a PID controller (Omega CNi32) which acts on one 3kW immersion heater. The second 3kW heater is controlled by a simple on/off switch to act as a rapid boost. A domestic hot water pump (Grundfos UP-20-45 N150) directs the hot water to a flow meter (Gems FT-110 type 1-10l/min turbine flow sensor for SEC1), then through a control valve and to the test section. The pump is also fitted with a bypass and polypropylene filter unit with a replaceable cartridge located upstream of the turbine flowmeter. The bypass and control valves are used together to set the flow rate. All piping is standard plumbing copper tube with brass compression fittings, and is insulated by Armaflex foam or fibreglass wool as appropriate.

SEC2 is almost identical, the differences being in the flowmeter range (Gems Sensors 0.1-2.5l/min sensor for SEC2) and in the use of flexible polyethylene piping to transfer

the water to and from the test section. Energy transferred to the HFE7000 working fluid from SEC1 and SEC2 is governed by the water outlet temperature and flow rate settings and is calculated as

$$Q_{SEC1} = \dot{m}_{WATSEC1} c_{pWAT} (T_{40} - T_{41}) \tag{81}$$

and

$$Q_{SEC2} = \dot{m}_{WATSEC2} c_{pWAT} (T_{20} - T_{31}) \tag{82}$$

3.1.3: Test Sections Used

3.1.3.1: Test Section A

This test section consists of a developing length, an electrically grounded transparent sapphire tube with concentric electrode held in polypropylene supports, a surrounding Perspex hot water shell, pressure taps and accompanying thermocouples.

In previous studies involving two-phase flow and EHD, the test section materials were typically fabricated from stainless steel or other metal [5, 8, 9, 11, 12, 28-30, 61, 68, 76, 77]. While this satisfied the engineering considerations of strength, corrosion resistance, electrical grounding and thermal conductivity, it had the disadvantage that flow regimes had to be inferred from thermocouple measurements in the test section wall, or utilising void fraction measurement by capacitive means. In other studies, transparent sections have been used with thin electrically conductive layers to afford Ohmic heating, but suffered from the drawback of limited heat flux capacity [13] due to burnout. An alternative was to provide a viewing section outside of the heat exchanger [38] but this remained separate from the main heat transfer area under study.

A test section fabricated from glass was investigated but modelling showed that its low thermal conductivity of 1-1.5 W/m.K inhibited the effective heat transfer to the working fluid. Modern ceramics were then investigated, and aluminium oxide (Al_2O_3) or sapphire was found to be available in various forms, with acceptably high transparency (up to 86% visible spectrum) and with a thermal conductivity bettering that of stainless steel (40W/m.K versus 15W/m.K). In the investigation being

described, use of a custom ordered transparent sapphire tube supplied by Cradley Crystals, Nizhny Novgorod, Russia, allowed the simultaneous heat transfer while permitting visualisation of the entire flow field. The sapphire tube has a thin layer of indium tin oxide (ITO) of thickness 30 nm deposited around the outer circumference so as to provide the electrical ground.

The first element of the test bed is a developing length of stainless steel tubing of outer diameter 9.8mm, inner diameter 8mm and length of 400 mm (50 diameters) to allow flow re-stabilisation of the working fluid before entry to the sapphire test section. The transparent sapphire tube test section is 500mm in total length, but with 10mm at each end inset into the custom built polypropylene supports, leaving a working test length of 480mm. Polypropylene was chosen over other polymers for its balance of good electrical insulation qualities, resistance to HFE7000, high resistance to hot water, and low water absorption rate assuring low dimensional variance during rig operation. A complete guide to the choosing of polypropylene is given in Appendix C.

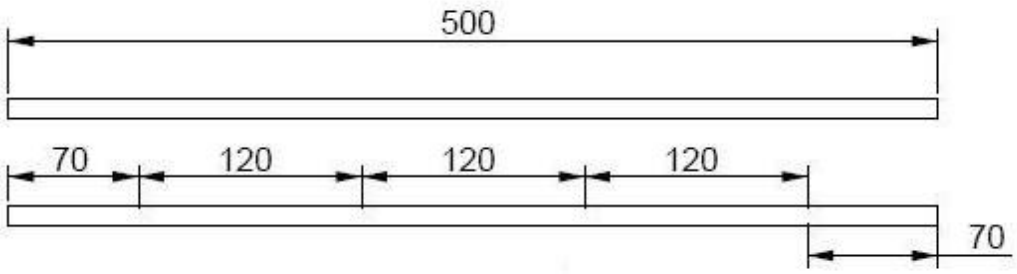

Figure 27: Location of 0.5mm deep pockets in sapphire tube wall

The sapphire tube has outer and inner diameters of 10mm and 8mm respectively, and is held at each end by machined polypropylene supports (Figure 28), which are in turn securely bolted to the test section frame. The polypropylene supports each contain a port to allow a differential pressure measurement to be made across the test section, and incorporate machined surfaces to provide a stable fixing for the Perspex heating water jacket. The sapphire tube fits into a recessed counterbore of 10mm diameter and depth 10mm in the supports. The sealing of the sapphire tube in the support is accomplished by a butyl rubber O-ring compressed by a threaded brass gland against the polypropylene support.

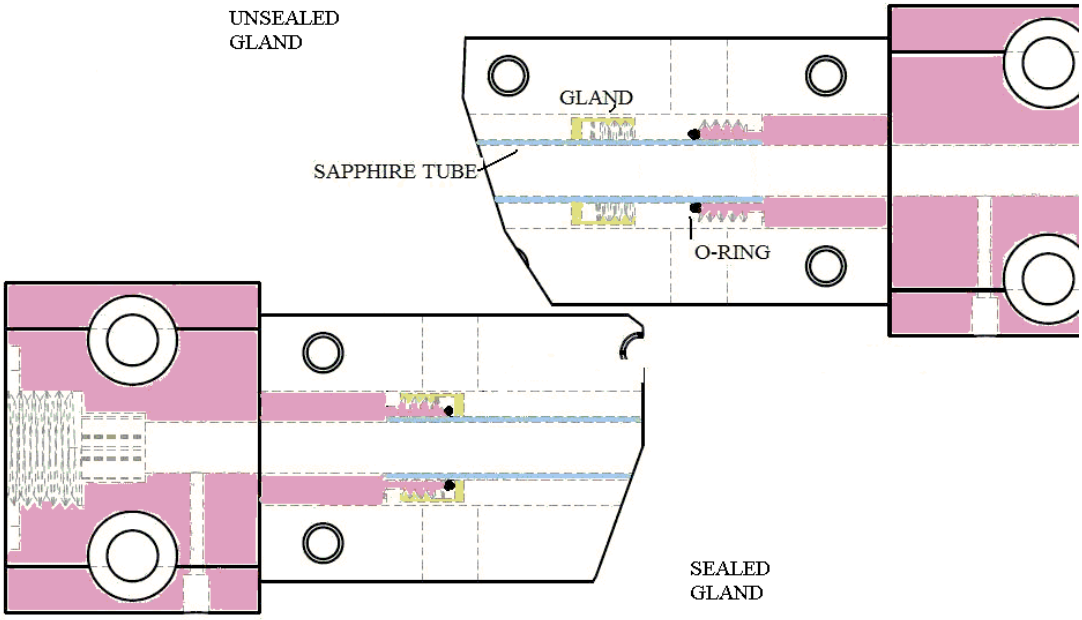

Figure 28: Polypropylene supports, O-ring seal and gland

The sapphire tube has eight pockets, 4 top and 4 bottom, 0.5mm diameter by 0.5mm deep drilled into the tube wall at 120mm intervals into which are placed the embedded type T miniature thermocouples (Omega type TMQSS-020(G)-6) to record the wall temperature. As a precaution against axial thermal conduction, the thermocouples are thermally insulated by a polyethylene sleeve as far as possible, after which the tip is potted into the 0.5mm deep pocket by a small amount of temperature resistant epoxy adhesive. The thermocouple and its sealing gland are shown in Figure 29.

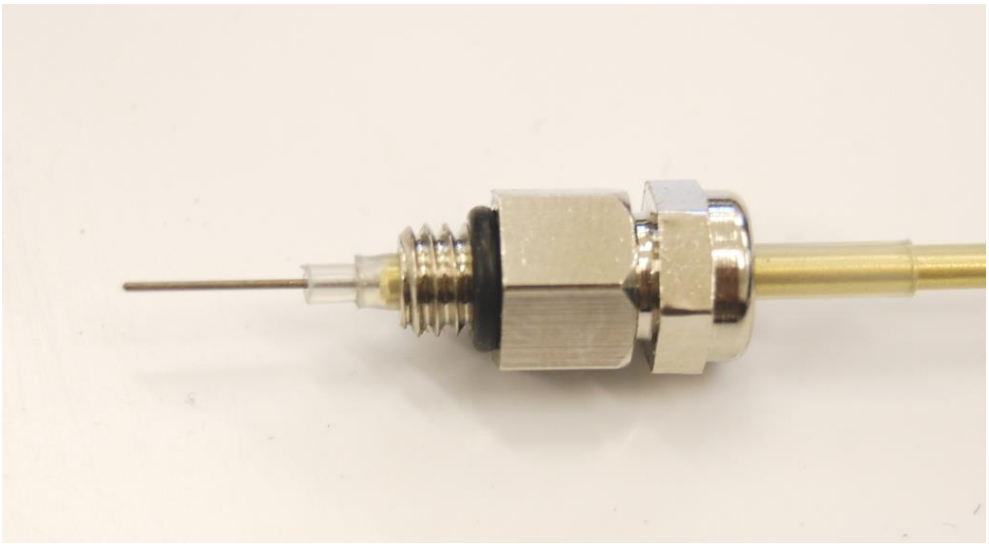

Figure 29: Miniature Type-T thermocouple with sealing gland

A transparent hot water jacket, (see Figure 30) fabricated from four mating pieces of 8mm and 10mm thick Perspex sheet, is assembled around the sapphire tube to create a square section channel around which the water from SEC2 flows and transfers its heat into the sapphire test section.

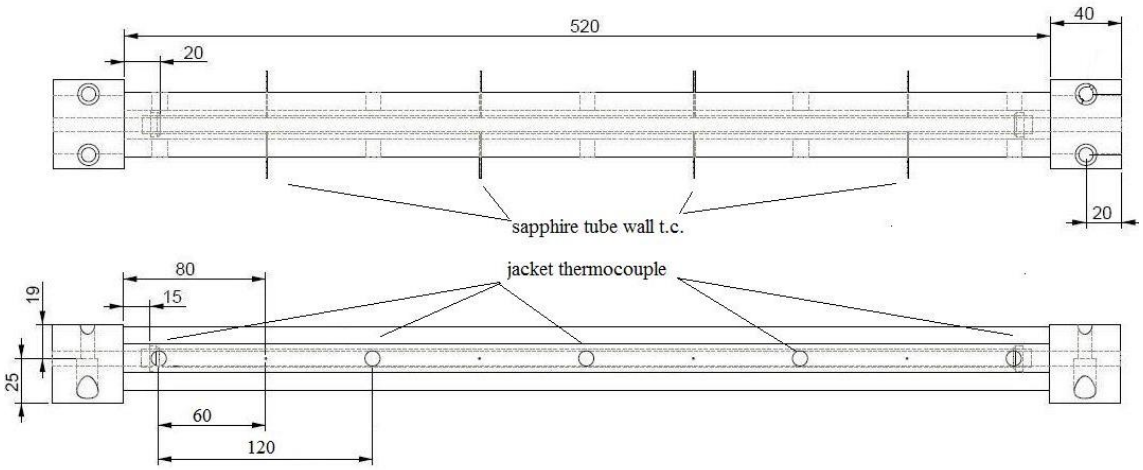

Figure 30: Sapphire tube and perspex jacket showing location of thermocouples

The Perspex jacket holds ten type T thermocouples (Omega Type TMQSS-062G-6), 5 along the top and five along the bottom at 120 mm spacing, each protruding into the SEC2 water stream, thus creating eight zones, four top and four bottom, across which the temperature drop of the water is measured.

The pressure drop across the sapphire test section is measured by a Taylor DP504T 0-70 mbar differential pressure sensor; the pressure tappings can be seen in Figure 31 and Figure 32. The 6 mm Ø pressure lines are surrounded over part of their length by a sealed copper tube of 10 mm Ø through which cold water is passed. This forms a miniature shell heat exchanger which condenses any vapour issuing from the test-section, thus ensuring that the measuring line is completely filled with liquid. Another view of the polypropylene support with the sapphire tube in location is shown in Figure 32. The Perspex water jacket is subsequently assembled around the sapphire tube and polypropylene supports. The water jacket thermocouples and one sapphire tube wall thermocouple can also be seen.

Figure 31: Test section showing developing length, sapphire tube, perspex jacket and polypropylene support pieces

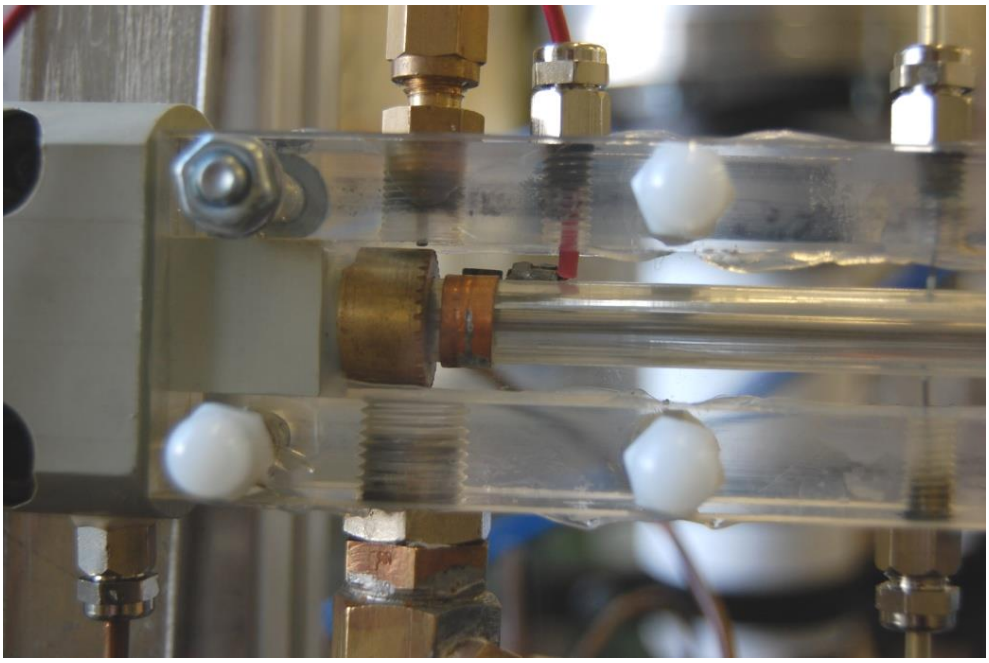

Figure 32: Test section close up showing perspex jacket, sapphire tube, ground connection, SEC2 water outlet, one jacket thermocouple, and two sapphire wall thermocouples.

3.1.3.2: Test Section B

This was dimensionally identical to Test Section A except that the tube was heated ohmically via an electrical power supply. A schematic is shown in Figure 33. Similar transparent ohmic heaters are already in use in similar flow boiling studies by Colin [81] and Ohta [13] who use an ITO layer on sapphire and a gold film on glass respectively.

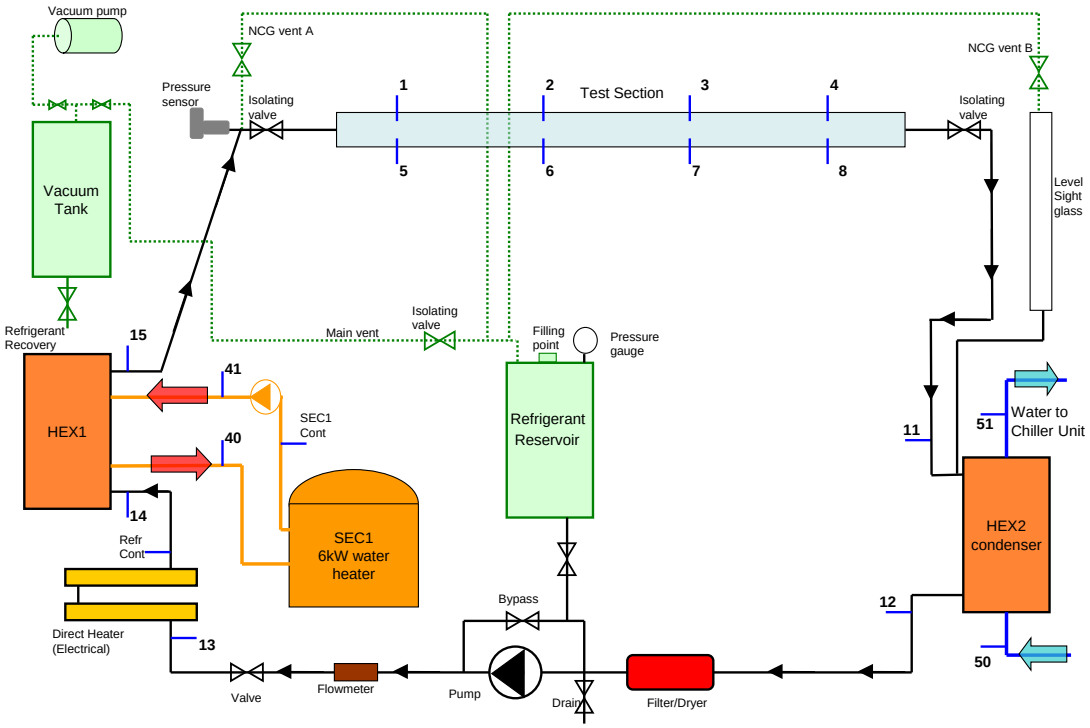

Figure 33: Schematic of rig with Test Section B

The heating was accomplished by a thicker ITO coating of 600 nm (the resistance was now 10 Ω/sq as opposed to 300 Ω/sq for the earlier test section) which also functioned as the EHD ground, but also permitted sufficient current flow to allow electrical heating. The end to end resistance of Test Section A was roughly 6000 Ω, and while adequate for grounding, was too high for practical ohmic heating. Test Section B however, with the ITO coating conductivity of 10 Ω/sq, led to a total resistance of roughly 200Ω permitting ohmic heating at lower voltages of around 150 – 200V.

A regulated power supply (Elektro-Automatik PS8000T) is used to provide current through the ITO coating in order to heat the tube. The current is provided via terminals affixed to a ring of conductive adhesive forming annular bus bars at each end of the

tube. In practice, the current was around 0.8A, and the voltage was regulated at around 190V so as to provide 150 W heat input into the refrigerant. A schematic of the test section is shown in Figure 34.

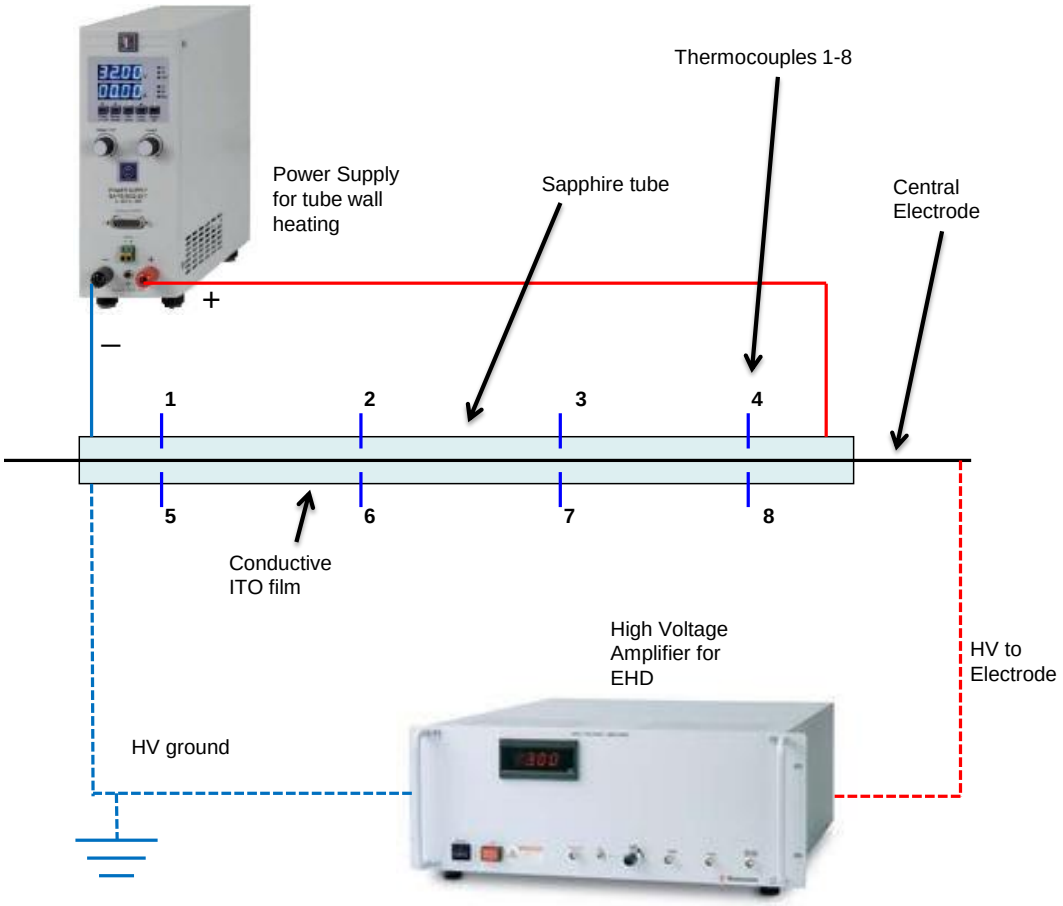

Figure 34: Electrical schematic of Test Section B

The new sapphire tube has the same dimensions as the first one, 500mm long (480mm working length), 8mm inner diameter and 10mm outer diameter. Again a central electrode of 3mm diameter runs concentrically through the tube. The sapphire tube has 8 pockets drilled into the wall, 4 along the top and 4 along the bottom into which are placed type T miniature thermocouples of 0.5mm diameter (Omega type TMQSS-020(G)-6). The locations of the holes are identical to the previous test section. An image of the new test section is given in Figure 35. A Perspex finger guard is affixed in the front of the tube for safety as the voltages used in both the heating and EHD circuits pose a shock hazard.

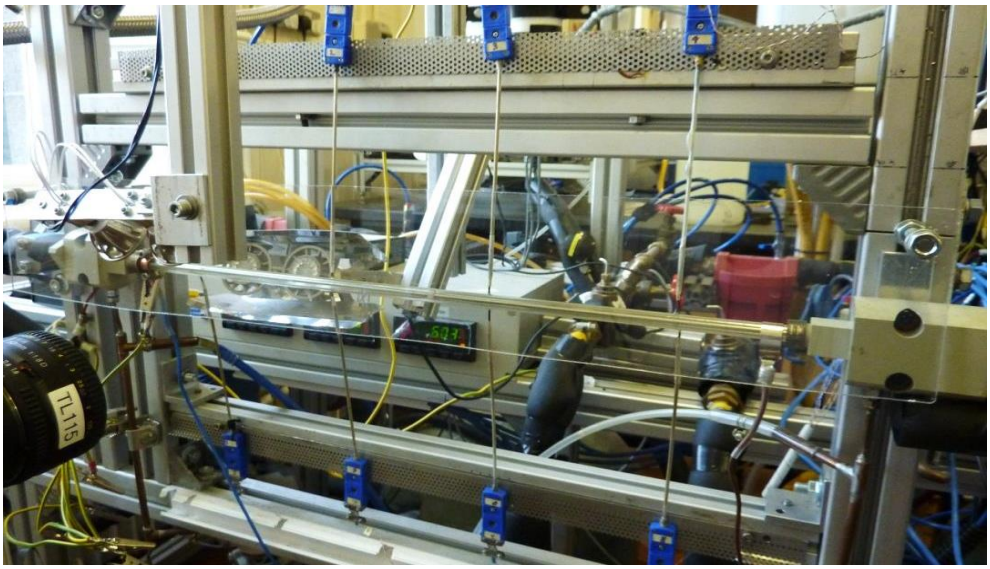

Figure 35 : Image of the second test section fitted with thermocouples

3.1.4: The Cooling Loop

After the two-phase working fluid leaves the test section, the mixture enters a second compact plate heat exchanger (up to 52kW) where it is condensed by a stream of cooling water pumped from a controlled chiller unit (Grant RC1400G). The cooling water flow rate is measured by a 1-10l/min turbine flow sensor (Gems FT-110) and is regulated by a gate valve and bypass. T-type thermocouples monitor the water temperatures at the condenser inlet and outlet, and again at the working fluid inlet and outlet. The heat extracted from the working fluid balances that gained by the condensing water stream; in single phase it is calculated from the water side by

$$Q_{COND} = \dot{m}_{COND} c_{pCOND} (T_{51} - T_{50}) \tag{83}$$

3.1.5: Expansion Vessel and Venting Arrangements

A closed stainless steel expansion vessel is fitted to the primary loop, allowing extra volumetric capacity for expansion. This vessel is fitted with a cooling water jacket so as to condense any vapour entering, thus helping to maintain the pressure inside the vessel below the rig pressure, allowing for safe venting of excess pressure at any time. System pressure is monitored manually by means of the electronic pressure transmitters P1 and P2. In addition, either the vessel or the primary loop vent is connected at all

times to an external vacuum vessel, allowing a vent if rig pressure were to increase to high levels. This external vacuum vessel also allows the system to be scavenged of air or non-condensable gases (NCGs) from bleed locations at the test section inlet, the condenser inlet, and from the top of the expansion vessel. Any refrigerant liquid carried over during purging of NCG settles in the bottom of the vessel and can be recovered via a drain valve. After draining refrigerant the vessel, a vacuum pump is used separately to replenish the vacuum in the external vessel, thus keeping refrigerant losses to a minimum.

3.1.6: The Electrode and High Voltage Supply

To apply the EHD forces, a stainless steel electrode of 3mm Ø and 600mm length runs along the centre of the test section. Two tripod support pieces locate the electrode concentrically within the polypropylene supports and within the sapphire tube. The electrode is flared at one end to act as an anchor (see Figure 36(a)), and is threaded at the other end to permit

- tensioning of the electrode,
- compression for the O-ring seal,
- secure attachment of the high voltage connection (see Figure 36(b)).

An auxiliary tripod spacer is fitted to the electrode along its length to prevent excessive oscillations of the electrode inside the tube induced by the EHD and fluid forces.

Figure 36: Electrode location in polypropylene supports (a) entrance and (b) exit

The sapphire tube has a thin layer of indium tin oxide (ITO) with a thickness of 30 nm and a conductivity of 300Ω/m^2 deposited around the entire outer circumference to provide a ground for the high voltage yet allow good visibility as seen in Figure 37. Transmissibility of the ITO coating is given in Appendix A. A ring of high silver content adhesive provides electrical continuity to the ITO coating. A copper clamp affixed to the annular adhesive ring completes the grounding via a wire to the rig frame (see Figure 37).

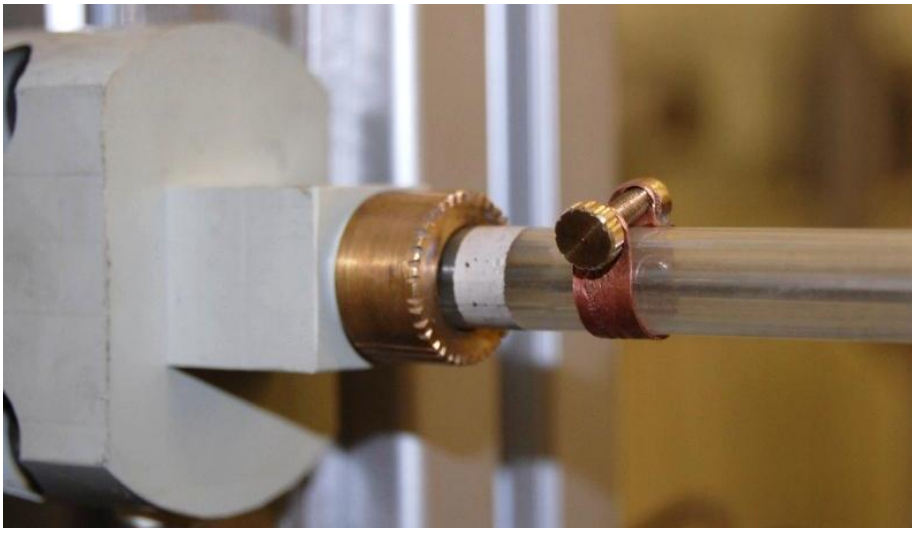

Figure 37: Conductive adhesive ring and copper earthing clamp

High voltage to the electrode is supplied from a Matsuda AMT10B10 series 0-10 kV high voltage amplifier (see Figure 38(a)), while the primary signals of amplitude and frequency are delivered from a Hewlett Packard 3325B synthesiser/function generator and verified by an ISO-Tech IDS 8064 oscilloscope. The high voltage amplifier features current and voltage monitor outputs which can be used to record actual current and voltage parameters of the high voltage wave.

3.2: Use of the ITO Coated Sapphire Tube

While it is believed that this is the first time that this type of novel test section has ever been used, which incorporates thermal conductivity, an electrical ground, and all the while allowing full visual access to the flow, there are a number of characteristics that made the test section differ from conventional metallic test sections. These are briefly considered in the next sub-sections.

3.2.1: Thermal Conductivity Considerations of the Sapphire Tube

The thermal conductivity of sapphire is published as around 40 W/m K depending on manufacturing method, individual suppliers etc. The Biot number (Bi) can provide a measure of the relative importance of conduction or convection through the tube wall. It is defined as

$$Bi = \frac{hL}{k} \tag{84}$$

where h is the convective heat transfer coefficient on the inside of the tube, L is the characteristic length, in this case the sapphire tube thickness, and k is the thermal conductivity of the sapphire tube wall.

The Biot number for the tube in the radial direction was found to be 0.03 and therefore as it is less than 0.1, it is the convective process and not conduction through the tube that is deemed to be the controlling resistance in the circuit [15]. Given the low Biot number of the tube, for the purposes of this thesis the temperature through the tube wall in the radial direction was assumed uniform.

Lateral heat transfer was also examined. This is to quantify the level of heat transfer through the tube wall in the axial direction. If this is significant, then errors will be introduced into the heat transfer coefficient calculations which are assumed to be wholly dependent on the fluid energy balance. For axial heat transfer the primary driver is ΔT in the lengthwise direction. A check using Fouriers Law quantified the heat flux in the axial direction. This is given as

$$q = k\frac{dT}{dx} \tag{85}$$

where k is the thermal conductivity of sapphire (40 W/m.K), dT is the difference in temperature, and dx is the length of the tube.

For the case of the water heated tube, the maximum thermal gradient between x/L =1/8 and x/L=7/8, a length of 0.36 m was 2.6 °C. Extrapolating this to the complete length of the tube of 0.48 m gives a dT of 3.43 °C. Inserting this into equation (86) returns an

axial heat flux of 286 W/m^2. Given that the total heat flux is 12400 W/m^2, this represents around 2.3% of the total heat flux and is sufficiently low to be negligible.

Likewise, for the ohmically heated test section, the largest axial variation in wall superheat was found to be around 5 °C but this occurred over a length of 0.24 m and only at the top of the tube towards the end where dryness was more prevalent. Substituting into equation (86) again yields a heat flux of 833 W/m^2 accounting for 6.7% of the total heat flux for this isolated case. This is a higher percentage than found in the water heated case, however given this is the worst case scenario, and the fact that it occurs only towards the driest end of the upper part of the tube it is again not a large enough factor to interfere significantly with the results presented.

3.2.2: Surface Finish of the Tube.

Most metallic test sections are stainless steel or brass or copper. Despite appearing superficially smooth, these metallic surfaces are often microscopically rough and contain surface asperities as a result of grinding or polishing finishing processes such as peaks and hollows. These surface features are found to initiate or "seed" nucleation, and are advantageous in boiling. The sapphire tube however was not ground or polished and was supplied "as grown" by Cradley Crystals and was glassy and smooth to the touch. It was most likely manufactured using the Stepanov technique by drawing from a molten pool of aluminium oxide (Al_2O_3). This method is fast and relatively cheap but dimensional accuracy can vary.

On inspection before fitting to the rig, the tube did have some undulations and a slight bow of around 0.5mm along its length. Some glassy undulations or ribs were also noticed on the inside of the tube. Therefore, it was noted that the surface of the sapphire tube may be very different form an equivalent metallic tube, especially in relation to the ability of the tube to seed bubbles or assist in nucleation. Grinding of the tube exterior to remove these dimensional undulations was in theory possible but the cost increases and the process is risky. Also, it may not have been technically feasible to grind the inside of the tube where the refrigerant boiled, as it was only 8mm in internal diameter and 500mm in length. Consequently it was decided to use the tube as supplied and accept the surface condition and manufacturing undulations as the novelty

of flow field visualisation under EHD conditions should outweigh any disparities in bubble nucleation or boiling when compared with metallic tubes.

3.2.3: Variation in thickness of the ITO coating.

The thickness of the ITO layer is much less of a problem for water heated test section A as the ITO was used only as a ground reference for the high voltage. But variations in the ITO thickness in test section B could cause uneven heating on the sapphire tube. While Diamond Coatings Ltd. used a Cary 500 Spectrophotometer to measure ITO coating thickness, and they gave assurances of an evenly distributed coating over the tube, in house verification of this proved difficult. The resistance of the ITO coating on the tube was measured before installation using a desktop multimeter and test probes and found to be generally even with axial and radial position. However, it was noted that variations in contact pressure could affect the resistance displayed. Also the resistive path taken by the resistance measurement need not necessarily be a straight line between the probes, but would be the path of least resistance. Therefore to quantify the evenness of the ITO coating by these basic resistance measurements may not be ideal and an option worth exploring in subsequent tests would be to request a certificate from Diamond Coatings confirming the evenness of the applied coating.

3.3: The Data Acquisition System

The data acquisition system consists of two National Instruments® Compact DAQ 9172 8-slot chassis units (see Figure 38(b)) with several types of modules used depending on the measurement type. Two NI9219 24bit 4-channel modules are used for the eight embedded test section thermocouples, set at the highest resolution of ±125 mV and giving a minimum accuracy of ±0.18 %. Seven NI9211 4-channel thermocouple modules which have an accuracy of 0.07ºC over the entire range were used for the remainder of the T-type thermocouples. Both NI9219 and NI9211 modules featured integral cold junction compensation circuitry. Two NI9215 4-channel modules with an accuracy of 0.029V over a range of ±10V were used for the high level analogue signals such as pressure, flowmeter output etc. A custom designed

program using Labview® displayed and logged the data. A picture of front panel is shown in Figure 39.

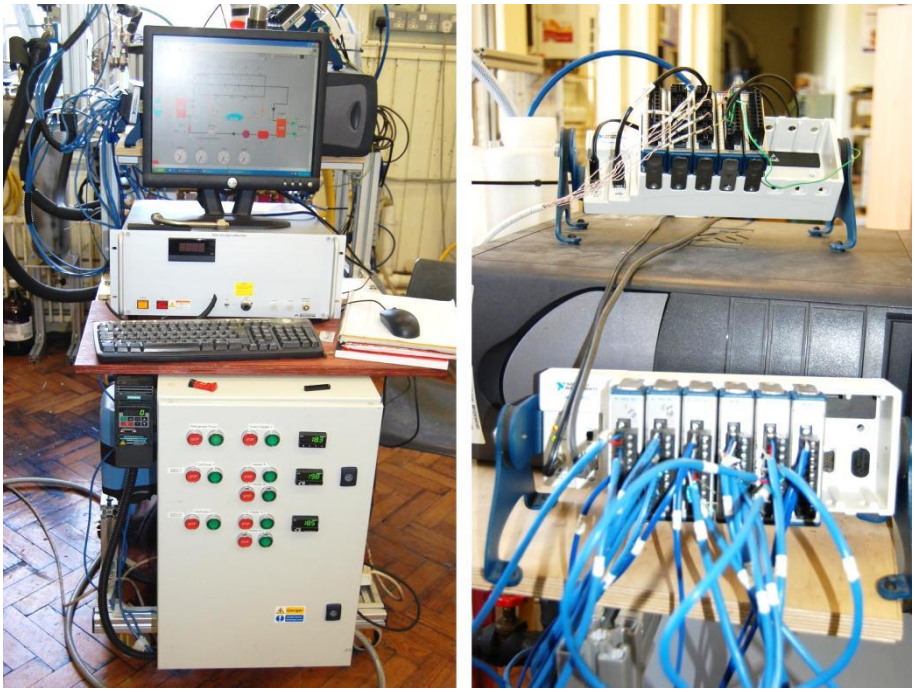

Figure 38: (a) Control cabinet, high voltage amplifier (b) datalogging hardware

All thermocouple inputs were calibrated in an Omega HCTB-3020 thermal bath calibrator against a reference 4-wire thermistor (type General Electric ES-215) accurate to 0.01°C and HP 34401A Multimeter.

While properties such as temperature, flow, and pressure were measured directly from instruments, other fluid properties varied with state, and could be calculated indirectly from look-up tables. The influence of pressure on the water was neglected as the water circuit was open and nominally at atmospheric pressure. As the working fluid was subjected to phase change within a closed loop, pressure as well as temperature varied. Properties such as density, viscosity and specific heat vs. temperature were plotted for water using property tables commonly available [82, 83] and the curves input into the Labview program. This enabled computation of water density, viscosity and specific heat versus temperature at that point. For HFE7000, again regression curves and their polynomials were generated from look-up tables supplied by 3M Corp. A list of the calculated values is provided in Table 4. The curves themselves and their polynomial equations are detailed in Appendix B: Calculation of Fluid Properties.

Table 4: Summary of Fluid Properties Determined from Temperature or Pressure Measurements

Fluid	Property	Calculated From	Data Source
Water	ρ	Temperature	NIST [83]
	μ	"	NIST
	C_p	"	Rogers and Mayhew[82]
HFE7000	ρ	Temperature	3M Corp
	C_p	"	3M
	h_f	"	3M
	h_{fg}	"	3M
	h_g	"	3M
HFE7000	h_f	Pressure	3M
	h_{fg}	"	3M
	h_g	"	3M

The Labview front panel showing the rig in schematic form with all measured parameters can be seen in Figure 39.

Two Labview programs were used for data collection. One of them logged at a frequency of 2Hz over a 30 second period and included a 30 second rolling average of the last 60 points. This was used when the rig achieved steady state for heat transfer measurements. However, the slow scanning frequency of 2Hz and subsequent averaging would not disclose rapid transient fluctuations of the wall thermocouples or the differential pressure gauge. Consequently, a second Labview program was created for that purpose. It was identical to the first except that the scanning frequency was increased to 1000Hz for 10 seconds and no averaging or filtration was employed. Any changes to the Labview program (e.g. recalibrations, new instruments) were made to the slower scan program, and this was then re-saved and the scan modified to create an updated fast scan program.

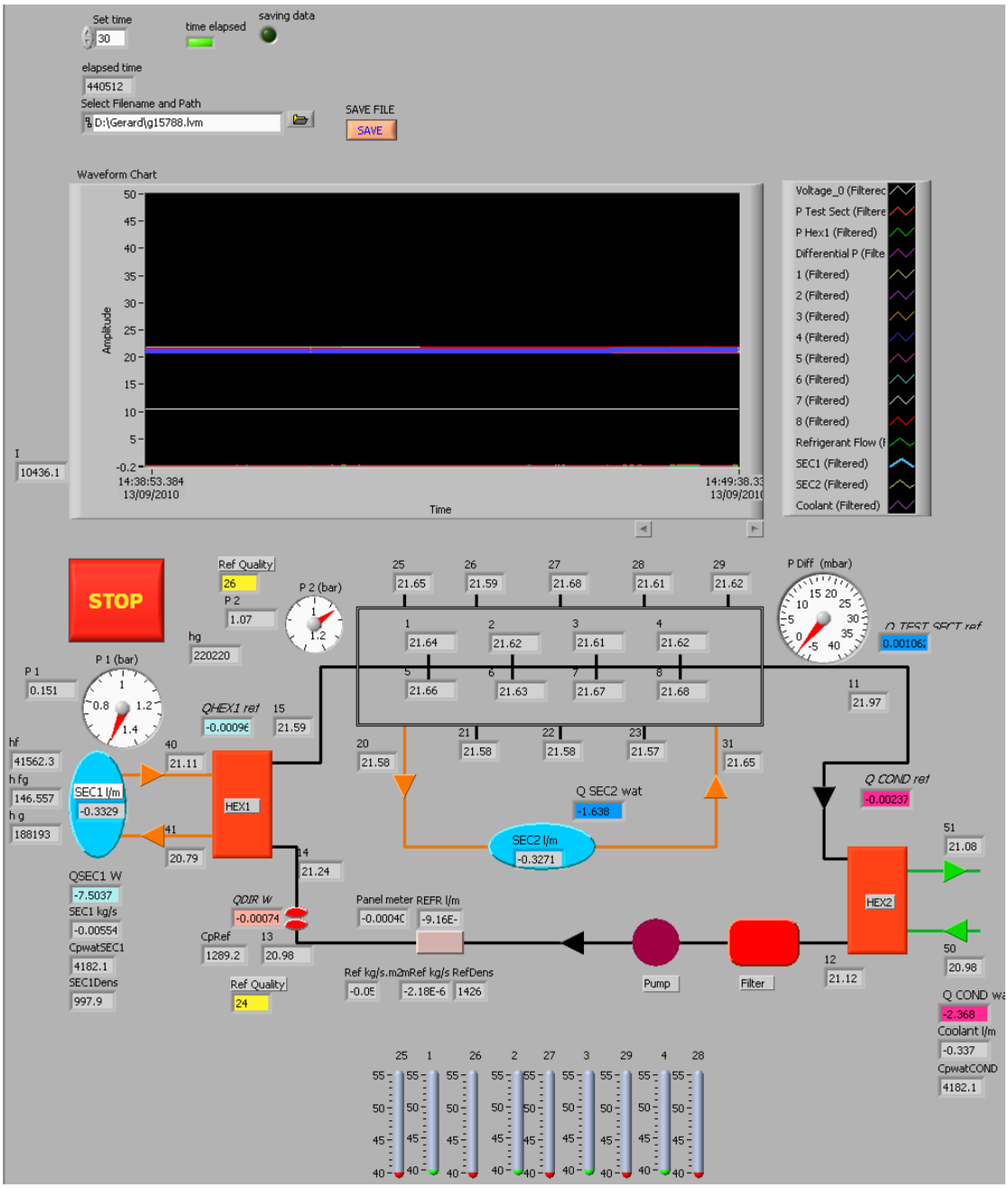

Figure 39: Front panel of Labview® data acquisition program

3.4: High Speed Imaging System

In addition to the data logging information, a Hot Shot 1280 (NAC Image Technology) black and white high speed camera with its associated software was used for recording video and photo stills of each experiment. Backlighting for the exit region of the sapphire tube was provided by two LED cluster lamps (Fawoo LH-03) of 240 lumen. Images were recorded at a shutter speed of $1/2000^{th}$ of a second in order to capture rapid liquid movements caused by the flow or electric field forces. For the tests at constant heat flux, 1.5 seconds worth of data were recorded (3000 frames) and stored as videos and images for later analysis. Images were recorded at 4 locations along the test section, centred at x/L =⅛, ⅜, ⅝ and ⅞. For later experiments at constant water inlet temperature and in the second electrically heated test section, a Photron camera and DaVis Software was used utilising a shutter speed of $1/3000^{th}$ of a second. 5 or 10 seconds of data were recorded (15000 frames) and stored as videos and images. Images were only recorded at one location, x/L = ⅜ in the constant water inlet case, and again at 4 locations during the electrically heated tests.

3.5: Experimental Procedure

There were three series of experiments carried out in this thesis. Series one and two used the water heated test section, while series three used the electrically heated test section. The main parameters of interest in this investigation are summarised below:

- Test fluid/ mass flow rate. This was fixed at G=100kg/m^{2}s for all tests.
- Inlet quality of the fluid in the test section x_{in}. In test series one, this was varied from 2% to15%, 30% and finally 45%. In test series two and three, inlet quality remained at 2% only.
- In test series one, the voltages tested were 0, 4 and 8kV, while in series two and three, voltages were varied in 1kV steps from 0 to 10kV.

In test series one, it was decided to fix the heat input across the test section. This was achieved by adjusting the water inlet temperature so that 150 watts of heat was transferred to the refrigerant at all times. Because of this imposed constraint, the change in quality would also remain constant across the test section. However, a side effect of this lowering of the inlet water temperature was that the phase change surface temperature (sapphire tube wall) dropped. This drop in superheat would be certain to affect flow boiling of refrigerant within the tube, most notably refrigerant.

Therefore in order to address this lowering of the phase change temperature, the second series of tests were conducted at a constant water inlet temperature. Now, the amount of heat transferred across the test section was allowed to vary with EHD augmentation. The exit quality of the refrigerant likewise increased with heat input. Only one quality was investigated and one region of interest was studied in this test series.

Finally, one of the original aims of this thesis was to investigate local heat transfer coefficients along the tube. Due to large uncertainties in the water side thermocouples of the heat exchanger, this was not possible. Therefore in order to combat this, test section three was used, which featured electrical heating. While this allowed measurement of the heat transfer coefficients at each imbedded thermocouple location, this test section had the shortcoming of not providing an overall heat transfer

coefficient as the earlier water heated test sections gave. Another characteristic of this test section was the fact that the upper temperature limit was unbounded. In the water test sections, the maximum wall temperature would be limited by the water temperature. However, in an ohmically heated test section, the wall temperature, especially in a region of dryout where cooling is less, can climb higher. Though a matter of debate, according to Thome [20], the favoured method in flow boiling research is water cooling. Thome notes that for annular flows, the heat transfer coefficients will be similar. In the case of a stratified liquid layer, water heating will produce a near uniform temperature field approximating a constant temperature wall boundary. However, a stratified flow under electrical heating can lead to circumferential heat transfer through the tube from the drier hotter top to the cooler wetted bottom leading to an unknown boundary condition, and can also lead to axial conduction. While lateral conduction was estimated for the worst case scenario (see section 3.2.1) and found to be within 6.7% of the total heat flux and thus not deemed significant in this study, at higher qualities where dryout is more prevalent towards the end of the tube, combined circumferential and lateral heat transfer would become a greater issue.

The experimental procedure for the two-phase flow operation of the rig is outlined in Table 5.

Table 5: Experimental Procedure

No.	Step
1	Set working fluid mass flux by fixing pump speed
2	Adjust electrical input to DIR1, adjust flow rate and temperature of SEC1 so as to control quality of working fluid leaving HEX1
3	Adjust flow rate and temperature of SEC2 (or in case of Test Section B, electrical power) to achieve desired heat flux in the test section
4	Monitor and regulate pressure, mass flux, SEC1/2 and allow to achieve steady state (from cold start, allow 2 hours, subsequently allow 20-40 minutes depending on magnitude of parameter change).
5	When conditions are near steady state, apply EHD voltage and allow to re-stabilise, re-tune as necessary.
6	Acquire averaged data (steady state),
7	Observe flow regime through transparent test section, acquire high speed photographs/video, this may involve high speed photography at several locations along the tube.
8	Acquire high speed data to record transient behaviour
9	Process data and videos
10	Repeat procedure for next test parameter.

It was found that after a parameter had been changed, thermal lag meant some Labview parameters could display counter intuitive readings. After 5 minutes, the real trend could usually be noticed, and after 20-40 minutes steady state was normally reached.

3.6: Experimentally Measured Parameters and Test Conditions

This section explains how the experimental measurements were collated to calculate the HTCs in the test sections under both field-free and EHD conditions. Experimental parameters which were key variables in the tests are summarised in Table 6. All experimental measurements are listed in Table 7.

Table 6: Summary of Experimental Conditions in Test Section

Parameter	HFE7000	Heating
TEST REGIME 1		
Mass Flux	100 kg/m^{2}s	Water at Re2500
Heat Flux	12.4 kW/m2	
Pressure	1.0 bar (abs)	
Inlet Quality	2,15,30,45%	
High Voltage	0, 4, 8 kV	
HV Frequency	60 Hz	
TEST REGIME 2		
Mass Flux	100 kg/m^{2}s	Water at Re2500
Heat Flux	12.4-18.6 kW/m2	
Pressure	1.0 bar	
Inlet Quality	2%	
High Voltage	0,1,2,3….10 kV	
HV Frequency	60 Hz	
TEST REGIME 3		
Mass Flux	100 kg/m^{2}s	Ohmic
Heat Flux	12.4 kW/m2	
Pressure	1.0 bar	
Inlet Quality	2%	
High Voltage	0,1,2,3….10 kV	
HV Frequency	60 Hz	

Table 7: Experimental Measurements

Rig reference	Property	Unit	Location
T1	Temperature	(ºC)	sapphire tube x/L=⅛ top
T2	"	"	sapphire tube x/L=⅜ top
T3	"	"	sapphire tube x/L=⅝ top
T4	"	"	sapphire tube x/L=⅞ top
T5	"	"	sapphire tube x/L=⅛ bottom
T6	"	"	sapphire tube x/L=⅜ bottom
T7	"	"	sapphire tube x/L=⅝ bottom
T8	"	"	sapphire tube x/L=⅞ bottom
T11	"	"	Condenser entry, refrigerant
T12	"	"	Condenser exit, refr
T13	"	"	Direct heater (DIR1) entry, refr
T14	"	"	Direct heater (DIR1)exit, HEX Inlet, refr
T15	"	"	HEX1 exit, Test Section inlet, refr
T20	"	"	Test Section x/L=0/4, bottom, outlet, water
T21	"	"	Test Section x/L=1/4, bottom, water
T22	"	"	Test Section x/L=2/4, bottom, water
T23	"	"	Test Section x/L=3/4, bottom, water
T31	"	"	Test Section, x/L=4/4, bottom, inlet, water
T25	"	"	Test Section x/L=0/4, top, water
T26	"	"	Test Section x/L=1/4, top, water
T27	"	"	Test Section x/L=2/4, top, water
T28	"	"	Test Section x/L=3/4, top, water
T29	"	"	Test Section x/L=4/4, top, water
T40	"	"	HEX1 exit, water
T41	"	"	HEX1 entry, water
T50	"	"	Condenser entry, water
T51	"	"	Condenser exit, water
ΔP	Pressure	mbar	Differential pressure across test section
P1	"	bar	Pressure at HEX1 exit
P2	"	bar	Pressure at Test Section inlet
I	Current	mA	Current from high voltage amplifier
REF	Flow rate	kg/sec	Mass flow rate of refrigerant
SEC1	"	kg/sec	Mass flow rate of SEC1
SEC2	"	kg/sec	Mass flow rate of SEC2
COOL	"	kg/sec	Mass flow rate of coolant

The Reynolds numbers of the working fluid in the sapphire test section (Re_i) and of the water in the heating jacket (Re_o) are calculated from the flow rates and annular areas respectively.

$$\mathrm{Re}_i = \frac{\dot{m}_{REF} D_{hREF}}{A_i \mu_{REF}} \tag{86}$$

and

$$\mathrm{Re}_0 = \frac{\dot{m}_{SEC2} D_{hSEC2}}{A_o \mu_{SEC2}} \tag{87}$$

Where D_h is the hydraulic diameter which in the case of the tube is $D_h = D_o - D_i$, while in the case of the Perspex channel, $D_h = 4A_o/P$ where P is the wetted perimeter. Subscripts $_{REF}$ and $_{SEC2}$ refer to working fluid and water in SEC2 respectively, A_i is the sapphire tube/electrode annular cross sectional area, and A_o is the water jacket/annular cross sectional area.

The working fluid quality, x_{in}, is calculated by an energy balance between the SEC circuit and the working fluid circuit across the heat exchanger.

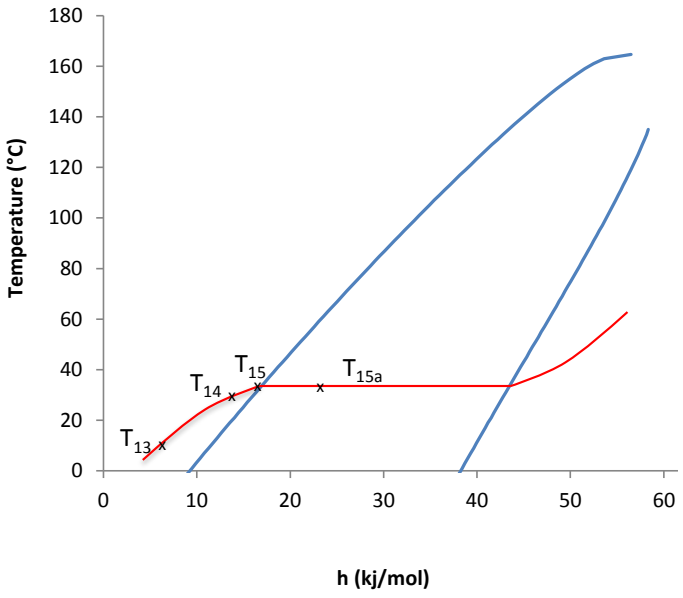

Figure 40: T-h diagram of HFE7000

The T-h diagram in Figure 40 (for illustration only) shows the basis for the quality calculation. Sensible heat from DIR1 (Direct electrical) is shown from T_{13} to T_{14} where

the working fluid temperature is raised to or near T_{sat} of 35ºC. Sensible heat is again added in HEX1 from T_{14} to T_{15} until T_{sat} is reached and boiling begins. Any further heat added from SEC1 will cause a phase change from liquid to vapour. An energy balance across the HFE7000 and water streams enables quality to be calculated. The energy thus used in latent heat is the total heat added to the working fluid, less the energy used for sensible heat:

$$Q_{DIR} + Q_{HEX1} = \dot{m}_{REF} c_{pREF} (T_{15} - T_{13}) + Q_{LAT} \tag{88}$$

$$Q_{LAT} = (Q_{DIR} + Q_{HEX1}) - \dot{m}_{REF} c_{pREF} (T_{15} - T_{13}) \tag{89}$$

such that

$$\frac{Q_{LAT}}{\dot{m}_{REF}} = (\frac{Q_{DIR} + Q_{HEX1}}{\dot{m}_{REF}}) - c_{pREF} (T_{15} - T_{13}) \tag{90}$$

Since $\frac{Q_{LAT}}{\dot{m}}$ =h_{15a}-h_{15} and h_{15a}=h_{15} + x h_{fg} it is easily shown that the quality can be determined from the expression

$$x = \frac{(\frac{Q_{DIR} + Q_{HEX1}}{\dot{m}_{REF}}) - c_{pREF} (T_{15} - T_{13})}{h_{fg}} \tag{91}$$

3.7: Data Reduction

Consistent with previous research [4] the overall heat transfer coefficient was calculated in this research using an average surface temperature method. This technique calculates overall heat transfer from 3 parameters:

- heat flux obtained from secondary fluid temperature measurement
- working fluid saturation temperature
- tube wall temperature

The heat transfer coefficient was chosen as the primary parameter of thermal performance. Nusselt number was also considered but as D_h and k_{refr} were constant throughout the investigation, this would be in effect a scaled version of the heat transfer coefficient.

3.7.1: The Averaged Heat Transfer Coefficient

This method calculated the averaged HTC of the evaporating working fluid by determining the total heat transfer rate on the water side. The method uses the total amount of heat transferred from the water to the tube across the test section. It then determines an average surface temperature using the embedded wall thermocouples, incorporates the difference between this average wall temperature and the saturation temperature of the fluid, and finally includes the surface area of the tube to calculate the HTC from the expression given by Thome [20]

$$HTC = \frac{q_W}{A(T_{WALL} - T_{SAT})} \tag{92}$$

where

$$q_w = \dot{m} c_{pw} (T_{w,in} - T_{w,out}) \tag{93}$$

The mean of the eight surface thermocouples is found from

$$T_{savg} = \frac{1}{8} \sum_{1-t,b}^{4-t,b} Ti_{S-t,b} \tag{94}$$

The inner HTC is then calculated from

$$\bar{h}_i = \frac{q_w}{S_i (T_{savg} - T_{SAT})} \tag{95}$$

This method requires many thermocouple readings for an accurate estimate of the wall temperatures. For Test Section A, this is reasonable since the wall superheat variations around and along the test section were minimal. Another weakness is that it is an averaging technique and therefore indicates the performance of the test section as a whole, ignoring local HTC variations. This shortcoming is addressed with Test Section B which is specifically designed to measure the local HTCs along and around the tube.

3.7.2: Data reduction for the Ohmically Heated Test Section B

For the second test section, all rig calculations are calculated in the same manner, except that the heat flux is known from the electric heater power which simplifies the calculation of the HTC.

3.7.2.1: Calculation of heat input

The power supply provides a potential difference V which induces a certain amount of current I through the ITO coating of the sapphire tube. Knowing those values, the total heat is calculated by

$$q_{total} = V \times I \tag{96}$$

However, the heated sapphire tube is subject to convective and radiative losses between its external surface and the ambient air. This heat loss has to be subtracted from the total heat in order to find the amount of heat transferred to the refrigerant:

$$q = q_{total} - q_{convrad} \tag{97}$$

An energy balance in steady state between the electric heating and the convection allows us to evaluate the thermal losses, $q_{convrad}$, through

$$q_{natconv} = h_0 S_0 \left(T_{wall} - T_\infty\right) \tag{98}$$

where T_{wall} is the temperature of the wall, T_∞ is the external temperature far from the tube and h_0 is the convective heat transfer coefficient.

A simple experiment has been conducted in order to obtain the value of the coefficient h_0. The experimental procedure is explained in Appendix F and the combined convective and radiative losses were found to be around 4-5W at the working experimental temperatures in this test.

3.7.2.2: Calculation of the heat transfer coefficient

As long as q is known, $h_i$can be easily calculated in the same way as in the first rig data reduction.

Overall

$$h_i = \frac{q_i}{S_i(T_{wall} - T_{sat})} = \frac{q_i''}{T_{wall} - T_{sat}} \tag{99}$$

Where T_{wall} is the average of the 4 top and 4 bottom wall temperatures.

$$T_{wall} = \frac{1}{8}\sum_{1-t,b}^{4-t,b} T_{wall,k_{t,b}} \tag{100}$$

Local

Two local heat transfer coefficients are defined, one on bottom and one on top for the 4 sections which give in total 8 different HTCs:

$$h_{i,k_t} = \frac{q_i''}{T_{wall,k_t} - T_{sat}} \tag{101}$$

$$h_{i,k_b} = \frac{q_i''}{T_{wall,k_b} - T_{sat}} \tag{102}$$

3.8: Instrumentation Accuracy and Experimental Uncertainty

Accuracy figures used for all of the instrumentation were as published by the instrument manufacturers with two exceptions, the refrigerant flowmeter (Titan 945), and the type-T thermocouples. The accuracy of the Titan turbine flowmeter was supplied calibrated for water use and due to the density and viscosity difference of HFE7000 had to be recalibrated using the working fluid HFE7000. This was achieved in the laboratory for the flow rate used during the test and was found to be within 3% of the indicated value.

The published accuracy of the type T thermocouples was ±1°C, but this was improved by calibrating all type T thermocouples in a water bath against a precision thermistor and 4 wire multimeter (GE 215 and HP 34401A) accurate to 0.01°C. An uncertainty analysis based on the methodology of Kline and McClintock [84] was carried out on all instrumentation. The expression

$$\Delta f = \sqrt{\sum_{i=1}^{n}\left(\partial f / \partial x\right)}\Delta x_i \tag{103}$$

forms the basis of the uncertainty calculation, where f is the uncertainty, and x_i are the parameters on which f depends where

$$f = f(x_1, x_2, x_3, \ldots\ldots x_n). \tag{104}$$

The basic formula for a two-instrument reading such as

$$\Delta T = T_y - T_x \tag{105}$$

takes into account the accuracy of both thermocouples giving

$$\sigma_f = \sqrt{\sigma_x^2 + \sigma_y^2} \tag{106}$$

where σ_f is the final uncertainty in percent, and σ_x and σ_y represents the published error of both thermocouples in percent. Table 8 shows the manufacturer's published accuracy of each instrument, with the exception of the thermocouples which were calibrated in-house to improve their accuracy.

Table 8: Accuracy of Instrumentation

Measurement	Device	Absolute Uncertainty	Relative Uncertainty
Temperature (calibrated)	Type T thermocouple (Omega)	0.1^0C (calibrated)	@1^0C ±10% @10^0C = ±1%
Refrigerant flow rate	Titan Instruments Type 945		±3.0 %
Water flow rate (SEC1, SEC2, COND)	Gems FT-110, 1-10l/min		±3 %
Pressure gauge (HEX 1) 1	Bourdon 1-10 bar		±0.2 %
Pressure gauge 2	Omega 1-3 bar		±0.25 %
Diff pressure gauge	Taylor DP 504t		±0.2 %
Voltage to DIR heater	Matrix MX22 Multimeter		±1 %
Current to DIR heater	Matrix MX22 Multimeter		±2.5 %

The general expression for heat in watts *Q*, extracted by the coolant water from a heat exchanger (HEX1, 2 or test section) is given by

$$Q = \dot{m}\, c_p (\Delta T) \tag{107}$$

The total uncertainty of the Q is then a function of the water mass flow rate $\dot{m}$ and the thermocouple temperature difference ΔT

$$\Delta Q_p = \sqrt{\left(\frac{\partial Q_p}{\partial_{\dot{m}}}\Delta_{\dot{m}}\right)^2 + \left(\frac{\partial Q_p}{\partial_{\dot{T}}}\Delta_{\dot{T}}\right)^2} \tag{108}$$

Dividing this expression by the general expression above

$$\frac{\Delta Q_p}{Q_p} = \frac{1}{\dot{m}\ c_p(\Delta T)} \sqrt{\left(\frac{\partial Q_p}{\partial_{\dot{m}}} \Delta_{\dot{m}}\right)^2 + \left(\frac{\partial Q_p}{\partial_{\dot{T}}} \Delta_{\dot{T}}\right)^2} \tag{109}$$

$$= \left[\frac{1}{\dot{m}c_p(\Delta T)}\right] \sqrt{\left(c_p(\Delta T)\Delta_{\dot{m}}\right)^2 + \left(\dot{m}c_p\Delta(\Delta_{\dot{T}})\right)^2} \tag{110}$$

$$= \sqrt{\left[\frac{1}{\dot{m}c_p(\Delta T)}\right]^2 \left(C_p\Delta T\Delta_{\dot{m}}\right)^2 + \left(\dot{m}C_p\Delta(\Delta_{\dot{T}})\right)^2} \tag{111}$$

$$\frac{\Delta Q_p}{Q_p} = \sqrt{\left(\frac{\Delta\dot{m}}{\dot{m}}\right)^2 + \left(\frac{\Delta(\Delta T)}{\Delta T}\right)^2} \tag{112}$$

The final equation shows that for the mass flow rate, the uncertainty will be a fixed percentage of the indicated reading. In the case of the working fluid flowmeter this will always be 3.0%. However as the temperature uncertainty contains a constant numerator of 0.1°C, the equation shows that the temperature uncertainty will increase as the ΔT or denominator decreases, with reduced uncertainty associated with larger temperature differences. The final percentage uncertainties of measured parameters are shown in Table 9.

Table 9: Percentage Uncertainties of Measured Parameters

Measurement	Uncertainty in %			
	x_{in}=0.02	x_{in}=0.15	x_{in}=0.3	x_{in}=0.45
Quality	±17.4	±10.2	±7.2	±6.4
Heat Flux SEC1 water	±17.1	±9.8	±6.5	±5.6
Heat Flux SEC2 water	±12.2	±11.9	±11.9	±11.9
Heat Flux Condenser water	±16.5	±11.6	±8.6	±7.5
Heat Transfer Coefficient (Test Section A)	±12.3	±12.0	±11.9	±12
Heat Transfer Coefficient (Test Section B)	±8.2	-	-	-

3.9: Energy Balance of Rig Heat Exchangers

The following section describes the results of a series of commissioning tests performed on each heat exchange process in the flow rig. Energy balances across each fluid stream in single phase heat transfer were compared.

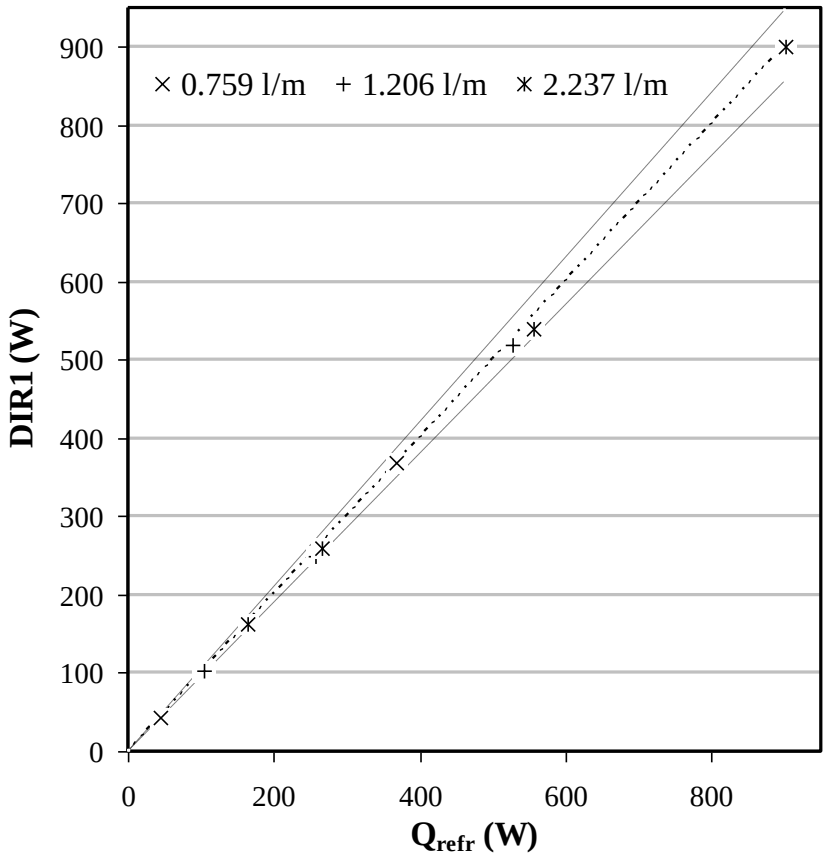

Figure 41: Electrical direct heater (DIR1) energy balance

Figure 41 shows a plot of the energy balances of DIR1, the electric heat exchanger. Q_{DIR1} represents the product of current and voltage (*VI*) to the heater, and Q_{refr} is found by a working fluid side fluid energy gain

$$Q_{refr} = \dot{m}_{REF} c_{pREF} (T_{14} - T_{13}) \tag{113}$$

The graph displays very good agreement over three flow rates: the dotted lines show ±10% limits.

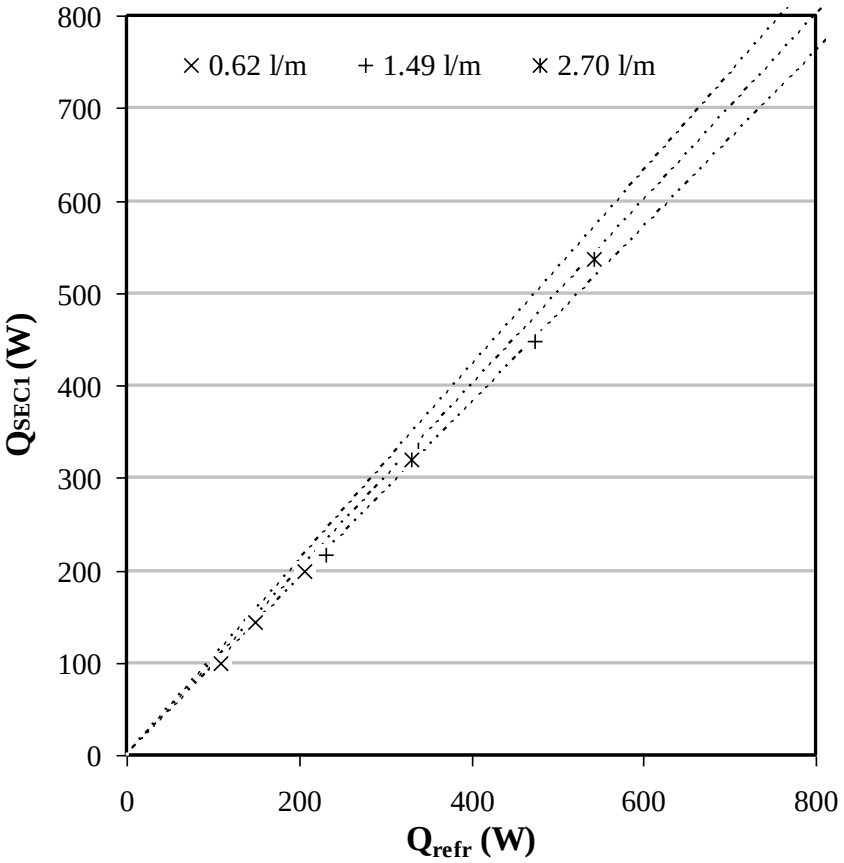

Figure 42: HEX1 energy balance

Figure 42 plots the energy balance of SEC1, the water/working fluid compact brazed heat exchanger. Q_{refr1} represents the working fluid side energy gain across the heat exchanger, and Q_{SEC1} is found by the water (SEC1) side fluid energy loss as described in equations (114) and (115).

$$Q_{refr1} = \dot{m}_{REF} c_{pREF} (T_{15} - T_{14}) \tag{114}$$

$$Q_{SEC1} = \dot{m}_{WATSEC1} c_{pWAT} (T_{40} - T_{41}) \tag{115}$$

The graph again displays good agreement over three flow rates at various heat loads, and is well within the 10% uncertainty limit lines.

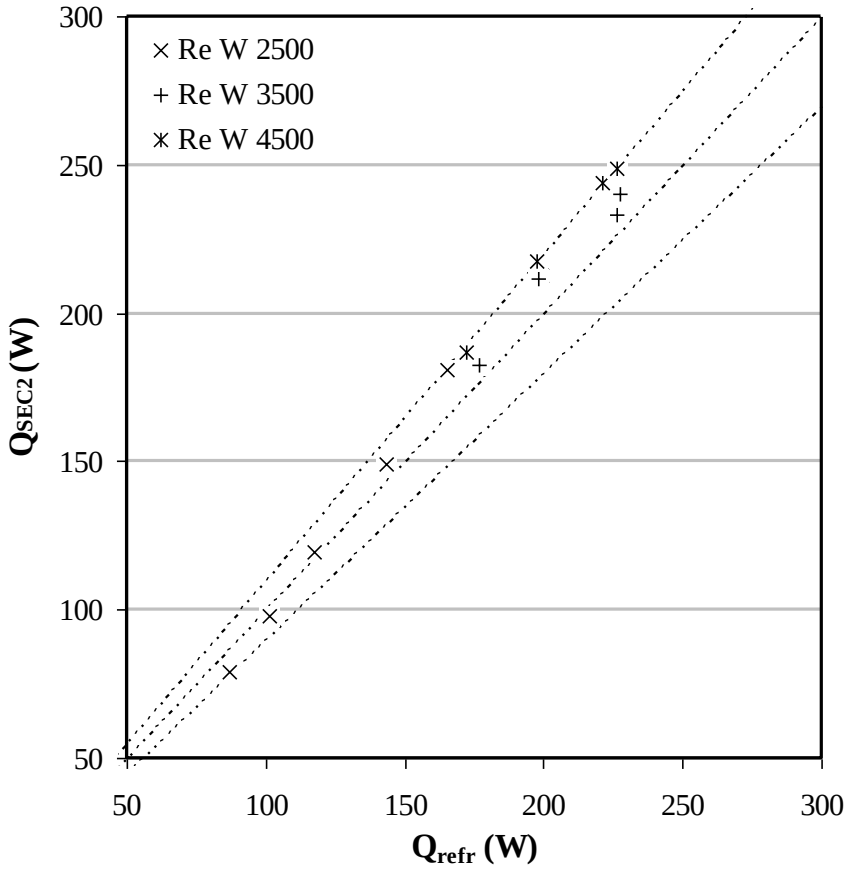

Figure 43: Energy balance for test section

Figure 43 plots the energy balance between the water of SEC2 and the working fluid in comprising Test Section A. Q_{refr} represents the working fluid side fluid energy gain across the test section, and Q_{SEC2} is found by the water (SEC2) side fluid energy loss

$$Q_{refr} = \dot{m}_{REF} c_{pREF} (T_{11} - T_{15}) \tag{116}$$

$$Q_{SEC2} = \dot{m}_{WATSEC2} c_{pWAT} (T_{20} - T_{31}) \tag{117}$$

The graph again displays reasonable agreement with ideal values, although some deviations are noticed. An important note is to ensure that temperature differences are kept large, as thermocouple errors lead to greater uncertainty values with lower delta T (ΔT) perhaps leading to greater deviation. In order to maintain large ΔT, the SEC2 flow rate must be minimised. However if the flow rate was too low, buoyancy effects within the water shell became noticeable. These buoyancy effects diminished with higher Reynolds numbers. Therefore a trade-off was necessary to achieve a

satisfactory temperature differential across the test section while maintaining a large enough Reynolds number inside so that buoyancy effects were negligible and the wall superheat along and around the test section did not vary considerably.

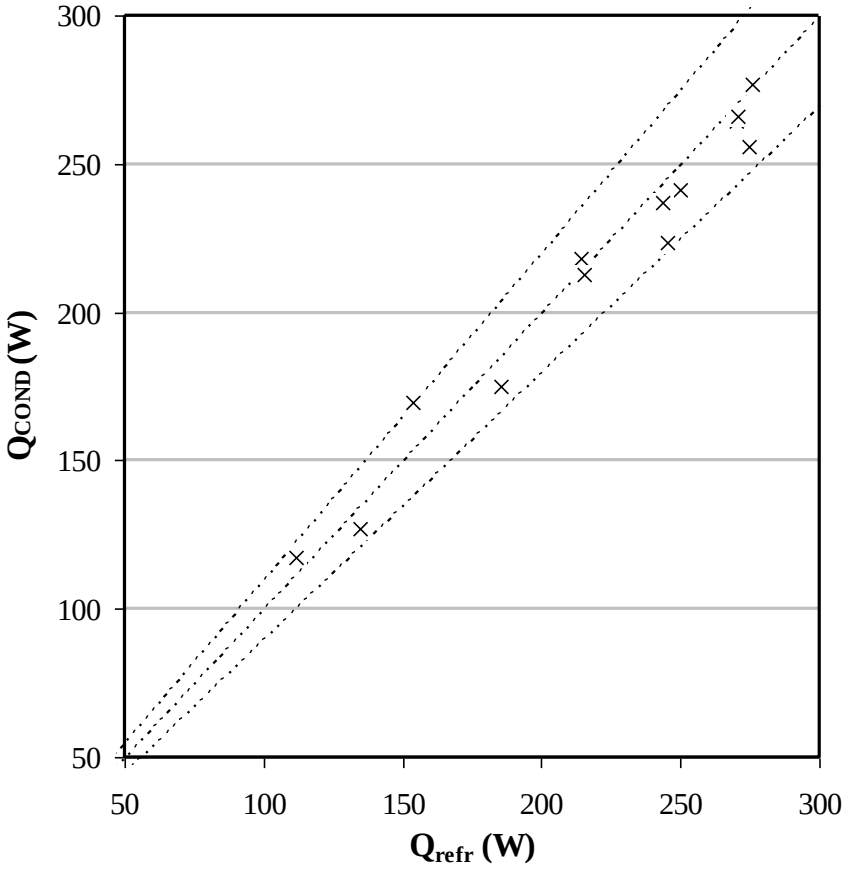

Figure 44: Energy balance for HEX3 (condenser)

Figure 44 plots of the performance of HEX3, the second water/working fluid compact brazed heat exchanger. Q_{refr} represents the working fluid side fluid energy loss across the heat exchanger, and Q_{COND} is found by the cooling water (COND) side fluid energy gain.

$$Q_{refr} = \dot{m}_{REF} c_{pREF} (T_{12} - T_{11}) \tag{118}$$

$$Q_{COND} = \dot{m}_{WATCOND} c_{pWAT} (T_{50} - T_{51}) \tag{119}$$

This unit also performs well with good 5% agreement at 3 flow rates.

3.10: Summary

This chapter outlined the design and construction of the experimental rig to permit visualisation of two-phase flow boiling inside a convective heat exchanger while under the influence of electrohydrodynamic forces. The rig, its main circuits and secondary circuits were described, and a detailed description of both test sections was furnished. The novel sapphire test sections which permitted the visualisation of the in-tube flow regimes during the boiling process were described in detail along with the methods of mechanical supporting, and the means by which completion of the EHD circuit was achieved. Specifics of the instrumentation and ancillary equipment were also given, and the method of rig commissioning, rig proving and calibration and data reduction were also detailed. An explanation of the different test section designs was given along with the reasoning behind their use, and a note on the limitations associated with both test sections was also explained.

Chapter 4: Experimental Results

4.1: Constant heat input and the influence of inlet quality

This chapter describes the thermal hydraulic results obtained from the water heated Test Section A at an approximate uniform wall superheat. In the first part, flow patterns and heat transfer correlations are presented and discussed. Next, data from the test section under field free conditions are presented. Heat input Q was maintained at 150 W across the test-section by adjusting the water inlet temperature accordingly. Inlet vapour quality is then increased from 2% to 45% in 15% steps and the test data is also presented and discussed. After this, a series of tests is presented where inlet quality was varied from 0 to 45% and EHD voltages of 4 and 8 kV were applied. Pressure drop was also measured and the overall relationship between EHD enhancement and pressure drop penalty is discussed.

The second section of the chapter presents data from a further series of tests intended to clarify some issues raised in the first section. This test remains at 2% inlet quality throughout while the EHD voltage is increased from 0 to 10 kV in 1 kV steps. However, in this case, the water inlet temperature is fixed at a constant temperature, and the heat transferred or input across the test section is allowed to change according to the level of EHD enhancement with the incremental changes in voltage. As in the first part, pressure drop and EHD electrical energy is logged throughout and this is compiled to compare the total EHD energy penalty against the overall energy gains from EHD augmented heat transfer.

Finally, based on the findings in the second section, a small note is given on the successful implementation of a PID controller to the test rig. This could successfully control either the test section exit quality or heat transferred (Q) within certain limits.

4.1.1: Field Free Flow Patterns Observed and Comparison with Flow Pattern Correlations

A series of visual tests were carried out on the rig under adiabatic conditions to record the flow patterns produced in the annular test section, and compare them to existing literature. Mass flux was varied from 50 to 300 kg/s m^2, while inlet quality spanned the range from 0.014 to 0.92%. The types of flow patterns observed in the sapphire tube are shown in the chart in Figure 45.

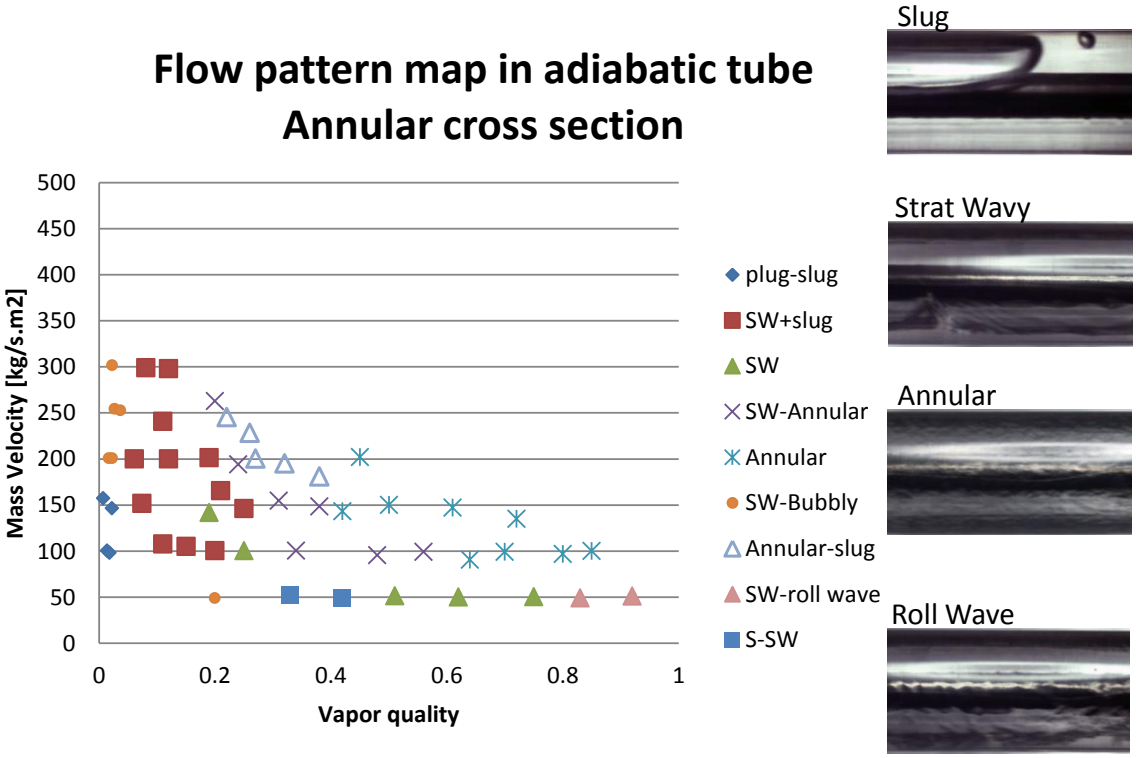

Figure 45: Flow patterns visible in test section during adiabatic tests in the range 50-300kg/s.m^2 (courtesy E. Decourchelle)

Although the presence of the concentric electrode necessary for EHD meant the test section is annular, the flow patterns correspond well with the tubular flow pattern maps of Steiner shown in Figure 10, and also with those of Kattan *et al*. and Wojtan *et al*. as seen in Figure 11, Figure 12 and Figure 13.

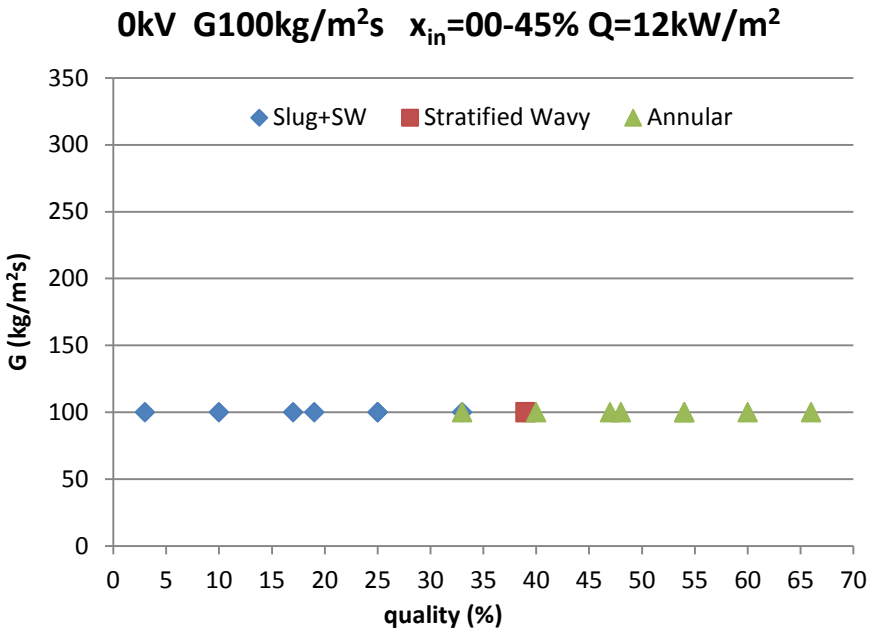

Figure 46: Flow patterns observed in test section during diabatic tests (Q=12kW/m^2, G = 100kg/s.m^2)

Figure 46 shows the flow patterns observed during diabatic flow conditions at G=100kg/m^{2}s. The overall flow patterns are similar to that observed in Figure 45 and the minor differences may be a result of heat input, or the subjectiveness of the researcher in identifying a particular pattern. The annular transition also appears to occur at qualities of between 30 to 40% in common with the Steiner and Kattan maps.

The Kattan *et al*. [28-30] method was considered initially to compare heat transfer coefficients. However the Kattan *et al*. method is less suitable for use in the stratified wavy regime at lower qualities where a significant proportion of our tests lie. Consequently, the method of Wojtan *et al*. [31, 40] was utilised which is known to give better accuracy in the 0-15% range and also includes the dryout and mist flow regimes which are not included in the Kattan *et al*. method. This newer method of Wojtan *et al*. was then used to prepare a flow pattern map for the test section and predict the heat transfer coefficient for qualities from 0% to 97%. In creating the flow pattern map, some assumptions were made regarding the vapour properties due to a lack of published information for HFE7000.

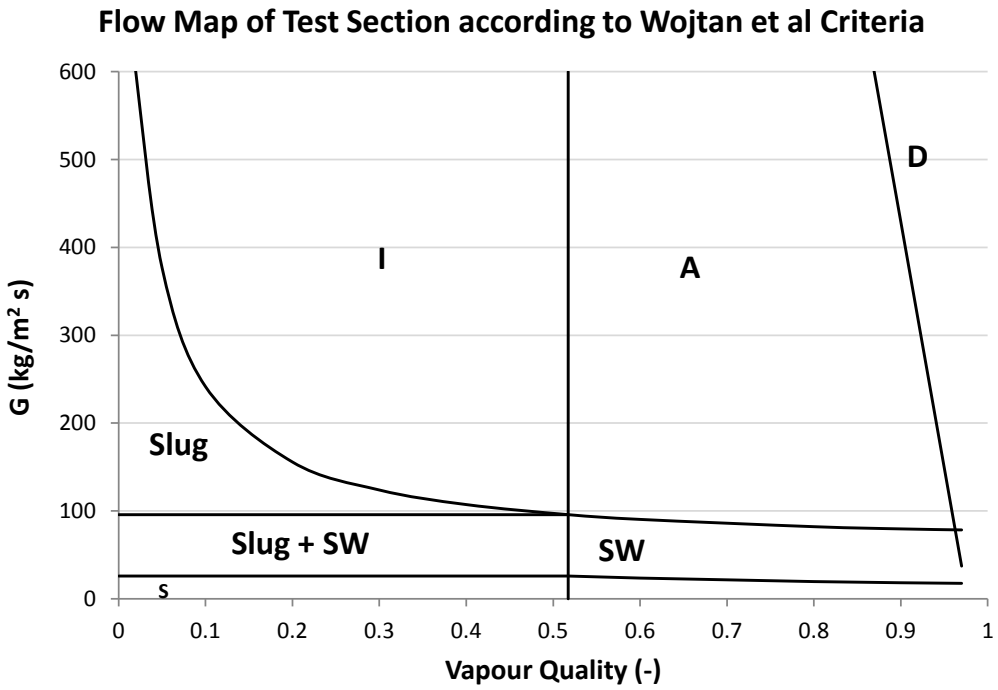

Figure 47: Wojtan et al. [31, 40] flow map predicting the test section flow patterns

Figure 47 shows the flow map prepared according to the method of Wojtan *et al*. [31, 40]. An important point to note is that the Wojtan map is designed for a tubular section, not an annular section as utilised in the present study. When compared to the actual flow patterns witnessed at G=100kg/m^{2}s in Figure 46 , the transition between Slug and Slug+SW zones occur just below our test mass flux of G=100kg/m^{2}s. From observations, it was noticed that the flow could be described as either Slug+SW or SW until around x_{in}= 40%, after which the flow becomes largely annular. This observed transition is somewhat lower than the x_{IA} of 52% predicted by the Wojtan map. However, the observed flow conditions below x_{in}=40% agree well where the observations from G=100kg/m^{2}s match closely, especially taking into account the transition boundaries are not sharp, and the dissimilar geometries of test section and model (plain tube vs. annular). Due to the close proximity of the transition area, and the fact that most observations were Slug+Stratified Wavy, the Slug +SW criteria were used in calculating HTC up to the Intermittent/Annular transition at 52%. From this quality to 97%, all calculations were deemed to be annular. The Annular/Dryout transition line was calculated and shown in the map although this quality was not reached in our experiments despite being observed in certain conditions. The Dryout/Mist transition line was also calculated but was outside the range of the flow map.

Using the map in Figure 47 and the method detailed by Wojtan et al. in [31, 40] heat transfer coefficients were then calculated and are shown in Figure 48. Better agreement is noticed at lower qualities. As quality increases, the Wojtan *et al*. method predicts annular flows with higher heat transfer coefficients. However, the experimental values show a possible decrease in heat transfer coefficient after x=45%. This could be due to the geometric incompatibility between model and experiment on two counts; the first, where the physical presence of the electrode in the test section may act as an obstruction to prevent top wetting and lead to earlier dryout than predicted by the Wojtan *et al*. method, and the second is where the cross sectional area of the electrode is non-negligible and cannot be deemed a plain tube to satisfy the model criteria.

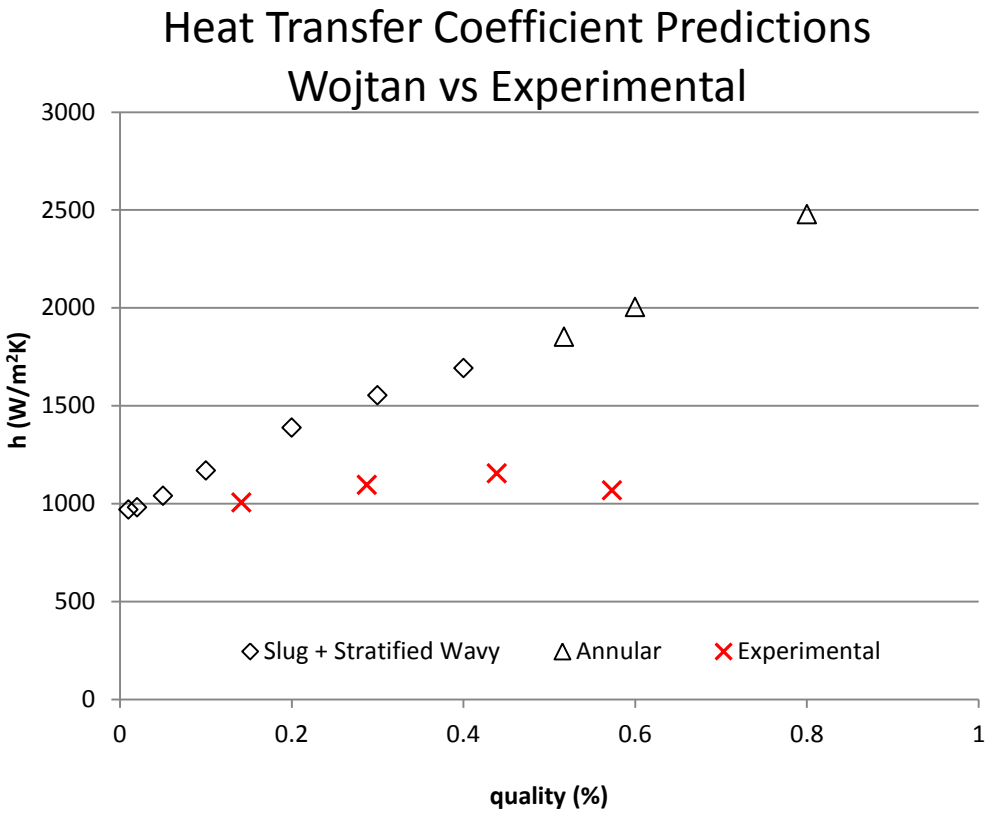

Figure 48: Comparison of predicted vs. experimental heat transfer coefficients from water heated test section

4.1.2: Heat Transfer under Field Free Conditions

Figure 46 show averaged heat transfer coefficients across the test section. The inlet quality varies from 2% to 45%. It had been intended to study an inlet quality of 0%, but in practice this was hard to achieve and the lowest reproducible quality fell closer to 2%, therefore this is used as the baseline. The heat transfer coefficient begins at 1006W/m^{2}K at 2%, and this rises to 1096 W/m^{2}K at 15% and rises again to a maximum of 1154 W/m^{2}K at 30%. At 45%, a reduction in HTC occurs down to 1068W/m^{2}K.

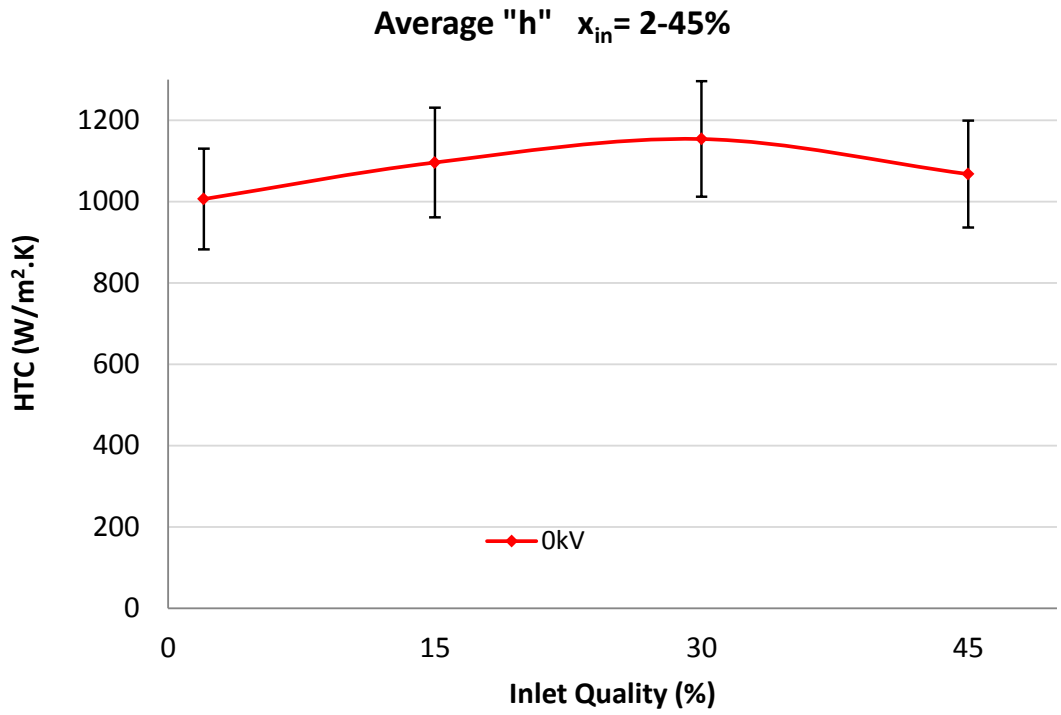

Figure 49: Averaged HTC in the tube versus inlet quality over a range on inlet qualities from 2% to 45%, G=100kg/m²s, Q=150 W

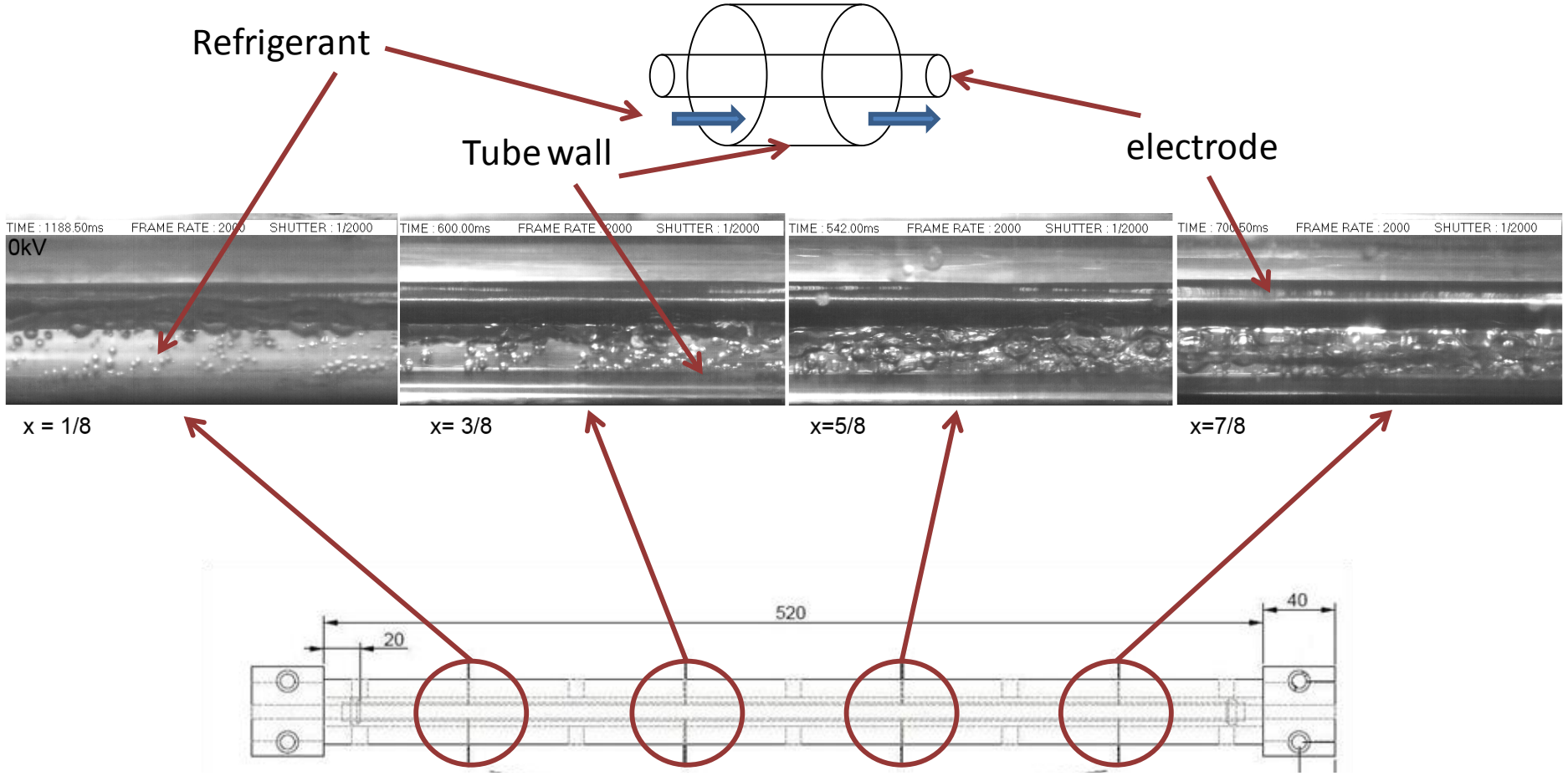

Figure 50: Flow regimes at locations x/L=⅛, ⅜, ⅝ & ⅞ at 0 kV, x_{in} = 2%

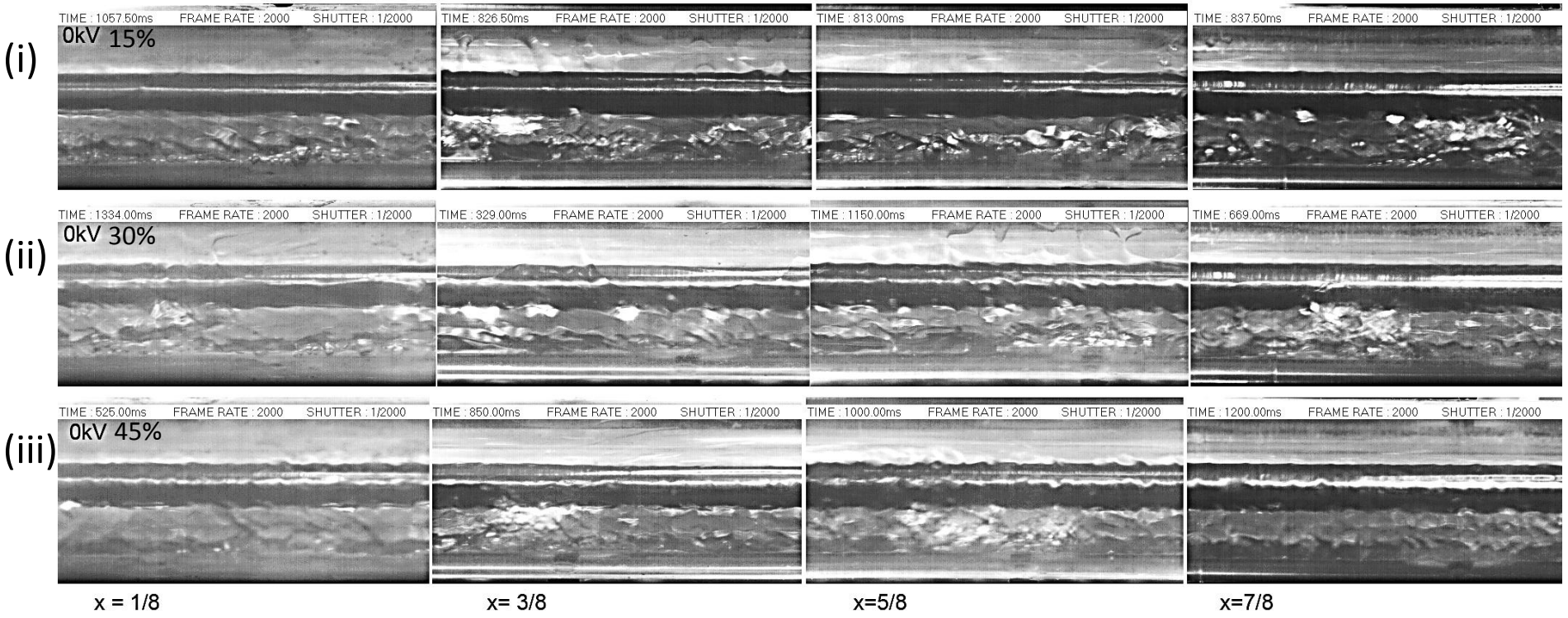

Figure 51: Flow regimes at locations x/L=⅛, ⅜, ⅝ & ⅞ at 0 kV, (i)x_{in} =15%, (ii) x_{in} =30% and (iii) x_{in} =45%

The flow regimes observed in the test section under field free conditions are shown in Figure 50. This photographic sequence shows the flow pattern for different locations along the test section length (x/L = ⅛, ⅜, ⅝ and ⅞). For these test conditions the flow remains largely stratified, with nucleate boiling occurring at the bottom surface of the test section.

With reference to Figure 50, refrigerant enters the viewing area (x/L=⅛) at a quality around 5%. The flow is stratified with the liquid level near the top of the electrode. Nucleate boiling is occurring at the lower surface and bubbles grow, depart and subsequently rise to the free surface or coalesce with other bubbles before reaching the free surface. The bubbles are carried with the flow to some extent since there is an interplay between liquid inertia forces and buoyancy forces acting on the bubbles. The top surface of the tube is difficult to show clearly with still photography, though inspection of the high speed video footage shows intermittent wetting due to slugs of liquid filling the tube and making contact with the top surface. These are illustrated in the time frame of images shown in Figure 52.

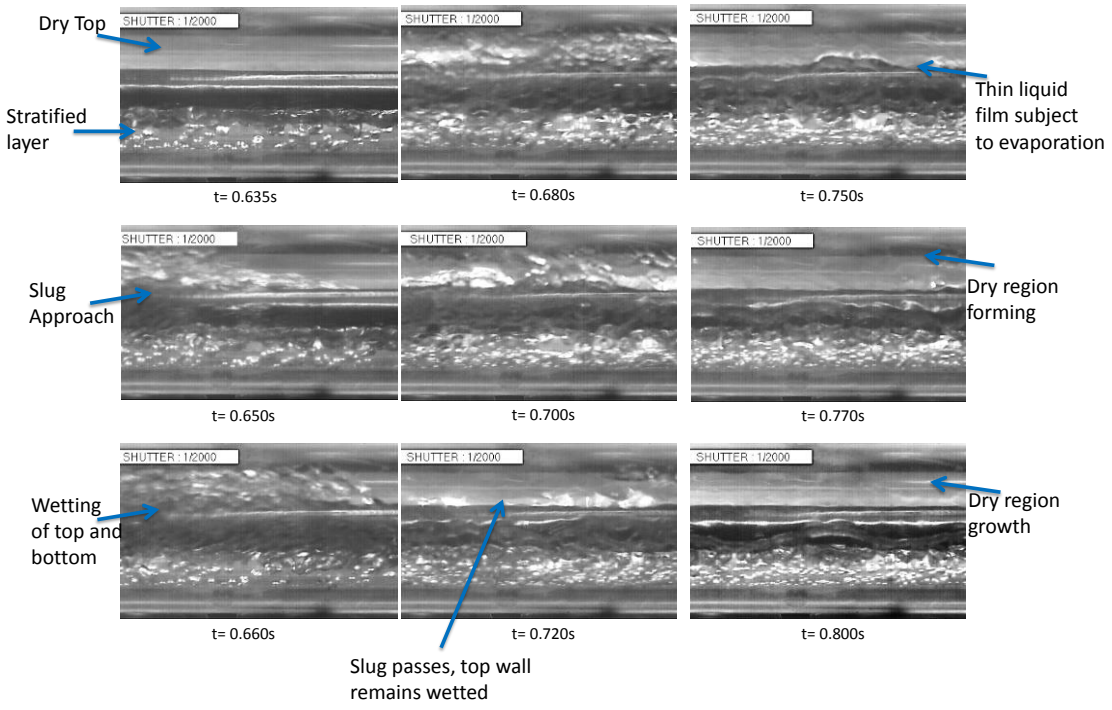

Figure 52: Time frame showing typical slug wetting event

The nature of the bottom wetting which is largely convective boiling is shown in Figure 53.

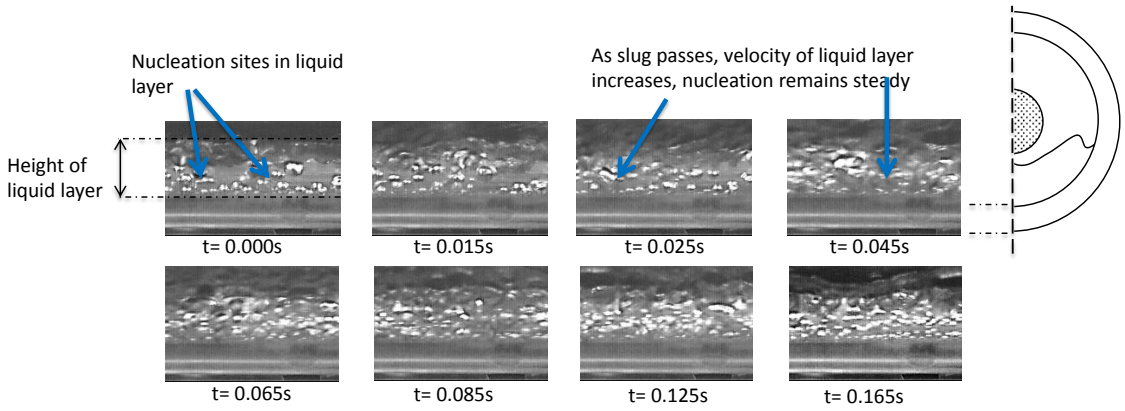

Figure 53: Time frame series showing flow behaviour in bottom liquid layer

At x/L=⅜, the flow pattern is similar with some obvious changes. Although the assumption that quality varies linearly between inlet and outlet is unlikely, it nevertheless allows an approximation. Consequently the quality at this location has increased to around 10%. Although remaining stratified, the height of the liquid layer has decreased due to upstream vapour generation. More nucleation sites are visible and the bubbles tend to be marginally larger. The mass flux remains constant though, because of the heat input between x/L=⅛ and x/L=⅜, the quality has increased slightly resulting in more vapour. This additional vapour fraction under the same mass flux gives rise to increased vapour and liquid stream velocities, hence the bubbles are carried further downstream in the faster liquid layer before breaking out at the liquid surface. As before, the top surface is periodically wetted due to intermittent slug flow events.

At x/L=⅝ the quality has increased to around 15% and the stratified liquid level has dropped below the electrode. Nucleate boiling is still vigorous within the liquid layer with bubbles being entrained in the faster moving liquid layer over a significant length, often coalescing and forming large bubbles which break through the vapour-liquid interface. The increased influence of liquid inertia, which keeps the bubbles from rising to the surface, subsequently results in there being a visible increase in the volume fraction of entrained bubbles within the liquid layer compared with the upstream sections. At this location the interface is noticeably more wavy. This may be due to the local quality increase causing increased vapour velocity which then results in higher

vapour/liquid shear at the interface, and also partly due to the coalesced bubbles breaking out of the liquid layer.

At x/L=⅞, quality is now about 20%. The stratified liquid layer has dropped further but nucleate boiling is still active and the entrained bubbles occupy more volume within the faster liquid flow. The bubbles coalesce near the surface and bridge across the liquid interface to the electrode surface. Occasional slugs still travel through, but the upper part of the tube does not appear to remain wetted to the same extent, appearing to dry out relatively quickly. Although these slugs are of a temporary nature and their effect on the heat transfer is non-negligible, they are not shown in the images for clarity reasons.

4.1.2.1: At Higher Inlet Qualities from 15-45%

The remainder of the field free flow regime images are shown in Figure 51. Figure 51(i) shows the patterns for the inlet quality now at 15%. The amount of vapour has increased and the stratified liquid layer has dropped significantly. This is immediately apparent all along the test section from Figure 51 at 0 kV. From the video analysis, the flow can be described as stratified wavy with slugs. However, these slugs now appear to be more annular in form than the "slugs" of liquid previously observed at x_{in}=2%. This transition to an annular flow regime is in line with the higher vapour and liquid velocities as quality increases. Due to the higher vapour velocity the liquid/vapour interface is much more wavy as a result of interfacial shear. Nucleate boiling is very visible at several sites along the tube and the top surface experiences intermittent wetting and drying by the slug events.

At x/L=¾, the flow is broadly similar although a slight decrease in nucleate boiling is observed. The top of the tube is subject to the periodic liquid slugs passing through as before causing re-wetting of the top surface.

At x/L=⅝, nucleate boiling can be observed at several preferential sites, and the liquid layer slows over the lower tube with greater axial velocity. The interface is also very wavy, composed of shorter ripples or waves of about 1mm length superimposed upon longer waves (5-20mm in length). The upper tube again continues to experience a pattern of alternate drying and re-wetting caused by the periodic slugs. These slug

events now appear to be of longer duration but this was difficult to verify owing to the intermittent nature and frequency of the slugs and the relatively short duration of the video.

It can be said that in the field-free case (0 kV) the dominant flow regime is stratified wavy with periodic annular slug events wetting the top wall.

With the change in quality from 15% to 30% more vapour is present in the tube. Liquid levels in the tube have visibly dropped, consequently under the constant mass flux of 100kg/m^{2}s, both liquid and vapour must experience a further increase in velocity. A reduction in height of the liquid layer is evident at x/L=⅛ and further decreases as the liquid progresses along the heat exchanger due to the increase in quality and the fact that the liquid layer does not contain a significant amount of vapour bubbles. The interface, as expected, is more wavy due to the increase in velocity of both the liquid layer and vapour phases. Nucleate boiling is visible but minimal, and compared to the x_{in}=2% flow regime, is much reduced at all locations along the tube.

At x/L=⅜ and ⅝ the flow pattern is similar, a thin stratified liquid layer at the bottom of the tube, with a wavy interface and occasional cresting of liquid waves, the tips of which are carried over into the faster vapour stream. The top surface remains largely dry apart from re-wetting brought about by periodic annular slugs. Some low level nucleate boiling occurs at x/L=⅝ along the tube bottom.

At x/L=⅞ the flow is similar again, with the only noticeable factor being the existence of nucleate boiling at one or two locations along the tube bottom and some occasional nucleation along the upper wall during slug events. This nucleation may be facilitated by the higher wall temperature near the end of the tube where the hot water inlet is situated. Figure 54 shows the nucleation sites after an annular wetting event. Most nucleation occurs at the bottom, but bubble trails are visible from several sites at the side of the tube wall above electrode level.

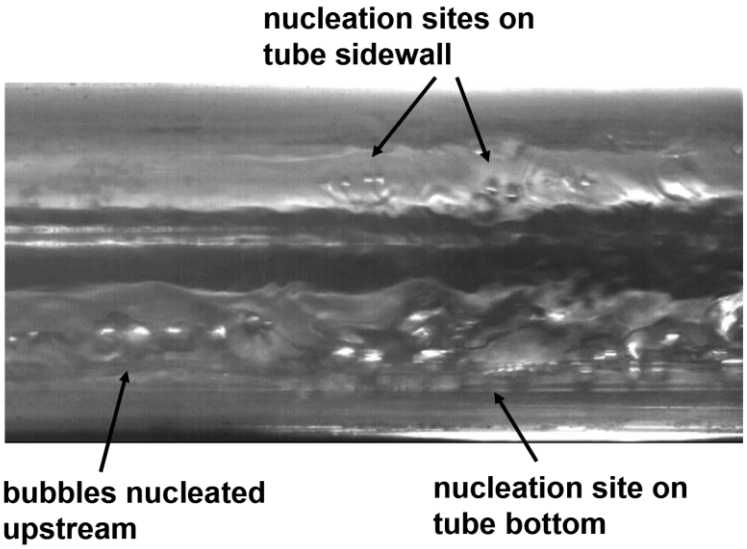

Figure 54: Nucleation sites at end of test section, x/L=⅞, x_{in}=30%, 0 kV

From the 0 kV images of 30% in Figure 51 the flow regime can again be described as stratified wavy with occasional weak annular slugs, but with a fast return to SW with the liquid concentrating around the lower section of the tube. The top of the tube is noticeably dry for long periods. This general pattern is true for all axial locations along the test section.

As mass flux remains at 100kg/m^{2}s but quality is now 45%, the in-tube velocities of vapour and liquid have increased, and the interface becomes notably more wavy. Dryout of the upper tube surface is witnessed more at locations x/L=⅝ and ⅞. As it is difficult to convey the flow regime from still images, a sketch of the most representative flow patterns is shown in Figure 55. Although slug events were witnessed in the high speed videos, for clarity they are not shown in the sketches. The sketches illustrate the stratified layer at lower qualities, and show how as quality increases, the liquid level both reduces in height and thickness and becomes pushed from the centre to the outer area of the tube

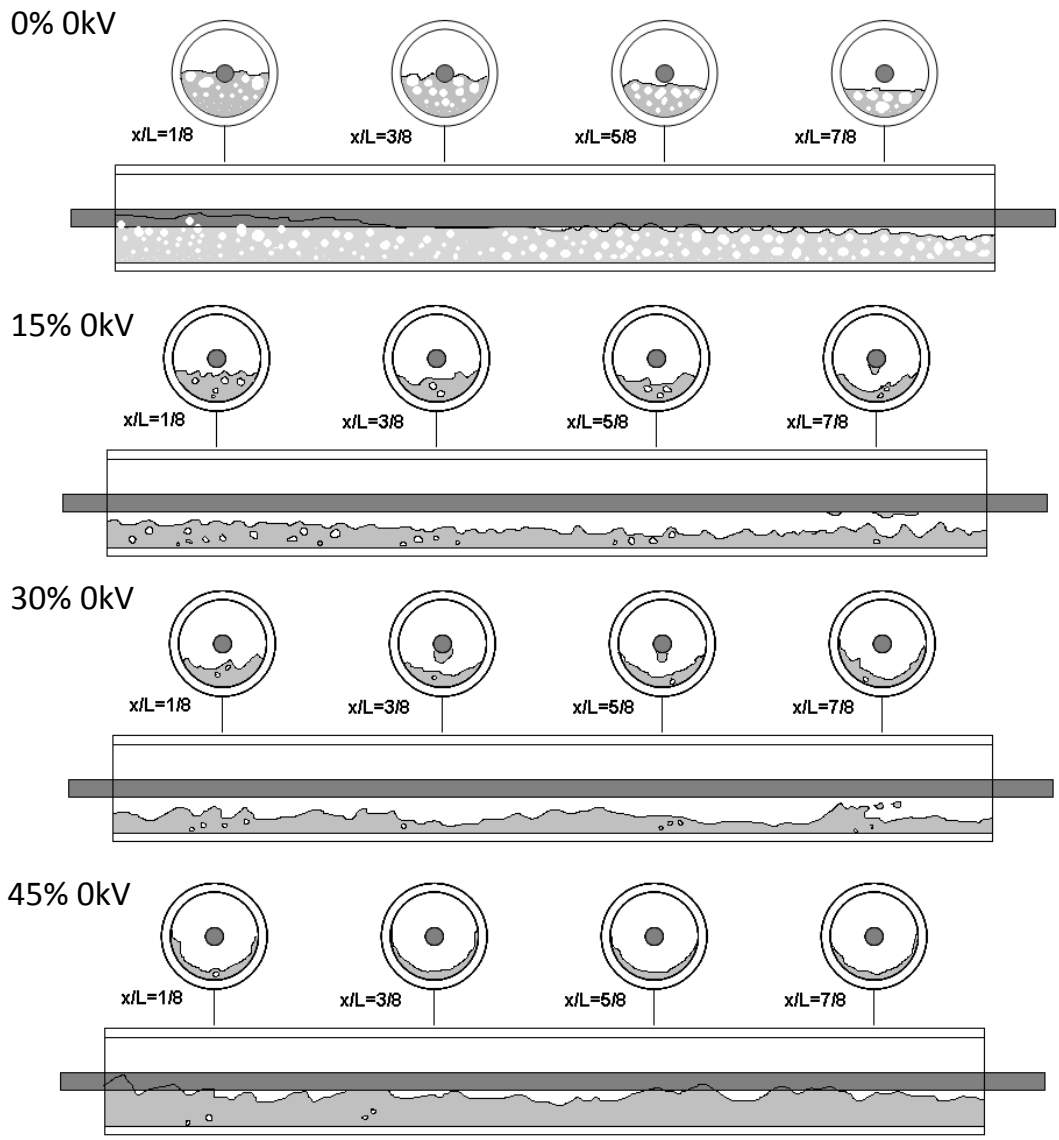

Figure 55: Sketches of flow regimes observed in field free conditions at x_{in}=0-45%

Wall thermocouple measurements were taken at eight locations along the tube, four top and four bottom. Figure 56 shows the top and bottom tube wall temperature traces for the inlet quality x=2% for each thermocouple location. These fluctuate along the top wall and are more steady along the bottom wall. This is in line with the stratified liquid layer consistently present along the lower surface of the tube, while the upper tube wall is generally marginally higher in temperature but displays variations caused by the periodic liquid slugs.

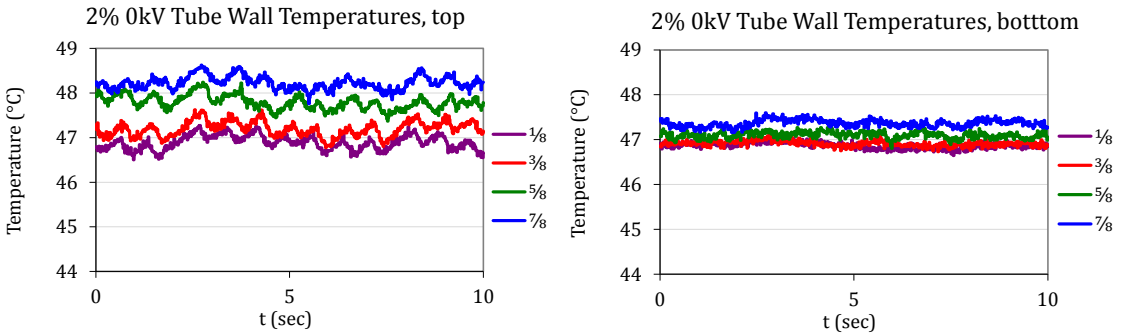

Figure 56: Tube wall temperature variations at x_{in}= 2%

In subsequent results, the above time trace information will be more conveniently portrayed by two graphs, one indicating averaged wall superheat temperature, but normalised in relation to the water inlet temperature and refrigeration saturation temperatures. The other indicates the standard deviation of the temperature to represent the amount of variation in the tube wall temperature. This format is introduced in Figure 57 which shows the standard deviations and the normalised superheats for the field-free case. Standard deviations in the region of 0.05-0.08°C are associated with a continually wetted surface [85]. The normalised superheat is expressed as

$$s_n = \frac{T_w - T_{sat}}{T_{water} - T_{sat}} \tag{120}$$

A normalised superheat close to unity indicates that the water side thermal resistance is much smaller than the refrigerant side. An increasing normalised superheat indicates reducing refrigerant side HTC.

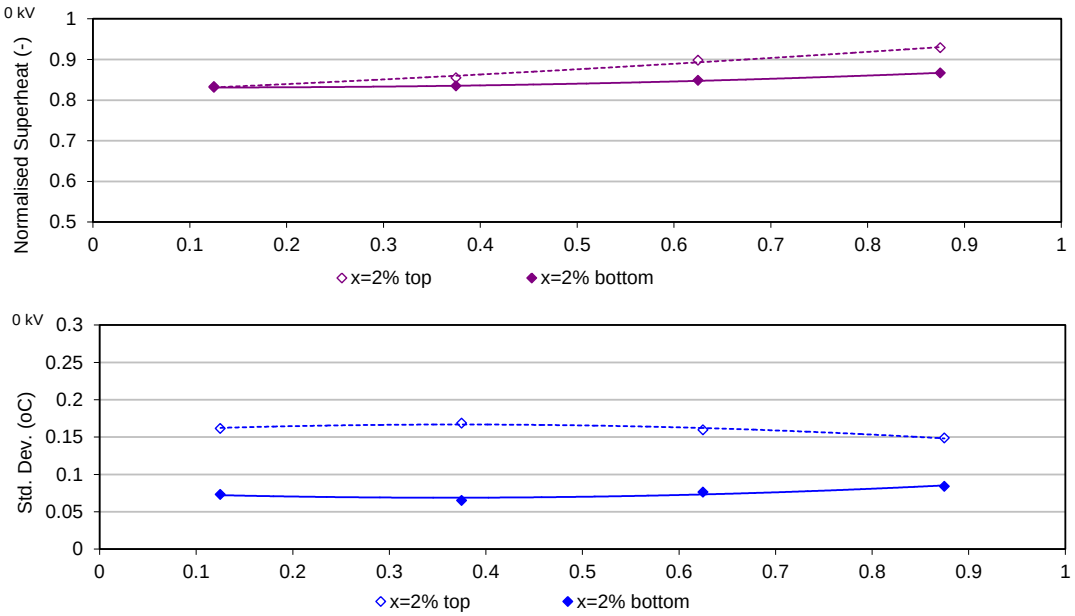

Figure 57: Normalised wall superheat temperatures and standard deviations for x_{in}=2%, 0 kV

It is clear that the top surface superheats exhibit fluctuations due to alternate heating and cooling caused by the intermittent bridging of the top surface and the liquid layer. The frequency of these bridging events and subsequent superheat fluctuations is around 1 Hz, a frequency which has been verified by the high speed video footage and pressure fluctuations. These fluctuations are represented by the standard deviations of the wall superheat readings as shown in Figure 57 where the bottom wall temperature fluctuations of about 0.07°C are lower than the top wall temperatures of 0.16°C. This is consistent with the presence of a liquid layer at the bottom, while the larger temperature fluctuations at the top wall are attributable to alternate wetting and drying.

The normalised superheats also shown in Figure 57 indicate that the bottom wall superheat remains almost constant along the length varying little from 0.83 to 0.87, again due to it being wetted by the liquid layer. The top wall superheats are slightly higher than the bottom and increase with length along the tube, from 0.83 at x/L=1/8 to 0.93 at x/L=7/8. This is likely due to the reduced contact with liquid as witnessed in the videos. The actual superheat temperature is 12.94 °C at x/L=⅞.

This steady bottom and increasing top superheat profiles are supported by the images where generally the flow regimes are of a stratified wavy profile. The lower surface is constantly wetted, thus also stable in temperature, while the upper surface, although

drier, is periodically wetted by the slug waves causing temporary temperature variations. Thus at this quality, the heat transfer coefficient of 1006W/m^{2}K as seen in Figure 49 is primarily due to convection by the stratified layer on the bottom, and also some convection and evaporation caused by the intermittently wetted area at the top of the tube.

4.1.2.2: For x_{in} = 15%

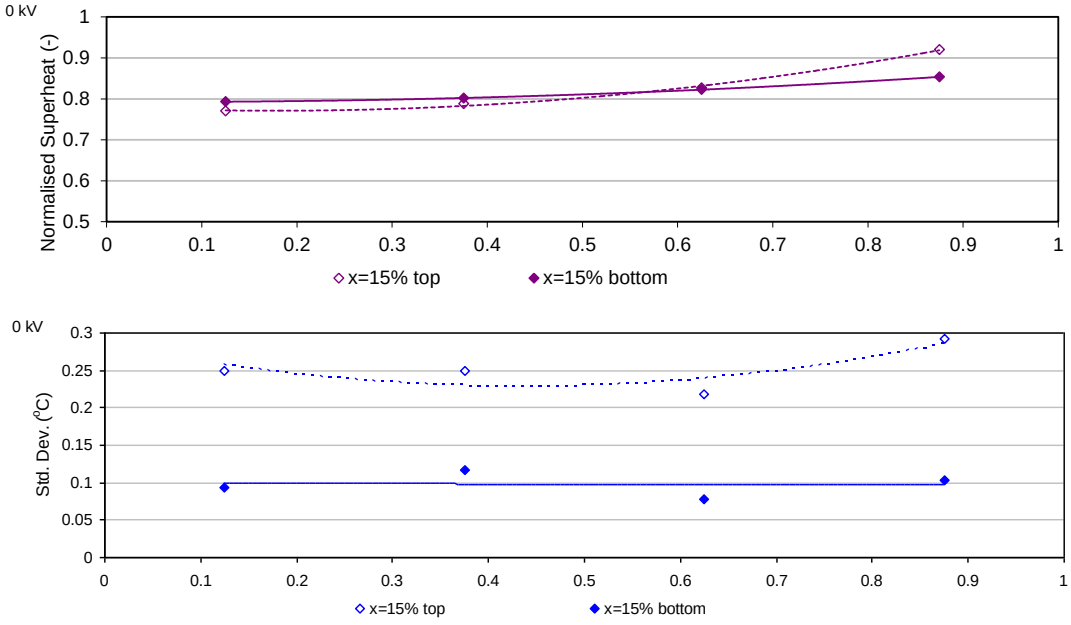

Figure 58: Normalised wall superheat temperatures and standard deviations for x_{in}=15%, 0 kV

For x_{in}=15%, the standard deviations shown in Figure 58 still indicate low fluctuations of around 0.10°C at the tube bottom which are again indicative of a liquid layer although they have increased slightly from the 0.07-0.08°C values found with the 2% inlet quality case. At the tube top, the standard deviation profiles also display more variation than the bottom because of the repeated wetting and drying, although this too has increased to 0.25°C, an increase from the 0.15°C found at 2% suggesting greater fluctuation in wall temperatures.

Both top and bottom wall normalised superheats are also shown in Figure 58. The actual superheats (not shown) have dropped to around 10.5-12.5°C at 15% quality, lower than the previous values of 11.6-12.9°C at 2%. This is because of the lowered water temperature so as to maintain a constant heat input of 150 W across the test

section. A similarity in both top and bottom surfaces is apparent, but as in the 2% case, the top does increase in temperature towards the tube end. The bottom normalised superheat increases from 0.79 to 0.85, while the top experiences a greater variation and rise from 0.77 to 0.92. This slight increase in temperature of the top tube near the exit region is consistent with the drier conditions observed in the video and images in Figure 73 at 0 kV and x/L = ⅞ as well as the increase in standard deviations at the same location. The lower superheats at the top of the tube near the tube entrance, which does not occur in the 0 kV case, (see Figure 57) point to a better heat transfer mechanism, perhaps due to the better wetting characteristics of the intermittent slug and bridging events, and subsequent evaporation.

Due to the increase in quality to 15% but at the same mass flux of G=100kg/m^{2}s velocities of the liquid and vapour have increased. Despite this increase in velocity of the liquid layer, and the reduction in superheat temperature, nucleation is still highly active therefore may contribute to the higher heat transfer coefficient. This may also be due to the differing nature of wetting observed in the 15% case. In the previous 2% case, top wetting was due to occasional slugs which were essentially large liquid charges containing vapour bubbles. The events were of infrequent duration but were a relatively large scale in terms of volume of liquid transferred. Thus, while the wetting was high, the relatively long timescale before the next slug allowed dryout to occur, inhibiting the heat transfer. Conversely, in the 15% case, the slugs do occur but are faster and more frequent. In addition, the slug events appear more annular than the previous slugs, and the large annular events are often preceded and followed by smaller bridging events, where crests of liquid touch the top surface.

As can be seen from Figure 49, all the factors in combination result in greater convection along the bottom liquid layer coupled with more wetting along the top of the tube thus contribute to better heat transfer of 1096W/m^{2}K than the 1006W/m^{2}K found at the 2% case. A major difference between the 0% and 15% case is the difference in slug wetting, which is borne out by video observations, and also by the normalised superheat differences along the first half of the tube.

4.1.2.3: For x_{in} = 30%

From Figure 59 it is noted that the x_{in}=30% top tube wall temperatures have significantly higher standard deviations compared with the x_{in}=2% case, indicating that the periodic wetting and drying events are different in nature. Interestingly, the high speed videos show that the periodic bridging events at x_{in}=30% are no longer the classical slugs of liquid, as in x_{in}=2%, but have changed to thinner transitory liquid slugs more akin to annular flow, which cause periodic complete wetting of the whole tube.

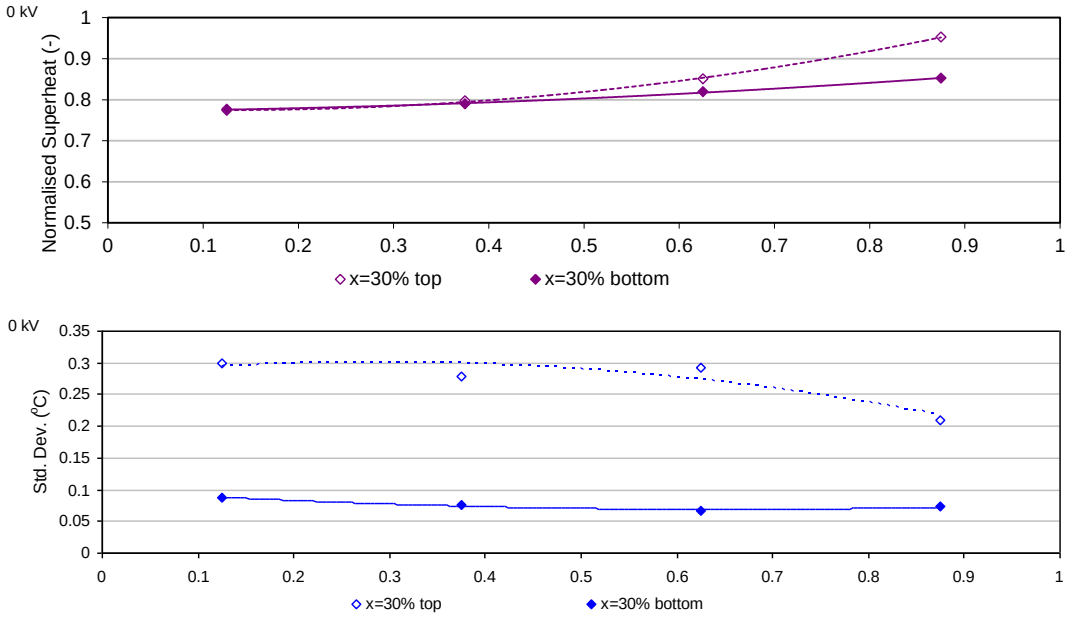

Figure 59: Normalised wall superheat temperatures and standard deviations for x_{in}=30%, 0 kV

The standard deviations of temperature in Figure 59 again show low fluctuations of 0.07°C for the bottom of the tube, corresponding with stratified liquid layer wetting. However, the top wall shows greater superheat variations of 0.3°C, indicating vigorous wetting and drying cycles. These large variations decrease slightly to 0.20 toward the tube end, although this is still indicative of repeated wetting and drying out but with lower intensity.

The x_{in}=30% field-free case experiences a further reduction in superheats compared to both x_{in}= 2% and x_{in}=15% cases. Again, this is due to the lowering in water inlet temperature to maintain a heat input of 150 W. It is these periodic slug events that

account for the similar average tube temperatures of 10.26°C and 10.29°C found at the beginning of the tube, top and bottom. These are both reduced from 10.49°C and 10.8°C top and bottom from the 15% case. However, as before, both top and bottom normalised superheats rise gradually along the tube. The top superheats increase with length from 0.77 to 0.95, more than the bottom normalised superheat which rises from 0.78 to 0.85. The similarity at the tube entrance points to high wetting top and bottom, while the increase at the top of the tube at the exit region denotes increased dryness. The standard deviations support this, as they also show a reduction in wall temperature fluctuations at x/l=⅞.

Again the increase in heat transfer with increasing inlet quality is likely due to the favourable heat transfer conditions caused by the departure from a more stratified flow as witnessed in the 0 kV case. The higher velocities of vapour and gas phases caused by the increase in vapour quality, despite a constant mass flux of G=100kg/m^{2}s, also result in the periodic slugs being more annular in nature as compared to the liquid bridge and slug type events witnessed at lower inlet quality. The result is that the bottom of the tube experiences a thinning in the liquid layer, while the tube top experiences more wetting, both contributing to the higher heat transfer coefficient of 1154W/m^{2}K as can be seen from Figure 49.

4.1.2.4: For x_{in} = 45%

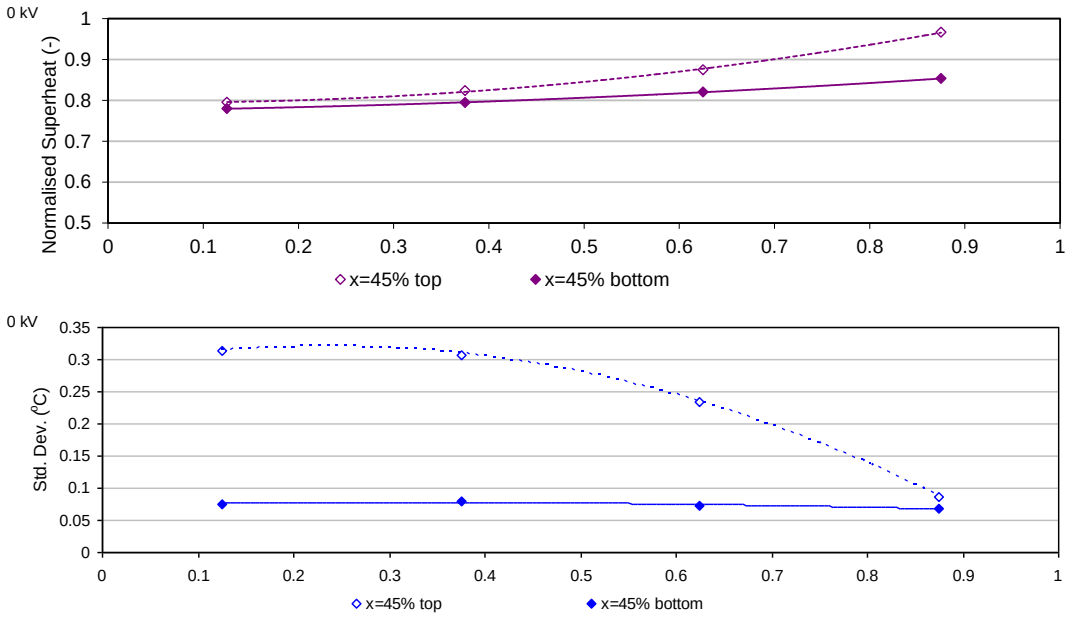

Figure 60: Normalised wall superheat temperatures and standard deviations for x_{in}=45%, 0 kV

The standard deviations in Figure 60 for x_{in}=45% also portray a fully wetted lower tube, but the top SD values depict highly fluctuating top wall temperatures, gradually lessening along the tube. This is consistent with the images and video analysis where the top tube is subject to occasional wetting at locations x/L=⅛, ⅜ and ⅝. However, the superheat standard deviations fall to 0.08 at x/L=⅞, indicating a stable temperature and the absence of alternate wetting and drying. The images confirm that at this location the tube top is much drier than before. The sketch in Figure 61 shows this flow regime of stratified wavy flow at the bottom yet dry on top which occurred at the end of the tube.

The normalised superheats shown in Figure 60 begin at 0.79 for top and 0.78 for the bottom. The bottom values then rise monotonically to 0.85, while the top values climb more sharply to 0.97. This normalised wall superheat close to unity is indicative of a dry surface and is backed up by both the standard deviations and video information.

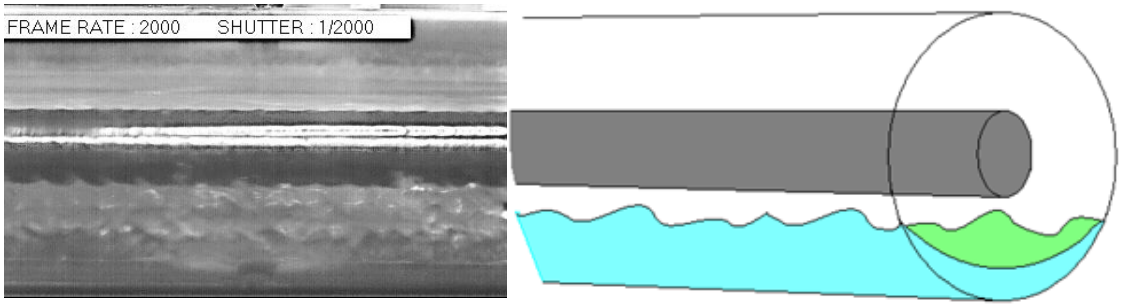

Figure 61: Image and sketch of dominant flow at x/L=⅞ for x_{in}=45%, non EHD

The heat transfer coefficient suffers a decline in the 45% case, down to 1068W/m^{2}K from a field free maximum of 1154W/m^{2}K at 30%. This is explained by the flow patterns witnessed where the top of the tube experiences increased dryout. This is supported by the rise in wall superheat and decrease in standard deviations. Interestingly, the actual wall temperature at the top of the tube at x/L=⅞ is 48.46°C, while the water temperature at the same location is estimated to be 48.75°C. Therefore, the tube wall temperature at this location is only around 0.3°C from the actual heating water temperature indicating very poor heat transfer from the tube side at this location.

4.1.2.5: Pressure Drop

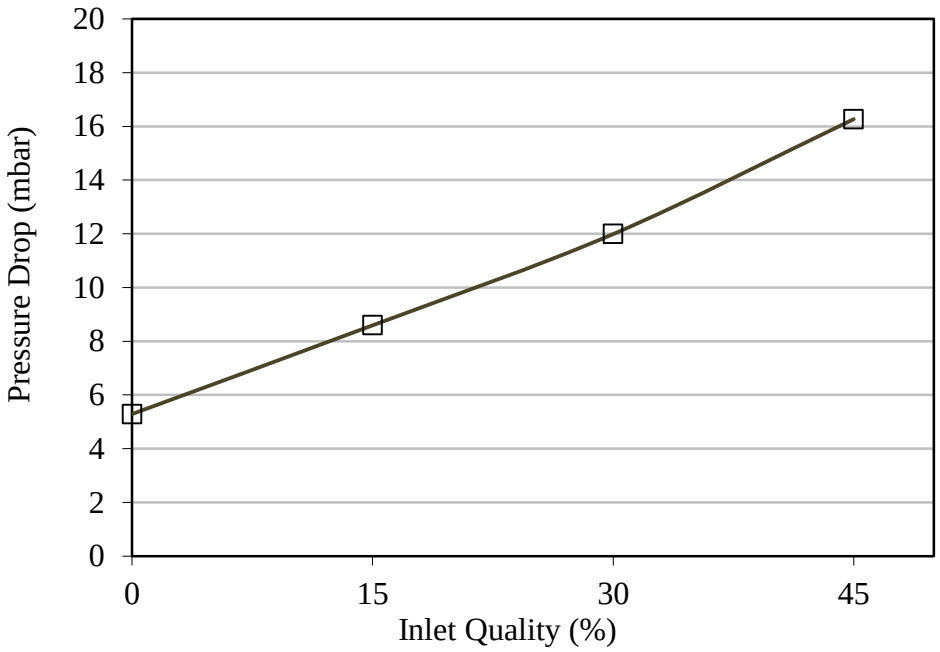

Figure 62: Pressure drop associated with increasing inlet quality

The averaged pressure drop along the test section versus inlet quality is shown in Figure 62. The trend is linear, showing a pro-rata increase in pressure drop with inlet quality. Pressure drop is 5.29 mbar at 0%, and increases to 8.59 mbar at 15%, 11.98 mbar at 30% and finally to 16.27 mbar at 45%. As has been noted earlier, the increasing levels of liquid redistribution as quality increases result in a greater amount of liquid reaching previously dryer areas of the tube than found in the 2% case. Consequently greater wall friction arising from the increased wetting would account for the higher pressure drop as quality increases. It is noted that despite the pressure drop continuing to rise with inlet quality, the heat transfer coefficients do not follow this trend exhibiting a decrease at 45% as shown from Figure 49.

4.1.3: Heat Transfer under EHD conditions

At an inlet quality of approximately *x*=2% and constant mass flux density of G=100 kg/m^{2}s and average heat flux of Q$^{//}$=12.43 kW/m^2, voltages of 0, 4 and 8 kV were applied and the average HTC and pressure drop were monitored. The average heat transfer coefficients are shown in Figure 63 and indicate the increase in averaged HTC with applied voltage. A larger relative increase in HTC occurs between 4 kV and 8 kV compared with 0 kV and 4 kV. In the field-free case, the average HTC is 1006W/m^{2}K, and this increases to 1255W/m^{2}K with 4 kV and again to 2000W/m^{2}K with the application of 8 kV.

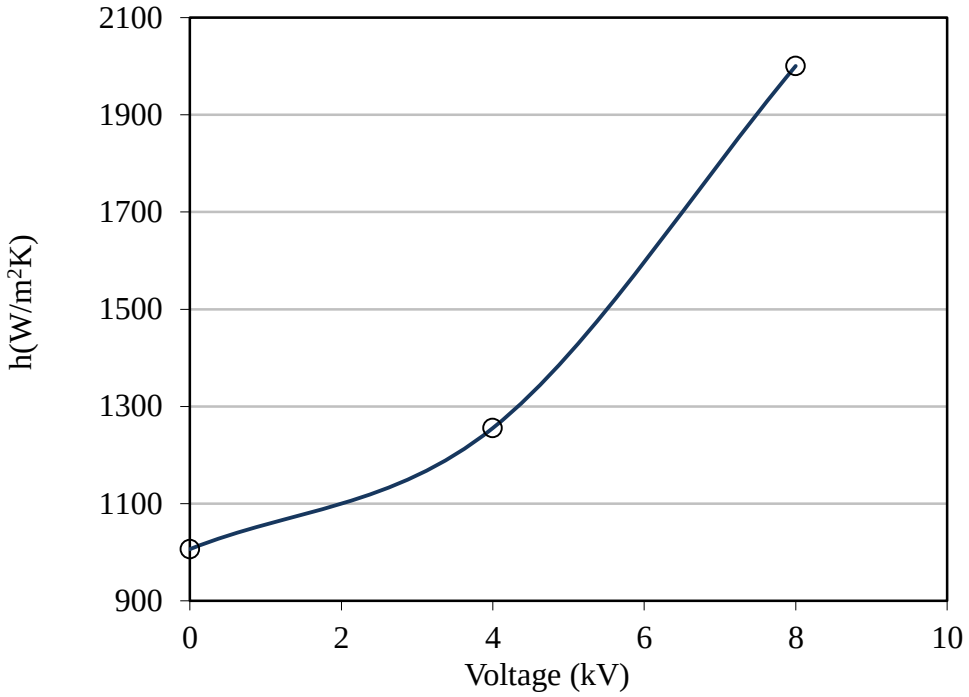

Figure 63: Variation of average HTCs with applied voltage, x_{in}=2%

The following subsections analyse this increase through a combination of thermometry measurements and high speed imagery.

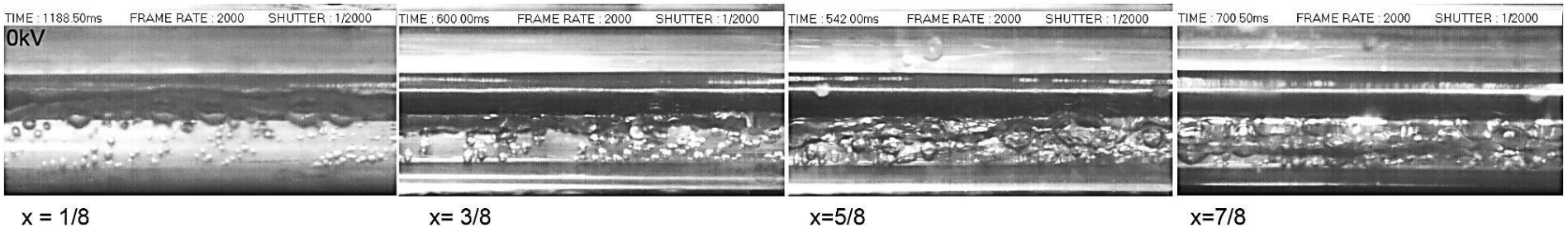

Figure 64: Flow at locations x/L=⅛, ⅜, ⅝ & ⅞ at 0 kV G=100 kg/m²s, x_{in} = 2%

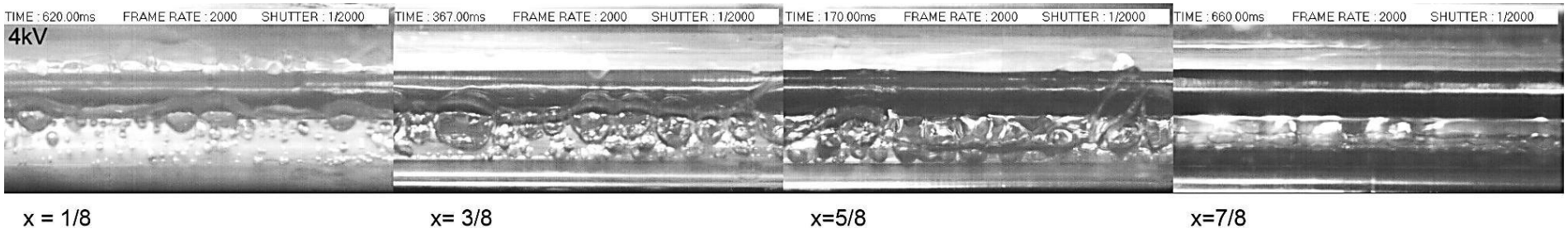

Figure 65: Flow at locations x/L=⅛, ⅜, ⅝ & ⅞ at 4 kV for G=100 kg/m²s x_{in} = 2%

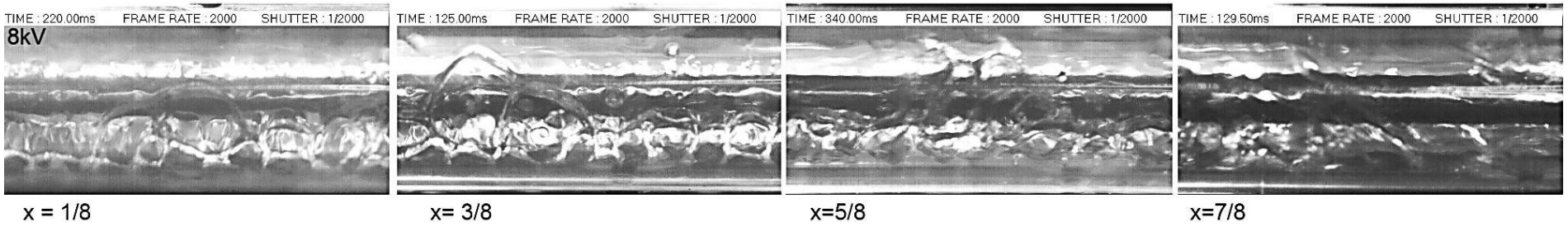

Figure 66: Flow at locations x/L=⅛, ⅜, ⅝ & ⅞ at 8 kV for G=100 kg/m²s x_{in} = 2%

4.1.3.1: Results for 4 kV

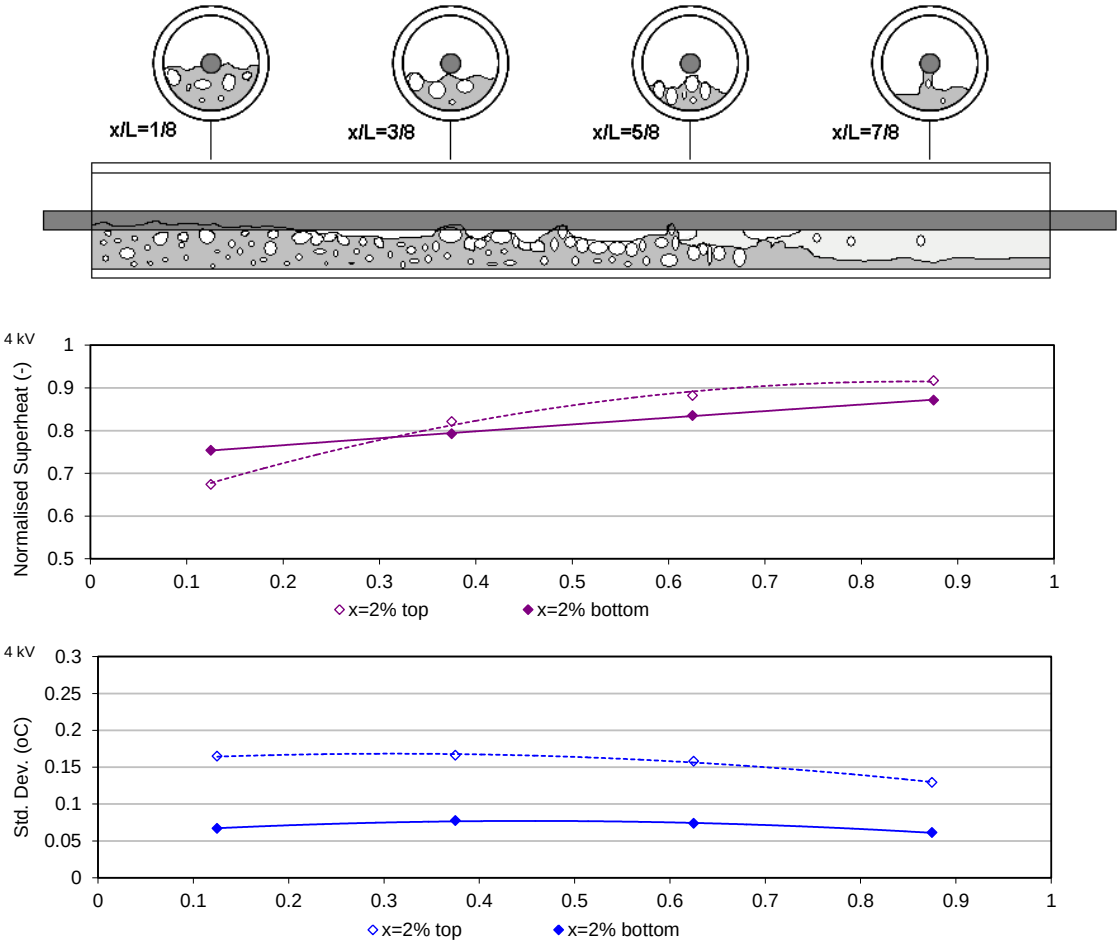

Figure 67: Sketch of flow regime with superheat standard deviations, and normalised superheats for x_{in}=2% 4 kV

Referring to the flow field images of 4 kV in Figure 65 and the sketch in Figure 67 the flow regime begins similarly to that at 0 kV. The liquid level is around electrode height as before (see Figure 55) and is again of a stratified type of flow with occasional slug events. Nucleation is still active and highly visible, but the bubbles are noticeably larger than in the field-free case. Mild oscillation of the bubbles is noticed at this stage, due to the varying forces set up by the oscillating AC voltage. As the flow progresses along the tube to x/L= ⅜, the liquid level drops slightly and bubble diameters increase. The interface is also more wavy. The top is wetted by intermittent slugs as seen before. However at x/L=⅝ an emerging difference is apparent. While the basic flow regime may be essentially similar, the nucleated bubbles now are seen to coalesce and bridge the tube at more regular intervals. Once these bubbles coalesce and "climb" they are

exposed to the vapour travelling at higher velocity which impinges against the protruding bubble interface causing these crests. A time sequence of images in Figure 68 shows this coalescence and growth of bubbles which impinge on the upper wall tube contributing to upper wall wetting.

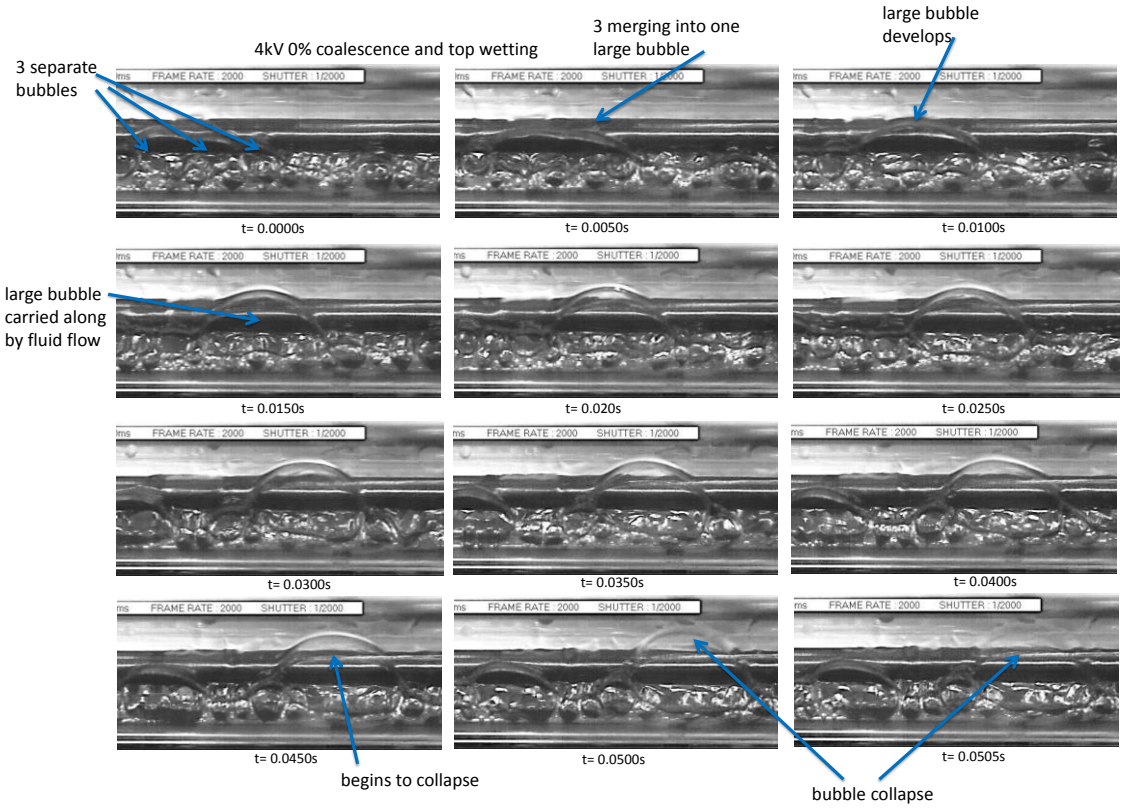

Figure 68: Time series of images showing top wetting by bubble coalescence at x_{in}=2%, x/L=⅜, 4 kV

In addition to the EHD effects on the bubble behaviour causing wetting of the top, oscillation of the nucleated bubbles in the liquid stratum also have an effect on heat transfer. These forced oscillations cause the bubbles to slide along the lower tube wall displacing liquid and causing more mixing thus leading to higher convection in this liquid stratum. An illustration of this is provided in the photo sequence in Figure 69. Although subject to a regular sine wave of 60Hz, the bubble path is not demonstrably regular in these photos, this is partly due to distortion of the bubble itself, and its interaction with neighbouring bubbles, also subject to EHD and inertial forces.

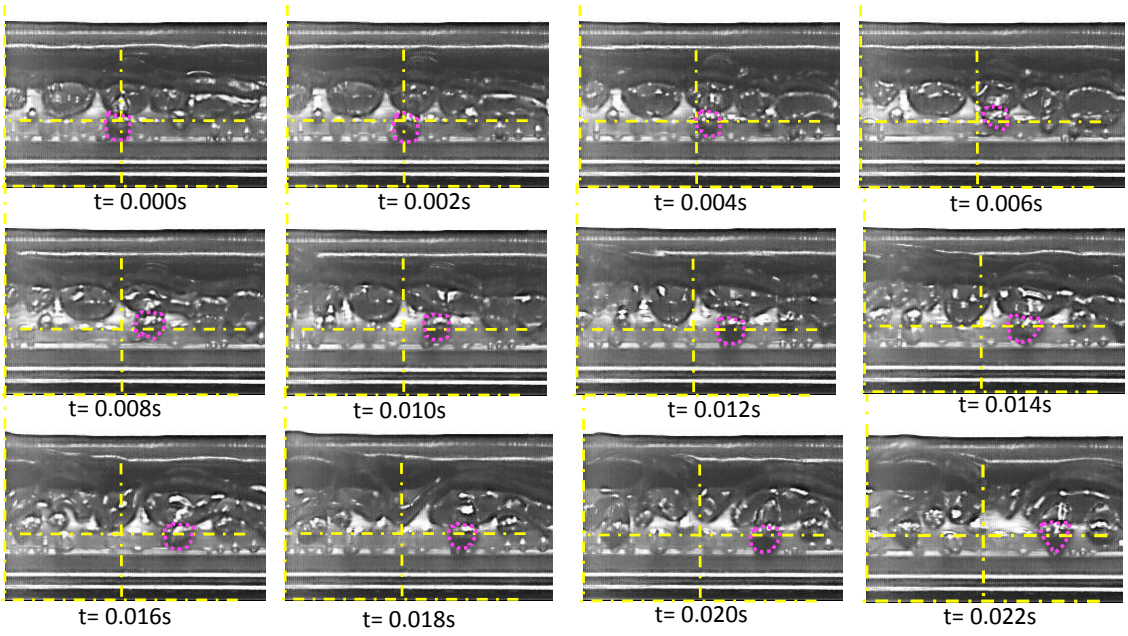

Figure 69: Time sequence of images showing faint bubble oscillation at 4 kV

At x/L=⅞, a further change is noted: the liquid layer stratification characterising the previous regions is intermittently replaced by a new type of flow regime. In this regime, the liquid layer can be seen to progress along the tube in the axial direction but with alternating long smooth waves free of nucleation. In addition, the liquid appears to display attraction to the centre electrode. A "curtain" or thick film of liquid is pulled from the bottom layer to the electrode and bubbles of oscillating vapour can be seen to be entrained in this attracted liquid "curtain". This attracted liquid curtain is known as the liquid extraction phenomenon which Cotton also documented [4]. However, the entrained bubbles witnessed here are in contrast to observations by Cotton [8]. Instead of oscillating bubbles, Cotton found droplets of liquid entrained and oscillating within the vapour phase during certain conditions in condensation experiments with 60Hz AC.

The tube-wall superheat variations are shown by the standard deviations presented in Figure 67 and they are of a similar pattern to that of the field-free case. The lower levels remain around 0.08°C, showing greater consistency of temperature, and the top layer at around 0.15°C experiencing greater fluctuations due to the slug wetting events. Once more, this was verified by imagery and video where a constant liquid presence was observed at the bottom, with the top of the tube subject to drying with periodic re-wetting by liquid slugs.

The normalised wall superheats are shown in Figure 67. The water inlet temperature was reduced by 2.09°C from 49.22°C to 47.13°C in order to maintain 150 W of heat input and consequently the wall superheats (not shown) have generally decreased from the range 10.5-12.5°C for the field-free case to 8.6-10.6°C for 4 kV. Referring to Figure 67, the bottom normalised superheats vary from 0.75 at the inlet rising gradually to 0.87 at the exit, while the top values begin around 0.67 and rise to 0.92. It is interesting to note that at the tube entrance the top of the tube is cooler than the lower tube, indicating the presence of an effective cooling mechanism, perhaps the wetting nature of the slug events, or perhaps redistribution assisted by EHD. Also the lower magnitude of the normalised superheats at the entrance compared with Figure 57 for 0 kV is a qualitative indication that the local HTCs are higher in this region also.

Video observation shows that the 4 kV forces cause additional motion both of the bottom layer of liquid and of bubbles within that layer. The video also shows that despite occasional wetting of the top surface at the end of the tube, it is not as effectively wetted as at the tube beginning. This is supported by the standard deviations which exhibit a downward trend at the tube top, and also by the tube wall superheats which towards the tube end, are also higher at the top than at the bottom suggesting a higher thermal resistance.

4.1.3.2: Results for 8 kV

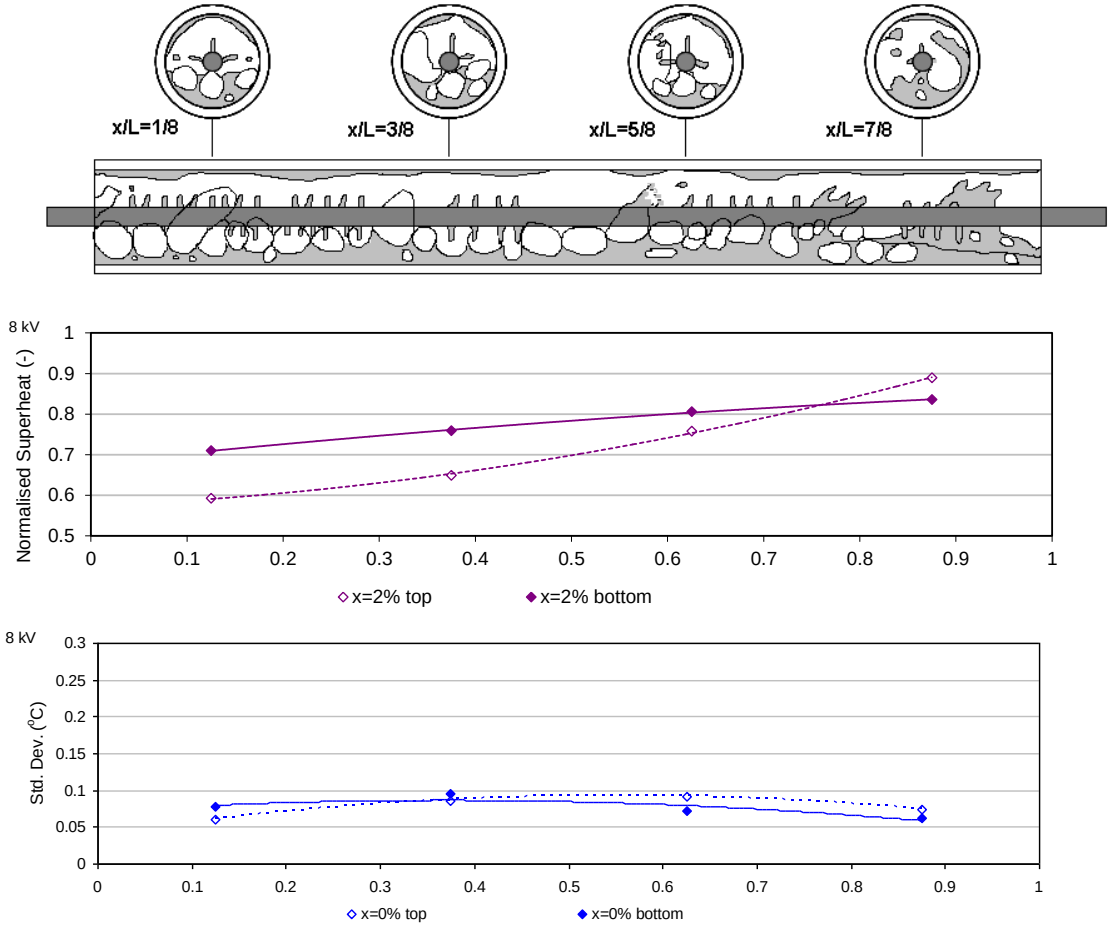

Figure 70: Sketch of flow regime with superheat standard deviations, and normalised superheats for x_{in}=2% 8 kV

From the images in Figure 66 and the sketch in Figure 70, a major change in flow regime is apparent with the application of 8 kV across the electrode and sapphire tube. The stratified liquid layer with nucleate boiling which was characteristic of the field-free case and the 4 kV case has been replaced with a much more complex type of flow composed of several unique and interesting phenomena. The slug events found at 0 kV and 4 kV have also ceased.

The most evident characteristic of this flow regime is the prevalence of large bubbles entrained in the lower liquid layer which is seen to occur at locations x/L=⅛, ⅜ and at ⅝. The bubbles are the result of multiple coalescence events and are alternately attracted and repelled by the electrode within the liquid layer along the tube. Bubbles coalesce to reach a large size (4-5mm diameter) after which bursting occurs at the vapour-liquid interface. These bubbles are of a large and repeatable size and oscillate

in the vertical direction while translating in the direction of the flow. This causes significant mixing near the lower wall of the tube. Nucleate boiling appears mostly suppressed, with very few intermittent nucleation events at the lower wall. The oscillating bubble phenomenon within the lower stratified layer occurs along the entire length of the test section in one form or another. This oscillating bubble regime is stable at x/L=⅛ and ⅜ but is noticed to change slightly at x/L=⅝, probably due to the increase in quality at this point, and hence the vapour velocity is higher which in turn affects the liquid interface to a greater extent.

However, towards the end of the test section at x/L=⅞, the oscillating bubble regime has transformed into a swirling type of flow, and again one can observe rapid bubble growth and coalescence. However, the bridging and climbing of bubbles is strongly affected by the high axial velocity of the vapour core, which impinges on the climbing bubble interface causing a flailing or swirling flow effect.

Another phenomenon in this regime is the existence of liquid columns or jets which emanate from the electrode surface and expel liquid from the electrode to the top surface of the tube causing re-wetting of dryer areas. These jets are more active with higher liquid levels, and tend to dissipate in occurrence and strength along the test section as the liquid level falls below the electrode. These are most active at x/L=⅛, ⅜ and ⅝. Although liquid jets are still formed at x/L=⅞, they do not have sufficient momentum to reach the upper wall from the lower liquid layer.

A very striking finding from Figure 70 is the fact that the temperature standard deviations for the top and bottom walls are largely equal at around 0.07°C and do not exhibit the periodicity observed for either the field-free or the 4 kV cases. The intermittent slug events present in the field-free case have largely disappeared with the application of EHD, although periodic bridging or cresting of liquid was noted. The application of 8 kV has produced a very wetted flow condition all around the tube wall.

In order to maintain a constant heat input across the test section of 150 W, the inlet water temperature was again lowered to 43.53°C, a significant drop from 49.22°C and 47.13°C at 0 and 4 kV respectively. Interestingly, from Figure 70, the normalised wall superheats along most of the top tube wall (x/L=⅛, x/L=⅜ and x/L=⅝) are lower than

that for the corresponding bottom wall superheats, rising from 0.59 to 0.89, while the bottom normalised superheats only increase from 0.71 to 0.84. Correspondingly, the HTCs would be expected to be high in this region of low superheat. This indicates that the liquid redistribution and wetting by the EHD forces including jets of liquid from the electrode create a superior mechanism of heat transfer at the top than the thin convective film at the bottom in this case.

It would thus appear that the creation and subsequent motion of the large oscillating bubbles is also partly responsible for the 2-fold increase in the average heat transfer coefficient from 1006 W/m^{2}K at 0 kV to 2000 W/m^{2}K at 8 kV. The oscillating bubble phenomenon within the lower stratified layer occurs along the entire length of the test section in one form or another so that the HTC and the enhancement remain almost consistent along its length. It has been noticed by Donnelly *et al*. [86] that high heat transfer occurs in the wake of sliding gas bubbles travelling in a liquid. At x/L=⅛ large bubble movements causing upward movement of liquid around the tube perimeter, combined with liquid jets being forced upward from the electrode, contribute greatly to wetting of the top surface. At the exit of the tube the bottom still has a liquid layer, while the top of the tube, despite the changed flow conditions, still experiences re-wetting by the swirling flow.

4.1.3.3: Pressure Drop

Based on previous knowledge on the application of EHD voltages, it was expected that the resultant redistributed flow patterns would increase fluid friction inside the test section and thus adversely affect the pressure drop. Accordingly, the plots in Figure 71 show the pressure drop measured across the test section at 0, 4 and 8 kV. A slight drop is observed with 4 kV, but the fluid flow field at 4 kV was basically an extension of that witnessed at 0 kV, therefore this drop may be within experimental variations and uncertainty given the similarity in flow field. However, the rise to 6.53 mbar seems more realistic and can be explained by the oscillating bubble regime, where redistribution of liquid around the tube wall causes higher wall friction. Figure 71 also shows the pressure fluctuations along the tube. At 0 and 4 kV a frequency of around 1Hz is seen. This fits well with the slug event frequency observed in the videos. However, this periodicity ceases at 8 kV in line with the disappearance of the periodic annular slug events found previously at 0 and 4 kV.

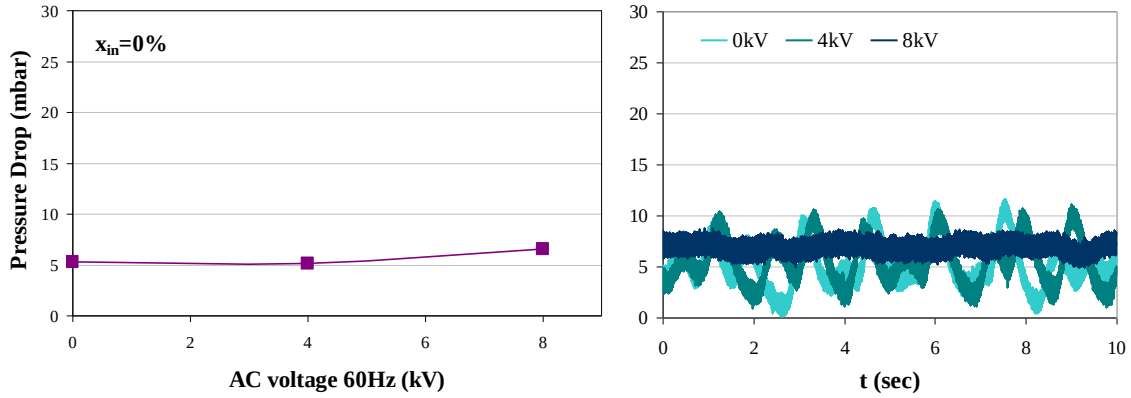

Figure 71: Averaged and real-time pressure drop, x_{in}= 2%, for 0, 4 and 8 kV

4.1.3.4: Summary

For an inlet quality of x_{in}=2%, the flow regime was stratified wavy with slugs, and nucleation was prolific. Application of 4 kV EHD voltage had a minor effect on nucleation and bubble activity and also a 1.25-fold increase on the heat transfer but with little change in pressure drop. An EHD voltage of 8 kV was sufficient to cause a large change in flow regime, with major changes in the bubble activity and also in liquid re-distribution mechanisms. Heat transfer was also augmented by two-fold as a result of the liquid disturbance and redistribution. The pressure drop was found to increase as a result of greater friction from the increased wetting of the tube.

4.1.4: Results for x_{in} = 15% and G=100 kg/m^{2}s

At an inlet quality of x_{in}=15%, again an increase in HTC is found with the application of EHD. Figure 72 shows this gradual increase and compares it with the previous case at 2% quality. The average heat transfer coefficient rises from 1096 W/m^{2}K at 0 kV to 1288 W/m^{2}K at 4 kV and finally to 1674 W/m^{2}K with an EHD voltage of 8 kV. While the 4 kV enhancement is around the same as that of the 2% case, it is a smaller degree of enhancement in percentage terms.

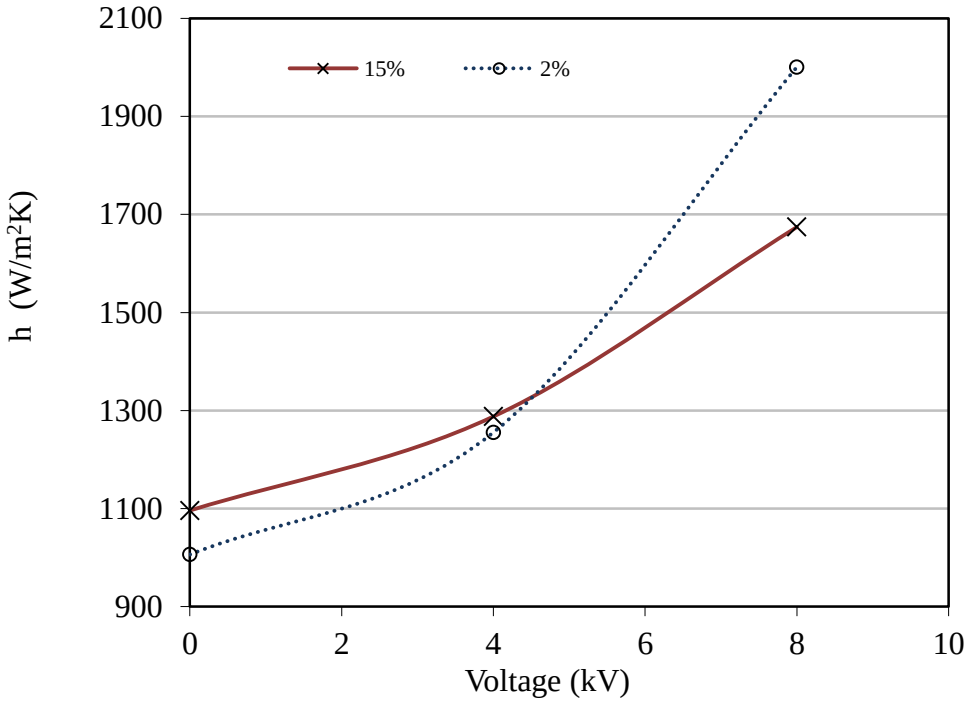

Figure 72: Variation of average HTCs with applied voltage, x_{in}=15% (2% shown dotted for comparison)

As before, the following sections present a breakdown of the heat transfer and flow conditions, together with the high speed imagery. Images of the flow field at x_{in}=15% with voltages of 0, 4 and 8 kV are presented in Figure 73.

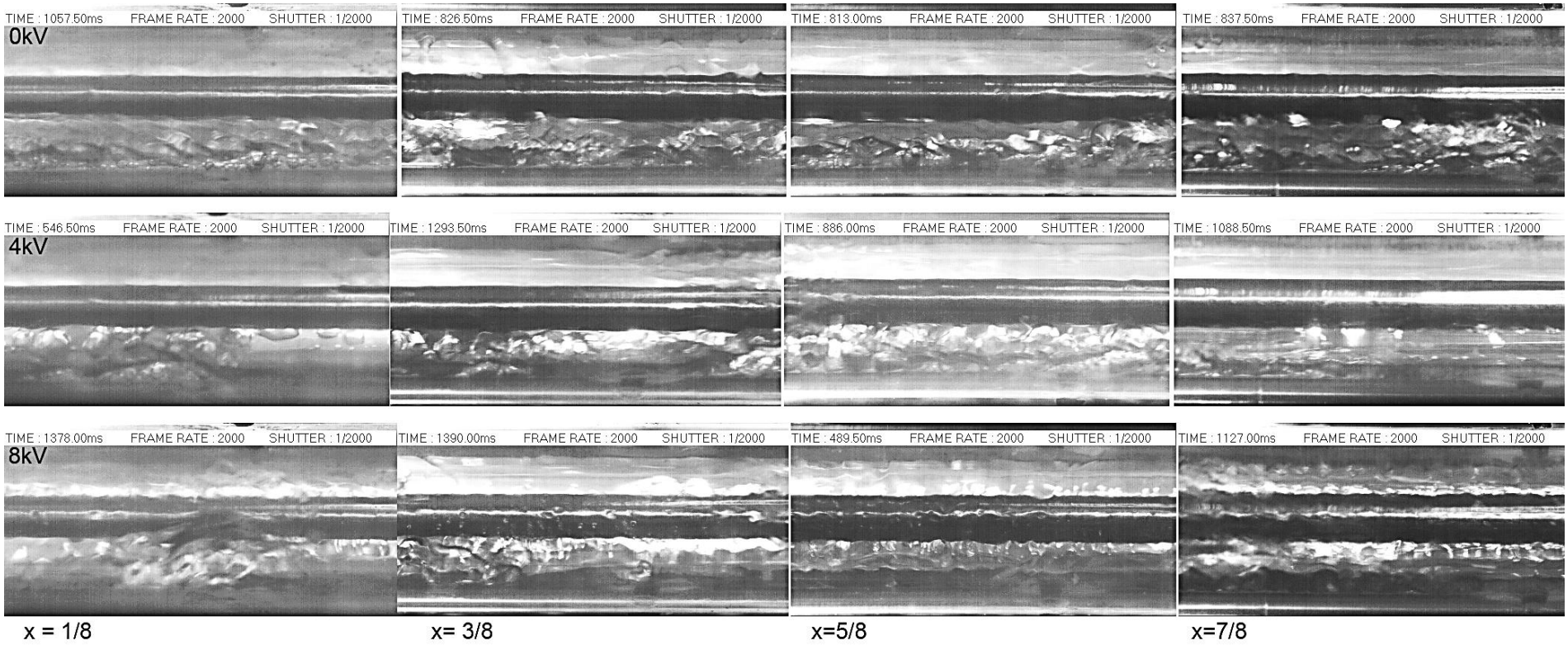

Figure 73: Flow at locations x/L=⅛, ⅜, ⅝ & ⅞ at 0, 4 and 8 kV for G=100 kg/m²s, x_{in} = 15%

4.1.4.1: Results for 4 kV

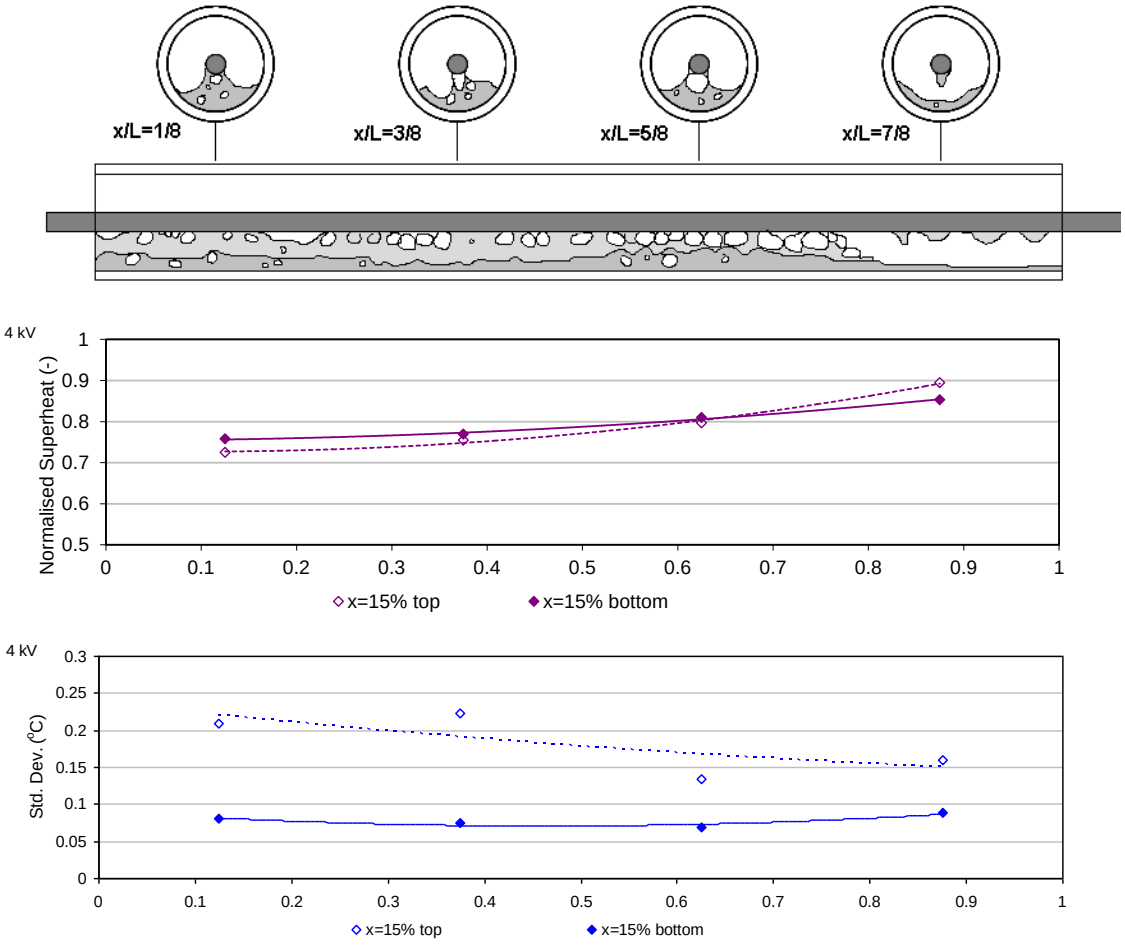

Figure 74: Sketch of flow regime with superheat standard deviations and normalised superheats for x_{in}=15%, V = 4 kV

With the aid of the flow regime photos and sketches of the 4 kV case in Figure 73 and Figure 74, the influence of EHD can clearly be seen. The first image at x/L=⅛ is characterised by a new type of flow regime which has a basis of a stratified wavy liquid layer, with nucleate boiling and oscillating entrained bubbles, but does exhibit periodic departures to a very plain stratified flow with no nucleation, entrained bubbles or waviness. As the fluid progresses along the test section this alternating pattern of transitory flow, changing from one flow regime to the other, persists until the last section at x/L=⅞, where the flow becomes a thin stratified liquid layer with periodic annular events. At the tube entrance, some nucleate boiling is visible but at a low level. At these entrance locations, wetting of the tube top is achieved by cresting and bridging of the liquid layer. This cresting may be as a result of interplay between interfacial forces between vapour and liquid and the additional EHD forces acting favourably on the crested liquid. At locations x/L=⅜, the same basic flow regime is apparent, except

that now the cresting events are more numerous and some precipitate the formation of transitory annular slugs as noticed before. Continuing along the tube, the underlying transitory flow described earlier persists, and the annular slugs are again more numerous at x/L=⅝. Finally at x/L=⅞, the flow becomes a stratified liquid layer at the bottom, with predominantly vapour at the upper part of the tube, wetted only by the less frequent annular events and occasional minor splashes.

From Figure 74, the consistent standard deviation values of around 0.07 °C again show low fluctuations at the tube bottom indicative of a liquid layer, while greater periodicity at the tube top is indicated by the larger standard deviations of 0.22 °C falling to 0.15 °C at the end. However, the top tube fluctuations are slightly lower at the end than at 0 kV where the values were around 0.25 °C. This lower variation was confirmed in the video where the tube top was largely dryer than earlier in the tube.

The normalised wall superheat temperatures are shown in Figure 74. The water inlet temperature was lowered from 48.61 °C to 46.876 °C, again to maintain Q_{in}=150 W at 4 kV. The normalised superheats at the top range from 0.73 to 0.89, while the bottom range from 0.76 to 0.85. Both superheat traces are similar in magnitude for most of the tube length except at the exit region where again, the top superheat rises slightly higher. Interestingly, the top traces indicate lower superheats pointing to better heat transfer than at the bottom. However, this ceases at the end of the tube, as the higher superheat at the top at x/L=⅞ denotes a drier surface. This is supported by the standard deviations and the imagery.

Referring to Figure 72 with 4 kV, the overall heat transfer of 1288 W/m^{2}K is 1.17 times higher than that of the field-free case of 1096 W/m^{2}K. The increase in duration of the annular slugs which cause greater top tube wetting, and the extraction and thinning of the lower liquid layer may help to account for this increase in heat transfer.

As mentioned earlier, with an applied voltage of 4 kV an unusual change has occurred in the case of x_{in}=15% and this will now be discussed in more detail. From video analysis, the flow can be seen to vary between two distinct flow regimes, from the previously described stratified basis to a new type of flow pattern, where the liquid layer appears to be attracted to the electrode. In this new flow regime, the

liquid/vapour interface can be seen to rise and fall along the tube, but a curtain of liquid is attracted to the electrode, within which vapour bubbles are seen to oscillate. The effect can be seen in Figure 73 at location x/L=⅛ at 4 kV.

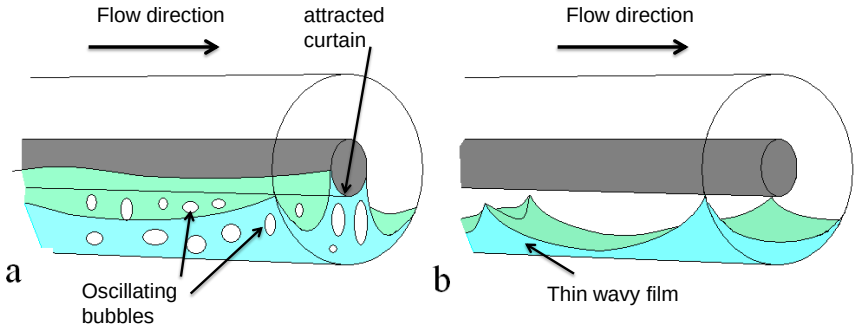

Figure 75: Sketches of (a) oscillatory entrained bubble flow and (b) the following thin-film flow regime

A representational sketch of the essential features is shown in Figure 75 (a) depicting the contact line with the tube wall, the curtain of liquid attracted to the electrode, and the oscillating vapour bubbles within the liquid. The flow regime then gradually transforms to a thin film stratified flow where the liquid layer becomes so thin in places it is difficult to discern. This second flow regime is shown in Figure 75(b). Additional high speed images of the phenomenon are depicted in Figure 76 to help explain the transition between these two flow regimes. The flow is initially composed of a wavy fluid/vapour/tube contact line with a central region of liquid drawn from the liquid layer up to the electrode.

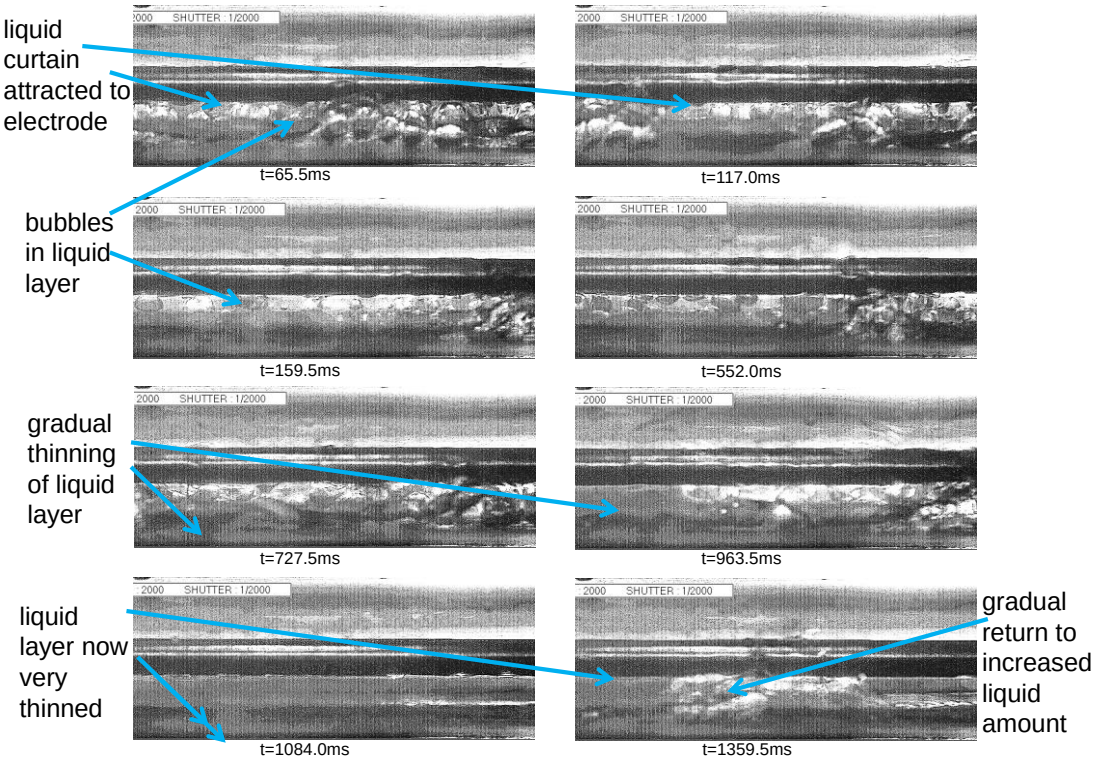

Figure 76: Transitional flow regime behaviour at location x/L=⅛, x_{in}=15% and 4 kV

This attracted curtain of liquid contains bubbles oscillating in response to the 60Hz of the AC EHD voltage. This regime then changes to a type of flow where crests of liquid form again with the curtain of liquid containing oscillating bubbles under the electrode. This gradually gives way to a flow containing little liquid and where just a thin film of liquid is discernible on the lower surface, (also in sketch in Figure 75 (b)).

Cotton [8] noticed a similar phenomenon to bubbles oscillating within the curtain of liquid which he termed "Oscillatory Entrained Droplet EHD Two-phase Flow". However, this was noticed in condensation not in evaporation, Cotton describes the reverse situation of a droplet of liquid oscillating in the vapour phase within an annular liquid film. However, in this case, by careful study of the video and photographs, it is certain to be vapour bubbles appearing with a liquid curtain such as shown in pictures in Figure 75(a) and Figure 76(a).

4.1.4.2: Results for 8 kV

With reference to the photographs of the 8 kV case in Figure 73, again a major change has taken place as a result of the EHD voltage. The transitory varying flow regime described earlier with the EHD voltage of 4 kV is again noticed here but in a stronger form. At x/L=⅛, a curtain of liquid is again attracted to the electrode and contains bubbles oscillating within the liquid. Periodic slugs serve to wet the tube top. Liquid jets are also noticed at this higher EHD voltage; these are jets or columns of liquid that are propelled from the electrode surface and also cause wetting of the upper surface of the tube. These jets are clearly visible in Figure 73 at locations x/L = ⅜ and ⅝.

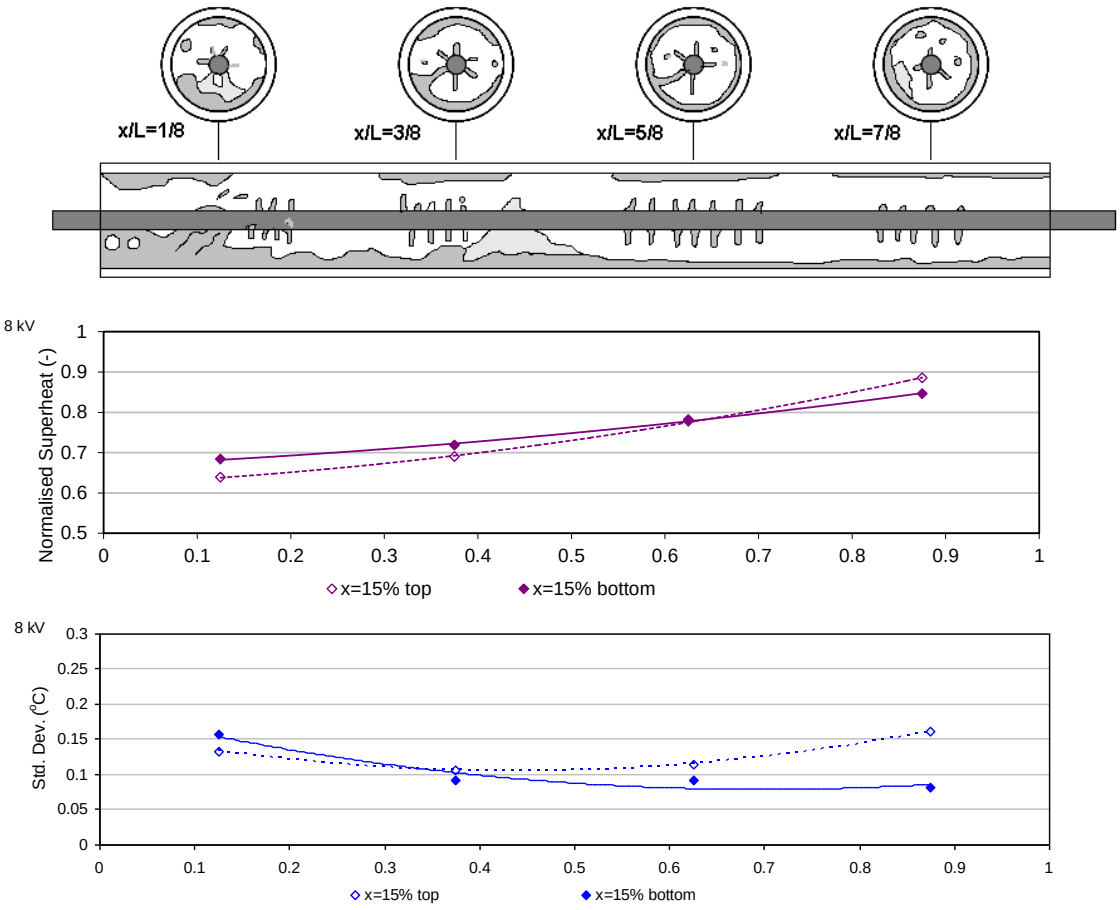

Figure 77: Salient flow features with superheat standard deviations, and superheats for x_{in}=15% 8 kV

As the fluid progresses, the flow regime begins to change, and the curtain of attracted liquid is diminished at location x/L = ⅜. The flow is now mainly a thin film along the bottom, but with occasional climbing bubbles and liquid swirls and also periodic slugs that are annular in nature. These in conjunction with the liquid jets serve to constantly

wet the tube top. Although the liquid jets on their own do not seem strong enough to propel liquid to a sufficient height, whenever the top liquid layer is on occasion sufficiently close it is noticeable that there exists a continuous column of liquid between the electrode and top of tube which travels in the direction of flow.

At x/L =⅝, a similar flow pattern exists, although the liquid layer at the bottom of the tube is lower. The top of the tube is still subject to continual wetting by annular slugs and swirls but areas of dryout begin to appear at the tube top. EHD assisted liquid jet bridging events as seen at x/L=⅜ are also thought to occur, but because of the highly disturbed annular wetting of the tube side wall, these phenomena are difficult to view definitively.

At x/L=⅞ the flow is characterised mainly by a thin liquid layer at the tube bottom and large redistribution of the liquid around the tube by swirling liquid and annular slugs. The whole of the tube is very wetted though some thinning of the liquid layer is noticeable at the top of the tube. Again, due to the short duration of the video, it is possible some dryout events may have occurred.

The superheat standard deviations seen in Figure 77 form a pattern not yet seen in the earlier cases. Both top and bottom show moderate fluctuations of around 0.13-0.15°C, and unusually the bottom value is higher than the top in this case at x/L=⅛. At certain times at x/L=⅛, it is very hard to discern if there is any liquid layer at the bottom at all, and this alternating presence and lack of liquid may account for the higher standard deviations. Subsequently, both top and bottom standard deviations settle to around 0.1 °C at x/L=⅜ and the bottom values continue decreasing through x/L=⅝ and ⅞ until a value of 0.08°C. However the upper values begin to increase again at x/L=⅝ and further again at x/L=⅞ until they reach 0.16°C indicating larger fluctuations or alternating wetting and drying.

The wall superheats have again dropped due to the lowering of the inlet temperature to 44.51°C in order to maintain a constant heat input of 150 W across the test section. This lowering of the water temperature may also explain the lower levels of nucleate boiling. However, referring to Figure 77 the rise in normalised superheats with length is slightly sharper than before, both at the top which rises from 0.64 to 0.89 and also the

bottom which rises from 0.68 to 0.85. As noticed at 4 kV, the top superheats are higher for most of the length except towards the tube exit. The lower temperatures suggest a better heat transfer, and conversely the higher superheat at the end corresponds to a region of lower heat transfer.

The standard deviations for the tube bottom are higher than previous and video observation verifies the transitory flow conditions described earlier, hence the transitory nature of the flow at the top and bottom may account for the heat transfer profiles. Progressing along the tube, this transitory flow still occurs top and bottom, however liquid thinning is more noticeable at the top along with dryout areas. At the bottom, the liquid layer also thins with length, probably due to the evaporation of earlier liquid, the increase in vapour quality, and perhaps also an increase in vapour velocity. A thinner liquid layer along the bottom should normally lead to improved heat transfer.

Under an EHD voltage of 8 kV, the overall heat transfer coefficient of 1674W/m^{2}K is a 1.52 fold rise compared to the field free case. This is explained by several complex flow regimes witnessed along the test section. One is a transitory fluid flow regime, in which a curtain of liquid is extracted from the lower layer while the extracted liquid is then redistributed to upper parts of the tube. This action serves to enhance both the bottom convective component and the top heat transfer by causing re-wetting. The other transitory flow pattern is dominated by slugs and wave crests passing through and causing complete tube wetting, and finally, the effect of liquid jets or cones emanating from the electrode serves to propel fluid to areas of the tube or into the flow where it is redistributed to the tube top. The increase in heat transfer is supported by the drop in superheats at the tube entrance, and by the relatively low standard deviations supporting large scale wetting of the tube walls.

4.1.4.3: Pressure Drop

Figure 78 shows the pressure drops measured across the test section at 0, 4 and 8 kV. Compared with the x_{in}=2% case, the pressure drop has increased, even for the field-free case. This is due to the greater liquid and vapour velocities associated with the increase

in quality, and the resulting higher levels of friction encountered against the tube and electrode surfaces.

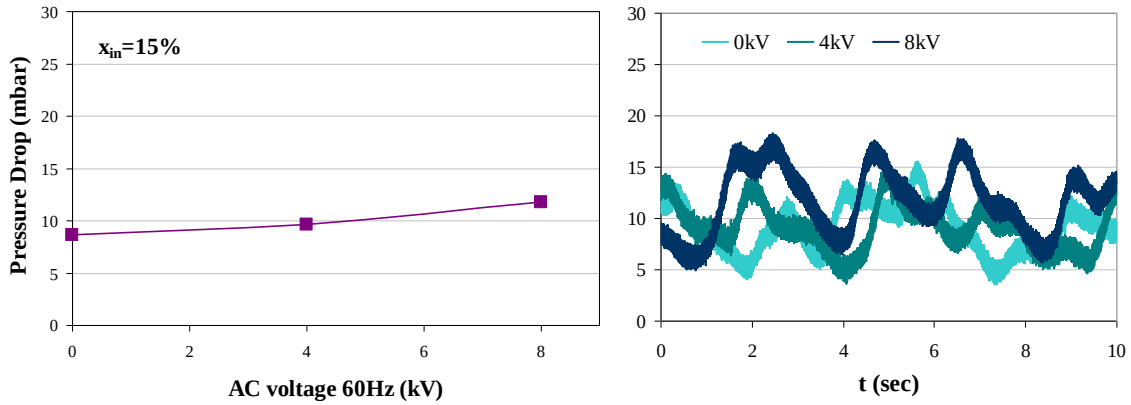

Figure 78: Averaged and real-time pressure drop, x_{in}=15%, for 0, 4 and 8 kV

The addition of high voltage causes redistribution of liquid to the walls which increases frictional forces further. The real-time pressure plots in Figure 78 are correspond to the periodic nature of the periodic slug events noticed in the videos. The pressures seem to have a complex pattern with larger waves occurring at about 0.5Hz overlaid with smaller pulses of a frequency around 1Hz. It was witnessed that the slug events appeared of longer duration, but this was difficult to quantify owing to the short video duration of 1.5 seconds. The pressure fluctuations however seem to validate the longer duration of these liquid slug events.

4.1.4.4: Summary

As quality increased to x_{in}=15%, the flow conditions gained higher velocities and heat transfer in the field-free case increased commensurately compared to the 2% case. Applying EHD voltages of 4 kV gave a further increase in heat transfer, and also induced a change in flow regime which included a new type of flow consisting of a "curtain" of liquid attracted to the electrode containing oscillating bubbles of vapour. At 8 kV this curtain effect is visible again but dissipates progressively with length. Heat transfer is higher, with substantial liquid redistribution to the top surface, but pressure drops have risen, this is thought to be primarily due to higher in tube fluid velocities and increased friction due to increased liquid contact with the wall.

4.1.5: Results for x_{in} = 30% and G=100 kg/m^{2}s

At an inlet quality of x_{in}=30%, a further increase in average HTC is found in both EHD and non-EHD cases. Figure 79 shows this gradual increase and for comparison, the dotted lines show the previous HTCs at x_{in}=2% and 15%. The average heat transfer coefficient rises from 1154W/m^{2}K at 0 kV to 1382W/m^{2}K at 4 kV before increasing again to 1487W/m^{2}K with an EHD voltage of 8 kV. In this case maximum heat transfer conditions are again attained at a voltage of 8 kV, though the 4 kV case also provides a reasonably high heat transfer coefficient. However, at 8 kV, the level of enhancement compared to the field free case is certainly lowered, only 1.29 times the field free case at 30% compared to enhancement levels of 1.53 and 1.99 at 15% and 2% respectively. To ascertain the cause of this the following sections analyse the heat transfer and high speed imagery.

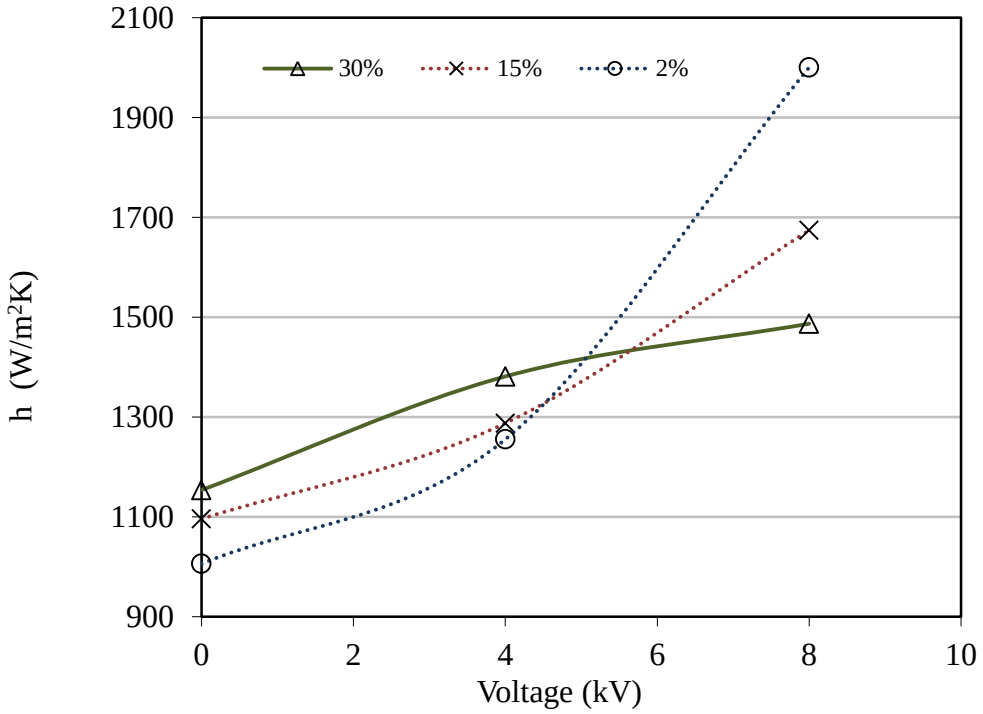

Figure 79: Variation of average HTCs with applied voltage, x_{in}=30%, (2% and 15% shown dotted for comparison)

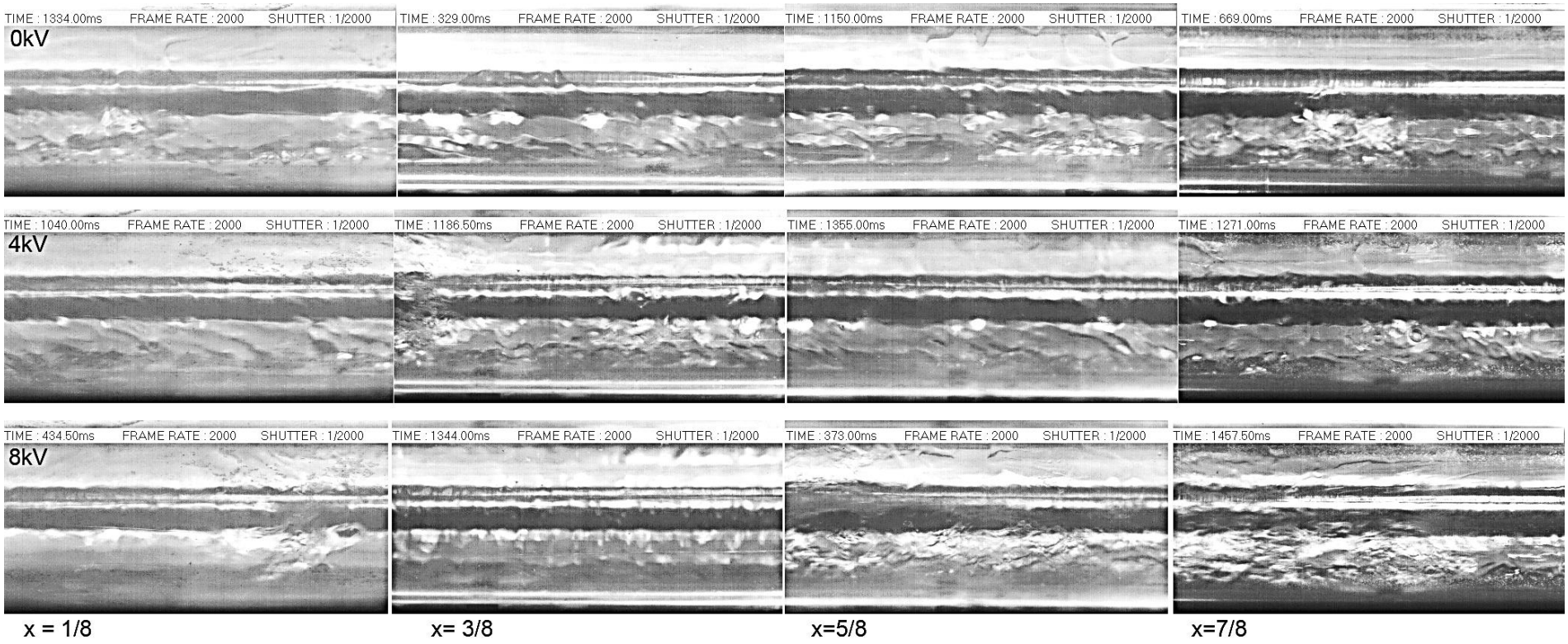

Figure 80: Flow at locations x/L=⅛, ⅜, ⅝ & ⅞ at 0, 4 and 8 kV for G=100 kg/m²s, x_{in} = 30%

4.1.5.1: Results for 4 kV

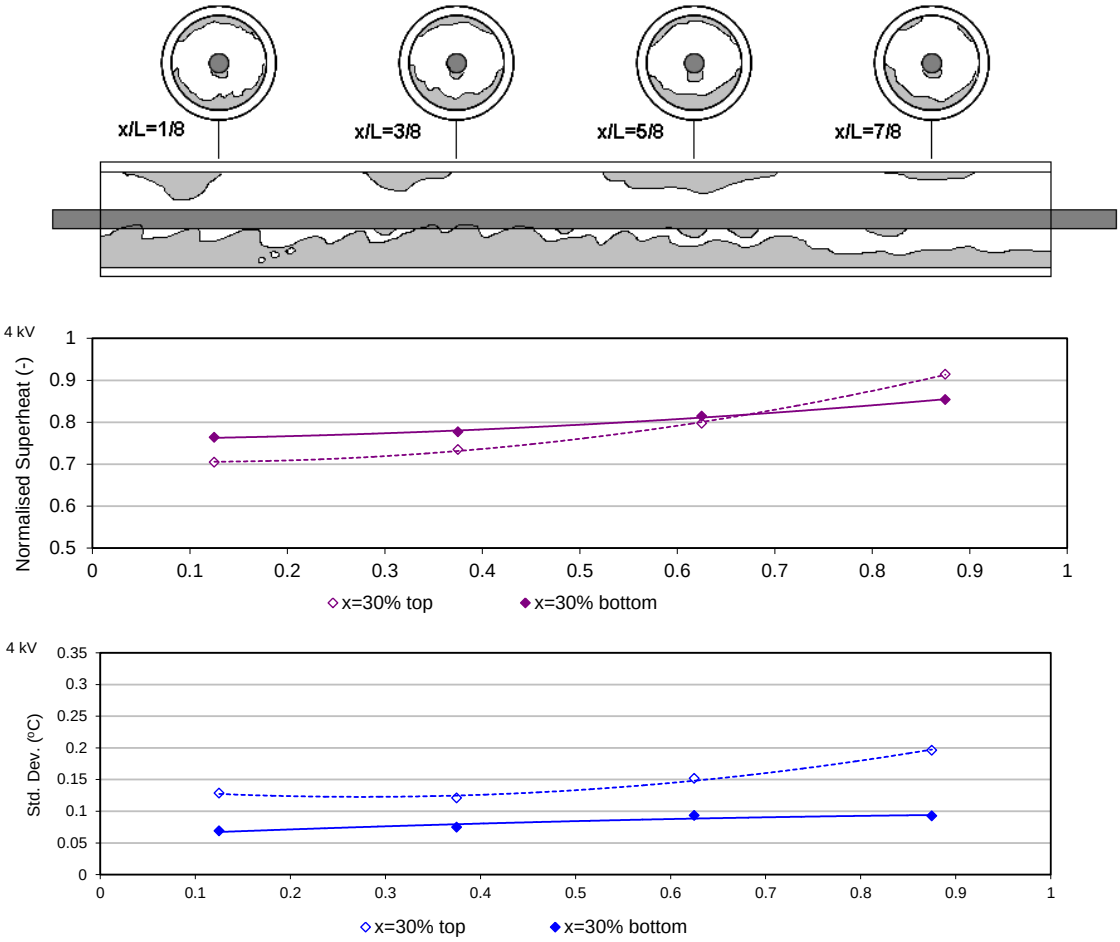

Figure 81: Sketch of flow regime with superheat standard deviations, and superheats for x_{in}=30%, V = 4 kV

The centre row of images in Figure 80 and the sketch in Figure 81 show the flow regimes for 4 kV of applied voltage at x_{in}=30%. While the flow again has a basis of stratified flow, the top of the tube is seen to be highly wetted, much more so than when compared to the 2% and 15% cases which only experienced intermittent top wetting due to the periodic liquid bridging or slugs. Conversely, the periodic annular slug events are now an almost constant feature, perhaps accounting for as much as 75% of the flow regime, and the flow conditions may be described as an annular flow induced by the effects of EHD. The 4 kV EHD force seems to provide enough additional force to cause much of this redistribution. The fluid flow conditions at all locations along the tube under 4 kV can be considered to be similar, i.e., a stratified wavy base but with a strong overlay of transitory annular slug flows that in effect "induce" an annular flow. Greater occurrence of dryout is noticed towards the top of the tube at locations x/L=⅝ and x/L=⅞.

With reference to the top wall superheat fluctuations in Figure 81, a significant reduction in the standard deviations to 0.15°C compared with the field-free case of 0.3°C is seen. This is particularly evident closer to the entrance region of the tube but tends to increase toward the tube end. This initial low magnitude of the standard deviation along with its gradual increase along the tube length is consistent with high speed video observations which show a highly wetted tube surface almost similar to an annular flow at the tube entrance. The liquid film gradually becomes less prevalent along the tube length and intermittent drying is more common, which is reflected in the increase of the standard deviation curves. The bottom standard deviations again remain around 0.08 and are in line with previous observations of a liquid layer.

The superheats of top and bottom have dropped by around 4°C as the inlet water temperature was reduced from 48.57°C in the field free case to 46.54°C at 4 kV in order to maintain a heat input of 150 W across the test section. The normalised superheats are shown in Figure 81 and the top values now range from 0.77 to 0.95. The bottom superheats likewise drop to a range of 0.77 to 0.85. Compared to the field free case in Figure 59 the top superheats are now lower than the bottom for much of the length denoting a higher heat transfer. As in earlier cases, this again changes towards the exit of the tube where the top superheat rises indicating lower heat transfer. This is supported by the top standard deviations which also remain relatively low for much of the length, but show a corresponding increase towards the tube end. The imagery also confirms that high wetting is visible for the first two locations all along the tube, and top wall dryout becomes more apparent from locations x/L=⅝ and ⅞ onwards.

The highly wetted flow at the tube inlet, especially the re-wetting of the top caused by the periodic annular slugs, must account for this high local heat transfer. Although the flow is re-wetted by annular slugs throughout, the increasing presence of dryout toward the tube end likely causes a reduction in heat transfer. The bottom surface is expected to maintain a more constant value of heat transfer as it is always in contact with a fast-flowing highly disturbed liquid film.

4.1.5.2: Results for 8 kV

High speed photos of 8 kV with x_{in}= 30%, are shown in the last row of Figure 80 and accompanying sketch in Figure 82. The flow regime is again an extension of that which occurred at 4 kV. At x/L=⅛, the 8 kV EHD voltage seems to have caused stronger redistribution of fluid so as to create a more complete annular flow than that seen at 4 kV. The series of hitherto annular slug events are now a permanent feature of the flow and overlap forming an almost continuous wetted layer. The stratified liquid layer previously discernible at 4 kV is no longer visible. Comparing the sketches of the flow regime in Figure 82 to those from Figure 70 and Figure 77, the flow regime is now more annular and features large redistribution of liquid from the bottom to the upper regions of the tube.

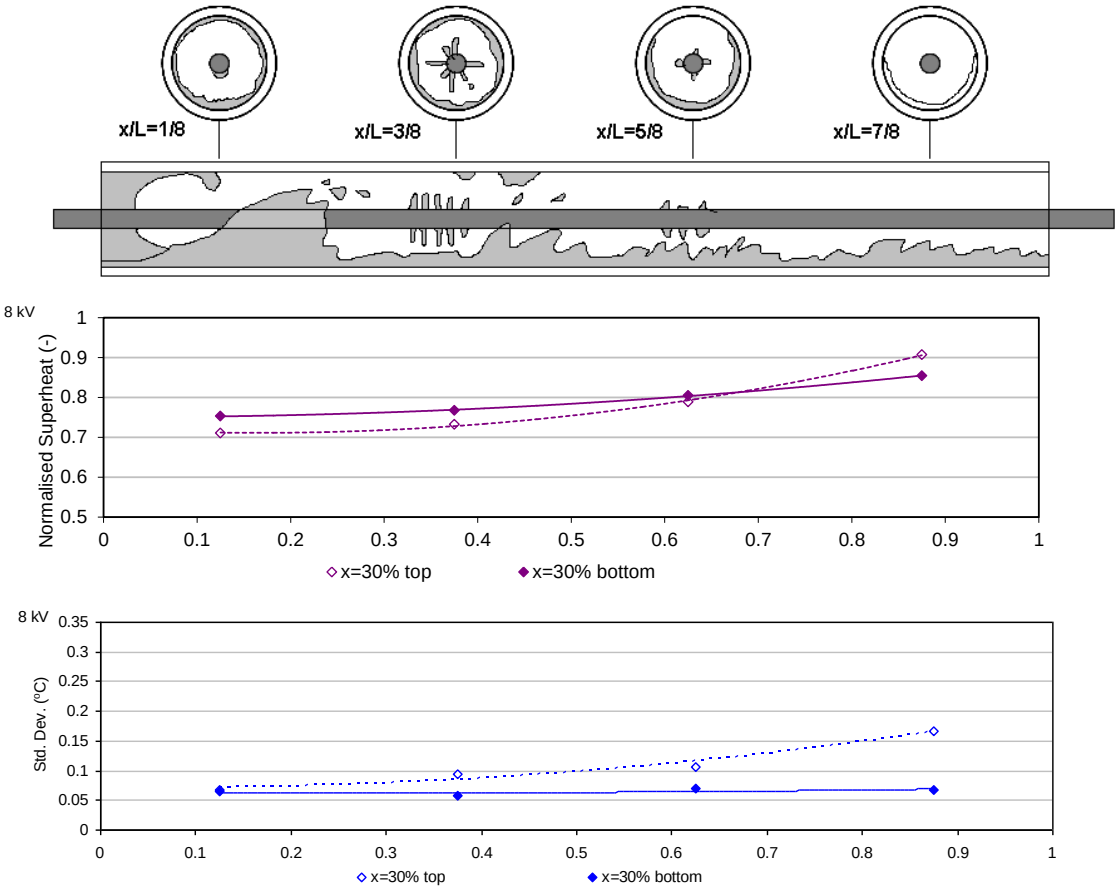

Figure 82: Sketch of flow regimes with superheat standard deviations and normalised superheats for x_{in}=30% 8 kV

At x/L=⅜, the flow is similar, remaining almost completely wetted with no stratified bottom layer of liquid visible. Dry areas form on the tube upper surface but are quickly

re-wetted by annular flushes. As the fluid passes through x/L=⅝, the flow is again similar but dryout at the upper surface is more common and longer lasting. Finally at x/L=⅞, dryout has become so strong at the tube top that the flow, once annular, has now reverted to a type of "semi-annular flow" where due to gravity only the bottom half of the tube is wetted. Liquid jets are visible but appear much weaker compared with tests at lower inlet quality at the same applied voltage. This may be due to the much reduced quantity of liquid available near the electrode.

The standard deviations for the lower wall in Figure 82 are uniform at around 0.07 °C, indicative of a constant liquid layer. The top standard deviations are seen to be almost equal to the bottom values near the beginning of the tube, thus suggesting a highly wetted liquid layer. This was exactly what was found in the video imagery. Also, the top standard deviations begin to increase more sharply near the end of the test section finishing at around 0.16 °C. This shows more fluctuations in temperature toward the tube end, and again the imagery verifies this, showing the greater presence of vapour and intermittent annular slug events at locations x/L=⅝ and ⅞.

The wall superheats have dropped by a further amount with 8 kV compared to the 4 kV case, this is due once more to the lowering of the water inlet from 48.25 °C to 46.64 °C to maintain a heat input of 150 W. The normalised superheats are shown in Figure 82. The top values now range from 0.72 to 0.95, a drop from the range 0.77-0.96 at 4 kV. The bottom superheats remain in the range of 0.76-0.86, almost the same as the 0.77-0.85 values found at 4 kV. The bottom normalised superheats undergo only minor changes, while the top normalised superheats drop progressively with increasing EHD voltage. This is indicative of EHD liquid redistribution to the top of the tube consequently improving the heat transfer at that location.

Again this increase in heat transfer from 1154 W/m^{2}K at 0 kV can be attributed to an augmentation of the enhanced flow regime found at 4 kV which increased the average HTC to 1382 W/m^{2}K. Here the 8 kV EHD forces manage to cause more fluid redistribution, leading to the increased heat transfer of 1487 W/m^{2}K. However, this is still only an enhancement factor of 1.29 and falls short of the factors of 1.99 and 1.53 found with 8 kV at 2% and 15%. Therefore the effect of increasing vapour quality itself appears to reduce the enhancement effect of EHD.

4.1.5.3: Pressure Drop

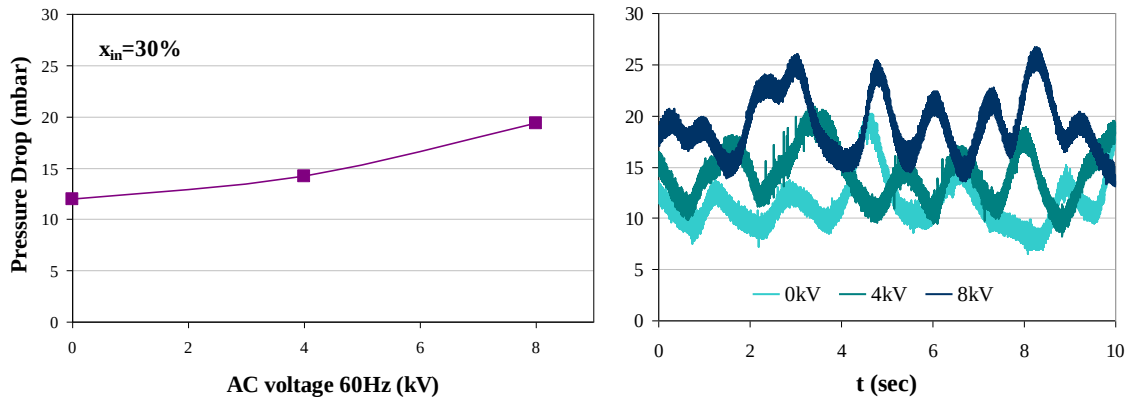

Figure 83: Averaged and real-time pressure drop x_{in}=30%, 0, 4 and 8 kV

At x_{in}=30%, Figure 83 shows the pressure drop under field-free (0 kV) conditions has increased from 8.59 mbar at x_{in}=15% to 11.59 mbar. With the quality increase to 30% for the same mass flux, the amount of vapour is increased therefore vapour and liquid velocity increases resulting in greater wall friction, and consequently higher pressure drop. EHD increases pressure drop to 14.22 mbar at 4 kV and again to 19.32 mbar at 8 kV. The real-time pressure plots in Figure 83 show a similar periodicity to that at 15% except for the generally higher average pressures. These are due to the pulsating annular slugs and again are composed of larger waves with a frequency of around 0.5Hz and smaller pulses with a frequency of around 1Hz.

4.1.5.4: Summary

At x_{in}=30%, the flow regime is essentially stratified wavy with periodic annular events causing re-wetting of the upper wall. It can be concluded that for x_{in}=30%, the application of 4 kV via redistribution of liquid causes a transition from a predominantly stratified wavy flow to an annular type of flow. The application of 8 kV further augments this annular flow, providing more effective liquid redistribution and creating a very wetted tube upper wall which is only curtailed by dryout towards the end of the tube. The high heat transfer coefficients provided by these redistributed annular flows are somewhat tempered by increased pressure drops.

4.1.6: Results for x_{in} = 45% and G=100 kg/m^{2}s

At the final test condition with an inlet quality of x_{in}=45%, the average heat transfer coefficients in Figure 84 exhibit an almost linear increase from 0 kV through 4 kV to 8 kV. However with the quality now at 45%, the field-free heat transfer coefficient has decreased to 1068 W/m^{2}K from the 1154 W/m^{2}K found at 30%. At 4 kV, though the HTC has risen to 1197 W/m^{2}K, this is only a factor of 1.12 times the 0 kV case, and is also lower than the 1382 W/m^{2}K found at 30%. Likewise at 8 kV, although the HTC values increase by a factor of 1.31 to 1401 W/m^{2}K, this is still lower than the 1487 W/m^{2}K attained with 8 kV at 30%.

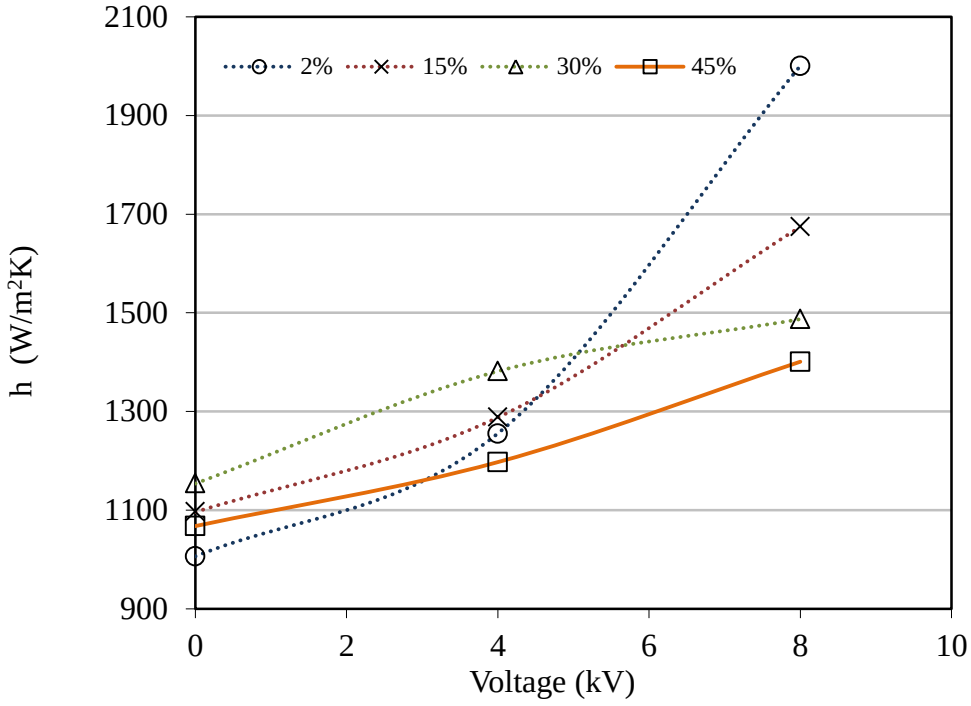

Figure 84: Variation of average HTCs with applied voltage, x_{in}=45% (2%, 15% and 30% shown dotted for comparison)

In contrast to the increasing HTC values found as quality increased up to x_{in}=30%, the profile at 45% now exhibits a decrease in heat transfer coefficient in the field-free condition and at 4 kV and 8 kV. With increasing quality generally, it is expected that the velocity of vapour and liquid within the annulus may increase. It may also be expected that the EHD forces have less influence at higher vapour qualities due to the increasing dominance of these inertial forces. As in earlier sections, the following subsections investigate these findings in more detail.

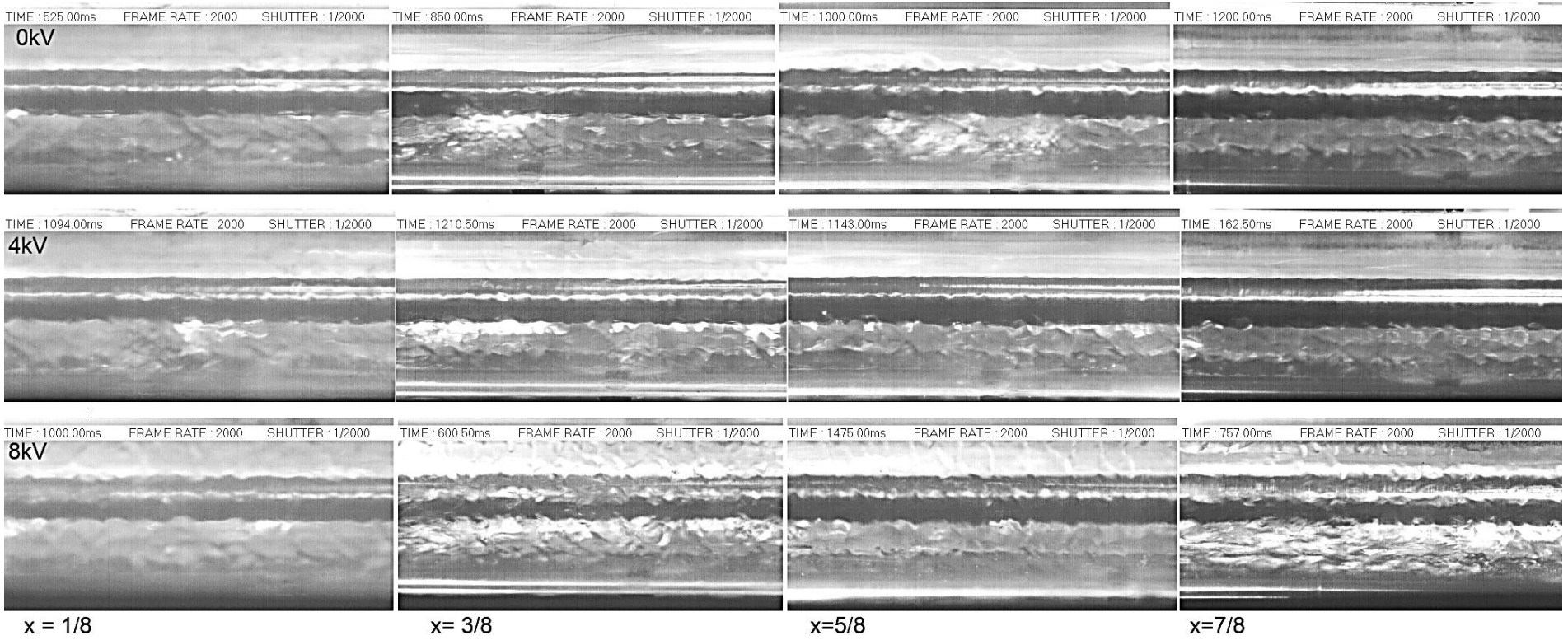

Figure 85: Flow at locations x/L=⅛, ⅜, ⅝ & ⅞ at 0, 4 and 8 kV for G=100 kg/m²s x_{in} = 45%

4.1.6.1: Results for 4 kV

With reference to the images in Figure 85 and sketch in Figure 86, the flow regime is very similar to that of 0 kV, but the top of the tube experiences more wetting. Some AC effect on the liquid was noted next to the electrode, where liquid is seen to pulse in large droplets along the lower electrode surface, but this did not appear to have an effect on the heat transfer. Either the electric field is not strong enough to cause redistribution or the liquid level is insufficient for satisfactory extraction to occur. However, the 4 kV electric field certainly does have an effect on the fluid flow regime. It causes increased liquid redistribution from the lower layer to the top wall, resulting in upper wall wetting.

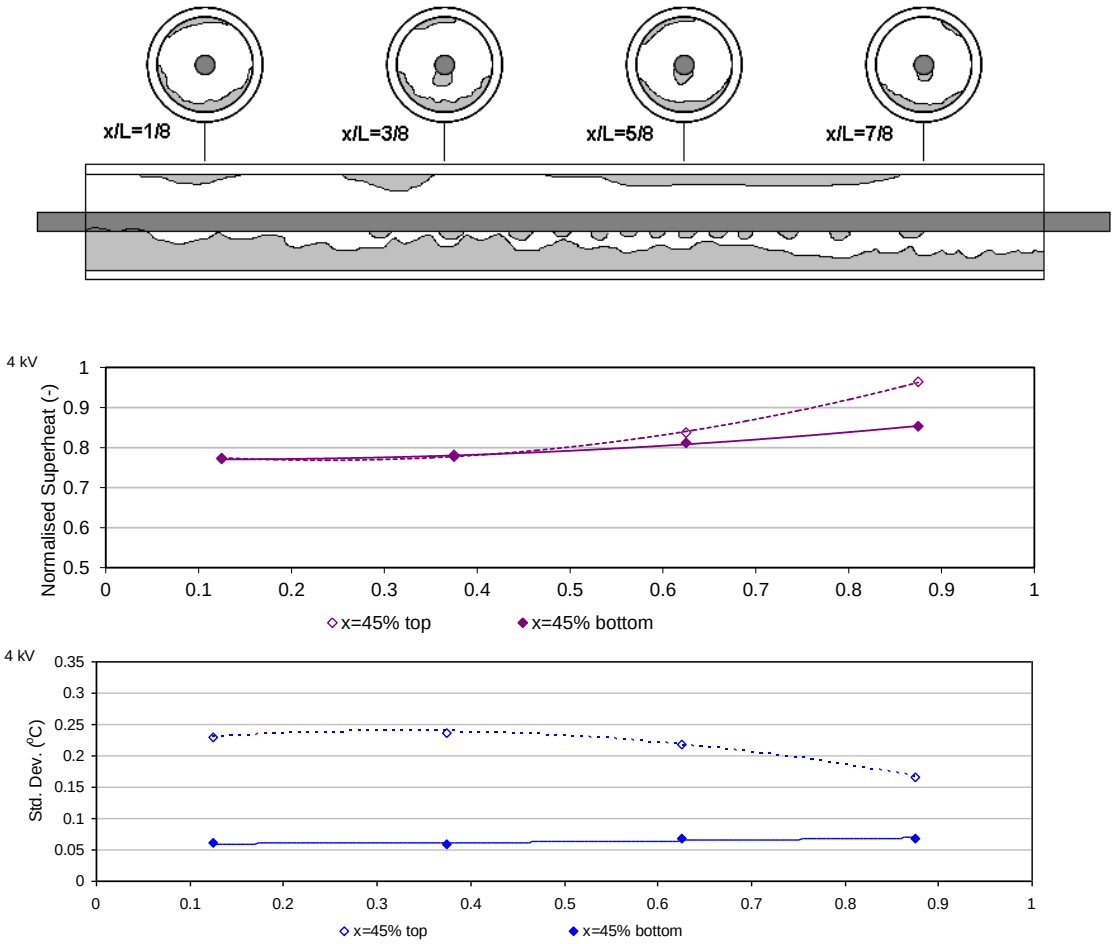

Figure 86: Sketch of flow regime with superheat standard deviations and normalised superheats for x_{in}=45%, 4 kV

The 4 kV EHD necessitates a reduction in water temperature from the 0 kV case of 48.91 °C to 48.25 °C. As seen before, the normalised bottom superheats in Figure 86

show a gradual increasing trend from 0.77 to 0.85. The top wall superheats similarly begin at 0.77 and run concurrently with the bottom until around halfway thereafter rising to 0.96 towards the end of the tube. In this case, the top wall superheats also remain closer to the bottom wall superheats than at 0 kV, indicating better wetting of the top wall with 4 kV.

The standard deviations of the bottom wall temperatures of 0.07 in Figure 86 again portray a constant liquid layer at the tube bottom. The top standard deviations however, have lowered to approximately 0.24 from the 0.30 seen with the 0 kV case, and continue to drop to 0.17 at the tube end. This indicates less temperature fluctuation, consistent with more liquid contact at the top wall, although the end of the tube still experiences higher fluctuations than found at 0 kV.

The average heat transfer coefficients rise from 1068 W/m^2K at 0 kV to 1197 W/m^2K with 4 kV. The general increase can be attributed to the redistribution of liquid all around the tube wall by the 4 kV EHD forces, whereby the additional electrical forces prolong the periodic annular events leading to all-round wetting and hence improved heat transfer. The bottom HTC remains fairly level, though the 4 kV forces may have augmented the HTCs from the field-free case by additional forces acting on the bottom liquid layer caused by the varying AC action. The top HTCs are more likely augmented initially by re-wetting of the more dry top surface of the tube, but this effect grows weaker with length and may be due to a combination of factors, namely

- The EHD effect appears less effective with increasing quality or lower liquid levels
- The higher quality with tube length lessens the available liquid for extraction and redistribution
- Increase in the top tube wall temperature promote the occurrence of dryout
- The stainless steel electrode itself may physically obstruct liquid from the lower levels reaching the top wall

4.1.6.2: Results for 8 kV

From the sketch in Figure 87 and the photographs of the 8 kV flow in Figure 85 the flow regime can be seen to be almost completely wetting and consistent along the length of the tube. Liquid and vapour velocities are high, and the liquid film is very thin. The liquid vapour interface is very wavy, and periodic annular slugs occur which transport large amounts of liquid. However this then settles to a stratified wavy flow with a wetted wall, where the liquid in contact with the upper wall possesses low velocity.

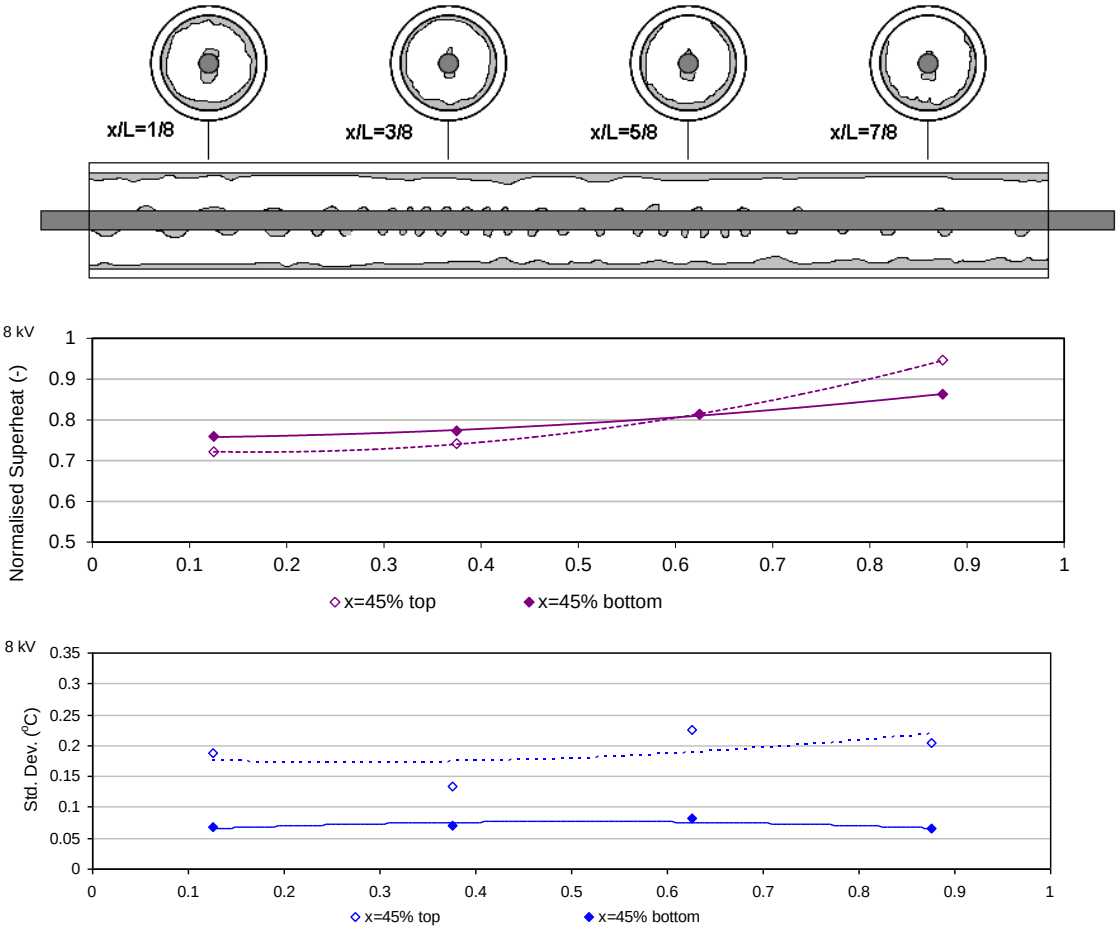

Figure 87: Sketch of flow regime with superheat standard deviations and normalised superheats for x_{in}=45%, 8 kV

Again the flow regime along the tube is quite consistent despite the quality changing from 45% at inlet to about 70% at the outlet. A thin annular film is present for much of the tube, but slowly disappears from the upper regions of the tube, as is depicted by the sketch in Figure 88. The bottom part of the tube always has a semi-circular shaped thin liquid layer that thins even more with height up the tube wall. During slug events, the

flow becomes fully annular temporarily, but gravity and dryout combine to gradually diminish the liquid presence at the tube top. Dryout in general becomes more noticeable toward the end of the test section. However dryout is not as prevalent as it was at 4 kV or at 0 kV, indicating that the EHD forces are significant enough to cause redistribution of liquid and more wetting at the top of the tube. Pulsations of liquid are noticed along the electrode, but are not strong enough to cause liquid jets or columns. The flow regime in Figure 88 might be expected to produce a high heat transfer, yet this may not be reflected in the thermo-hydraulic measurements as it may not be picked up by the instrumentation as the thin liquid film itself is not present at the thermocouple location which is at the very top of the tube and not subject to the thin liquid film witnessed.

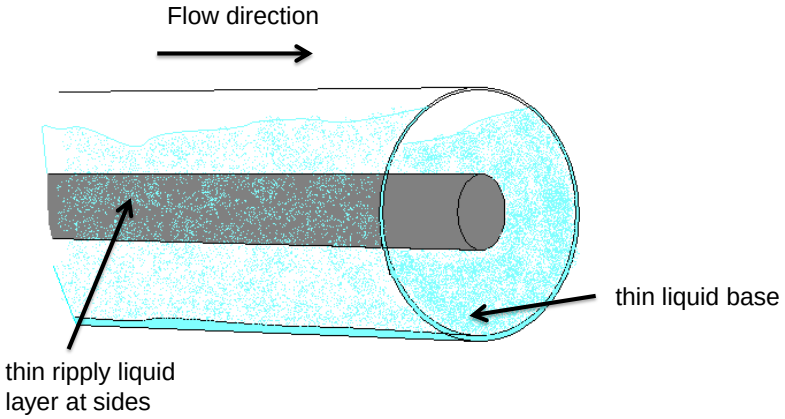

Figure 88: Typical flow regime associated with x_{in}=45% and at 8 kV

As before, to maintain Q=150 W, water inlet temperature at 8 kV dropped to 46.63 °C from 48.24 °C at 4 kV. Comparing Figure 87 with the 0 kV and 4 kV cases in Figure 60 and Figure 86, the normalised superheats reveal that the bottom superheats change little, but that the most of the change occurs along the top of the tube. Indeed, it is now evident that the top superheats initially were above the bottom superheats at 0 kV, but decreased with 4 kV and 8 kV. In the 8 kV case the lower normalised superheats range from 0.76 to 0.86, while the top superheats are much lower at the tube entrance, beginning at 0.72 and only crossing above the bottom values at x/L=⅝ and finally reaching 0.95 at the tube exit.

The standard deviations in Figure 87 show bottom values of around 0.08 while the top values remain at around 0.2 approximately. These again are consistent with a constant

liquid layer at the tube bottom and mixed wetting at the top of the tube. The standard deviations are broadly similar in magnitude to those seen at 4 kV. In general the standard deviations indicate temperature variations suggestive of intermittent wetting, and this is at odds with the video imagery which finds increased dryout at the top of the tube towards the exit. This may be due to the slight differences in sampling periods. However, the increase in superheat at the top of the tube near the exit does support the video findings.

The average HTC at 8 kV is 1400 W/m^{2}K which is an increase from an average of 1067 W/m^{2}K at 0 kV and 1197 W/m^{2}K at 4 kV. The general increase can again be attributed to the improved redistribution of liquid all around the tube wall by the stronger EHD forces associated with 8 kV. The bottom HTCs may increase due to the increased disturbance and thinning of the liquid layer by the greater forces from the 8 kV as explained above. Likewise, the top heat transfer may also benefit from more liquid redistribution and wetting of the upper wall, again caused by the oscillating AC forces of high magnitude. On the upper surface however, less wetting was seen with length along the tube due to the same reasons as found at 4 kV, diminished EHD effectiveness with lower liquid levels, less available liquid for extraction and finally, increased dryout.

4.1.6.3: Pressure drop

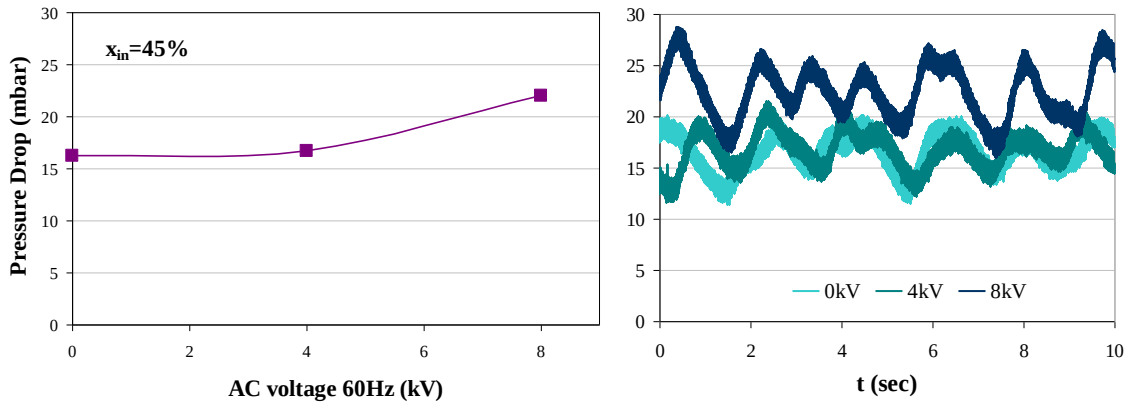

Figure 89: Averaged and real-time pressure drop, x_{in}=45%, 0, 4 and 8 kV

At x_{in}=45%, Figure 89 shows that the pressure at the field-free condition has increased from 11.59 mbar at x_{in}=30% to 16.26 mbar. This higher pressure drop is primarily due to the mass flux remaining constant while the quality has increased to 45%. This creates increased vapour and liquid velocities, giving rise to extra friction at the walls

and higher shear at the liquid/vapour interface. However, at 4 kV the effect of EHD is found to increase that pressure drop only marginally to 16.7 mbar, but 8 kV leads to a sharper increase of 22 mbar. The real-time pressure plots in Figure 89 show a similar periodicity to that at 30% except for the generally higher average pressures. These are again due to the periodic annular slug events and are composed of larger waves with an approximate frequency of between 0.5 Hz to1 Hz. A similarity in average pressure drop as well as pressure wave form is noticed between 0 and 4 kV despite the flow regimes being slightly different.

4.1.6.4: Summary

The general flow regime throughout x_{in}=45% was categorised as stratified wavy with periodic annular slugs. Liquid and vapour velocities were high, and the liquid/vapour interfaces were rippled and wavy. Nucleate boiling was minimal. EHD voltage did produce heat transfer augmentation most noticeably by promoting wetting of the top surface of the tube by fluid redistribution which prolonged the wetting events creating an artificial or induced annular flow along much of the tube. Higher EHD voltage produced increases in heat transfer but caused higher pressure drop. Despite the EHD enhancement effects of 4 kV and 8 kV compared to the field free case at 45%, the enhancement factor was noticed to decrease steadily with increasing inlet quality.

This may be a function of several inter-related phenomena within the test section, but the primary reason is suspected to be due to the decrease in the amount of liquid. As inlet quality increases, the amount of vapour increases and consequently the liquid amount drops. Therefore, the drop in liquid levels may serve to lessen the amount of liquid previously available for redistribution further from the central electrode. In addition, as quality increases, the flow regimes depart from the predominantly stratified type patterns to more annular type patterns. This progressive change in flow regime has the effect of diverting liquid away from the influence of the central electrode where electrical fields are strongest [6, 75].

4.1.7: Summary of Section 4.1

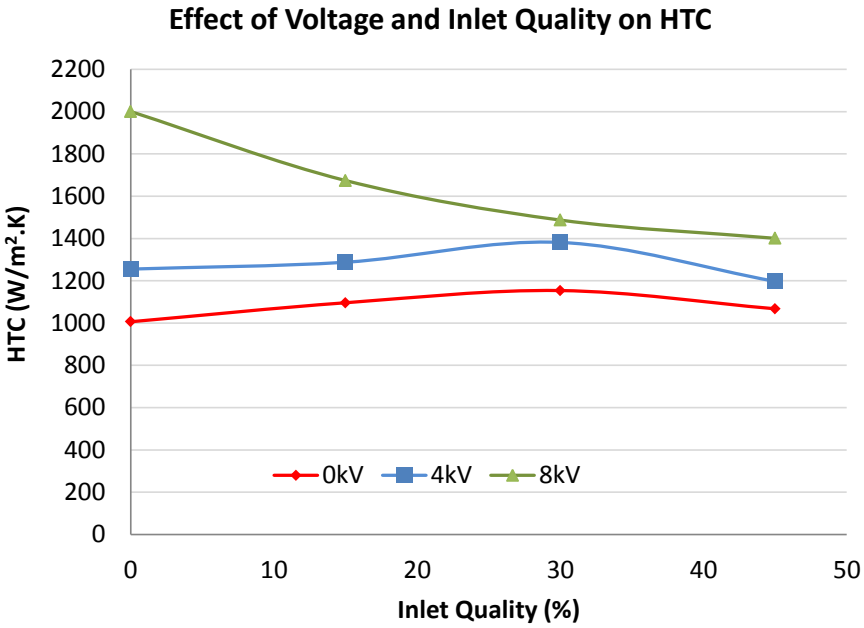

Figure 90: Effect of voltage and inlet quality on averaged HTCs (x_{in}=2-45%)

An overall view of the test results is shown in Figure 90. For the field-free case (0 kV) the general increase in HTC with inlet quality up to x_{in}=30% and subsequent decrease is purely dependent on conventional liquid/vapour forces within the tube. The addition of 4 kV is seen to augment this basic pattern, where the 4 kV force initially assists heat transfer by acting on the bubbles at lower quality. This augmentation process then changes as the EHD forces initiate a radical departure in the stratified layer flow regime to the "attracted curtain" flow pattern and to the wavy thin film type flows. As quality increases, the 4 kV EHD force precipitates a flow regime change to an "induced annular" type of flow which is responsible for a further increase in heat transfer. At a quality of 45%, a drop in heat transfer is noticed as the amount of liquid available for redistribution is less, and dryout along the upper tube becomes more prevalent.

At 8 kV EHD voltage, the flow regime at low quality experiences large changes in bubble activity, especially growth phenomena, oscillations and wiping, as well as coalescence and climbing causing wetting of the tube top which all contribute to deliver high HTCs at the tube top and bottom. Liquid jets are also a feature of these high EHD voltages and contribute to the redistribution of fluid. As inlet quality increases however, the amount of liquid available is seen to decrease, and nucleation also lessens,

but the high EHD forces effectively assists in redistribution of liquid from the bottom layer to wet the top of the tube, again creating an "induced annular flow". As quality increases further, this redistribution effect reduced in effectiveness because of the increased visibility of dryout conditions at the tube top. The amount of nucleate boiling decreases with applied voltages of 4 kV and further with 8 kV. However, in order to maintain constant heat flux as EHD was applied, the water inlet temperature had to be reduced. Therefore, the apparent suppression of nucleation by the EHD voltages may be in part due to the lowered superheats along the tube wall.

4.1.8: Assessing EHD enhancement and penalty

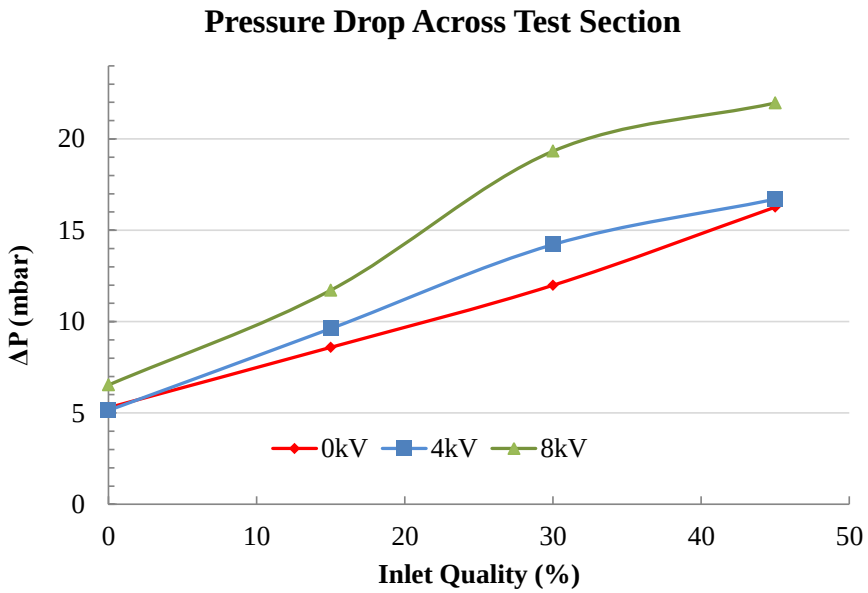

Figure 91: Pressure drop with voltage plotted against quality for x_{in} =0-45%

The effect of EHD forces on pressure drop is summarised in Figure 91. In field-free conditions (0 kV) the pressure drop rises in a linear trend with inlet quality. With the application of 4 kV and 8 kV, pressure drop also increases linearly initially and at a sharper rate, however at 45% the increase in pressure drop tails off at both 4 and 8 kV. Pressure drop clearly increases with EHD, but not in direct proportion to voltage magnitude. A substantially greater penalty is seen with 8 kV where the average pressure penalty factor is 1.38 compared to 4 kV with an average pressure penalty factor of 1.07. A fluctuating pressure field is apparent at all test conditions except for 2% inlet quality at 8 kV, where the pressure drop along the test section does not

fluctuate with time. At this regime, an oscillating bubble regime is present without either periodic slugs or annular slugs found in other regimes.

As mentioned earlier, a shortcoming of altering the water inlet temperature to maintain a fixed Q (150 W) across the test section was the reduction in wall superheats. While the higher heat transfer coefficients in themselves are a true indicator of EHD enhancement, this forced lowering in water inlet temperature in effect created another variable in the test section, that of changing superheat. This may affect bubble nucleation and dryout.

Consequently it was decided to perform another series of tests with inlet water temperature fixed. All changes in flow, including nucleation, would thus be more dependent on EHD forces and independent of a changing wall superheat. This test series maintained one inlet quality of x_{in}=2%, and attempted to determine the precise nature of the EHD effect on the bubble dynamics and how the transition from bubbly stratified evolves to the oscillating bubble regime. The tests were carried out in a more incremental manner, by testing at finer voltage intervals of 1 kV up to 10 kV rather than at 4 kV intervals. This facilitated investigation of the impact of gradual increases in voltage so as to better determine the series of flow changes seen in Chapter 4.1 and 4.2, from stratified wavy flow, on to the oscillating bubble regime, and beyond that to the transition regime.

4.2: Heat Transfer Augmentation at Constant Inlet Temperature – Experimental Results and Discussion

In the previous section, a study on EHD was performed with a constant heat input of 150 W across the test section. However, as voltage was increased, the water inlet temperature had to be reduced in order to maintain a fixed value of 150 W due to the enhancement of EHD. While this demonstrated the efficacy of EHD in itself and is consistent with past methodologies [4, 7, 9, 12, 47, 58, 60, 73-76, 79, 85, 87], it is not possible to define the true enhancement by comparing in watts, the heat transfer increase with EHD with the associated power penalties. Furthermore, maintaining the constant heat transfer between tests by reducing the water temperature ostensibly reduces the wall superheat which may have some influence on the flow regimes and nucleation characteristics.

Consequently, this stage of tests again examine the effects of voltage on heat transfer coefficient but this time under a constant water inlet temperature between tests. In effect this means that the wall superheat is approximately the same for each test. This also means that changes across the test section such as Q, ΔP and heat transfer coefficient would be solely EHD influenced and not a result of changing superheat. For these tests the inlet quality was maintained at x_{in}=2% as this low quality demonstrated the largest influence on the heat transfer enhancement in the previous tests. EHD forces are also expected to be of greater significance at lower qualities due to lower inertial forces in the fluid. Also by investigating a single inlet quality it is feasible to test more resolved voltage increments. To this end, the applied voltage was increased in 1 kV increments from 0 to 10 kV rather than the 0, 4 and 8 kV steps of earlier tests. In this way these tests are better suited to determining the precise nature of the EHD effect on the bubble dynamics and how the change from bubbly stratified flow evolves to the oscillating bubble regime and so forth. Q_{TOT} was monitored and found to increase from 150 W at 0 kV to 230 W at 10 kV.

High speed images were recorded but only those at the approximate midpoint, x/L=⅜, will be discussed so as to focus on the small changes occurring in the flow at a region

which can be considered representative of the test section. It should be noted that local heat transfer along the test section will be the topic of the next subsection of this chapter. As this location was upstream from the inlet, the quality was approximately x=12%. During these tests, an improved new high speed camera was available giving significantly higher quality images and faster video resolution (3000 frames/second) thus providing more clarity for discussing the flow phenomena.

For the first test at 0 kV, the inlet water temperature required to sustain an average test section heat flux of 12.4 kW/m^2 (or 150 W across the test section) was set. This water inlet temperature was then kept constant and EHD voltage increased incrementally while the heat transfer was allowed to change in response to the flow field changes enacted by the EHD forces. The heat transfer gained will subsequently be related to the hydraulic and electrical power in order to gauge the true level of enhancement by comparing rewards versus penalties.

4.2.1: Overview of Results at Constant Inlet Temperature

During these tests, the water inlet temperature to the test section was maintained at 48.45 °C, which is that which provides an average heat flux of 12.4 kW/m^2 or 150 W across the test section under field-free conditions. This water temperature results in a nearly constant wall superheat of 11.5 °C ±1 °C for all of the voltage levels tested. Figure 92 shows the inlet temperature profile measured over the entire range of voltages tested. Temperature fluctuations of the water inlet were less than ±0.1 °C. However greater fluctuations in refrigerant saturation temperature are seen, but it remains between 34.27 °C and 33.74 °C.

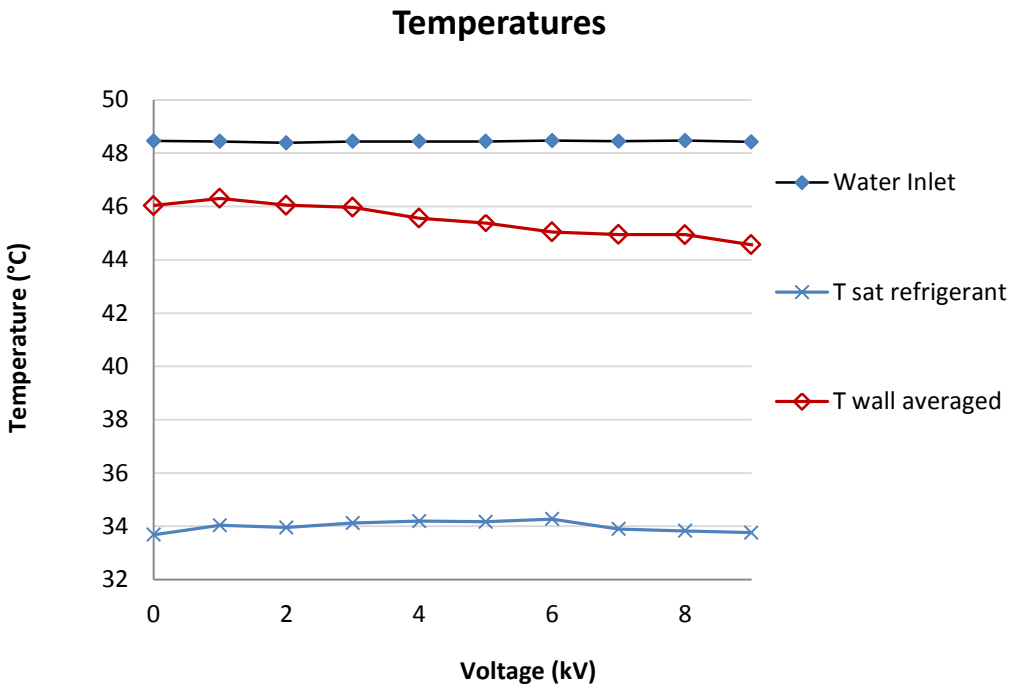

Figure 92: Constant water inlet temperature

A larger decrease in average wall temperature of 1.82°C also occurs, however this is due to the reduction in wall temperatures associated with higher heat transfer across the test section as EHD voltages were increased. System pressures at the exit of heat exchanger 1 (HEX1) were at 1.04 ± 0.03 bar while the pressure at the test section inlet remained at 1.00 ± 0.03bar.

4.2.2: Field-free thermal hydraulics

The field-free flow pattern is depicted in Figure 93 and is classified here as stratified wavy with vigorous nucleate boiling in the lower stratified layer. A sketched representation is given in Figure 94(i). The bottom surface is continually wetted and bubbles are observed to grow and detach and be carried within the moving liquid. Gradual coalescence of detached bubbles within the stratified liquid layer was observed and these larger coalesced bubbles gather at the liquid vapour interface of the stratum and thereafter burst. Some of the larger bubbles attach to the tube sides near where the liquid-vapour interface intersects the wall, presumably due to the presence of the electrode which is partially submersed in the liquid layer at this low vapour quality. These attached bubbles travel much slower compared to the smaller bubbles being

carried within the bulk of the liquid layer due to the higher resistance of the contact region and the lower liquid velocities near the wall due to the no-slip condition.

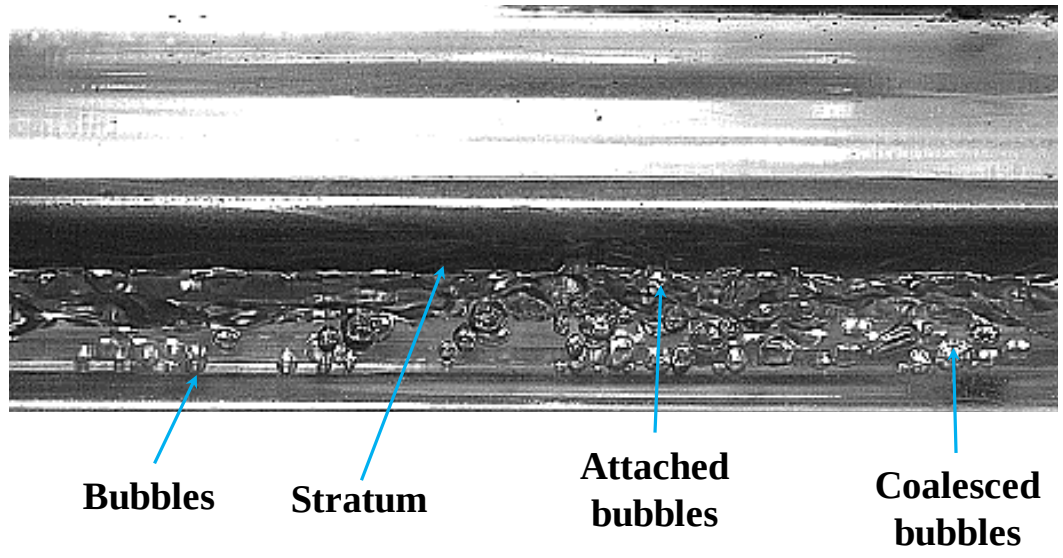

Figure 93: Picture of flow pattern at x/L=⅜ for field-free case of V=0 kV.

The bottom wall is thus continually wetted and this is evident from the nearly constant wall superheat as indicated by a low standard deviation as seen in Figure 96(b). Standard deviations in the region of 0.05 °C are indicative of a uniform temperature.

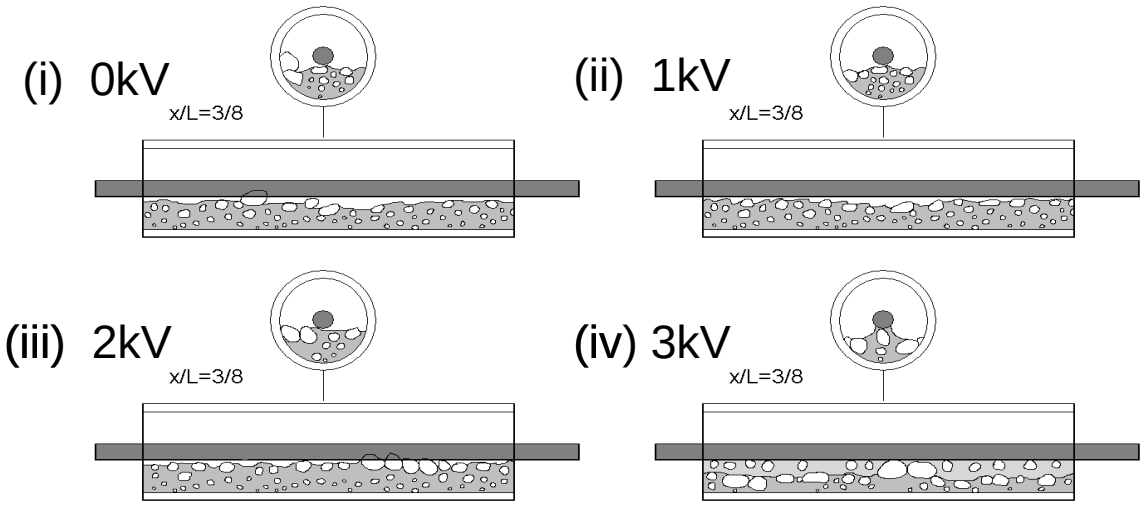

Figure 94: Sketches of flow pattern at x/L=⅜ for voltage range of 0 kV-3 kV of Region (i).

Although not shown in the sketches for clarity, the occasional occurrence of liquid bridging events which periodically rewet the top surface of the tube are a key mechanism of heat transfer. These occur because the flow regime is a transitional one between stratified wavy and slug flow as previously discussed. Figure 95 shows a sequence of one a typical slug event. The slugs are preceded by a period of stratified flow with a wetted lower region and a dry upper region. As the front of the slug advances, the flow is of an agitated high speed wave. As it passes through the viewing section, the slug becomes more annular in form with rigorous nucleation all round the tube. As the wave subsides, velocities decrease but the upper half of the tube remains highly wetted and some nucleation is observed in the liquid film. Subsequent to this, a stratified flow is once again re-established and the liquid film remaining on the tube upper section evaporates.

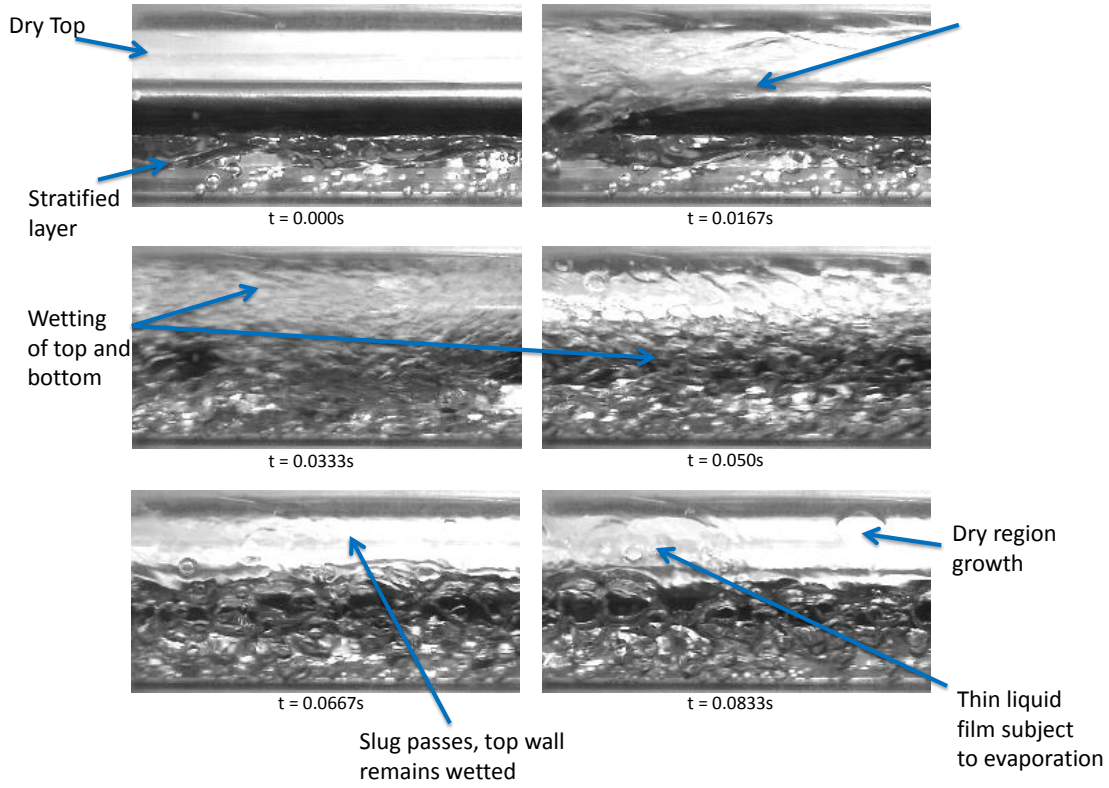

Figure 95: Slug event and its effect on tube wetting

The periodic wetting of the top surface occurred at an approximate frequency of 1.2 Hz and resulted in notable variations in the top wall superheat as is evident from the much higher top wall superheat standard deviation given in Figure 96 (b).

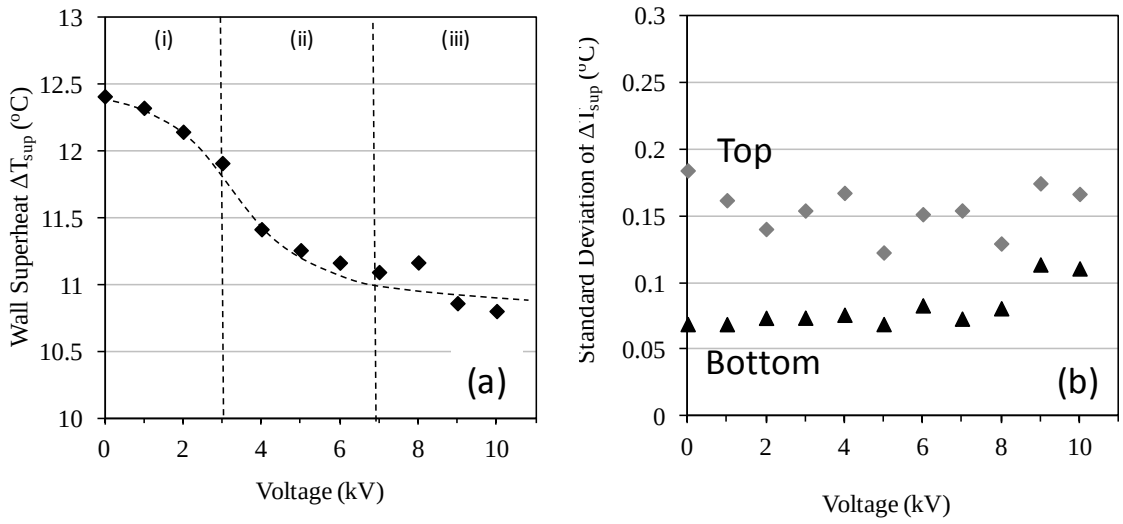

Figure 96: (a) Average wall superheat and (b) average superheat standard deviation versus applied voltage.

The frequency of the top wetting events observed in the video footage corresponds well with the temperature variations found from the high speed thermocouple traces (see Figure 97) of the top tube wall which also had an approximate frequency of 1.2 Hz.

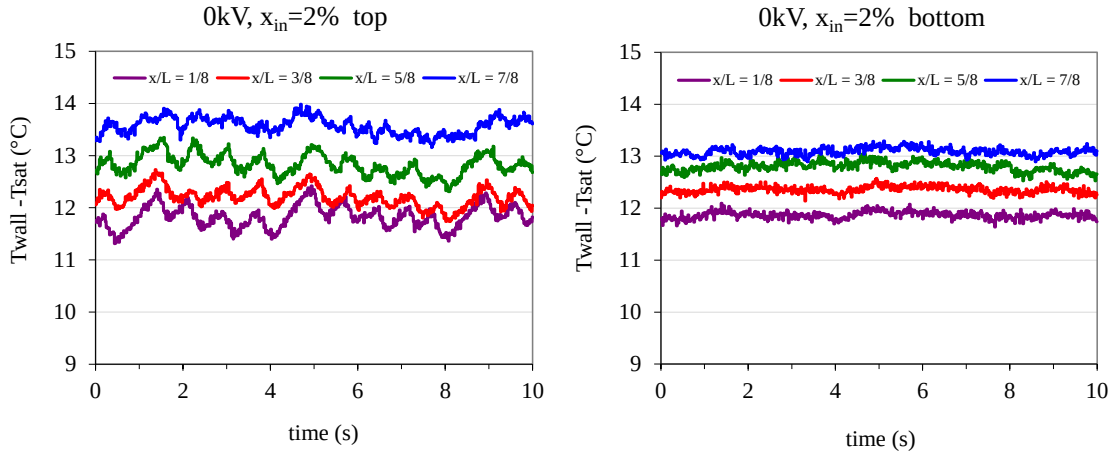

Figure 97: Superheat temperature traces of top and bottom walls

The primary mode of heat transfer in the stratified layer is convective boiling in the liquid stratum. The upper portion of the tube is alternately wet and dry because of the liquid bridging events, leading to the heat transfer in this region being evaporation of the subsequent liquid film followed by forced convective heat transfer to the vapour phase. Figure 98 shows that the average heat flux was 12.72 kW/m^2 which equated to 153 W of heat transferred to the refrigerant. The corresponding pressure drop was 7.06 mbar.

4.2.3: EHD-augmented thermal hydraulics

While maintaining a relatively constant wall superheat, 60 Hz AC EHD voltage was then applied in 1 kV steps up to 10 kV. The average heat flux to the refrigerant increases with voltage in an approximate "S" shape curve which for convenience is divided into three regions; Region (i), (ii) and (iii) as shown in Figure 98(a). Upon initial increase in the applied AC voltage the average heat flux to the refrigerant increases marginally until around 3 kV, which is considered to mark the end of Region (i). Thereafter the heat transfer increases more sharply until around 7 kV thus ending Region (ii), after which the rate of increase becomes marginally less for Region (iii). The pressure drop versus EHD voltage trend shown in Figure 98(b) is similar indicating a correspondence between the two. As will be discussed, due to increased liquid contact with the heated tube surface along with increased agitation within the liquid phase, the increased heat transfer rates are expected. However, the increased liquid to wall contact as well as liquid contact with the electrode creates more fluid friction, while in-tube acceleration of vapour together contribute to the increased pressure drop.

Subsequent analysis of the high speed videos identified three different prevailing flow regimes for Regions (i), (ii) and (iii) and the salient features of each are shown in Figure 94, Figure 100 and Figure 105 for location x/L=3/8, and will be discussed in turn.

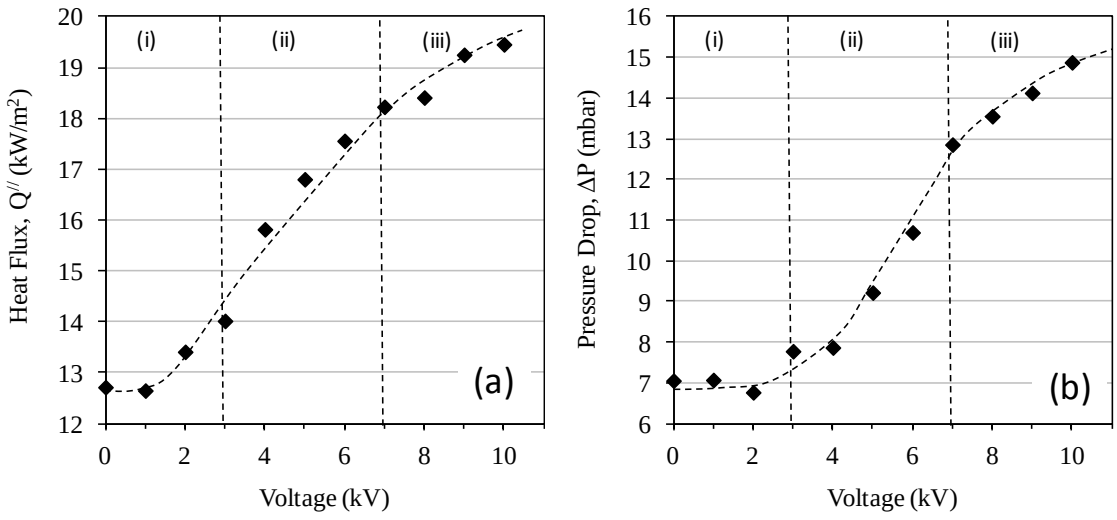

Figure 98: Variation of average heat flux (left) and pressure drop (right) across test section versus applied voltage.

The flow regimes of Region (i) are sketched in Figure 94. It is identified as a transition regime between stratified-wavy and slug flow as described earlier, and is the dominant flow pattern in Region (i). With increasing applied voltage to 2 kV little difference is observed in the base flow regime compared with the field-free case and this is depicted in Figure 94(iii). Even still, close inspection of the video footage reveals some small differences in the flow regime at an applied voltage of 2 kV indicating that the electric field is beginning to have an influence on the flow dynamics. It is observed that the diameters of the bubbles near the vapour-liquid interface have generally increased. Coalescence of bubbles plays a large role in this, both in the enlargement of the bubbles rising to the surface, and again when the bubbles form a series of regular spherical bubbles near the interface, where they subsequently coalesce and form large unstable oblong bubbles which rise higher up the tube wall and burst. Faint alternate oscillations of these larger bubbles were also noticed as a result of the interaction with the AC electric field. In Figure 98 the influence of EHD on the heat transfer and pressure drop at V=2 kV is small yet becoming apparent. Figure 96 shows that the average wall superheat has begun to drop, indicative of improved cooling by the tube side refrigerant since the water-side thermal resistance is unchanged. The sketch in Figure 94(iv) illustrates what can be considered a marked difference in flow regime when the voltage was increased to 3 kV and this point is considered the transition point between Regions (i) and (ii). The bubble diameters are notably larger and oscillations and deformations of the bubbles are far more pronounced.

Another interesting feature which differentiates this flow regime from the field-free case is the attraction of the liquid layer to the central electrode. This is termed the liquid extraction phenomenon. The attracted curtain of liquid is discernible by virtue of a lower stratum height at the tube wall and visible translation and oscillation of bubbles within the central portion of liquid. The lowered three-phase contact line is depicted in Figure 94(iv), along with the bubbles entrained in the central curtain of liquid.

Despite that fact that the AC voltage is oscillating at 60Hz, the liquid curtain itself does not appear subject to any oscillating displacement, remaining attracted to the electrode throughout. However, the bubbles within the liquid stratum, whether in the liquid curtain or at the outer wall, are clearly affected by the alternating EHD forces and are seen to oscillate and change shape in response to AC electric field. From Figure 96 the

bottom surface is still completely wetted as indicated by the low standard deviation and the wall superheat has decreased. The periodic bridging events still occur similar to the field-free case and this being the case the top wall superheat standard deviation is still higher than for the bottom wall though not notably different than that of the field-free case. It is clear that the occurrence of this flow regime is atypical and unique to EHD augmented two phase flow. Importantly, Figure 98(a) shows that the heat transfer begins to notably improve.

The 5 kV case is representative of the prevailing flow regime for Region (ii) which is associated with a steep increase in rate of rise of both the heat transfer and the pressure drop as shown in Figure 98.

At 5 kV, several distinct changes to the field-free flow regime are observed. The flow regime is depicted in Figure 99 and shown schematically in Figure 100. As is shown in the figures the base flow regime remains stratified wavy, and still features periodic wetting events of the top and side walls, though of a different nature than the bridging events of the field-free case.

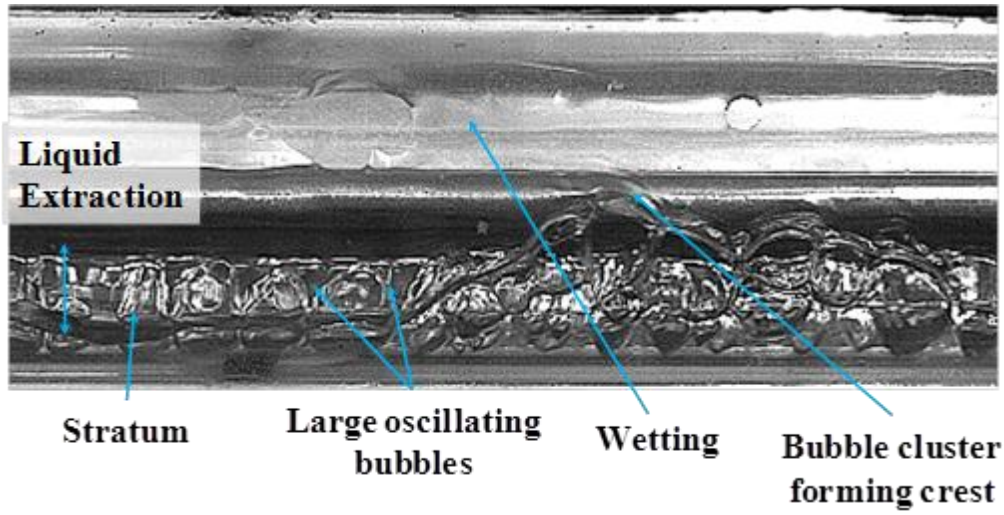

Figure 99: Picture of flow pattern at x/L=⅜ for V=5 kV

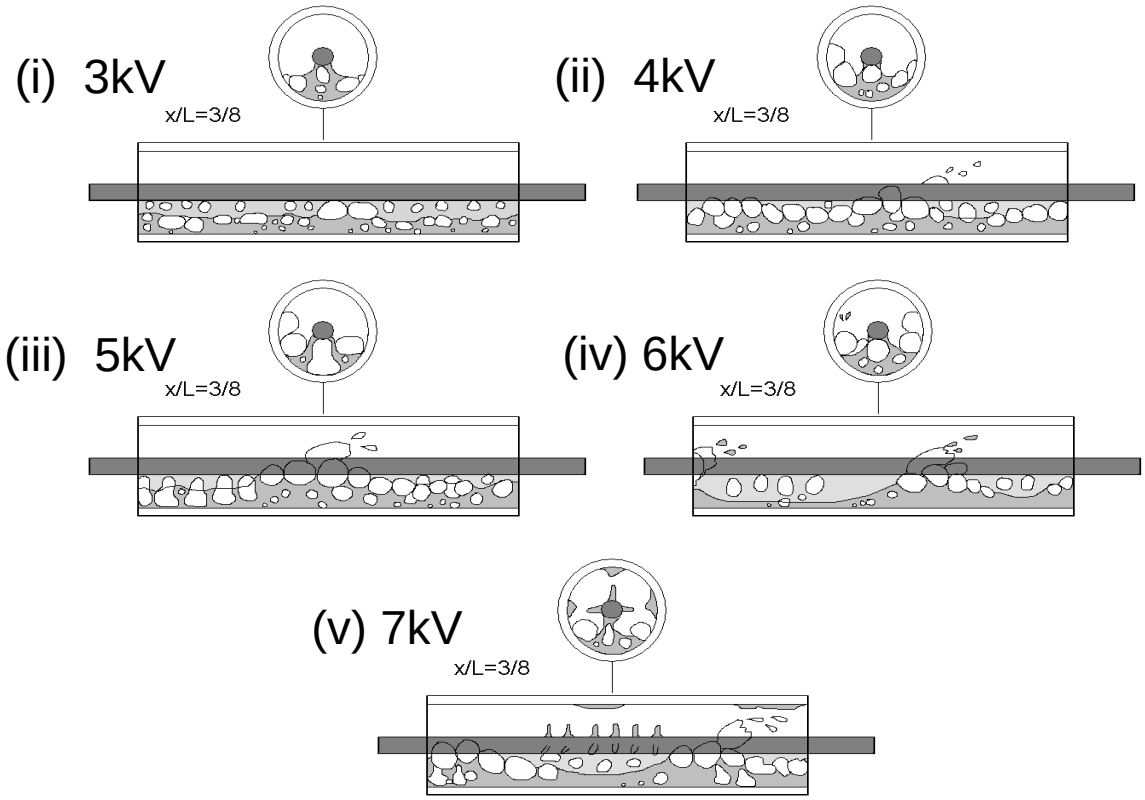

Figure 100: Sketches of flow pattern at x/L=⅜ for voltage range of 3 kV-7 kV of Region (ii).

A curtain of liquid is now drawn from the liquid layer towards the electrode by the EHD forces. In addition, nucleated bubbles oscillate strongly within the liquid layer and seem to be retained within the liquid layer by the EHD forces preventing them from rising to the surface and breaking through. This leads to coalescence with other bubbles also held within the stratum. These larger bubbles then oscillate transversely to the flow at a frequency of 120 Hz. This is double the frequency of the applied AC voltage which indicates that the bubbles are responding to the 'on-off' nature of the electric field. The large oscillating bubbles group together and cluster along the tube side wall forming crests which climb up the side walls before bursting. The crests are able to reach the top surface before being swept into the vapour flow. A time sequence series of images showing one such event is shown in Figure 101.

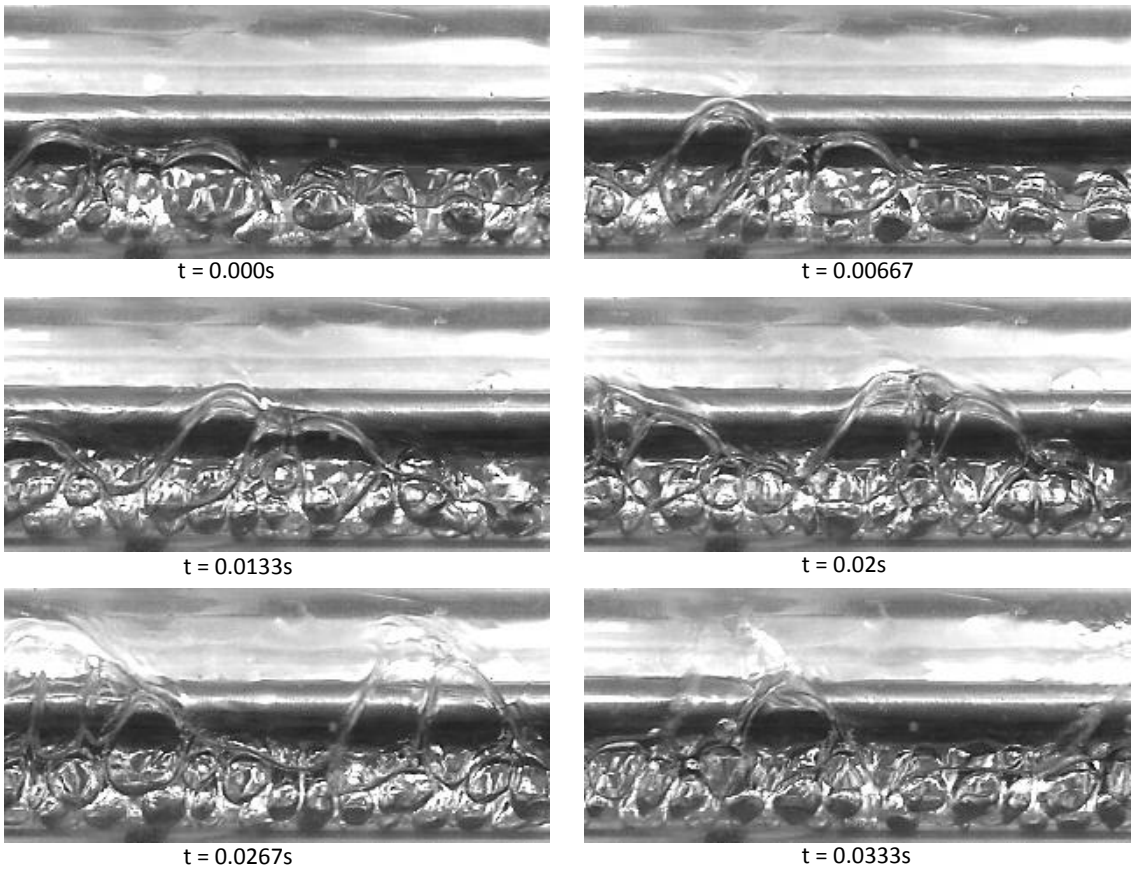

Figure 101: Time sequenced images of bubble coalescence and cresting event occurring at 4 kV

In this sequence a progressive coalescence of several bubbles is witnessed, which build on each other and the phenomenon of "cresting" takes place. This culminates in the bubble touching the top wall as seen at t=0.0267s after which the bubbles burst. An incipient crest is also seen to develop at t=0.02s and this also cause top wetting before collapse as shown at t=0.0333s. This cresting of bubbles is not witnessed in field-free cases and the conditions for the growth and cresting of such bubbles is thought to be strongly dependent on the EHD force between the electrode and the bubbles themselves. In this study, although the EHD voltage is sinusoidal (60Hz AC) bubble oscillation has been observed to be double this frequency. Therefore the EHD force may be surmised to act at double the AC frequency in this case (see Figure 102). From the second term in equation (74) this suggests that the dominant force acting on the bubble is dielectrophoretic as proposed by Cotton et al [85].

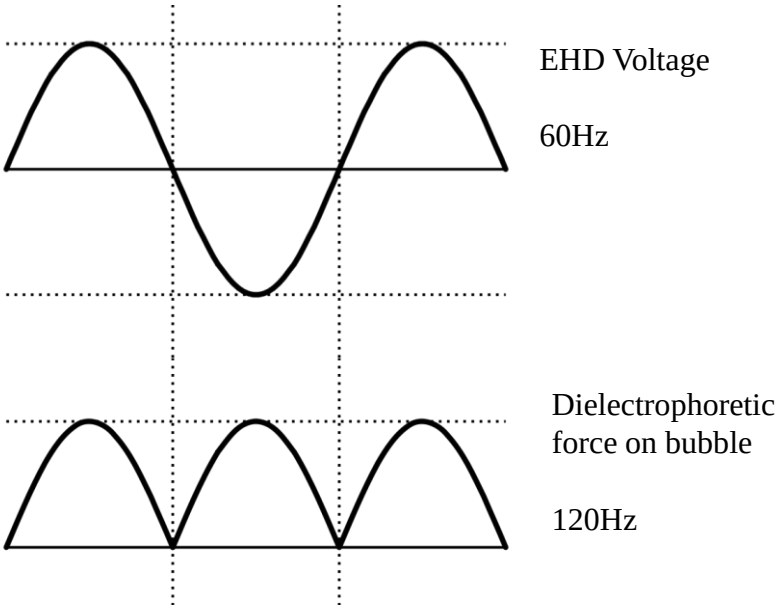

Figure 102: Nature of dielectric force acting on bubble within the liquid layer

If one considers this force acting perpendicularly downward from the electrode, the result is that the EHD force suppresses the rising of the bubble in such a way as it dominates over the buoyancy force. This is in line with recent findings by Siedel et al. [88]. who found that the electrohydrodynamic force reduced the terminal velocity of a free rising bubble. In addition Di Bari and Robinson [89] also showed that the direction of the EHD force is downwardly directed. However, once a bubble strays from directly under the electrode to either right or left of centre, due to the circular geometry of the electrode the EHD force may no longer be directly downward in nature though would still be radially outward forcing the bubbles towards the tube. As such, the resultant vertical component of the EHD forces on the bubble would at some point become less than the buoyancy force thus permitting the bubble to rise.

In the video sequences studied, this pattern of bubble travel has been witnessed, from being held and suppressed under the electrode, then migration from under the electrode to being pressed radially outward against the tube wall, and finally in rising to the free surface. It is at this point that coalescence with other bubbles occurs forming the large bubbles which create the cresting events described. This migration and cresting of bubbles serves to wet the upper tube walls, either via direct wetting because of bubble sliding, or by flinging of liquid against the upper tube and into the vapour core as the

bubbles burst. The presence of this liquid layer enhances heat transfer through both convection and also via post wetting evaporation.

The net effect is that the bubbles within the stratum oscillate, become expelled from under the electrode, and then coalesce and cluster which contributes to further wetting of the side and upper portions of the tube and partially accounts for the increased heat transfer due to film evaporation.

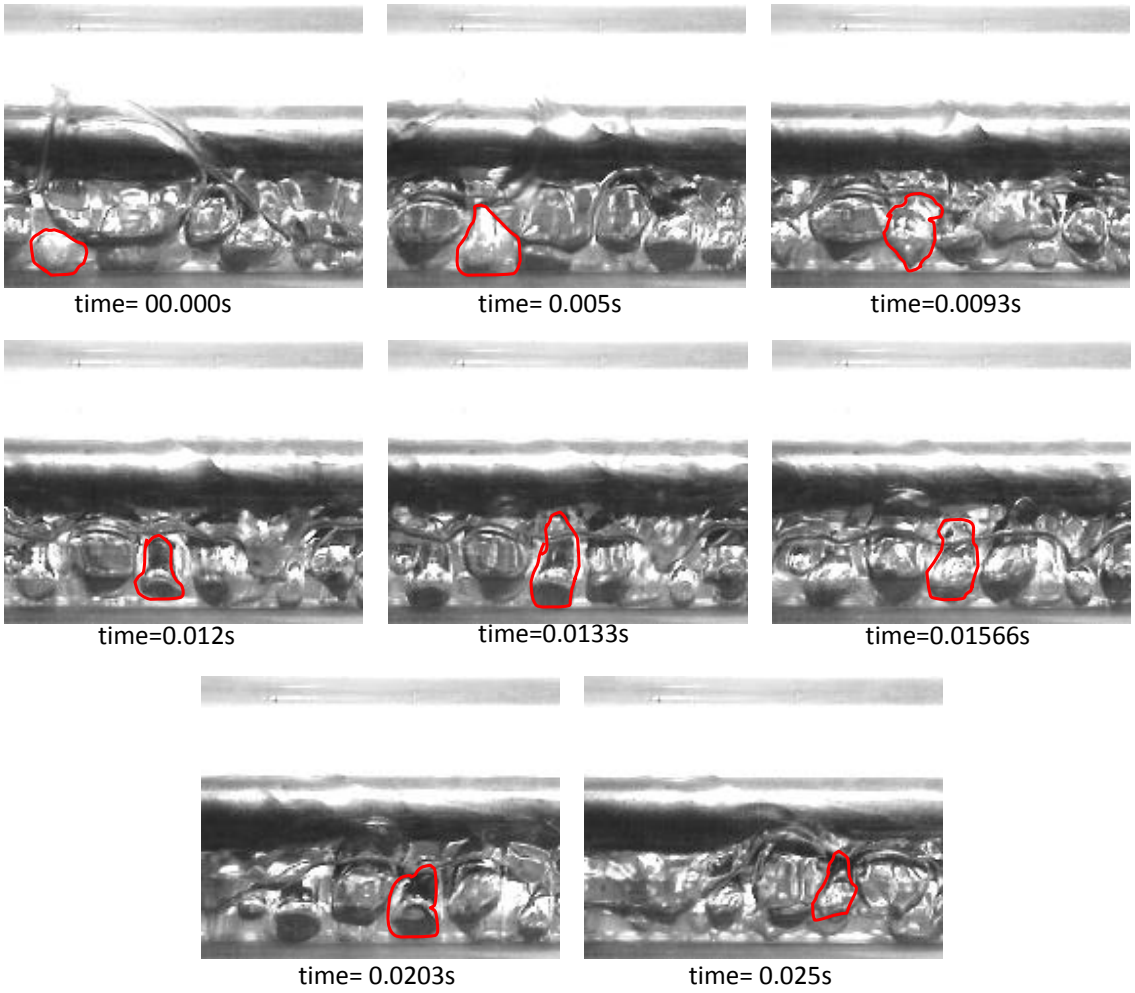

Figure 103: Bubble distortion and bouncing along bottom liquid layer

Likewise, the same oscillating bubble phenomena act within the liquid stratum to enhance the heat transfer in the lower region also. The same mechanism of bubbles being held within the stratum by EHD forces is again consistent with the recent investigations of Di Bari and Robinson [89] and Siedel et al. [88]. The liquid extraction to the electrode which thins the lower liquid layer in combination with the

agitation and disturbance of the liquid layer by the large oscillating bubbles most likely improves convective heat transfer. A video sequence is given in Fig. 101 where the motion and shape of one bubble is represented. Although it is difficult to show this precisely without the aid of the actual video, the picture does illustrate that the bubble not only oscillates in a direction transverse to the flow, but its shape is also severely distorted, likely due to a combination of electric field and hydrodynamic forces. The end result is increased liquid agitation within the stratified layer and enhanced heat transfer.

The pressure drop is affected in two ways; firstly, liquid re-distribution, where the electrode and tube walls are now in greater contact with the liquid, creates an increased pressure drop due to frictional forces and secondly, the velocity change of the fluid as it accelerates requires additional energy which, in turn causes the pressure drop to escalate with applied voltage, as is evident in Figure 98(b).

As the applied voltage level is further increased to 6 kV the flow pattern is fundamentally the same but with some differences which highlight the stronger influence that the electric field is having on the flow. Clustering and coalescence of vapour bubbles is once more observed at the side wall. These bubble clusters climb the side wall until at a certain height they form crests and are carried over by the higher velocity vapour phase. This has the effect of destroying the stacked bubble clusters which subsequently entrains the remaining liquid into the upper vapour region as before causing wetting of the top surface.

Figure 98(a) clearly shows that the EHD augmented flow regime of Region (ii) significantly improves the heat transfer and the improvement increases with the applied voltage level. The heat flux increases with increasing electric field strength and this, together with the decreasing wall superheat shown in Figure 96, indicates a lower thermal resistance to heat transfer. Evidently the bubble dynamics in the lower liquid layer and the wetting mechanisms for the top surface improve the heat transfer from the wall. At 7 kV a new type of flow structure appears and is considered the transition from Region (ii) to Region (iii) and will be discussed below.

At approximately 7 kV, a flow regime transition occurs once again. The main features of this flow regime are illustrated in Figure 104 and Figure 105. The flow regime tends to fluctuate between a flow regime similar to that of Region (ii) i.e. large oscillating bubbles with a liquid curtain drawn to the electrode, and a regime whereby a liquid film covers the electrode from which liquid jets or spouts protrude out radially and spray the walls. There is clear indication of liquid films and droplets on the top surface as well. This forms the predominant flow regimes for applied voltages in Region (ii) which exists between 7 kV and 10 kV.

As stated, the base flow regime is composed of two alternating flow patterns that cycle between large oscillating bubbles and a thin film regime which features liquid jets. The oscillating bubble regime is an extension of the previous regime, but now the EHD forces are sufficiently strong to cause large scale enlargement and elongation of the bubbles. The bursting of these bubbles along with the liquid jets cause considerable droplet entrainment into the vapour core. The sketches in Figure 105 (i) and (ii) shows the flow features observed at 7 kV and 8 kV respectively.

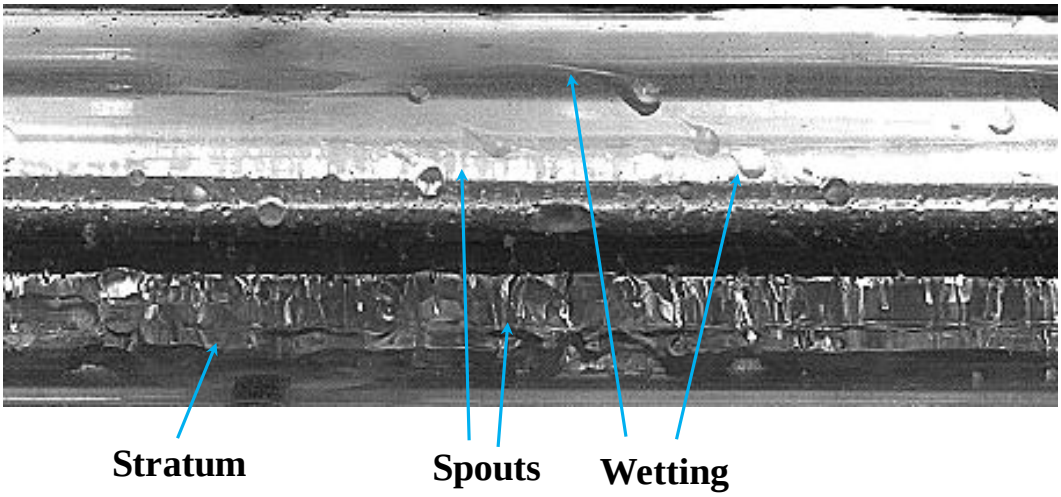

Figure 104: Picture of flow pattern at x/L=⅜ for V=10 kV.

As the applied voltage is increased the thin film regime with the spraying jets tends to have a longer resident time compared with the oscillating bubble regime. The oscillating bubble regime is preceded by liquid bridging events which eventually settles back to the thin film regime. During this phase, nucleation is observed at discrete nucleation sites on the bottom of the tube where bubble growth is very rapid and the

bubbles expand to very large bubble sizes. Clustering and bridging of these bubbles causes wetting of the top of the tube. Bubble clusters that do not climb to the top of the tube often burst and expel liquid droplets into the vapour stream which also contribute to the wetting of the top of the tube.

As the voltage increases to 9 kV and 10 kV the influence of EHD is observed to increase. Figure 105(iii) and (iv) are renderings of the flow patterns for 9 kV and 10 kV respectively and a still photo of the 10 kV case is given in Figure 104. Even still, flow conditions can be divided into two alternating "thin film" and "oscillating bubble" regimes. As the applied voltage is increased the liquid spouts are noticed to be greater in number but smaller in size. Despite the increase in the number of jets, the height reached above the electrode is relatively unchanged. In contrast with lower voltage levels, more wetting of the side wall is observed, presumably due to the radial expulsion of liquid from the jets. In other respects, the flow at 10 kV could be classed as thin film flow with occasional liquid bridging events.

The wall superheat and standard deviations given in Figure 96 clearly demarcate Region (ii) from Region (iii). It is first noticed that the standard deviation of the bottom wall begins to increase in Region (iii). This may be due to the alternating nature of the flow whereby the mechanism of heat transfer alternates between that of forced convection to thin film evaporation. On the other hand, the standard deviation of the top wall remains high which is indicative of intermittent wetting and drying.

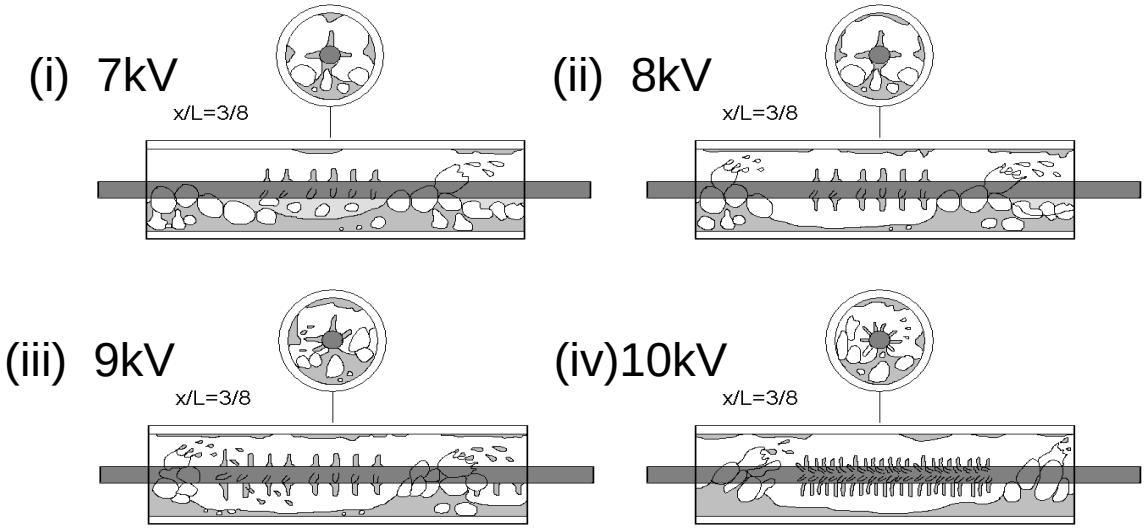

Figure 105: Sketches of flow pattern at x/L=⅜ for voltage range of 7 kV-10 kV of Region (ii).

Figure 96 also indicates that although the wall superheat still decreases with increased voltage, the rate at which it decreases appears to diminish. This may hint to the possibility that the influence of EHD on the flow regime is such that the jetting regime is gaining prominence over the oscillating bubble regime and thus the mechanisms of heat transfer are different. This hypothesis is confirmed when considering Figure 98(a) where it appears that rate of increase of the average heat flux with applied voltage is diminishing. Even still, increased liquid contact with the electrode and tube wall leads to increased friction and thus pressure drop, as shown in Figure 98(b). This coupled with flow acceleration leads to a higher pressure drop, albeit at a lower rate than witnessed in Region (ii).

4.2.4: EHD Enhancement

The average heat transfer coefficient of the test section for voltages from 0 kV to 10 kV is shown in Figure 106(a). This curve again follows an approximate "S" shaped trend, where at low voltages (0-3 kV) the heat transfer coefficients vary from 1024 W/m^{2}K to 1176 W/m^{2}K. The sharpest rise occurs from 3 kV to 7 kV, where the heat transfer coefficients jump from 1176 W/m^{2}K to 1643 W/m^{2}K. Beyond 7 kV the heat transfer coefficient values increase from 1643 W/m^{2}K up to 1801 W/m^{2}K at 10 kV. The "S" shaped trend is of course expected since the wall superheats have varied little from 10.7 °C to 12.4 °C as shown in Figure 96(a) while the heat transfer to the refrigerant increases with applied voltage as seen in Figure 98(a).

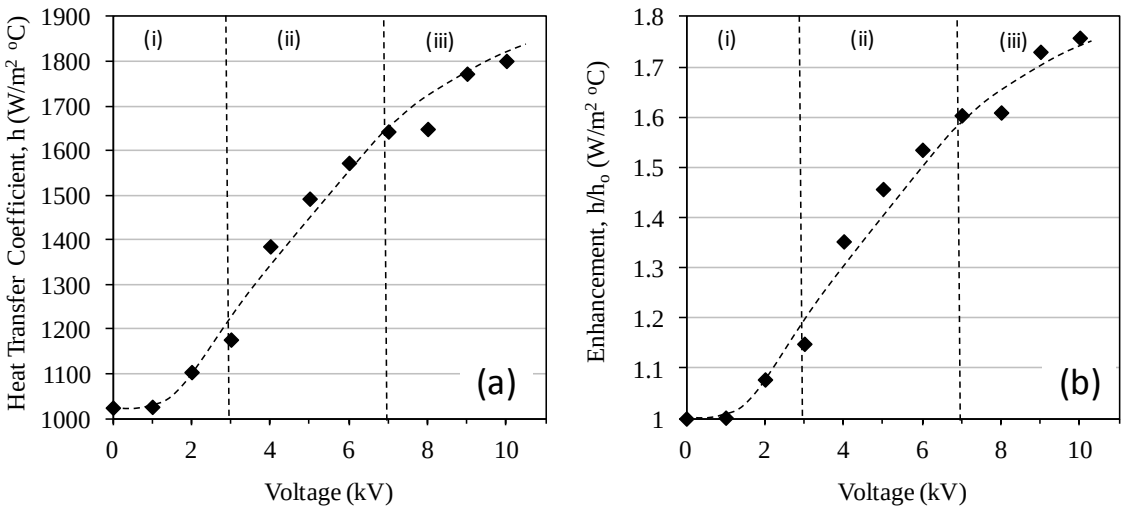

Figure 106: (a) Average heat transfer coefficient and (b) enhancement ratio versus applied voltage.

The enhancement levels, where the heat transfer coefficient at voltages 1 kV to 10 kV are divided by the field free heat transfer coefficients (h/h_o), are shown in Figure 106(b). In Region (i) the heat transfer enhancement only reaches 1.15 fold at 3 kV, after which it tends to increase sharply. In Region (ii) enhancement rises from 1.15 fold at 3 kV to 1.6 fold at 7 kV. In Region (iii) the enhancement continues to increase with applied voltage though at a lower rate between 7 to 10 kV achieving 1.76 fold enhancement at 10 kV.

If the EHD enhancement is examined in terms of heat transfer gained, $Q-Q_o$, a similar pattern is of course noticed and is plotted in Figure 107(a). As before, the largest gains are delivered in Region (ii), while Regions (i) and (iii) tend to be less. At 10 kV the heat exchanger delivers approximately 80 W more than that of the field free case (~153 W) which represents a 50% increase from the field-free baseline.

While EHD provides a large thermal power gain, this must be compared to the penalties required for EHD electrical power and increased hydraulic pumping power. A breakdown of pressure drop and electrical power penalties is shown in Figure 107(b). While the pressure penalty increases to a maximum of 0.6 W at 10 kV, this is still very small compared to the heat transfer enhancement of around 80 W. However, Figure 107(b) reveals that the electrical power penalty rises parabolically with applied voltage and dominates over the pressure drop penalty reaching 4.5 W in electrical power at 10 kV.

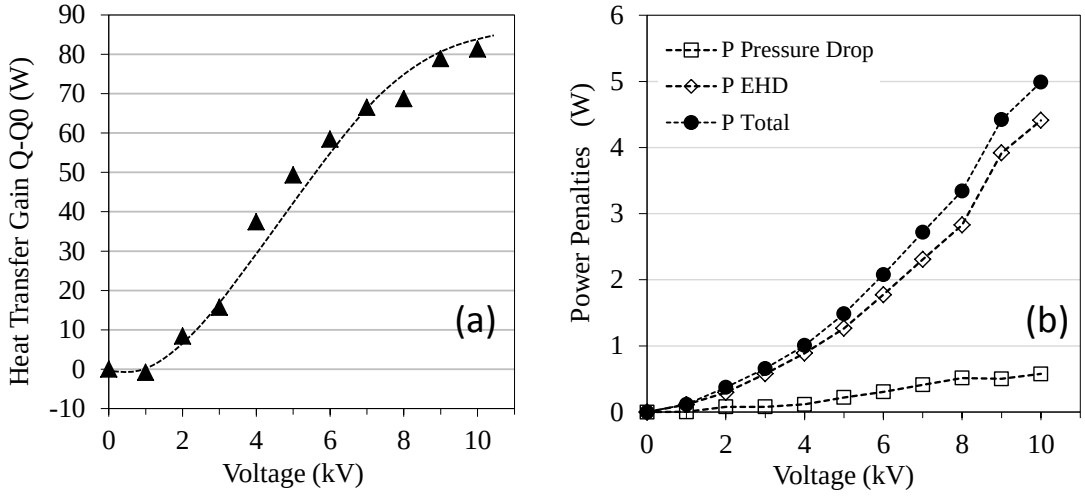

Figure 107: (a) Heat transfer gain and (b) power penalties versus applied voltage.

Defining the true enhancement as a ratio of thermal power gained divided by total power penalty gives the expression;

$$\eta = \frac{Q - Q_{0\,kV}}{(P_{\Delta P} + P_{EHD}) - P_{\Delta P\,0\,kV}} \tag{121}$$

This is plotted in Figure 108 against applied voltage. With initial increase in voltage to 1 kV there is minimal enhancement though it increases sharply between 1 kV and 4 kV where it peaks at a 40 fold gain in thermal power per unit penalty power cost. The initial steep rise is due to the fact that at lower voltages, the heat gain increases at a higher rate than the power penalty. The peak at 4 kV occurs because the rate of increase of the power penalties with applied voltage continually increases whereas the rate of increase of the thermal power gain begins to decrease. Beyond this point, the enhancement decreases since the thermal gains increase at a rate which is lower than the power penalty curve which continues to increase parabolically, as seen in Figure 107(b). The net effect is that despite further gains in heat transfer, the power penalties are now beginning to account for a larger share thus causing a reduction in overall enhancement with higher voltages. Even still, the overall enhancement is approximately 16 times more heat transfer gains per unit penalty power at 10 kV.

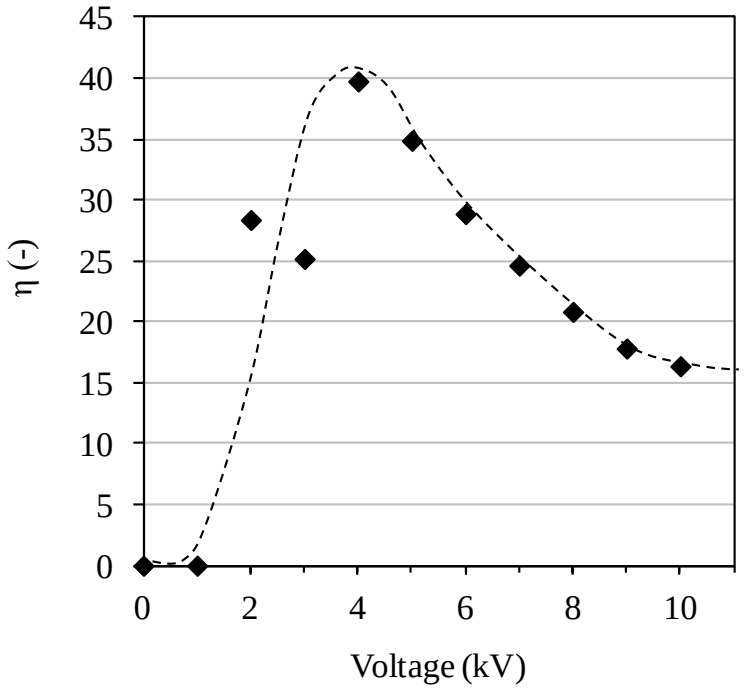

Figure 108: True enhancement (η) plotted versus voltage.

4.2.5: Application of PID control to flow loop

Referring to Figure 98 and Figure 107 it is clear that the application of EHD provides the capacity to extract additional heat from the hot water source and the amount of additional heat extraction depends on the applied voltage level. For the given inlet states of the refrigerant and water, the base is defined by the field-free case and the ceiling is defined, in this case, by the maximum safe operating voltage or equipment limits. It is thus feasible that the power extracted by the refrigerant could be controlled to a specific set point so long as it exists between the base and ceiling.

To prove this concept a PID control program was implemented in Labview. In the Labview program a set point thermal power could be entered and the PID controller automatically varied a low voltage output from a digital to analogue converter which was subsequently stepped up by the high voltage amplifier.

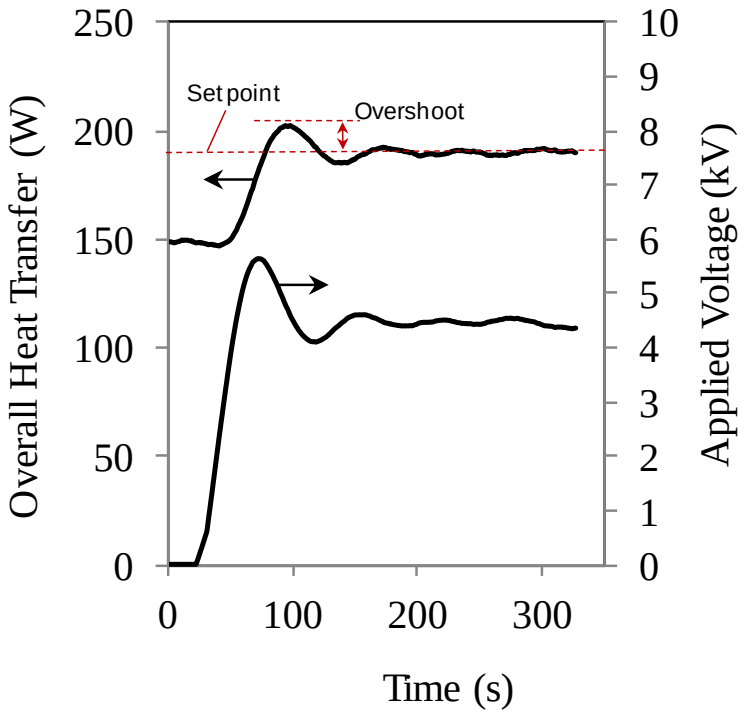

Figure 109: Heat transfer and applied voltage time traces for a tuned PID controller and a set point thermal power of 190 W.

A typical plot of the output voltage and system power response is shown in Figure 109 for a set point thermal power of Q=190 W, the approximate midpoint between the base and ceiling power. Before EHD is applied, the heat transfer remains steady at around

150 W. With the PID control algorithm activated the system EHD voltage rises sharply. There is a delay between the time that the voltage begins to increase and the time the heat transfer begins to increase due to the thermal mass associated with the heat exchanger. The voltage overshoots to around 6 kV before settling at around 4.5 kV. The voltage overshoot tends to cause a similar overshoot in the heat transfer as the PID controller hunts for the voltage setting required to produce the set point thermal power output. From the moment that the voltage begins to rise it takes approximately 2 minutes for the system to settle at the desired set point thermal power. At steady state, the controller very accurately controls the heat transfer and does so with minimal oscillations as is clear in Figure 109.

4.2.6: Summary of Section 4.2

The tests described in this section were performed at a fixed water inlet temperature and thus an almost constant wall superheat. The applied voltage was increased in 1 kV steps from 0 to 10 kV and heat flux was allowed to vary. A high-speed camera recorded videos and images at one location, x/L=⅜. For the current test section it was found that application of 60 Hz AC EHD voltages between 0 to 10 kV resulted in thermo-hydraulic outputs that could be categorised into three distinct zones.

At low voltages up to 3 kV, thermal gains and pressure drop increased moderately, while at medium voltages between 4 to 7 kV, thermal gains increased more sharply, as did pressure drop. After 7 kV, the level of increase in thermal performance and pressure drop began to diminish, perhaps due to the lower availability of fluid in the tube available for redistribution. These thermo-hydraulic measurements were corroborated by visualisation within the test section, which were also found to form three distinct flow regimes caused by EHD influences on the flow regimes.

For the voltage range of 0 to 3 kV, the flow was of a stratified wavy nature with occasional slugs. As voltage increased, this basic regime persisted but bubble diameters increased. At 3 kV, bubble oscillation due to the AC EHD voltage was visible and a curtain of liquid from the liquid layer base was extracted toward the electrode. The heat transfer enhancement reached a maximum of 1.1 or about 12% of the total enhancement.

In the voltage range 4-7 kV, the curtain of extracted liquid became more evident, bubble diameters grew larger and oscillation amplitude increased. Heat transfer and pressure drop increased more rapidly in this range. Coalescence and cresting of bubbles was evident, and these phenomena became more persistent with increased voltage. The crested bubbles climbed on one another, conveying liquid to the upper parts of the tube. Slug events also occurred but were reduced in number and these appeared to cease altogether at 5 kV, where top wetting of the tube was solely due to bubble clustering and bridging events. At 7 kV, a new characteristic of liquid jets or spouts was seen. Heat transfer enhancement in this 4-7 kV ranged from 1.3 to 1.59 but accounted for 55% of the overall enhancement.

In the region 8-10 kV, the flow regime displayed an alternating pattern, switching between two flow regimes, the oscillating bubble regime, as seen in the 4-7 kV range, and a thin film regime, where bubbles are fewer, and liquid jets emanate from the electrode. The number of the liquid jets increases with voltage. However, the strength of the jets does not appear to increase as they always reach a similar height above the electrode regardless of voltage. Heat transfer continues to increase albeit at a slower rate than at 4-7 kV. The heat transfer enhancement ranged from 1.65 to 1.84, which made up 37% of the overall enhancement range. A 1.84 fold increase in heat transfer was determined which was partially offset by power penalties of which electrical power was dominant. A peak of 37 times more power gain per unit power penalty was measured in this heat exchanger.

Finally, a simple PID controller was implemented to the test section and found to maintain heat exchanger heat transfer at a set point within satisfactory limits. However despite the wall temperatures being measured by embedded thermocouples, and the surrounding water temperature being measured in flow, it was found that the uncertainty related to the water side thermocouples was too high to provide satisfactory breakdown of the heat transfer coefficients at a discretised level. Consequently only average heat transfer coefficients have been discussed in Chapter 4.1 and 4.2. Therefore in order to obtain local heat transfer coefficients at the four axial locations top and bottom, this led to the second test section which was ohmically heated and is described in the next sub-section.

4.3: Heat Transfer Augmentation with Ohmic Heating - Experimental Results and Discussion

4.3.1: Aims of this Section

This section discusses the thermal-hydraulic results obtained from the second test section which was electrically heated via a thin conductive coating of ITO on its perimeter. In this new test section, no heating water was present on the outer wall of the tube as in previous sections so the wall temperature was allowed to vary as determined by the electrical heating power and the flow regime inside the tube. In the previous results sections using the water heated tube, only a broad overall sense of the heat transfer coefficient was available across the exchanger. Further discretisation of the local heat transfer coefficients was considered but deemed infeasible due to high uncertainty of the heat input in the discretised local sections due to small water temperature differences along the heated channel. Therefore this final section attempts to overcome this shortcoming via a more uniform method of electrical tube heating enabling an accurate method of calculating the local heat transfer coefficient, and thus being able to link the flow phenomena more closely with local heat transfer.

It should be noted that this is the first investigation ever performed which is capable of measuring the local wall heat transfer coefficients while under EHD conditions, and with full visual access to the flow regimes in the tube.

As before, the wall superheats were recorded by thermocouples inset into the sapphire tube walls. This coupled with the constant electrical heating input of 150 W allowed a local heat transfer coefficient to be determined as discussed in Chapter 3. As before, refrigerant mass flux (G) was 100 kg/m^{2}s and the inlet quality(x_{in}) was 2%. First, to get a general sense of the HTC coefficients with voltage, the averaged heat transfer coefficients for the top and bottom wall thermocouples are presented in Figure 110.

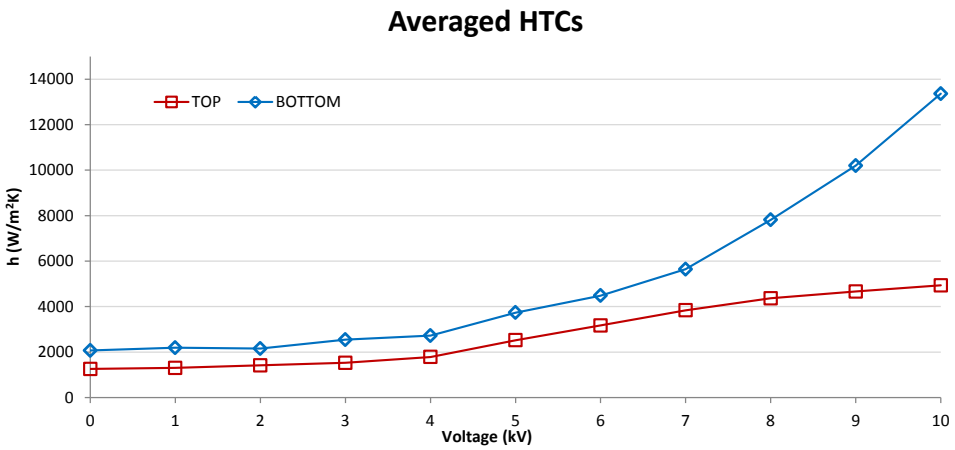

Figure 110: Averaged heat transfer coefficients of top and bottom tube walls for G=100 kg/m²s x_{in} = 2%

Figure 110 shows that the bottom heat transfer coefficients are consistently higher than the top. This is in line with expectations from previous tests, while not being able to provide local top or bottom heat transfer coefficients, the visualised flow patterns coupled with the superheat measurements suggested a higher heat transfer coefficient from the convective liquid layer present at the bottom of the tube than from the top of the tube which experienced intermittent wetting and drying. In the case of the electrically heated tube, this is also confirmed from the imagery in Figure 111 and Figure 112 which show photos of the flow conditions at four locations along the length of the test section. Unsurprisingly, these are similar in flow pattern to those witnessed in the water heated test section. Although the voltage was increased in 1 kV intervals, only images from every 2 kV increments are presented for clarity.

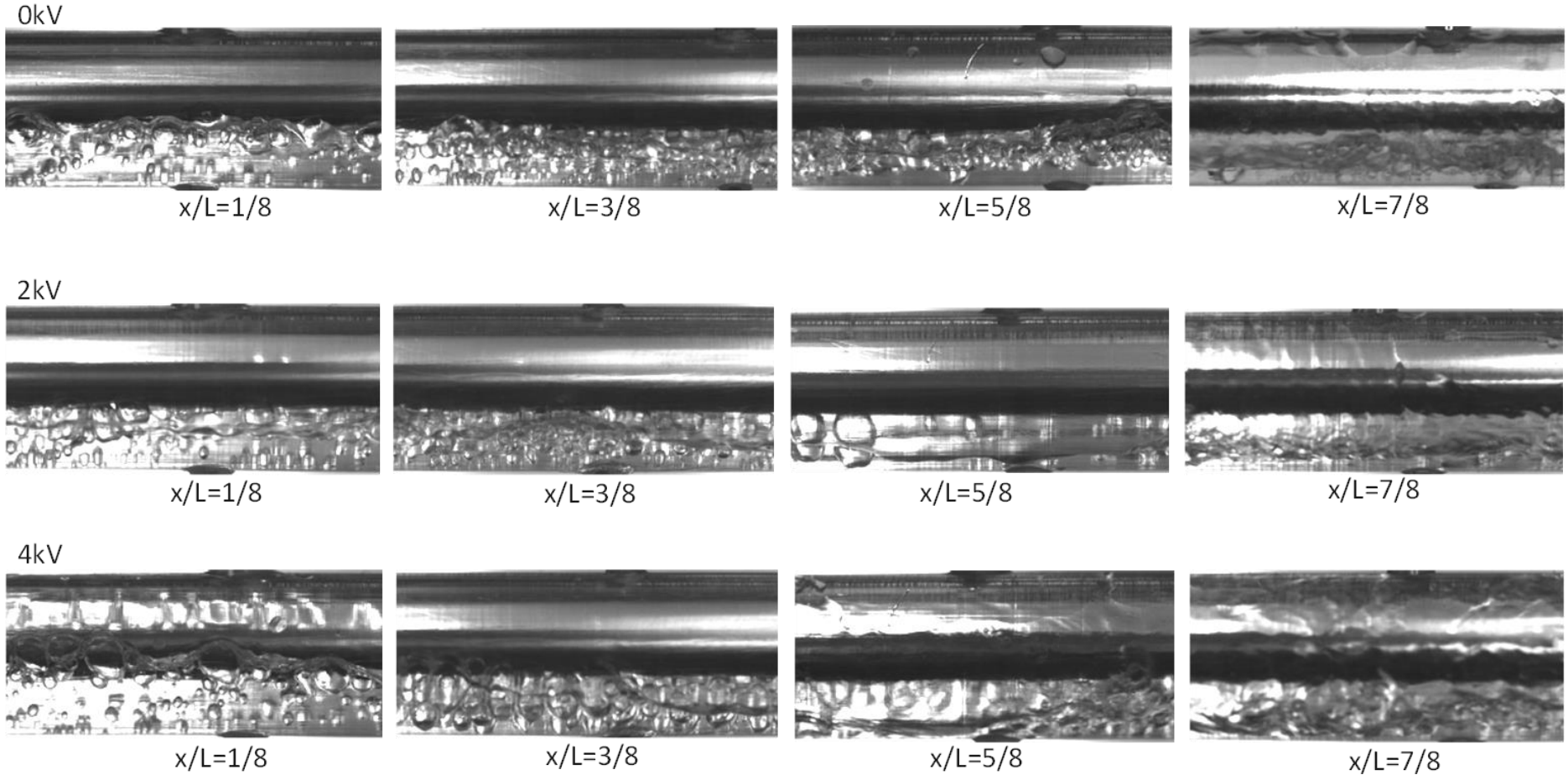

Figure 111: Flow at Locations x/L=⅛, ⅜, ⅝ & ⅞ at 0, 2 and 4 kV for G=100 kg/m²s x_{in} = 2%

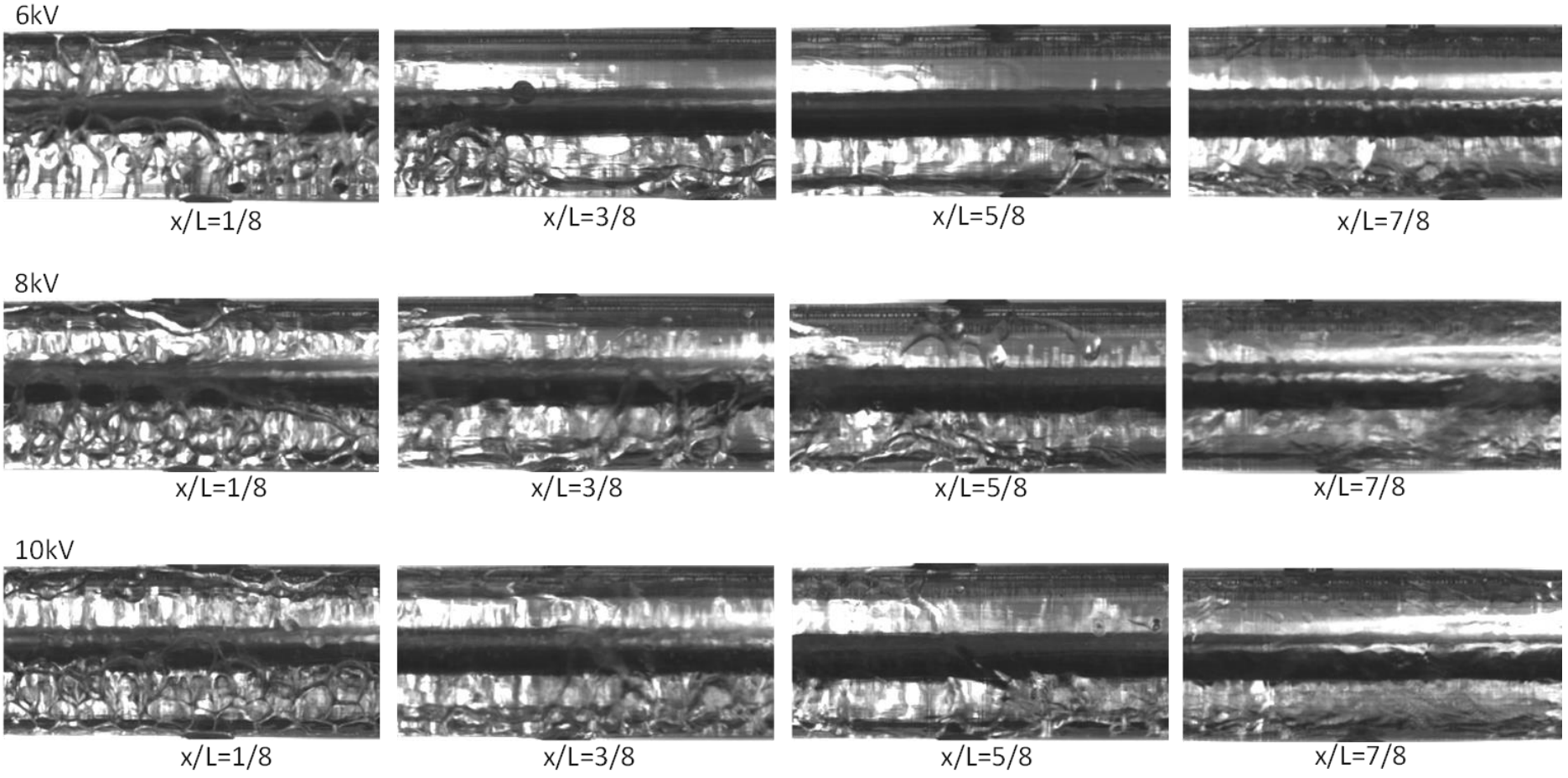

Figure 112: Flow at Locations x/L=⅛, ⅜, ⅝ & ⅞ at 6, 8 and 10 kV for G=100 kg/m²s x_{in} = 2%

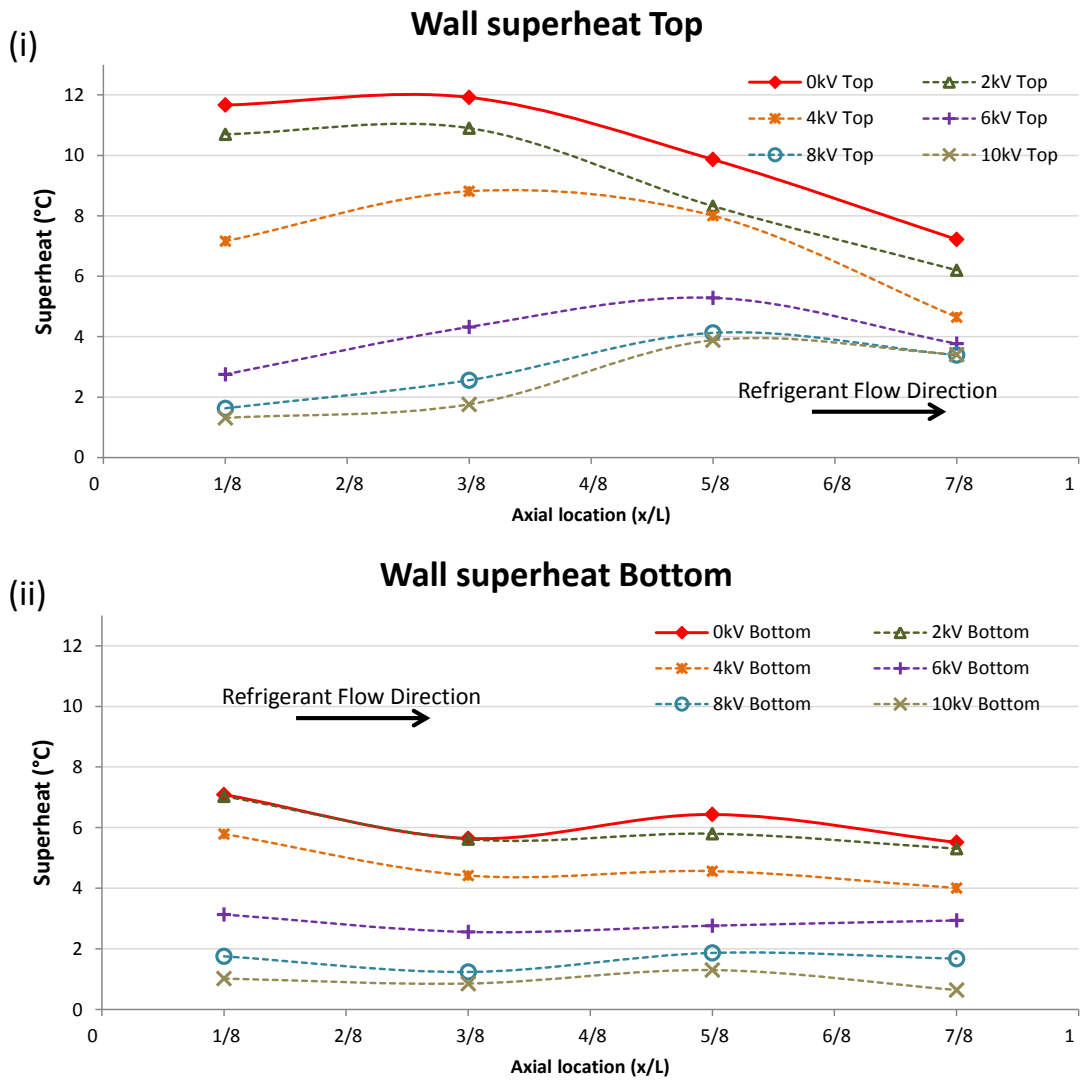

Figure 113: Tube wall superheat profiles with EHD voltage for (i) top and (i) bottom

The wall superheats for the top and bottom of the tube are shown in Figure 113. Again, for clarity, only voltages in increments of 2 kV are shown. These all show a clear decrease from the 0 kV case thus indicating an improvement in wall cooling with increasing EHD voltage. For the top of the tube in the field free case alone, the superheats gradually drop by 5 °C along the test section length from around 12 °C down to 7 °C indicating an improved heat transfer mechanism along the tube. This is consistent with the existing literature where the top wall heat transfer increases with increased quality as found by Grauso et al. [90], and Sun et al [91]. This is also substantiated by the video images where the upper part of the tube is generally dryer at the beginning due to the predominantly stratified flow and the top only experiences wetting by the intermittent slug events. Conversely, at the end of the tube, the top is

much more wetted by these slug events which have evolved to become longer in duration and provide a more wetted surface thus reducing the superheats.

In spite of this drop in superheat along the tube at 0 kV, with the application of EHD, the exit region of the tube is less affected by EHD effects than at the entrance region where the largest drop at the top of the tube occurs. The exit region superheats decrease by only around 4 °C with 10 kV, while the superheats at the entrance of the tube decrease by around 10 °C for the same EHD voltage. The largest changes occur between 4 kV and 8 kV.

The bottom of the tube exhibits much less variation in superheat varying only between 7 °C to 5.5 °C from entrance to exit. Again from the video footage, a stratified liquid layer is noted all along the lower surface with length, thus accounting for the relative uniformity in superheat along the tube. When the effect of EHD is examined, referring to Figure 113 the bottom surface experiences an almost stepwise lowering in superheats from 7 °C down to approximately 1 °C with increasing EHD voltage up to 10 kV. This decrease in superheat points to an improvement in the mode of heat transfer. Interestingly, as with the top superheats, the largest changes along the bottom occur between 4 kV and 8 kV.

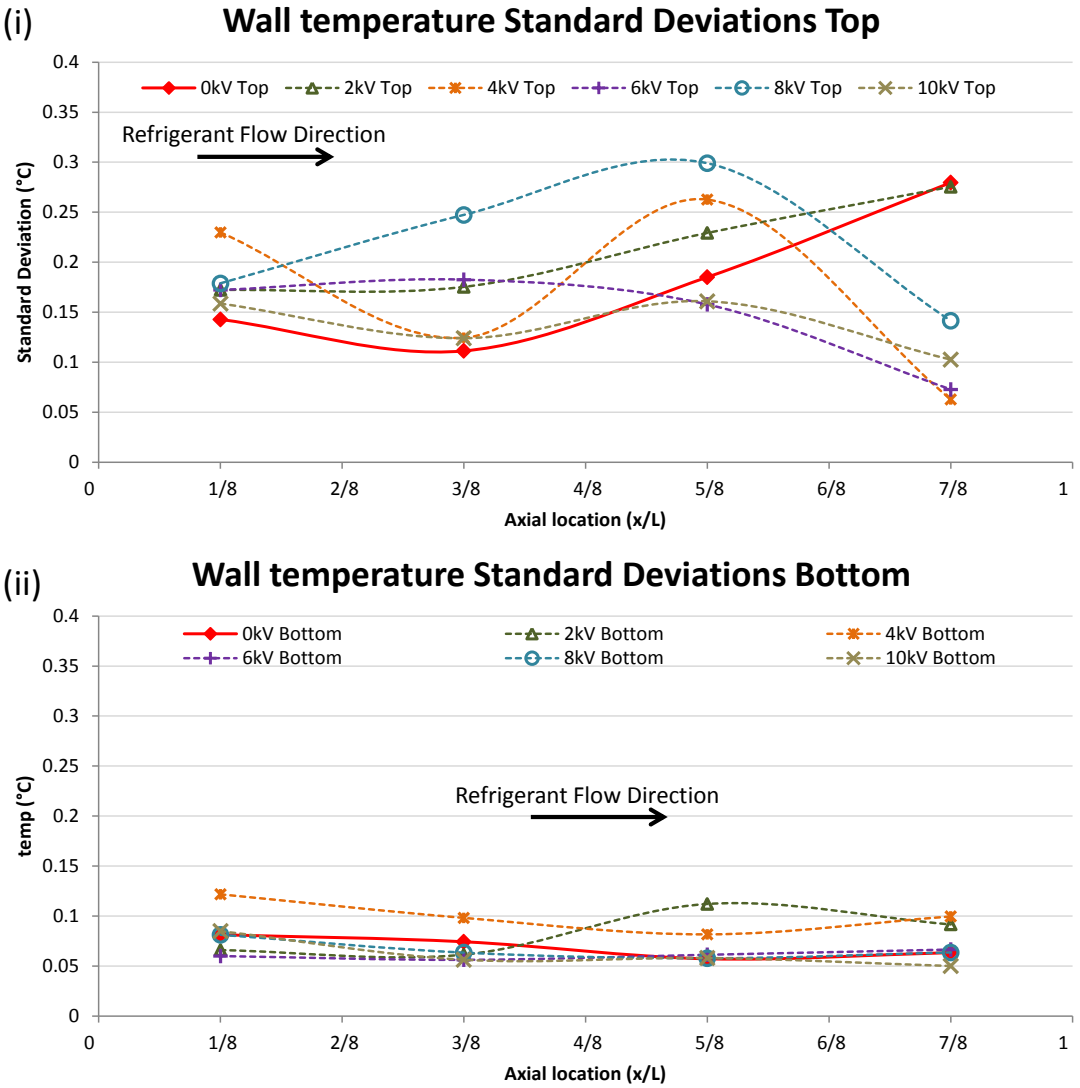

Figure 114: Wall temperature standard deviations for (i) top and (ii) bottom

Referring to the superheat standard deviations in Figure 114 these again indicate that the bottom of the tube experiences lower deviations generally in the range of 0.05 °C to 0.08 °C consistent with a more uniform temperature and in this case supporting the existence of a liquid layer along the bottom. The top standard deviations are more varied and generally higher ranging from 0.1 °C to 0.3 °C except near the end of the tube at higher EHD voltages where the values decrease to below 0.15 indicating a more constant wall temperature. This is due to the drier conditions. The higher values are due to temperature fluctuations and point to intermittent wetting and drying.

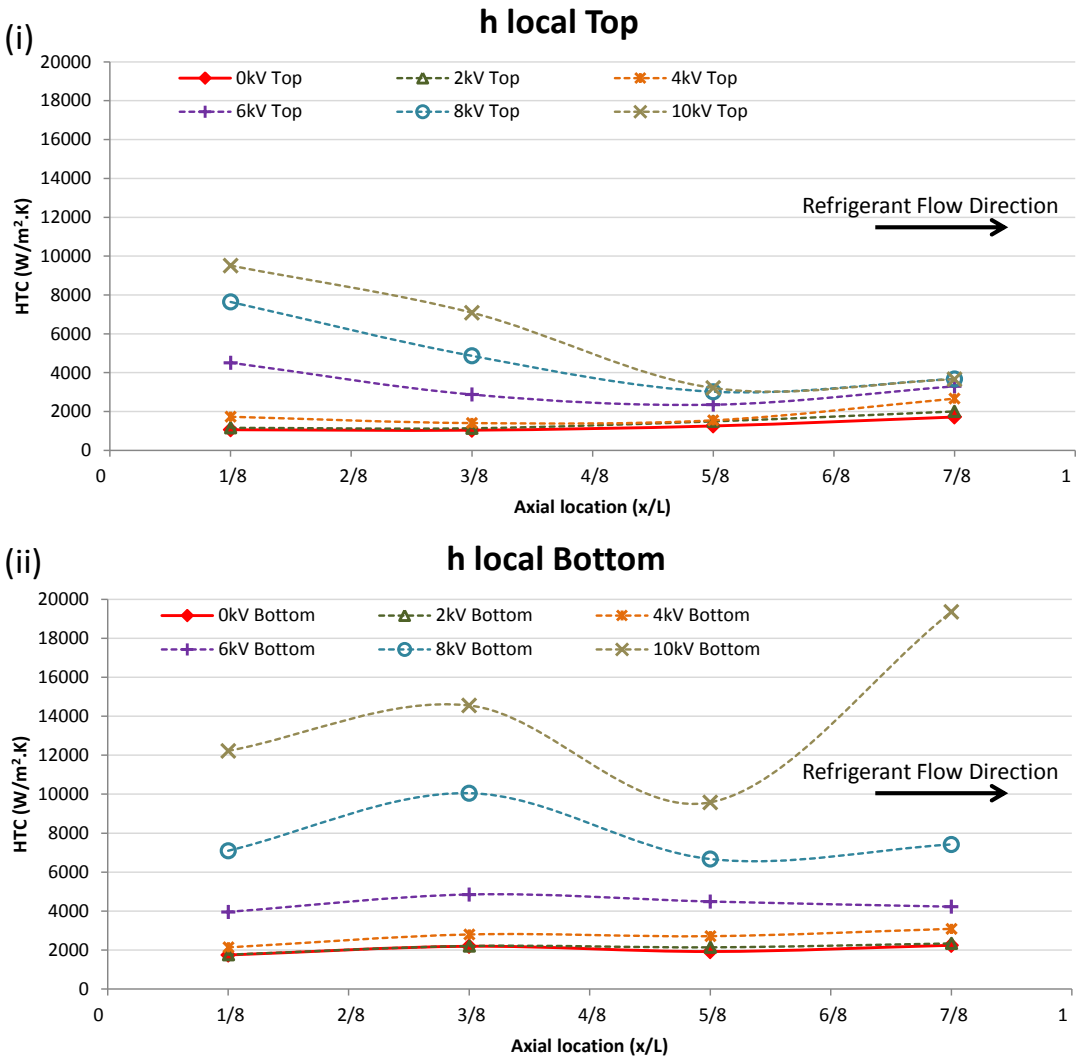

Figure 115: Local heat transfer coefficients along tube for both (i) top and (ii) bottom

The local heat transfer coefficients for top and bottom of the tube are shown in Figure 115. In the field free case the heat transfer coefficients begin at 1062 W/m^{2}K and rise to 1717 W/m^{2}K, whereas for the bottom, the heat transfer coefficients are higher, beginning at 1747 W/m^{2}K and rising to 2247 W/m^{2}K at the end of the tube. This is expected as the bottom is subject to a constant convective liquid layer which thins along the tube due to the increasing quality, therefore increasing the convective component, while the poorer heat transfer at the top is explained by the dryer conditions, wetted only by intermittent slug or wave events.

As EHD of 2 kV is applied, a minor improvement is noticed along both top and bottom of the tube, where the heat transfer coefficients rise from 1161 W/m^{2}K to 2004 W/m^{2}K for the top and from 1765 W/m^{2}K to 2340 W/m^{2}K for the bottom. This is also evident

from the slight increase in the average coefficients top and bottom as witnessed in Figure 110. A large increase is not expected in this region due to the minimal effect of EHD on the flow regime at 2 kV in Figure 111, where despite larger bubbles, some oscillations and slightly longer slug wetting, the flow regimes are broadly similar to those in the field free case. However as EHD is increased from 4 kV through to 10 kV, the EHD effects on the flow regime cause a greater change from the field free flow regimes and increases of a much larger scale are seen at both top and bottom of the tube.

There are differences in the amount of EHD augmentation depending on location of the tube. The gains along the bottom of the tube increase almost evenly, whereas at the top of the tube, the greatest gains occur at the tube entrance region. In addition, the magnitude of the top gains are generally smaller, the maximum value of 9513 W/m^2K attained is with 10 kV at x/L=⅛, whereas the corresponding heat transfer coefficient at the bottom is 12219 W/m^2K. Nevertheless, the top heat transfer coefficients are seen to fall off with length more sharply than those at along the bottom of the tube where the values remain more level. It must be mentioned that the dip in heat transfer coefficients that occur at 8 and 10 kV at location x/L=⅝ which may be within the effects of thermocouple uncertainty which increase as the amount of superheat decreases. Complete graphs of the heat transfer coefficients plotted with their uncertainty bars are given in Appendix D.

It is now proposed to examine the causes of this variation in heat transfer profiles, more specifically to elucidate the reason for the trend in augmentation and to answer why

- the increases in EHD augmentation along the bottom of the tube are less dependent on axial location along the tube
- the increases in EHD augmentation along the top of the tube experience a greater gain at the entrance of the tube, and why these values decline with length along the tube.

This will be performed by analysing the flow regimes at each tube location. First the largest increases which occur at the beginning of the tube (x/L=⅛) will be studied, thereafter, the flow regimes at the end of the tube will be studied, and finally the regimes at x/L=⅜ and ⅝ will be investigated. In the subsequent graphs and

discussions, voltages over 8 kV are deliberately excluded due to the higher levels of experimental uncertainty associated with 9 and 10 kV.

4.3.2: Comparison between 0 kV and 8 kV at the entry region

A more detailed view of the heat transfer coefficients versus EHD voltage at the test section entrance region (location x/L=⅛) is given in Figure 116. It can be seen that the top surface heat transfer coefficient of 1062 W/m^{2}K is lower than the bottom value of 1747 W/m^{2}K for the field free case. This situation persists up until 5 kV when a reversal takes place and the top of the tube rises to 3560 W/m^{2}K outperforming the bottom which reaches 3197 W/m^{2}K. The top of the tube outperforms the bottom up until 8 kV. The tube wall superheats are also shown in Figure 116 and indicate a drop in top superheats from 11.66 °C to 1.6 °C with EHD, while the bottom drops from 7.09 °C to 1.76 °C with 8 kV. The reversal between top and bottom superheats at 5 kV is also visible.

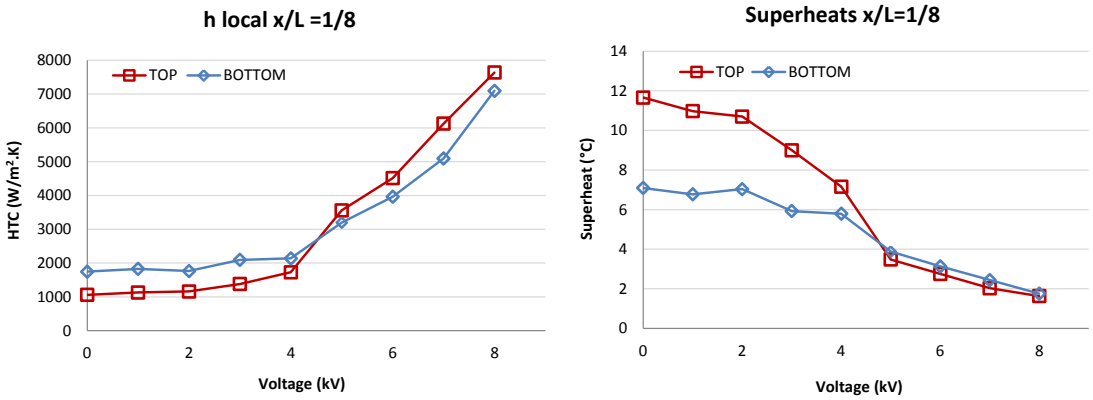

Figure 116: Top and bottom heat transfer coefficients and wall superheats for the location x/L=1/8

In order to address the reasons for the overall gain and the reversal at 5 kV the flow regimes at each voltage will be studied in more detail. First a comparison between the flow patterns occurring in the field free case and at 8 kV were made so as to account for the obvious mechanisms responsible for the largest increase at that tube location. Representative images of the flow regimes from 0 kV and 8 kV are given in Figure 117.

At location x/L=⅛ a familiar picture is evident as the flow is largely stratified wavy with the periodic annular slugs as witnessed earlier in Sections 4.1 and 4.2. The lower layer is of a stratified liquid flow with nucleate boiling, the upper part of the tube is

largely dry except when wetted by the occasional annular slugs. The same location in the tube has a very different flow pattern when subject to 8 kV. In this regime the dominant structure in the flow at first appears to be large oscillating bubbles within the liquid layer, all subject to vertical and transverse displacement due to a combination of EHD and fluid forces.

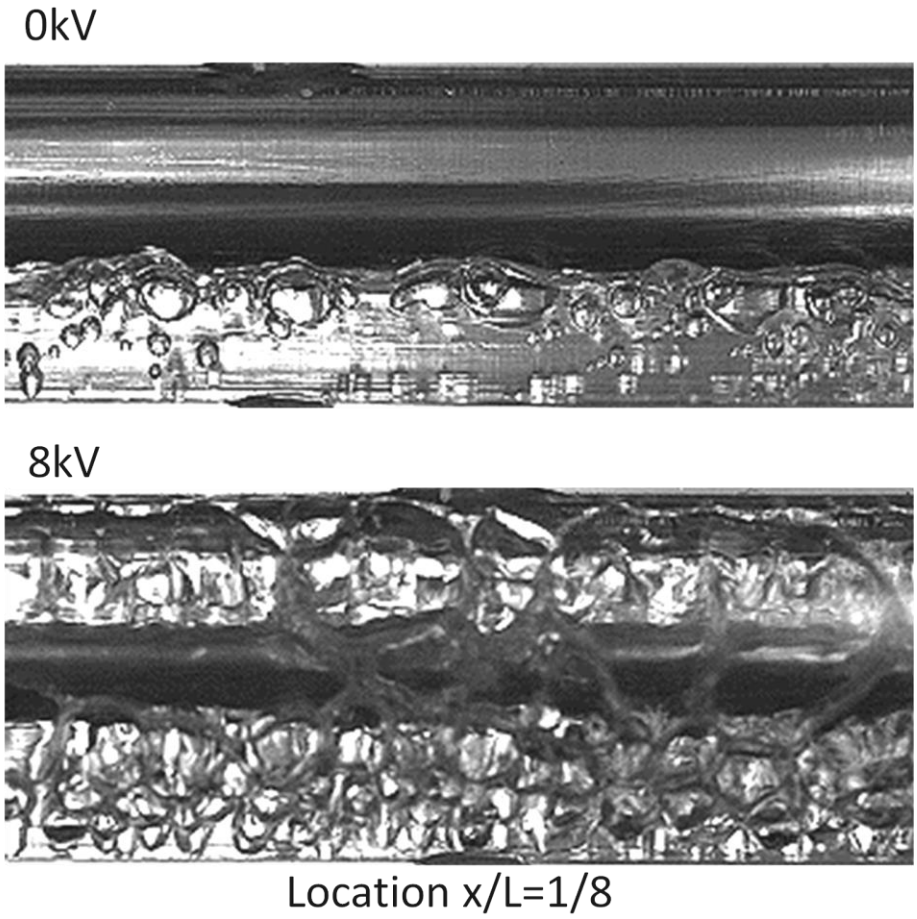

Figure 117: Flow patterns near entrance region at x/L=1/8 for 0 kV and 8 kV

The lower liquid stratum is clearly perceptible from the lower picture in Figure 117, however it is almost totally filled with oscillating bubbles. Fresh nucleated bubbles generated from upstream enter the viewing area and as they rapidly grow are seen to oscillate between the tube wall and electrode, again in tandem with the EHD forces. Once a certain size is reached, the bubbles are noticed to be slowly squeezed out from under the electrode toward the side walls where they continue to oscillate and grow. Some coalescence takes place also. Fresh bubbles keep replacing the bubbles pushed out from under the central electrode in a continual process.

A substantiation of this difference in flow regimes is also provided by high speed scan of the wall superheat temperatures. These superheats are plotted in Figure 118 for 0 kV and 8 kV respectively. For the field free case, the top superheats are clearly much higher than those at the bottom of the tube and the difference at location x/L=⅛ is around 5 °C. Compare this with location x/L=⅛ at 8 kV where the superheats are broadly similar at around 1.5 °C. The bottom superheats are generally level due to the liquid layer, while the top superheat is more irregular, probably due to the continuous construction and deconstruction of the flow pattern which will be discussed later.

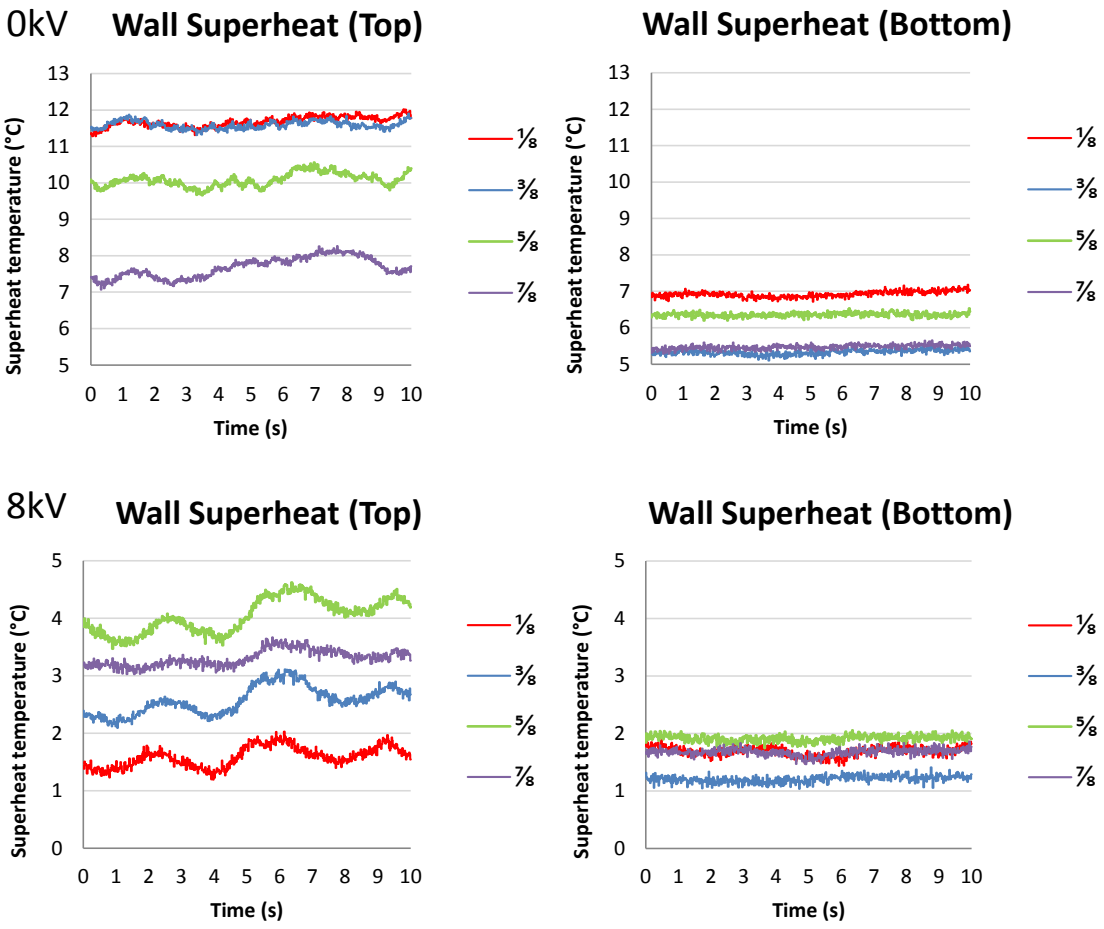

Figure 118: Top and bottom wall superheats at 0 kV and 8 kV

The other point to note about Figure 118 is the decrease in superheats between the field free and 8 kV cases. The top superheats decrease from 7 °C to 12 °C at 0 kV to 1.2 °C to 4.5 °C at 8 kV, while the bottom superheats also decrease from 5 °C to 7°C at 0 kV to between 1 °C to 2 °C at 8 kV. This decrease also points toward an increase in the heat transfer.

Upon first inspection of Figure 119, the flow conditions at the top of the tube appear to mirror the lower section. However, once studied more carefully, there are major differences. No bubbles were observed to be generated at the top of the tube and none travelled from the lower area up to the top area.

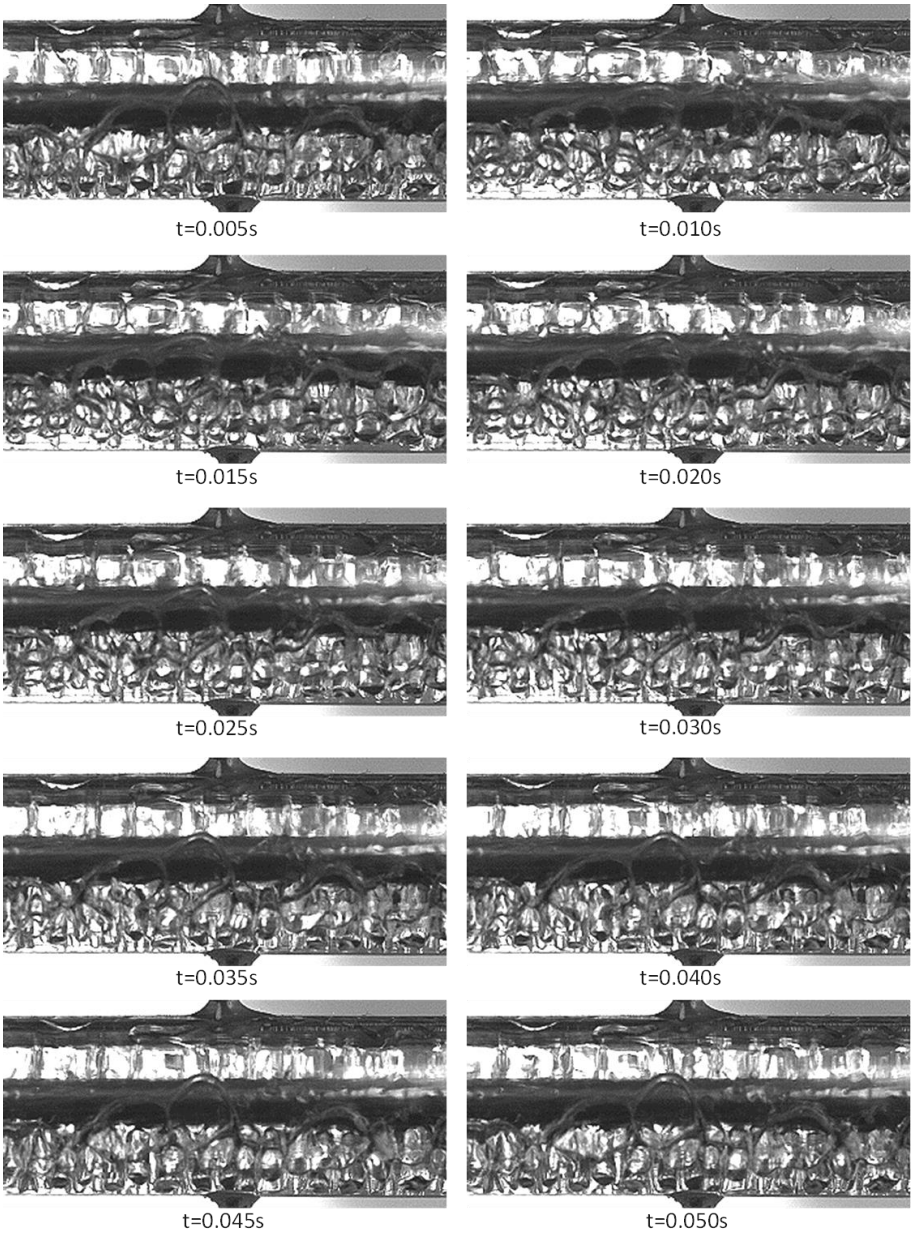

Figure 119: Flow patterns near tube entrance at 8 kV, oscillating bubbles at the lower layer and liquid jets or spouts emanating from electrode to top of tube

Instead of bubbles as in the lower liquid layer, the top structures appear to be a regular system of liquid jets and bridges which are at first similar in appearance to bubbles.

These bridges are also subject to oscillation in time with the EHD forces. The cause of this may be the accessible amount of liquid available to substantially wet the electrode since the quality is low, and secondly the nature of the EHD forces to set up the liquid bridging. Almost total wetting of the top of the tube is apparent. Nevertheless some dry areas are witnessed along the side of the tube as can be seen in Figure 119. This may be seen in the superheats if locations at x/L=⅛ are compared (see Figure 118), where both top and bottom are at similar superheats, yet the top experiences more fluctuations than the bottom. The presence of liquid jets to the sides of the tube is also seen, and these do cause significant wetting of the side walls. The liquid bridges are regular in spacing, and also move along the electrode and tube wall with the flow, thus providing a liquid film to dissipate heat.

Referring to the heat transfer coefficients in Figure 116, and the images from Figure 117, the flow patterns explain the mechanisms of heat transfer in the field-free and 8 kV cases. In the field free case, the heat transfer coefficient of 1747 W/m^2K at the bottom of the tube is better due to the convective liquid layer, while at the top of the tube where wetting is only provided intermittently by periodic slug events, a drier wall condition dominates giving a lesser HTC of 1062 W/m^2K. This drier wall condition is further corroborated by the superheat plots in Figure 118. The 4.5 °C difference in superheat is clearly visible between top and bottom at location x/L=⅛. Interestingly, for the 8 kV case, the top and bottom superheats are very similar, the bottom is more uniform, while the top experiences fluctuations related to changes in the liquid jet and liquid bridge pattern.

However, in the 8 kV case, the bottom still retains the liquid layer, albeit this time highly populated by oscillating bubbles which wipe and bounce along the lower wall, providing a highly disturbed flow along the bottom which provided a 4 fold increase in heat transfer over the plain stratified layer in the field-free case. On the other hand, the new type of liquid bridging flow phenomena created by EHD increases the top heat transfer rates by a factor of 7.2 where it surpasses that of the bottom. This level of enhancement of the top surface is related to the fact that the vapour quality is low and levels of liquid are high.

The flow regimes at intervening voltages are shown superimposed on the HTC chart in Figure 120 and show a gradual progression from the stratified wavy layer to the oscillating bubble and EHD induced liquid bridges found at 8 kV. At 4 kV the bottom flow is still stratified wavy, but the top now has fully developed liquid bridges. From the video analysis these liquid bridges were transitory and unstable and the structures did not maintain for long enough to cause the large amounts of liquid redistribution and wetting found at higher EHD voltages. At 6 kV these bridges were noticeably more stable and more consistent in spacing and number, and thus helped account for the higher wetting and replenishment of liquid at the tip, in turn augmenting the heat transfer. At the bottom of the tube, at 6 kV, the regime has clearly departed from the stratified liquid layer and is now more of an entrained oscillating bubble flow pattern.

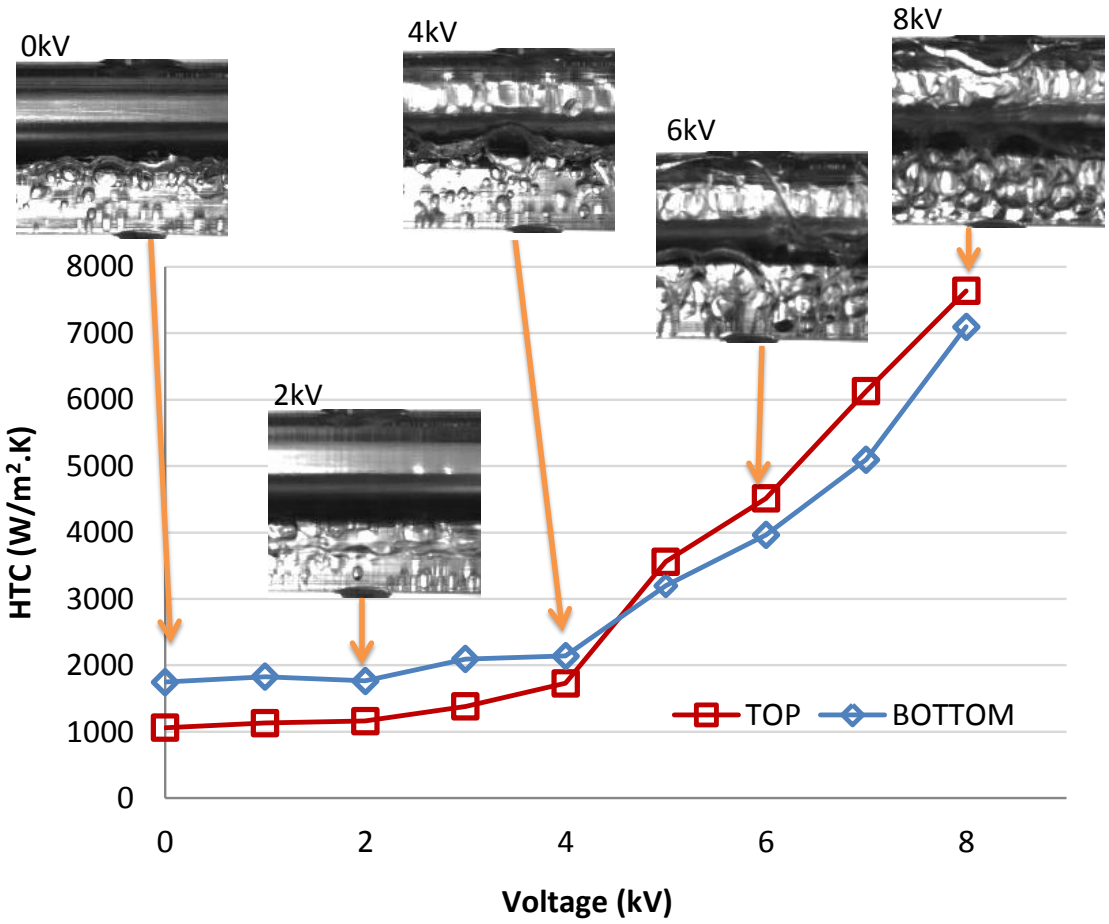

Figure 120: Flow patterns at location x/L=1/8, voltages 0-8 kV

It is thought that the EHD voltage effect at this location induces several phenomena beneficial to heat transfer; it extracts liquid from the lower liquid layer improving its convective characteristics via liquid layer thinning, it redistributes this liquid to the top

of the tube via liquid bridging, and it has an oscillating and growth promoting effect on nucleated bubbles within the remaining stratified layer at the bottom.

4.3.3: Comparison between 0 kV and 8 kV at the exit region

The next section considers the flow patterns and heat transfer associated with the outlet region of the test section. Referring to Figure 115, the bottom HTC values were uniform for the field-free case irrespective of axial location along the tube. As EHD voltage was increased, all locations of the tube, including the location x/L=⅞ now under study, experienced a similar rise with EHD. Contrary to this, the HTCs at the top of the tube, although higher at the tube entrance in the field free case, tend to decrease after locations x/L=⅝ and ⅞ due to the increased vapour quality. Also, EHD voltages of 8 kV did not have as high an enhancement effect at these locations as witnessed at the bottom of the tube, though the enhancement can still be up to two fold.

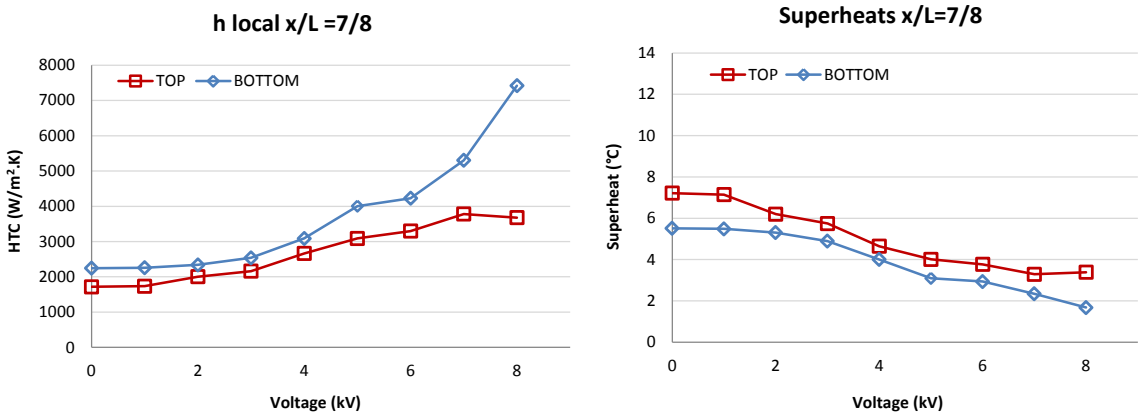

Figure 121: Top and bottom heat transfer coefficients and wall superheats for the location x/L=⅞

Referring to Figure 121, and comparing this with Figure 116, the heat transfer coefficients versus voltage for the bottom of the tube show similar trends and magnitudes as found at location x/L=⅛, experiencing a 3.3-fold rise in heat transfer from 2247 W/m^{2}K to 7421 W/m^{2}K. The top HTCs however, beginning at a lower initial value of 1717 W/m^{2}K, only experience a 2.1-fold rise to 3678 W/m^{2}K. A more striking feature of the bottom HTC curve is the sharp disparity between top and bottom that occurs after 6 kV. This is also reflected in the superheats and will now be investigated.

Again, if one compares the superheats from Figure 121 with Figure 116, one notices common trends in the bottom profiles with a minor decrease from 7.09 °C at x/L=⅛ to

5.51 °C at x/L=⅞, but that the top wall superheats have now decreased more to an outlet superheat of 7.22 °C as opposed to 11.06 °C at location x/L=⅛. Again, further study of the high speed imagery provides an insight into the physical mechanisms. Figure 122 shows pictures of the flow patterns at tube location x/L=⅞ for 0 kV and 8 kV.

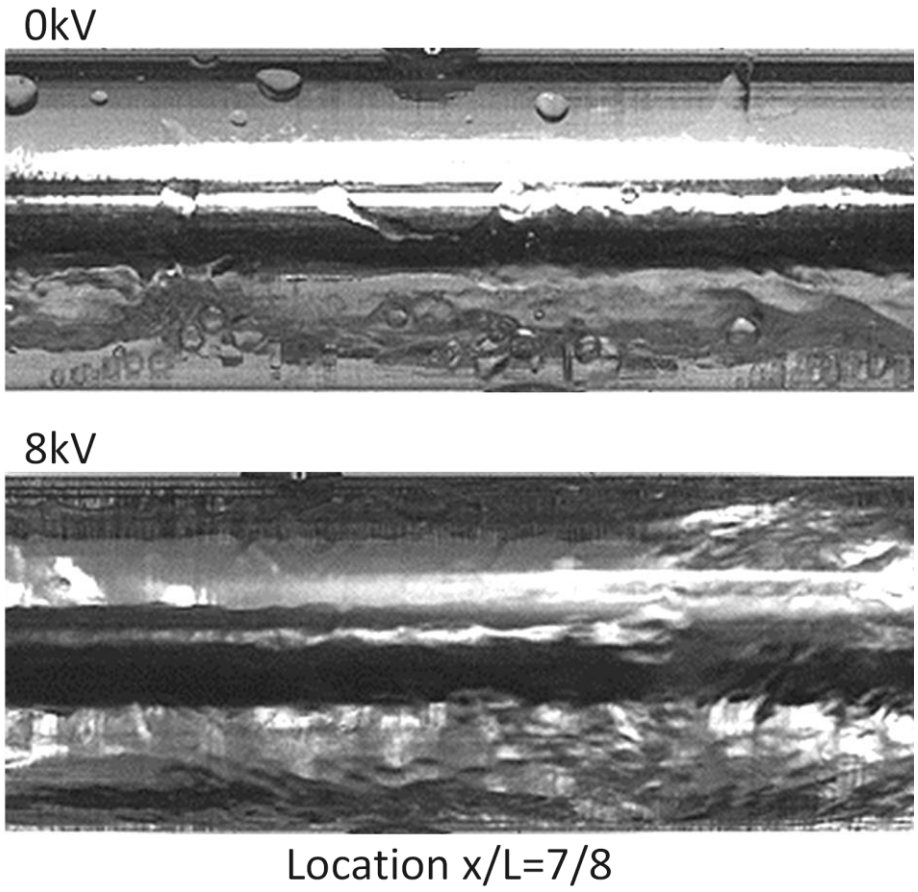

Figure 122: Flow patterns at exit region, 0 kV and 8 kV

At 0 kV the flow pattern is at first a stratified flow, albeit with a reduced liquid level in the tube compared to the entrance due to an increase in quality from approximately 6% at x/L=⅛ to 28% at x/L=7/8. Some nucleation is present in the liquid layer. The top part of the tube is intermittently wetted and more so than at the beginning of the test section as is confirmed from Figure 114. Large waves are seen to form at the liquid layer and vapour interface and these temporarily wet the upper parts of the tube, some even reaching the top of the tube. Likewise the periodic slug events still occur and are responsible for most of the intermittent wetting of the top surface. Although dryout after the slug is rapid, the longer duration of the slug and its more annular nature provide a higher degree of wetting at the top surface.

As the EHD voltage is zero, the reason for this gradual change in flow regime is thought to be the increased amount of vapour present at this region of the tube. Due to upstream vapour generation, the quality near the test section exit is higher at around 28%. The mass flux is constant, yet with increased vapour quantity, the velocity of the vapour is subject to an increase [92, 93], and the liquid layer may be subject to an increase in velocity also by interfacial friction. Consequently, a thinner and faster moving liquid layer on the bottom could account for higher convective heat transfer along the bottom of the tube at the exit region (2247 W/m^{2}K at x/L=⅞ compared to 1747 W/m^{2}K at x/L=⅛) whereas increased liquid wave generation, and longer duration slug events contribute to higher wetting and improved heat transfer coefficients at top of the tube (at x/L=⅞ the top is now 1717 W/m^{2}K compared to x/L=⅛ where the top was 1062 W/m^{2}K).

At a voltage of 8 kV the flow can be seen to alternate between two states, one is a low liquid level condition where the liquid layer at the bottom is thinned and barely perceptible. Incipient forms of liquid jets are visible in this region and can be seen in Figure 122. However the amount of liquid available is not enough to permit satisfactory extraction toward the electrode and consequently little is then available for redistribution to the upper walls or sides of the tube. Some splashes from entrained droplets are noticed but these are thought to be less significant in heat transfer terms.

A verification of this transition is also visible in the superheat plots in Figure 118. At location x/L=⅞ the bottom superheat is largely uniform at around 1.7 °C. However, the corresponding top superheat varies between 3.0 to 3.5 °C. The higher superheat indicates only a slightly dryer surface, and the superheat fluctuations along the top support the variations in flow regime discussed earlier. On the other hand, the bottom superheats fluctuate much less showing that the changing flow structures primarily influence the top wall while a liquid layer is maintained along the bottom.

Conversely, the other type of flow regime encountered here can be described as almost an “annular flow” though it is thought to be an extension of the previous slug events as described earlier. However the slug now appears to be of such long duration and of an annular nature that less liquid is carried in the main ”slug body”, but is now thinned out

over a greater distance and time, consequently producing an annular wetting of long duration. In addition, these slugs, once clearly defined events with distinct beginnings and ends, now appear to run into each other, hence the EHD voltage may precipitate a general transformation of the clearly defined slug events to a more homogenised general annular flow much more beneficial to heat transfer. It is noticed from the video that dryout near the end of the tube is more prevalent at the 8 kV case. This is supported by the higher superheats at the tube exit in Figure 118 which corroborate the higher enhancement at the bottom of the tube but also the fall off in HTCs at the top of the tube at location x/L=⅞ seen in Figure 115 and Figure 121.

A final illustration of this is given in Figure 123 where the flow patterns at intermediate voltages are superimposed onto the local heat transfer coefficient plots. It can be seen that the bottom of the tube is always subject to the liquid layer, and that the thickness of this decreases with length along the tube.

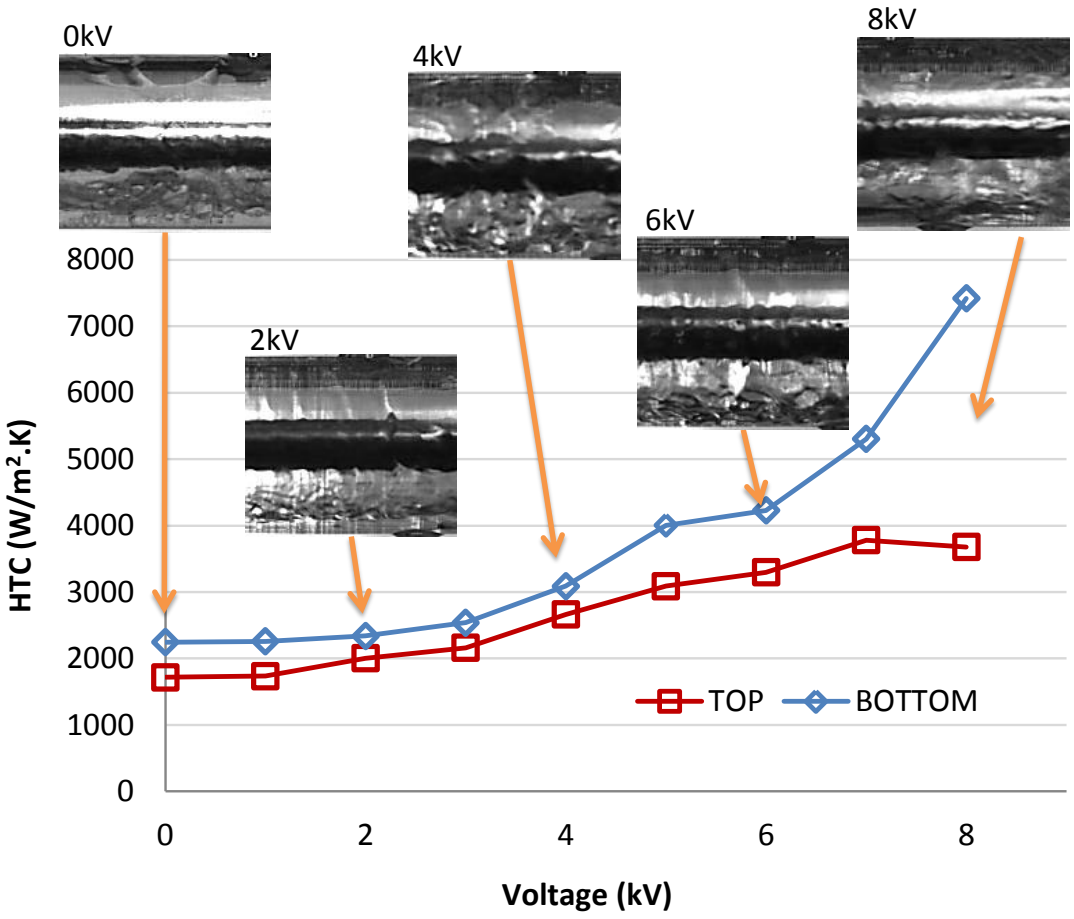

Figure 123: Flow patterns at location x/L=7/8, voltages 0-8 kV

An interesting phenomenon noticed was that EHD forces seemed to cause breakup of waves travelling along the liquid layer. One such event is shown in Figure 124. A wave is generated in the liquid layer and travels along with the fluid. This can be seen at times t=0.000 and t=0.0025s. At t=0.005s, distortion of the wave is evident, and at t=0.0075s the wave is seen to be violently broken up and expelled towards the walls of the tube. At t=0.0075s liquid jets can also be seen and this is thought to be when the EHD forces are strongest, thus the EHD voltages which produce the liquid jets also acts on the liquid wave precipitating its disintegration and expulsion of fluid to the tube walls. Given that the region of highest electrical field is in the vapour region closest to the electrode [75], this means that lower liquid levels in the tube will be less susceptible to extraction and redistribution from the weaker EHD forces. It is interesting to see this actually occur from the sequence in Figure 124 only when the liquid (in the form of a wave) attains close proximity to the electrode that EHD forces of a sufficient magnitude occur within the fluid thus causing is redistribution. This may counter the argument that as inertial and viscous forces increase within the fluids, that EHD forces have lesser effect. The images in Figure 124 suggests that despite higher liquid and vapour velocities, it may be the proximity of the liquid to the electrode that has a major effect of the magnitude of the EHD forces and thus on redistribution and likewise heat transfer.

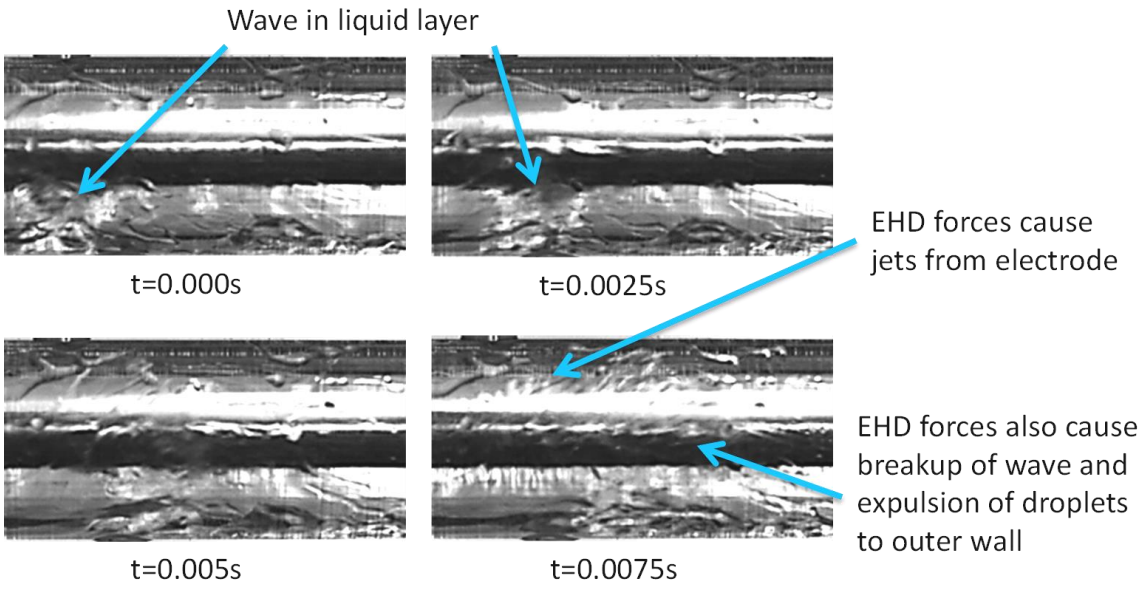

Figure 124: Image sequence showing wave break up due to EHD forces (8 kV, x/L=⅞)

This relationship between liquid level and proximity to the electrode is thought to be also true in all other locations of the tube and may partly explain the high levels of EHD augmentation noticed at the beginning of the tube where liquid levels are highest and therefore in close proximity to the electrode. On a related note to this expulsive force that causes breakup of the wave, it was also found that at 8 kV at x/L=⅞ EHD can also attract liquid from the lower liquid layer.

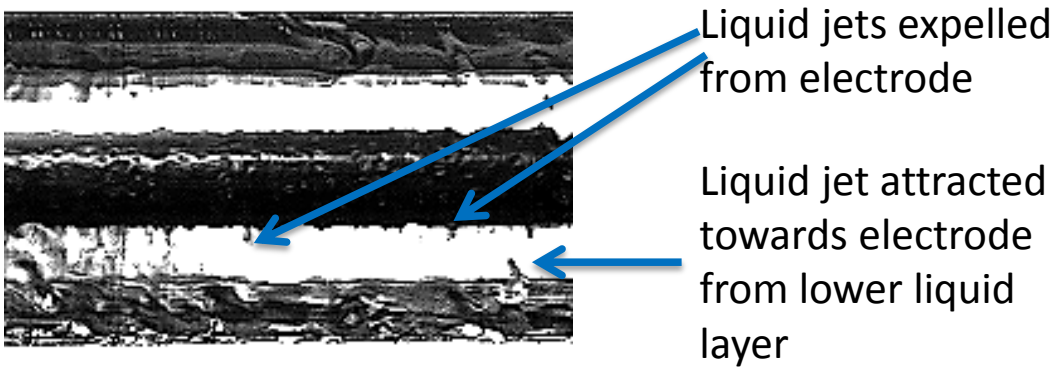

Figure 125: Attracted jets or columns from lower liquid layer towards central electrode at 8 kV at location x/L=7/8

Therefore it appears that the EHD forces can provide either an attractive or repulsive force, probably as a result of the AC voltage wave.

In summary, if liquid does come into close proximity to the electrode and is subject to the EHD forces, then it is likely that fluid redistribution will take place. However, it seems that due to the inevitable production of vapour that must occur in any convective boiling or two-phase heat exchange process, this itself places a limit on the amount of EHD enhancement that can be attained. This is supported by Cotton et al. [6] who performed a numerical analysis of the electrical fields on a similar tube and electrode configuration and found that in an annular flow, the electrical field strength was lower as liquid film thickness decreased. In the same study, Cotton also analysed stratified flows and found that at low liquid levels, the electric field attracted the liquid towards the electrode. This explains the attracted curtain encountered in many of the earlier images and sketches. Cotton also found that for stratified flows where the liquid level was higher than the electrode, the net force would repel the fluid opposite to gravity. This would also help to explain the liquid bridging leading to large scale liquid redistribution from the tube bottom to the top witnessed at the tube entrance at location

x/L=⅛ at 8 kV, as in this case the fluid levels are normally close to the electrode but raised somewhat by the extra volume of the entrained bubbles in the liquid layer.

At a constant mass flux, with the increase in quality the liquid and vapour phases experience changes in flow pattern. In the field free case this has been shown to produce a departure from the stratified wavy and slug regime to an incipient annular flow, where the heretofore slug events are now of longer duration and consist of liquid film washing around the tube wall with the higher velocity vapour core. Therefore as quality increases and the beginning stages of annular flow develop, most of the liquid in the tube is distributed to the tube wall. However from an EHD point of view the tube wall is furthest from the electrode and does not experience the larger electric fields near the electrode. This resultant liquid deficit in regions of high electric field strength may explain why the flow regimes at the tube end (x/L=⅞) do not experience the same degree of heat transfer augmentation as found at the tube entrance under EHD conditions.

4.3.4: Comparison between 0 kV and 8 kV at x/L=⅜ and x/L=⅝

Figure 126 shows the top and bottom wall heat transfer coefficients for the location x/L=⅜ with the flow pattern images superimposed. Compared to those at x/L=⅛ the HTCs have changed slightly. In the field free case, the top HTCs start at 1040W/m^{2}K, similar to the 1062W/m^{2}K at x/L=⅛. However the rise with EHD voltage is slow until 4 kV and thereafter the maximum value reached is also lower, only attaining a value of 4867W/m^{2}K at 8 kV. This is a marked drop from the 7640W/m^{2}K achieved at x/L=⅛.

Conversely the bottom of the tube experiences a general rise in HTC from the start. The field free HTCs are up from 1747W/m^{2}K at x/L=⅛ to 2195W/m^{2}K. Likewise, the initial rise with EHD voltage is also low until around 4 kV when the HTCs rise sharply with voltage to a maximum of 10052W/m^{2}K at 8 kV, an increase from 7097W/m^{2}K at x/L=⅛. The images in Figure 126 show that the bottom flow regime is stratified wavy even up until 4 kV, when the liquid layer is strongly attracted towards the electrode. At this point the nucleated bubbles with the flow are seen to be greatly enlarged.

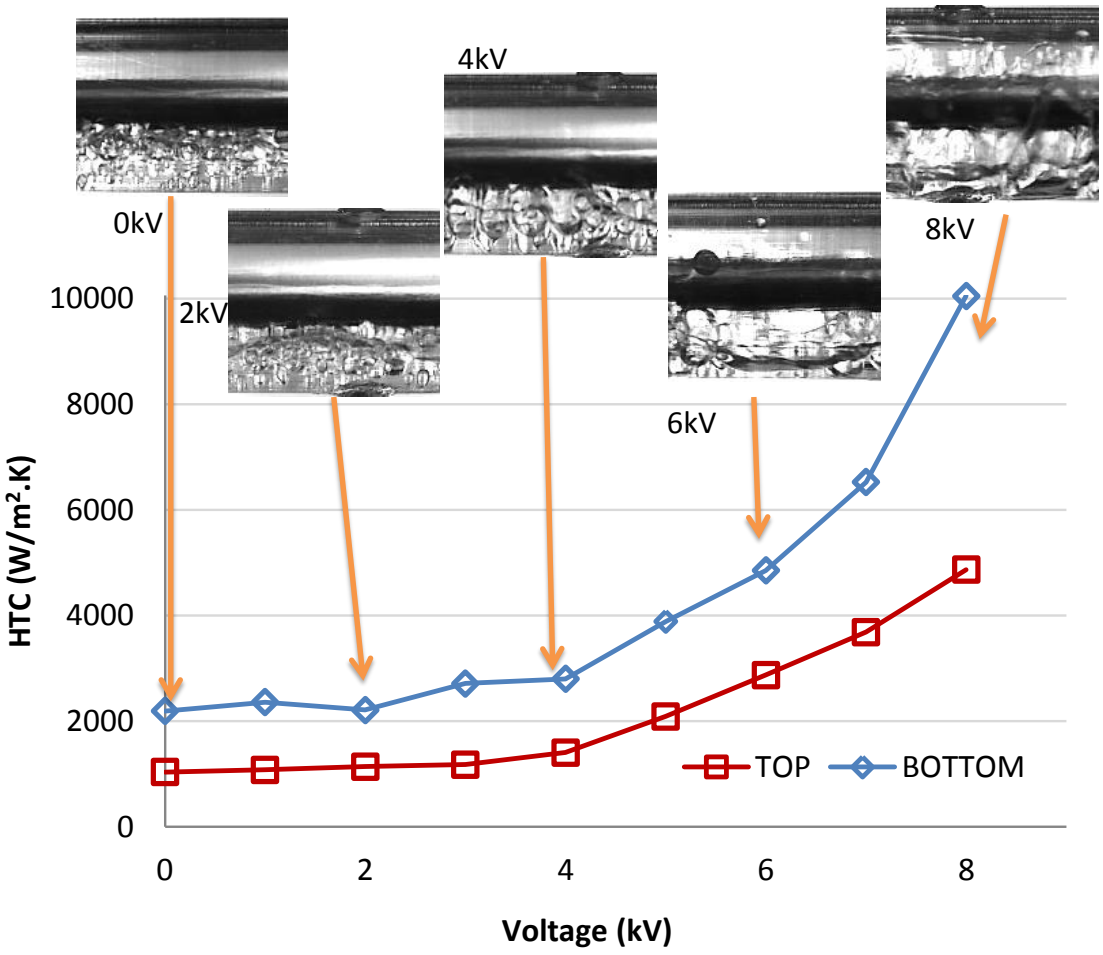

Figure 126: Flow patterns at location x/L=3/8, voltages 0-8 kV

As found before, the bubbles oscillate within the liquid layer causing wiping and re-distribution of fluid increasing the lower convective coefficient. The liquid vapour interfaces are also generally wavier at this location compared to the interfaces found at x/L=⅛, likely as a result of the greater vapour quantity and resulting higher fluid velocities.

At 6 kV, the lower liquid layer is much thinned, yet still transports large oscillating bubbles. The electrode is wetted all round and an increased amount of liquid is seen at the top of the tube, where it has been redistributed via liquid bridging. These bridges are still not robust and collapse readily, but are replenished by the arrival of enough liquid in the proximity of the electrode. At this voltage, top wetting is significantly affected by the EHD forces, rather than by the drawing out of the slug events witnessed at lower voltages.

At 8 kV the flow conditions evolve to the alternate transit between regimes as witnessed earlier in the water heated test section. The photo in Figure 126 does not convey this transiting regime therefore images of both regimes are shown in Figure 127.

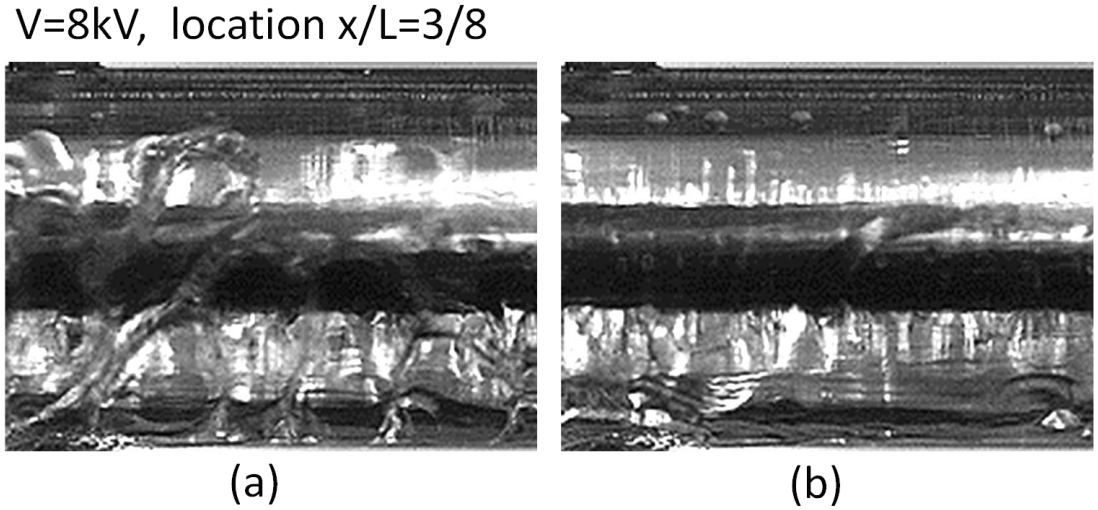

Figure 127: The transitory flow regimes found under 8 kV at location x/L=3/8

In this case the patterns seem dependent on the amount of liquid visible in the test section window. One is associated with higher liquid amounts (Figure 127(a)) and comprises a vigorous bottom layer with large oscillating bubbles engulfing the electrode, and coupled with high liquid bridging, liquid jets and top wetting. The other regime occurs when the liquid levels have abated (Figure 127(b)) and comprises a thin film liquid layer along the bottom, some nucleation and bubble growth is also present as are wave cresting events. Liquid jets or spouts are expelled to the top and sides from the wetted electrode, though the jets from the electrode top generally do not reach the top of the tube wall. Moving on to the next location in the tube at x/L=5/8 the heat transfer coefficients and flow images are both shown in Figure 128.

It is now seen that the top heat transfer coefficients do not experience the same rise as was noticed after 4 kV in both locations x/L=⅛ and ⅜. The bottom HTCs begin at 1926 W/m^{2}K and increase monotonically to 2713 W/m^{2}K at 4 kV. Thereafter a sharper rise occurs up until 6672 W/m^{2}K. This however is lower than the maximum reached at location x/l=⅜ which was 10052 W/m^{2}K.

The top HTCs begin at a higher value than at x/L=⅜ and run from 1256 W/m^{2}K in the field free case up to 1548 W/m^{2}K at 4 kV and on to 3021 W/m^{2}K at 8 kV. But this too, although higher at the outset, is lower than the 4867 W/m^{2}K achieved with 8 kV at the location x/L=⅜.

At 0 kV the bottom liquid layer is still a stratified wavy flow but the level of liquid has dropped due to the higher quality at this location. The top is wetted by periodic waves of liquid which are now becoming more annular rather than solid slug of liquid. In addition, these slug events last longer.

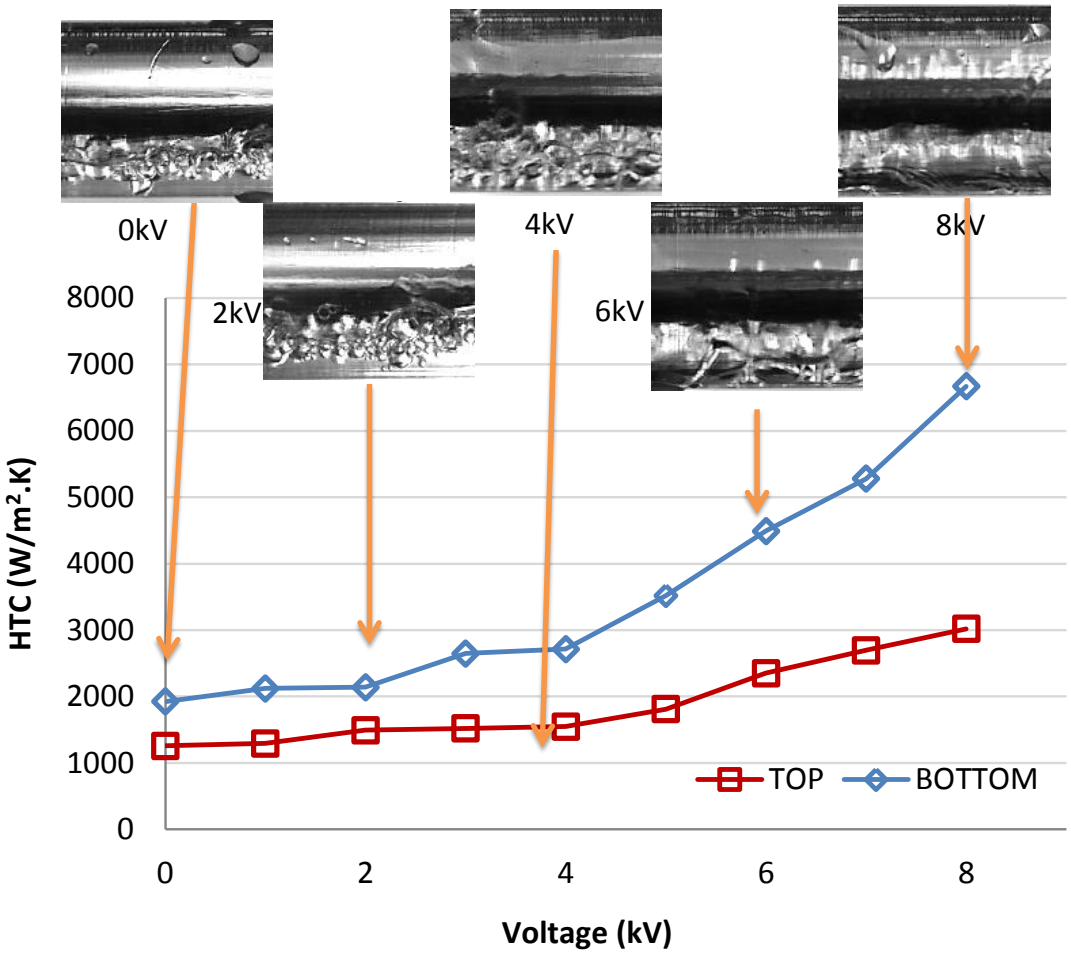

Figure 128: Flow patterns at location x/L=5/8, voltages 0-8 kV

As the voltage rises to 2 kV the bubble diameters increase slightly, especially in periods where liquid velocity drops temporarily. Generally, fewer bubble nucleation sites are observed. The top of the tube remains dry apart from the longer lasting slug events.

The liquid layer is subject to more waviness, likely as a result of interfacial shear between the vapour and liquid interface.

As voltage increases to 4 kV the stratified liquid layer becomes more wavy, and seems to become a precursor to the creation of long duration slug events. As a result of the waves and slugs, top wetting becomes more frequent. Liquid attraction towards the central electrode occurs as does minor expulsion of fluid from the electrode. However, this expulsion is not yet strong. The transitory nature, changing between two flow regimes as found earlier is also evident at this voltage. This too alternates somewhat between an active high liquid level bubble rich flow, to a thin film regime with less bubble activity.

At 6 kV the bottom liquid layer is very wavy and still some nucleate boiling is witnessed. Liquid waves occur frequently and are coupled with the coalescence and nesting of bubbles as seen previously. Slug events have now become more like annular washes of long duration. Consequently the top of the tube is well wetted and the heat transfer improves markedly at this voltage. Some liquid jets or spouts are visible from the electrode, more than seen under 4 kV yet they are still not great in number or strength.

As the voltage reaches 8 kV the flow becomes highly disturbed top and bottom and consequently good wetting is seen with accompanying high heat transfer. Nonetheless, the top of the tube is not seen to be as well wetted as found at tube locations x/L=⅛ and ⅜.

4.3.5: Discussion of the Ohmically Heated Test Section Results

A plot summarising the EHD augmentation at each axial location is shown in Figure 129, and the enhancement ratios are shown in Figure 130.

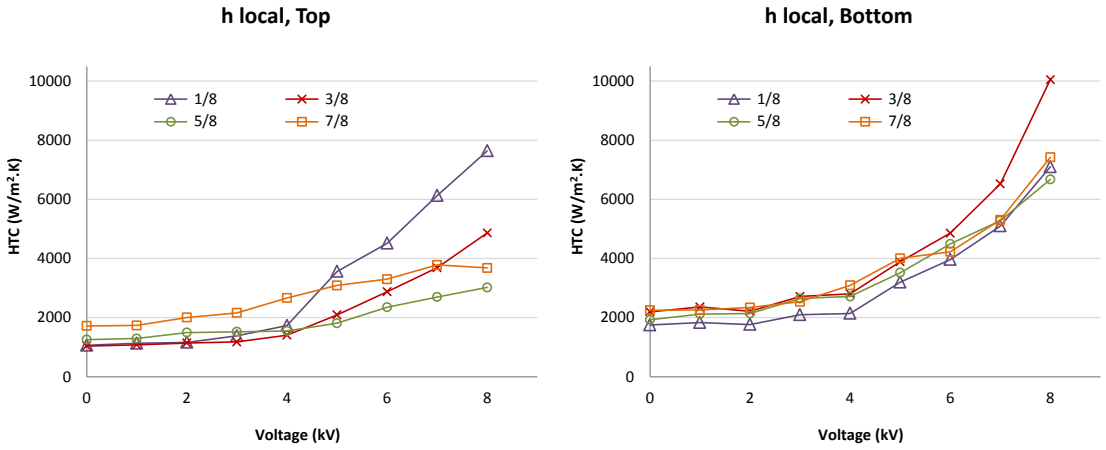

Figure 129: Local heat transfer coefficients for axial location versus EHD voltage

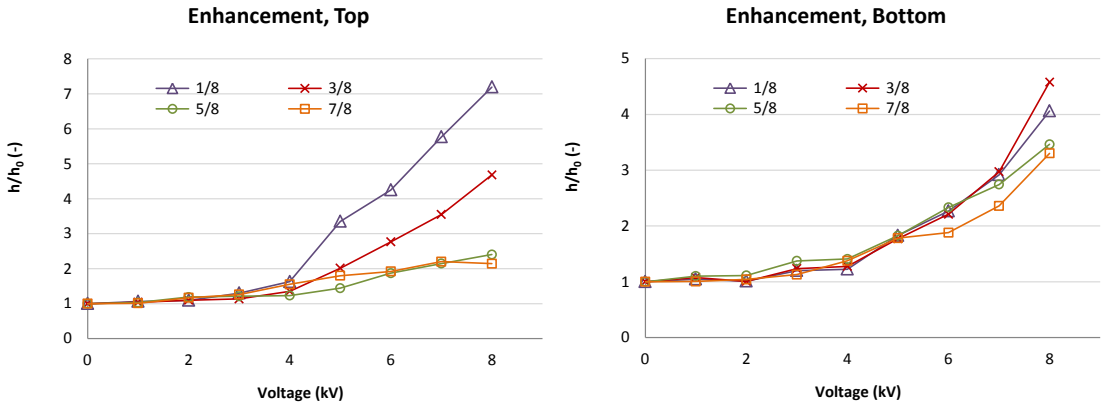

Figure 130: Enhancement as a ratio of h/h_0, plotted versus voltage for both top and bottom of the tube

Figure 129 shows the enhancement in local heat transfer coefficients versus voltage at the four axial locations along the tube. It can be seen that the bottom of the tube accounts for the most of the heat transfer regardless of voltage level. Only one exception to this was found occurring at x/L=⅛. At this location, the bottom heat transfer coefficients were higher than the top until a reversal occurred at 5 kV when the top accounted for more heat transfer than the bottom. At this stage EHD forces caused the flow at the top to be highly wetted by liquid bridging phenomena that travelled with

the fluid flow. Therefore the mechanism was a type of highly enhanced liquid convection.

Another point to note about the shape of both top and bottom curves is that EHD does not seem to have a strong effect until around 4 kV is reached. This is especially apparent in the enhancement plot of the top in Figure 130. All of the curves except two experience an initial slow rise with low EHD values up till around 4-5 kV. After that both top and bottom HTCs rise more sharply, creating a "knee" in the plots. It is noticed that at the top of the tube, this sharp rise decreases with axial location leading to the two exceptions to the "knee" shaped curve at the top of the tube near the exit region at location x/L=⅝ and ⅞.

Here the heat transfer coefficients are higher than at other locations below 4 kV, yet do not experience the sharp rise after this voltage but increase at the slower initial rate. This is due to the lack of liquid reaching the top of the tube with length and may be due to several inter-related reasons. Firstly, the fact that the flow at this location is at a higher quality than at the other locations therefore the amount of liquid available for redistribution is lower. Secondly, as quality is higher, and given the fixed mass flux, vapour and liquid velocities are higher than at the tube entrance. This higher vapour velocity is conducive to the formation of annular flow therefore redistributing liquid against the tube walls where the electric field strength is lower [6, 75] away from the electrode. Consequently body forces on the liquid are much reduced so little redistribution takes place. An illustration of this happening was shown in Figure 124 where in a semi stratified thin film flow no redistribution of liquid took place until the crest of a liquid came in close proximity to the central electrode in time with the AC EHD pulse. The resulting forces on the liquid wave (these are highest at the liquid/vapour interface where the ratio of electrical permittivity between liquid and vapour is at a maximum) cause its rapid break up and expulsion outward against the tube walls.

Therefore as the flow at this location is becoming closer to annular, the heat transfer under field free conditions is already higher than those further upstream. Given the aforementioned reasons, it is less likely that EHD voltages would be able to affect the flow in any meaningful way. Nevertheless, it is noticed that EHD does augment the

flow regime at this location albeit to a lesser extent. From Figure 130 this is seen to be a factor of 2 at locations x/L=⅝ and ⅞ in contrast to a factor of 4 to 7 for locations x/L=⅛ and ⅜. This may be due to redistribution caused by the liquid jets and spouts from the electrode, or by the EHD forces acting radially on liquid that comes in close proximity to the electrode. Or it may be in part due to upstream redistribution of liquid to the outer areas of the tube in the entry and mid regions of the tube. This is not clear as yet.

Again referring to Figure 129, the bottom heat transfer coefficients are all very close in heat transfer terms (all between 1747 W/m^{2}K and 2247 W/m^{2}K) regardless of location along the tube. This is supported by the high speed imagery which confirms the presence of a liquid layer along the bottom at all locations. However what is very interesting is that EHD can provide such a high augmentation even along the tube bottom which should always be highly wetted due to the gravitational influence on the liquid.
As noted for the top HTCs, EHD enhancement does not have a high effect until a voltage of 4 kV is reached. Thereafter, even along the bottom, a much sharper rise in heat transfer occurs with increasing voltage.

In the field free case, the bottom heat transfer coefficients increase with tube length due to progressive liquid thinning and resulting better convective heat transfer. This was observed to continue with EHD, although enhancement was higher at the tube entrance and decreased towards the tube exit. From Figure 130, highest enhancement of around 4.5 fold occurs near the entrance, yet these are still lower than the 4-7 fold factors experienced by the top. However, toward the tube exit, the bottom enhancement factors ranged around 3 fold, whereas those at the top decreased to around 2 fold.

The heat transfer enhancement on the already wetted bottom surface is thought to be due to several mechanisms. At lower voltages up to 4-6 kV, an attracted layer of liquid is drawn towards the central electrode, and the EHD forces cause major changes to nucleated bubbles within the liquid layer. Bubbles are seen to oscillate at double the EHD frequency, and are also seen to be maintained and prevented from reaching the surface of the liquid layer. During this state they enlarge and their subsequent sliding

and oscillation along the bottom of the tube displaces liquid from wall and disturbs the thermal boundary layer thus augmenting convection.

At higher voltages, beginning at around 5-6 kV the oscillating bubble regime begins to become replaced by a thin film flow regime, though periodic transitions in flow pattern are still seen depending on transient liquid levels along the tube. As the liquid film thins, this in itself will improve the convective heat transfer coefficient. It was also noticed, that despite a general reduction in nucleation within the very thin liquid films, some bubbles do appear, and subsequently grow very rapidly and make their way upward along the tube wall. This again provides agitation in the liquid layer and mixing improving convective heat transfer. At 8 kV, liquid jets emanating from the thin film at the tube bottom were seen indicating strong attractive forces are still at play.

4.3.6: Differences between Water heated and Ohmically Heated Test Sections

Despite the fact that both water heated and ohmically heated test sections were subject to 150 W of heat input generally, the heat transfer coefficients for the electrically heated test section were much higher than for the water heated section. This may be explained by two important differences.

In the water heated test section the boundary condition along the sapphire tube was dependent on the temperature of the water flowing past it. As the water temperature drop was generally in the order of 1 to 1.5 °C, this approximated a constant wall temperature condition. This helps to explain the “s” shaped curve noticed in section 4.2, whereby even in a dryout condition inside the tube, the wall superheats could never rise above the temperature of the surrounding water.

In contrast, in the electrically heated test section, the boundary condition was more akin to a constant heat flux. This meant that in a region of dryout, the wall surface temperature could rise to a higher temperature as it is unbounded by the surrounding water jacket. This explains why in the ohmically heated test section, the trend in heat transfer coefficients is a knee shaped curve as the wall temperature, being unbounded by the water jacket is now governed predominantly by the refrigerant flow condition

inside the tube. Thus if the tube top becomes drier, the temperature will rise higher as seen in the "knee" shaped curve. Therefore, the electrically heated trends do not exhibit the "s" shape curve, as when dryout occurs, the wall temperature cannot rise beyond that imposed by the temperature of the surrounding water.

Another difference between water heated and electrical test sections is in the magnitude of the heat transfer coefficients. Comparing two similar experiments for G=100 and x_{in} =2% for the water heated and electrically heated sections (compare Figure 49 with Figure 110), the heat transfer coefficients are higher in the electrically heated test section. For the water, the average heat transfer coefficient is around 1000 W/m^{2}K, while for the electrical test section, the heat transfer coefficients are also 1269 W/m^{2}K for the top, but at 2029 W/m^{2}K for the bottom.

This difference can also be seen in the superheats (on which the HTCs are dependent) when comparing figures Figure 56 and Figure 113 at 0 kV. For the water heated tube, the superheats are generally around 12 °C top and bottom, while for the electrically heated section, the top superheat is around 11 °C, but the bottom is approximately 6 °C. This is because the hot water stream provides an almost constant temperature around the tube, therefore the wall temperatures are largely driven by this, and thus changes in temperature brought about by the internal flow regime have lesser effect. In contrast, the wall temperature in the electrically heated section is governed by the cooling ability of the refrigerant flow regime. Thus in the electrically heated section, the stratified flow in the lower tube is responsible for the 6 °C superheat while in the drier upper tube the superheat rises higher.

4.3.7: Summary of Section 4.3

Effective discretization of the test section was permitted by the ohmically heated test section which allowed calculation of the local heat transfer coefficients at eight locations, four top and four bottom. These allowed the identification of favourable flow patterns for effective heat transfer.

It was found that for the field free case, the heat transfer coefficients top and bottom increased with length along the tube. EHD enhanced the overall coefficients further but in general enhancement was low up until 4 kV. From 5 kV onwards enhancement increased sharply but the top and bottom were affected in different proportions. The top was primarily enhanced at the beginning of the tube due to the low amount of vapour and large amount of liquid redistribution from the lower layer to the top wall. However this top EHD enhancement tailed off with length. This was thought to be due to lower liquid availability for redistribution as quality increased along the tube, specifically, the tendency to annular flow caused by increasing quality or earlier redistribution diverted liquid from the region of high electric field near the central electrode. This is supported by Gidwani *et al.* [74] who noted that liquid extraction decreased during annular wavy and annular flows.

The bottom of the tube was also enhanced considerably by EHD, and unlike the top enhancement profiles, was independent of axial location along the tube. It is thought that several factors influence this augmentation. For lower quality flows, the lower stratified layer is agitated by bubble growth and oscillation increasing the convective heat transfer. Also, the extraction phenomena attracts liquid up to the central electrode pulling liquid away from the lower layer resulting in further thinning. At higher qualities despite lower liquid levels, EHD enhancement still continues. This may be partly due to the AC voltage which produces alternating attractive and repulsive forces on the fluid layer. These forces are likely to be greater during waves or surface ripples which serve to reduce the distance between the liquid and electrode.

An explanation was also given for the difference in the shape of the heat transfer coefficient profiles along the length between water heated and electrically heat test sections, and the difference in magnitude of the heat transfer coefficients themselves.

Chapter 5: Conclusions and Future Work

5.1: Summary of Work Completed

Chapter Five now contains a final summary of the thesis leading to the conclusions and recommendations for further study.

5.1.1: Summary of Chapters 1-3

An introduction to the thesis was given in Chapter One to highlight the rationale behind the study followed by the thesis objectives, and the thesis layout.

Chapter Two was divided into three sub-sections. The first sub-section covered the background theories of two-phase flow, followed by a discussion on flow patterns, flow mapping and prediction methods for flow pattern transitions and heat transfer calculations. The second sub-section began similarly with an outline of electrohydrodynamics, and then provided more advanced EHD theory with specific relevance to the present study. The final subsection comprised a literature review reporting the major studies in combined two-phase flow with EHD, hence leading up to the present state of the art. The aim of Chapter Two was to highlight the reason for the present research through an appreciation of techniques in heat transfer enhancement and the need for mechanistic models as the interactions between two-phase flow and electrohydrodynamics are too complex to be solved analytically. The literature review re-capped the advances in two phase flow prediction methods leading to models that were a phenomenological reflection of the flow field, overcoming the shortcomings of previous models based on general correlations. The literature review also showed that although EHD visualisation studies existed in pool boiling, and to some extent in adiabatic flows, a gap existed in visualisation of EHD augmented flows under diabatic conditions.

Chapter Three described the novel two-phase flow test rig constructed to address the flow visualisation problem. The test rig, its various flow loops, as well as complete descriptions of both transparent test sections used along with associated instrumentation were detailed. It also described the commissioning and validation of the rig and an error analysis. In addition, the experimental methods, operation, calculations, and data reduction were specified.

5.1.2: Summary of Chapter 4

In Chapter Four, all the results from the experiments on both water heated and electrically heated test sections were presented and discussed. Details were given of the first series of two-phase flow tests with EHD enhancement carried out under boiling at a constant heat input.

5.1.2.1: Summary of Constant Heat Input Tests

The initial test was performed at 2% inlet quality without EHD to act as a field-free baseline case and subsequent tests were performed increasing voltage to 4 and 8 kV. This format was then repeated but with increased inlet qualities of 15, 30 and 45%. The results indicate that the enhancement of the heat transfer depends on the applied voltage level and the vapour quality. For the field-free case, the average heat transfer coefficient increased with inlet quality up to x_{in}=30% and thereafter decreased. This was due to conventional liquid/vapour forces within the tube.

For V=4 kV the overall flow regime is quite different from the baseline field-free case and the heat transfer is enhanced by between 1.12 and 1.24 with the enhancement generally decreasing with vapour quality. The 4 kV force augments heat transfer by acting on the bubbles at lower qualities but this process then changes with quality along the tube as the EHD forces precipitate a change from stratified flow by attraction of fluid from the lower liquid layer. This progresses to a wavy thin film type flow as quality increases and then the flow regime changes to an “induced annular” flow which is responsible for a further increase in heat transfer at x_{in} = 30%. However, at a quality of 45%, a drop in heat transfer is noticed as the amount of liquid available for redistribution is less, and dryout along the upper tube becomes more visible. For this applied voltage the pressure drop penalty is not severe.

For the V=8 kV case the enhancement levels reach 2 fold for the lowest quality tested and decreases with increased quality to 1.3 fold for the highest inlet quality. For this applied voltage the pressure drop penalty is more substantial, ranging from 30% to 60% over the field-free case. At 8 kV EHD voltage, the flow regime at low quality experiences large changes in bubble activity, especially growth and oscillation, as well as coalescence and climbing which all contribute to deliver higher heat transfer at the tube top and bottom. High liquid levels near the electrode enable this disturbance and redistribution. Liquid jets are also a feature at 8 kV and contribute to the redistribution of fluid increasing convection at the bottom, and wetting of the top. As inlet quality increases, heat transfer drops as the amount of liquid available is seen to decrease, but the high EHD forces assists in redistribution of liquid from the bottom layer to wet the top of the tube, again creating an "induced annular flow". As quality increases further, this redistribution effect appears subdued due to increased visibility of dryout conditions at the tube top. Maximum heat transfer augmentation of two-fold occurs at the tube beginning while at the tube end this drops to 1.3 fold.

5.1.2.2: Summary of Constant Water Inlet Temperature Tests

The next series of tests again utilised the water heated test section but this time at only one refrigerant inlet quality and under a constant water inlet temperature condition. Again a field-free base case was established and voltage was increased in 1 kV increments up to 10 kV. Heat input across the test section was allowed to vary with EHD voltage. For a 12 cm long viewing section located near the refrigerant entrance three distinct flow regimes were identified.

For the field-free case the flow was predominantly stratified wavy with nucleate boiling occurring in the lower stratified layer and slugs or intermittent liquid bridging to the top of the tube. The heat transfer enhancement reached a maximum of 1.1 or about 12% of the total enhancement. This dominant flow regime remained until approximately 3kV when a regime consisting of large vertically oscillating bubbles and a liquid curtain drawn to the inner electrode appeared. Bubble diameters increased with voltage as did their oscillation amplitude. Likewise, coalescence and cresting of bubbles became more persistent, conveying liquid to the upper parts of the tube. This flow regime was dominant in the 3kV to 7kV range and caused a very appreciable increase in the heat

transfer coefficient, with an enhancement reaching h/ho~1.6 and accounting for 55% of the overall enhancement.

Between 7kV and 10kV the heat transfer coefficients continued to increase reaching a 1.84 fold enhancement. The flow pattern alternated between two flow regimes, the oscillating bubble regime, as seen in the 4-7 kV range, and a thin film regime. The number of the liquid jets increased with voltage, however, their strength did not appear to increase. This region accounted for 37% of the overall enhancement.

In addition, the power gained from EHD was compared to the power penalty to give an idea of overall benefit. The maximum return for energy gained by EHD over energy expended by EHD was around 37 fold at 4 kV.

5.1.2.3: Summary of Ohmically Heated Tests

The final series of tests were performed on an electrically heated test section designed to overcome the lack of local heat transfer coefficients using the water heated test section. This method of heating allowed the local heat transfer coefficient to be measured at eight locations, four top and four bottom thus permitting linking of the local flow regimes and heat transfer coefficients.

The application of EHD substantially increased the heat transfer coefficient at all measurement points along the heat exchanger especially so at voltages above 4 kV. From 5 kV onwards enhancement increased sharply but the top and bottom were affected in different proportions. Near the entrance, the top surface heat transfer enhancement peaked at over 7.2 fold and decreased monotonically to 2.4 fold at the exit region. The reduction is attributed to the lower level of the bottom stratified layer making it more difficult for the EHD effect to redistribute liquid to the top surface, more specifically, the tendency to annular flow caused by increasing quality, or earlier redistribution which diverted liquid away from the region of high electric field near the central electrode.

The bottom enhancement was also enhanced considerably by EHD although more uniform along the heat exchanger and less sensitive to EHD voltage ranging between 3 to 4 fold at the highest applied voltage tested. It is thought that several factors

influence this augmentation. For lower quality flows, the lower stratified layer is agitated by bubble growth and oscillation increasing the convective heat transfer. Also, the extraction phenomenon attracts liquid up to the central electrode pulling liquid away from the lower layer resulting in further thinning. At higher qualities despite lower liquid levels, EHD enhancement still continues. This may be partly due to the AC voltage which produces alternating attractive and repulsive forces on the fluid layer. These forces are likely to be greater during waves or surface ripples which serve to reduce the distance between the liquid and electrode.

5.2: Conclusions

For three series of experiments, using a novel and innovative sapphire test section under water heated and electrically heated conditions, a range of thermo hydraulic measurements and visual and photographic information combined to give a novel and unique insight into two phase flow boiling under electrohydrodynamic forces. Based on the preceding chapters, results analysis and discussion, the following conclusions can be drawn.

Throughout all experiments, it can be concluded that EHD affects the flow regime and thus heat transfer in the flowing ways

- By acting on the bubbles within the liquid layer. EHD voltages of 3 to 6kV were seen to affect bubbles via enlargement, elongation, oscillation and retention of bubbles within the liquid layer. This serves to disturb the liquid boundary layer causing increased heat transfer.
- By acting on rising bubbles breaking through the liquid layer. This was witnessed at medium to high voltages of 5 to 8kV where EHD forces impinged on bubbles leaving the liquid layer again causing elongation and deformation of the bubbles resulting in cresting and bridging of bubbles thus re-wetting dry areas of the tube.
- By redistributing liquid in close proximity to the central electrode. This was especially noticed at lower qualities where the liquid levels are higher. However at higher qualities, despite generally lower liquid levels, it was noticed that liquid waves passing near to the electrode were influenced by EHD forces and subject to redistribution. Higher voltages were especially effective in bulk redistribution of liquid where liquid columns or jets emanated from the central electrode.
- EHD forces via the redistribution of liquid, cause changes in flow regime. Among other flow regime changes documented in the thesis, EHD forces led to the re-establishment of annular flow.

Heat transfer enhancement was higher at lower qualities, and tends to decrease with increasing quality. Central to this heat transfer enhancement via liquid redistribution was the availability of liquid in proximity to the central electrode. At higher qualities, the amount of liquid available for redistribution has decreased. Moreover the location of the liquid at higher qualities tends to be around the periphery of the tube, furthest from the central electrode and therefore subject to lowest electrical forces.

Increasing EHD voltages can provide equivalent heat transfer at lower superheat temperatures. In the constant heat input tests, as increasing voltage provided EHD enhancement, the water inlet temperatures were dropped to maintain a constant heat input across the test section. This could be of benefit in applications using low grade heat such as geothermal or waste heat recovery.

EHD gains outweigh the penalties. Although the energy penalty increased with voltage because the electrical power needed for EHD increased, in the voltage range of 2 to 10 kV, the extra heat transfer in watts due to EHD enhancement was always greater than 15 times the power needed for EHD. A maximum enhancement to voltage ratio of 37 fold was obtained at 4 kV.

5.3: Recommendations for Further Study

Carry out further observations at higher frame rate to ascertain the contributory factors that cause the rapid and large bubble growth seen with increasing EHD voltage. By focusing on a small area of the transparent tube, it may be interesting to further elaborate the mechanism of bubble formation, growth and collapse under both field-free and EHD conditions.

Investigate the fitting of a smaller diameter electrode to study the effect on both EHD augmentation and to reduce the annular geometry within the sapphire tube. While the reduced electrode diameter would pose less physical disturbance to the flow, the reduced electrode surface area and electrode height may result in differing liquid extraction or expulsion mechanisms. In addition, the reduced electrode surface area may also have an effect on the electric field intensity and thus on the electrohydrodynamic forces.

Determine the method of charge injection into the working fluid and investigate if there are any charge injection differences between metallic test sections and the use of a sapphire tube. The research of Ng [75] may be a good starting point in this regard.

Over a longer period of research on diabatic experiments at a range of mass fluxes and heat input levels, it may be possible to create a flow map similar to that of Wojtan et al. A first point would be a complete field free flow pattern map, and this could then be overlaid with EHD voltages.

Investigation of the EHD voltage levels and frequencies or duty cycles should be performed to optimise voltages and durations for low and high qualities, and also to find the optimum enhancement to power penalty ratio. Work on this could be done in conjunction with Dr James Cotton of McMaster University who has already experience in this area.

References

[1] R. K. Shah, Sekulić, Dušan P, *Fundamentals of heat exchanger design*: Wiley, 2003.

[2] J. R. Thome, *Enhanced Boiling Heat Transfer*. New York: Hemisphere Publishing Corp, 1990.

[3] P. Di Marco, "The Use of Electric Force as a Replacement of Buoyancy in Two-phase Flow," *Microgravity Science and Technology,* vol. 24, pp. 215-228, 2012/06/01 2012.

[4] J. S. Cotton, "Mechanisms of electrohydrodynamic (EHD) flow and heat transfer in horizontal convective boiling channels," Ph.D, McMaster University, Hamilton, 2000.

[5] J. S. Cotton, A. J. Robinson, M. Shoukri, and J. S. Chang, "A two-phase flow pattern map for annular channels under a DC applied voltage and the application to electrohydrodynamic convective boiling analysis," *International Journal of Heat and Mass Transfer,* vol. 48, pp. 5563-5579, 2005.

[6] J. S. Cotton, D. Brocilo, J. S. Chang, M. Shoukri, and T. Smith-Pollard, "Numerical simulation of electric field distributions in electrohydrodynamic two-phase flow regimes," *Dielectrics and Electrical Insulation, IEEE Transactions on,* vol. 10, pp. 37-51, 2003.

[7] J. S. Cotton, J. S. Chang, M. Shoukri, and T. Smith-Pollard, "Electrohydrodynamically enhanced flow boiling in an eccentric horizontal cylindrical channel," in *Electrical Insulation and Dielectric Phenomena, 2002 Annual Report Conference on*, 2002, pp. 220-223.

[8] J. S. Cotton, M. Shoukri, and J. S. Chang, "Oscillatory entrained droplet EHD two-phase flow," *Transactions of the ASME,* vol. 123, p. 622, 2001.

[9] H. Sadek, "Electrohydrodynamic (EHD) enhancement of In-Tube convective condensation," Master of Applied Science, Department of Mechanical Engineering, McMaster University, Hamilton, Ontario, 2004.

[10] H. Sadek, J. S. Cotton, C. Y. Ching, and M. Shoukri, "Effect of frequency on electrohydrodynamic enhanced tube-side condensation," in *Thermal Issues in Emerging Technologies: Theory and Application, 2007. THETA 2007. International Conference on*, 2007, pp. 145-149.

[11] H. Sadek, J. S. Cotton, C. Y. Ching, and M. Shoukri, "Effect of frequency on two-phase flow regimes under high-voltage AC electric fields," *Journal of Electrostatics,* vol. 66, pp. 25-31, 2008.

[12] H. Sadek, A. J. Robinson, J. S. Cotton, C. Y. Ching, and M. Shoukri, "Electrohydrodynamic enhancement of in-tube convective condensation heat transfer," *International Journal of Heat and Mass Transfer,* vol. 49, pp. 1647-1657, 2006.

[13] H. Ohta, "Experiments on microgravity boiling heat transfer by using transparent heaters," *Nuclear Engineering and Design,* vol. 175, pp. 167-180, 1997.

[14] V. P. Carey, *Liquid-Vapour Phase-Change Phenomena*: Taylor and Francis, 1992.

[15] F. P. Incropera and D. P. DeWitt, *Fundamentals of Heat and Mass Transfer*: Wiley, 1996.

[16] J. P. Holman, *Heat Transfer*: McGraw-Hill, 2002.
[17] A. Bejan, *Convection Heat Transfer*: Wiley Interscience, 1995.
[18] F. Kreith, Boehm, R.F., *Mechanical Engineering Handbook*: CRC Press LLC, 1999.
[19] Y. Taitel, "Flow Pattern Recognition in Two-phase Flow," presented at the 2nd Annual Meeting of the Institute of Multifluid Science and Technology, Santa Barbara, 1999.
[20] J. R. Thome. (last accessed 25th March 2013). *Wolverine Heat Transfer Engineering Data book III* [Online Reference Book]. Available: http://www.wlv.com/products/thermal-management-databooks.html
[21] G. F. Hewitt and D. N. Roberts, "Studies of Two-phase flow patterns by simultaneous X-ray and flash photography," *AERE-M 2159,*, 1969.
[22] N. A. Radovcich and R. Moissis, "The transition from two-phase bubble flow to slug flow," MIT Report No. 7-7673-221962.
[23] Y. Taitel and A. E. Dukler, "Flow regime transitions for vertical upward gas liquid flow: A preliminary approach through physical modelling," presented at the AIChE Annual Meeting, New York, 1977.
[24] A. Porteus, "Prediction of the Upper Limit of the Slug Flow Regimes," *British Chemistry Engineering*, vol. 14, pp. 117-119, 1969.
[25] G. B. Wallis, *One Dimensional Two-Phase flow*. New York: Wiley, 1965.
[26] K. Hashizume, "Flow Pattern and Void Fraction of Refrigerant Two-phase Flow in a Horizontal Pipe," *Bulletin of the JSME*, vol. 26, pp. 1597-1602, 1983.
[27] J. R. Thome, "On recent advances in modelling of two-phase flow and heat transfer," presented at the 1st International Conference on Heat Transfer, Fluid Mechanics and Thermodynamics, Kruger Park, South Africa, 2002.
[28] N. Kattan, J. R. Thome, and D. Favrat, "Flow Boiling in Horizontal Tubes: Part 1---Development of a Diabatic Two-Phase Flow Pattern Map," *Journal of Heat Transfer*, vol. 120, pp. 140-147, 1998.
[29] N. Kattan, J. R. Thome, and D. Favrat, "Flow Boiling in Horizontal Tubes: Part 2---New Heat Transfer Data for Five Refrigerants," *Journal of Heat Transfer*, vol. 120, pp. 148-155, 1998.
[30] N. Kattan, J. R. Thome, and D. Favrat, "Flow Boiling in Horizontal Tubes: Part 3---Development of a New Heat Transfer Model Based on Flow Pattern," *Journal of Heat Transfer*, vol. 120, pp. 156-165, 1998.
[31] L. Wojtan, T. Ursenbacher, and J. R. Thome, "Investigation of flow boiling in horizontal tubes: Part I—A new diabatic two-phase flow pattern map," *International Journal of Heat and Mass Transfer*, vol. 48, pp. 2955-2969, 2005.
[32] J. C. Chen, "Correlation for Boiling Heat Transfer to Saturated Fluids in Convective Flow," *Industrial & Engineering Chemistry Process Design and Development*, vol. 5, pp. 322-329, 1966/07/01 1966.
[33] M. M. Shah, "Chart Correlation for Saturated Boiling Heat Transfer: Equations and Further Study," *ASHRAE Transactions*, vol. 88, pp. 185-196, 1982.
[34] J. G. Collier and J. R. Thome, *Convective boiling and Condensation*: Oxford, 1994.
[35] K. E. Gungor and R. H. S. Winterton, "A general correlation for flow boiling in tubes and annuli," *International Journal of Heat and Mass Transfer*, vol. 29, pp. 351-358, 1986.
[36] M. G. Cooper, "Heat flow rates in saturated nucleate pool boiling-A Wide-Ranging Examination Using Reduced Properties," *Advances in Heat Transfer* vol. 16, pp. 157-239, 1984.

[37] Y. Q. Zu and Y. Y. Yan, "A numerical investigation of electrohydrodynamic (EHD) effects on bubble deformation under pseudo-nucleate boiling conditions," *International Journal of Heat and Fluid Flow,* vol. 30, pp. 761-767, 2009.

[38] K. E. Gungor, Winterton, R.H.S., "A general correlation for flow boiling in tubes and annuli," *International Journal of Heat and Mass Transfer,* vol. 29, pp. 351-358, 1986.

[39] S. Z. Rouhani and E. Axelsson, "Calculation of Void Fraction in the Subcooled and uality Boiling Regions," *International Journal of Heat and Mass Transfer,* vol. 13, pp. 383-393, 1970.

[40] L. Wojtan, T. Ursenbacher, and J. R. Thome, "Investigation of flow boiling in horizontal tubes: Part II—Development of a new heat transfer model for stratified-wavy, dryout and mist flow regimes," *International Journal of Heat and Mass Transfer,* vol. 48, pp. 2970-2985, 2005.

[41] D. Biberg, "An explicit approximation for the wetted angle in two-phase stratified pipe flow," *Canadian Journal of Chemical Engineering,* vol. 77, pp. 1221-1224, 1999.

[42] Castellanos, *Springer Handbook of Experimental Fluid Mechanics, Volume 1*: Springer, 2007.

[43] J. S. Chang and I. Maezono, "The effects of electrohydrodynamic flow on a corona torch," *Journal of Electrostatics,* vol. 23, pp. 323-330, 1989.

[44] J. S. Chang and A. Watson, "Electromagnetic Hydrodynamics, ," *IEEE Transactions on Dielectrics and Electrical Insulation,,* pp. 871-895, 1994.

[45] B.-T. Chu, "Thermodynamics of Electrically Conducting Fluids," *Physics of Fluids,* vol. 2, pp. 473-484, 1959.

[46] T. B. Jones, "Electrohydrodynamically enhanced heat transfer in liquids - A review," *Advances in Heat Transfer,* vol. 14, pp. 107-148, 1978.

[47] J. Seyed-Yagoobi and J. E. Bryan, *Enhancement of heat transfer and mass transport in single-phase and two-phase flows with electrohydrodynamics* vol. 33. New York: Academic press, 1999.

[48] J. E. Bryan and J. Seyed-Yagoobi, "Influence of Flow Regime, Heat Flux, and Mass Flux on Electrohydrodynamically Enhanced Convective Boiling," *Journal of Heat Transfer,* vol. 123, pp. 355-367, 2001.

[49] J. S. Cotton, ed, 2012.

[50] A. Faghri and Y. Zhang, *Transport phenomena in multiphase systems*. Burlington, MA: Elsevier Academic Press, 2006.

[51] I. W. Eames and H. M. Sabir, "Potential benefits of Electrohydrodynamic Enhancement of two phase heat transfer in the design of refrigeration systems," *Applied Thermal Engineering,* vol. Vol 17, pp. pp 79-92, 1997.

[52] P. H. G. Allen and T. G. Karayiannis, "Electrohydrodynamic enhancement of heat transfer and fluid flow," *Heat Recovery Systems and CHP,* vol. 15, pp. 389-423, 1995.

[53] S. Laohalertdecha, P. Naphon, and S. Wongwises, "A review of electrohydrodynamic enhancement of heat transfer," *Renewable and Sustainable Energy Reviews,* vol. 11, pp. 858-876, 2007.

[54] 3MCorporation, "3M™ Novec™ 7000 Engineered Fluid Product information brochure," ed, 2010.

[55] K. Cheung, M. M. Ohadi, S. Dessiatoun, and A. Singh, "EHD-Enhanced Boiling Coefficients and Visualization of R-134a Over Enhanced Tubes," *Journal of Heat Transfer,* vol. 119, pp. 332-338, 1997.

[56] C. Chen, L. He, X. Li, and L. Fu, "Experimental investigation of nucleate boiling heat transfer enhanced by non-uniform electric field," in *Electrical Insulation and Dielectric Phenomena, 2007. CEIDP 2007. Annual Report - Conference on*, 2007, pp. 554-557.

[57] Y. Feng and J. Seyed-Yagoobi, "Linear instability analysis of a horizontal two-phase flow in the presence of electrohydrodynamic extraction force," *Journal of Heat Transfer*, vol. 124, pp. 102-110, 2002.

[58] W. Grassi, D. Testi, and M. Saputelli, "Heat transfer enhancement in a vertical annulus by electrophoretic forces acting on a dielectric liquid," *International Journal of Thermal Sciences*, vol. 44, pp. 1072-1077, 2005.

[59] Y. Jia-Xiang, D. Li-Jian, and Y. He, "An experimental study of EHD coupled heat transfer," in *Electrical Insulation and Dielectric Phenomena, 1996. IEEE 1996 Annual Report of the Conference on*, 1996, pp. 348-351 vol.1.

[60] T. G. Karayiannis, "EHD boiling heat transfer enhancement of R123 and R11 on a tube bundle," *Applied Thermal Engineering*, vol. 18, pp. 809-817, 1998.

[61] T. G. Karayiannis, M. W. Collins, and A. P.H.G., "Electrohydrodynamic Enhancement of Nucleate Boiling Heat Transfer in Heat Exchangers," *Chemical Engineering Communications*, vol. 81:1, pp. 15-24, 1989.

[62] H. Kawahira, Y. Kubo, T. Yokoyama, and J. Ogata, "The effect of an electric field on boiling heat transfer of refrigerant-11-boiling on a single tube," *IEEE Transactions on Industry Applications*, vol. 26, pp. 359-365, 1990.

[63] Y. Liu, R. Li, F. Wang, and H. Yu, "The effect of electrode polarity on EHD enhancement of boiling heat transfer in a vertical tube," *Experimental Thermal and Fluid Science*, vol. 29, pp. 601-608, 2005.

[64] R. S. Neve and Y. Y. Yan, "Enhancement of heat exchanger performance using combined electrohydrodynamic and passive methods," *International Journal of Heat and Fluid Flow*, vol. 17, pp. 403-409, 1996.

[65] J. Ogata and A. Yabe, "Basic study on the enhancement of nucleate boiling heat transfer by applying electric fields," *International Journal of Heat and Mass Transfer*, vol. 36, pp. 775-782, 1993.

[66] P. K. Watson, "Influence of an Electric Field upon the Heat Transfer from a Hot Wire to an Insulating Liquid," *Nature*, vol. 189, pp. 563-564, 1961.

[67] K. Yamashita and A. Yabe, "Electrohydrodynamic Enhancement of Falling Film Evaporation Heat Transfer and its Long-Term Effect on Heat Exchangers," *Journal of Heat Transfer*, vol. 119, pp. 339-347, 1997.

[68] S.-D. Oh and H.-Y. Kwak, "A study of Bubble Behaviour and Boiling Heat Transfer Enhancement under Electric Field," *Heat Transfer Engineering*, vol. 21, pp. 33-45, 2000.

[69] K. J. Cheng and J. B. Chaddock, "Effect of an electric field on bubble growth rate," *International Communications in Heat and Mass Transfer*, vol. 12, pp. 259-268, 1986.

[70] J. Ogata and A. Yabe, "Augmentation of boiling heat transfer by utilizing the EHD effect--EHD behaviour of boiling bubbles and heat transfer characteristics," *International Journal of Heat and Mass Transfer*, vol. 36, pp. 783-791, 1993.

[71] P. Cooper, "EHD Enhancement of Nucleate Boiling," *Journal of Heat Transfer*, vol. 112, pp. 458-464, 1990.

[72] K. Cheung, M. Ohadi Mike, and S. V. Dessiatoun, "Boiling Heat Transfer Enhancement of R-134a in a Tube Bundle Utilizing The EHD Technique," *Journal of Enhanced Heat Transfer*, vol. 3, 1996.

[73] J. S. Paschkewitz and D. M. Pratt, "Electrohydrodynamic (EHD) Heat Transfer Enhancement in an Aviation Working Fluid: Effect of Electrode Material and Polarity," *Journal of Enhanced Heat Transfer,* vol. 7, pp. 371-383, 2000.

[74] A. Gidwani, M. Molki, and M. M. Ohadi, "EHD-Enhanced Condensation of Alternative Refrigerants in Smooth and Corrugated Tubes," *HVAC&R Research,* vol. 8, pp. 219-237, 2002/07/01 2002.

[75] K. Ng, "Mechanisms of E;ectrohydrodynamic Two-Phase Flow Structures and the Influence on Heat Transfer and Pressure Drop," MASc, Mechanical Engineering, McMaster, Hamilton, 2010.

[76] M. Salehi, M. M. Ohadi, and S. Dessiatoun, "EHD-enhanced convective boiling of R-134a in grooved channels—application to compact heat exchangers," *Journal of Heat Transfer,* vol. 119, pp. 805–809, 1997.

[77] A. Yabe, T. Taketani, H. Maki, K. Takahshi, and Y. Nakadai, "Experimental Study of Electrohydrodynamically Enhanced Evaporator for Nonazeotropic Mixtures," *ASHRAE Transactions,* vol. 98,, pp. 455-461, 1992.

[78] J. E. Bryan, and Seyed-Yagoobi, J., "Electrohydrodynamically Enhanced Convective Boiling: Relationship between Electrohydrodynamic Pressure and Momentum Flux," *Journal of Heat Transfer,* vol. 122, pp. 266-277, 2000.

[79] Y. Feng and J. Seyed-Yagoobi, "Mechanism of annular two-phase flow heat transfer enhancement and pressure drop penalty in the presence of a radial electric field - Turbulence analysis," *Journal of Heat Transfer,* vol. 125, pp. 478-486, 2003.

[80] P. Tuma. (2001) Using Segregated HFEs as Heat Transfer Fluids. *Chemical Processing*.

[81] C. Colin, M. Narcy, and E. De Malmazet, "Flow boiling in straight heating tubes under microgravity conditions.," presented at the ECI-8th International Conference on boiling and Condensation Heat Transfer, Lausanne, Switzerland, 2012.

[82] G.F.C. Rogers and Y. R. Mayhew, *Thermodynamic and Transport Properties of Fluids: S. I. Units,* 5th Edition ed.: Blackwell, 1994.

[83] NIST, "Thermophysical Properties of Fluid Systems," in *http://webbook.nist.gov/chemistry/fluid/,* ed: National Institute of Standards and Technology, USA., 2011.

[84] S. J. Kline, McClintock, F. A., "Describing Uncertainties in Single-Sample Experiments," *Mechanical Engineering,* vol. 75, pp. 3-8, 1953.

[85] J. S. Cotton, A. J. Robinson, M. Shoukri, and J. S. Chang, "AC voltage induced electrohydrodynamic two-phase convective boiling heat transfer in horizontal annular channels," *Experimental Thermal and Fluid Science,* vol. 41, pp. 31-42, 2012.

[86] B. Donnelly, T. O'Donovan, and D. B. Murray, "Surface Heat Transfer due to Sliding Bubble Motion," *Applied Thermal Engineering,* vol. 29, pp. 1319-1326, 2009.

[87] M. Ohadi, Papar RA, Ng TL, Faani MA, Radermacher R. , "EHD enhancement of shell-side boiling heat transfer coefficients of R-123/oil mixture," *ASHRAE Trans,* pp. 427–34, 1992.

[88] S. Siedel, S. Cioulachtjian, A. J. Robinson, and J. Bonjour, "Electric field effects during nucleate boiling from an artificial nucleation site," *Experimental Thermal and Fluid Science,* vol. 35, pp. 762-771, 2011.

[89] S. Di Bari and A. J. Robinson, "Experimental study of gas injected bubble growth from submerged orifices," *Experimental Thermal and Fluid Science*, 2012.

[90] S. Grauso, R. Mastrullo, A. W. Mauro, J. R. Thome, and G. P. Vanoli, "Heat Transfer and pressure drops during the evaporation of R-1234ZE(E) in a circular smooth tube," presented at the ECI 8th International Conference on Boiling and Condensation Heat Transfer, Ecole Polytechnique Fédérale de Lausanne, 3-7 June, Switzerland, 2012.

[91] G. Sun, G. F. Hewitt, and V. V. Wadekar, "A heat transfer model for slug flow in a horizontal tube," *International Journal of Heat and Mass Transfer*, vol. 47, pp. 2807-2816, 2004.

[92] E. T. Hurlburt and T. A. Newell, "Characteristics of Refrigerant Film Thickness, Pressure Drop and Heat Transfer in Annular Flow," Air Conditioning and Refrigeration Centre, University of Illinois, 1206 West Green St, Urbana, Illinois, 618011997.

[93] D. Baba, T. Nakagawa, and S. Koyama, "Flow Boiling Heat Transfer and Pressure Drop of R1234ze(E) and R32 in Horizontal Micro-fin tube," presented at the International Refrigeration and Air Conditioning Conference, Purdue, 2012.

[94] P. K. Biswas, A. De, N. C. Pramanik, P. K. Chakraborty, K. Ortner, V. Hock, and S. Korder, "*Effects of tin on IR reflectivity, thermal emissivity, Hall mobility and plasma wavelength of sol-gel indium tin oxide films on glass*," *Materials Letters*, vol. 57 pp. 2326-2332, 2003.

Appendices

Appendix A: Optical Transmission Qualities of ITO coating

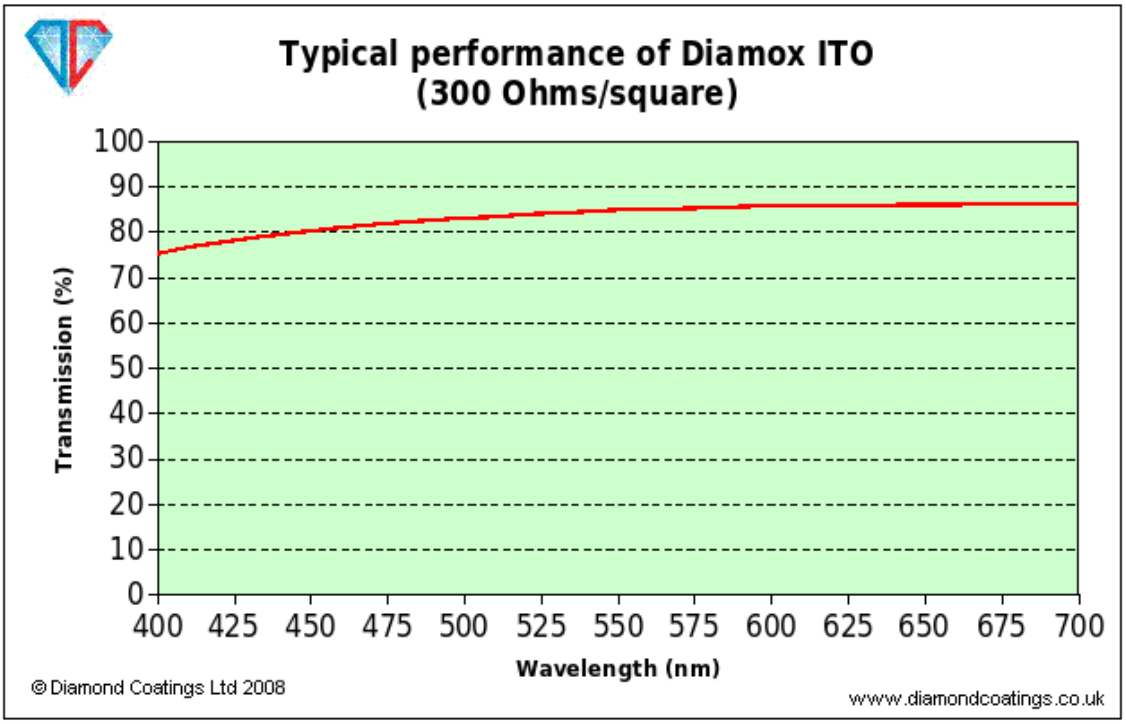

Figure 131: Optical transmissibility of Diamox ITO coating at 300Ω/m^2,

Source Diamond Coatings Ltd,

Unit 2a
Harvey Works Industrial Estate
Shelah Road
Halesowen
West Midlands
B63 3PG England

Appendix B: Calculation of Fluid Properties

The following graphs from Figure 132 to Figure 138 were prepared from look-up tables and graphed in Excel. Best-fit polynomial curves were then derived. These polynomials were then input into Labview to determine fluid properties based on the variables of either temperature or pressure as appropriate.

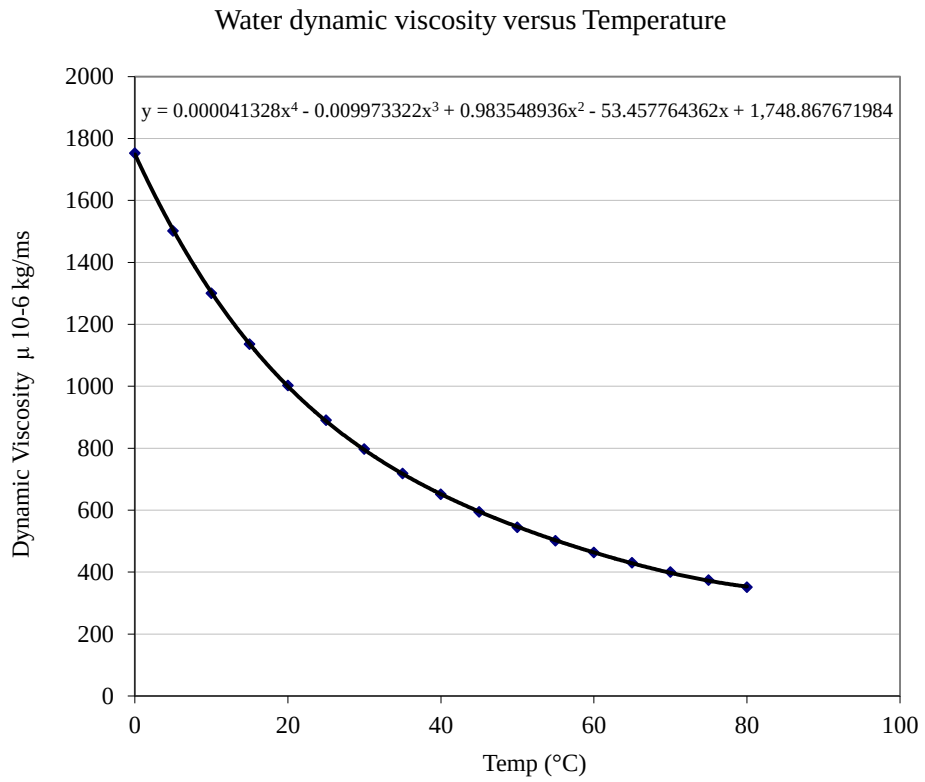

Figure 132: Variation of dynamic viscosity against temperature for water, source [83]

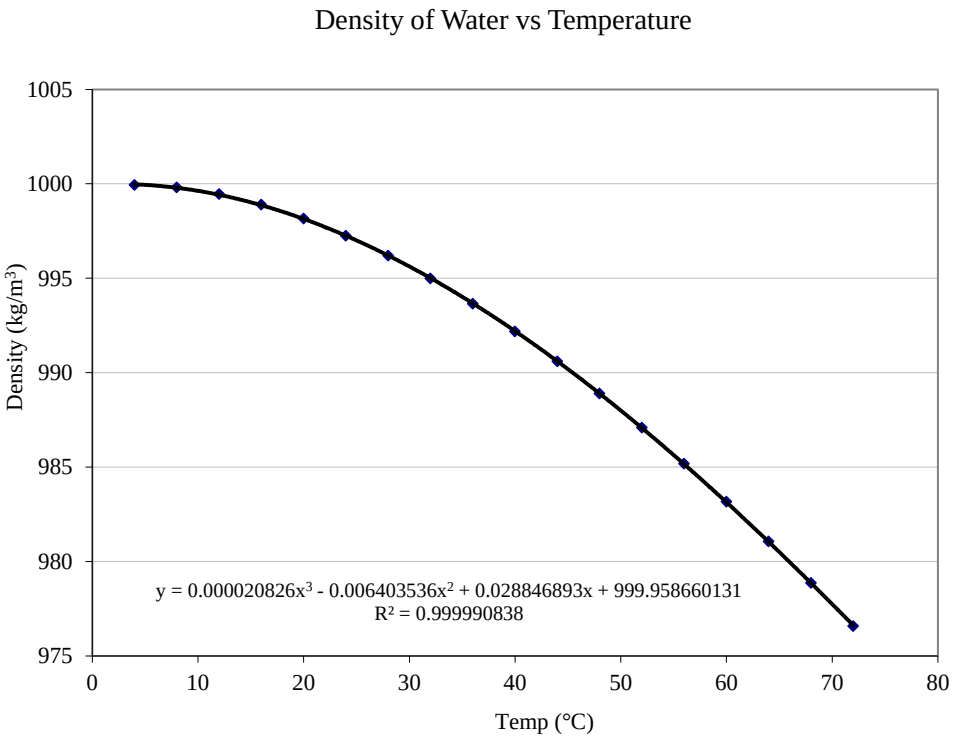

Figure 133: Variation of density against temperature for water, source [83]

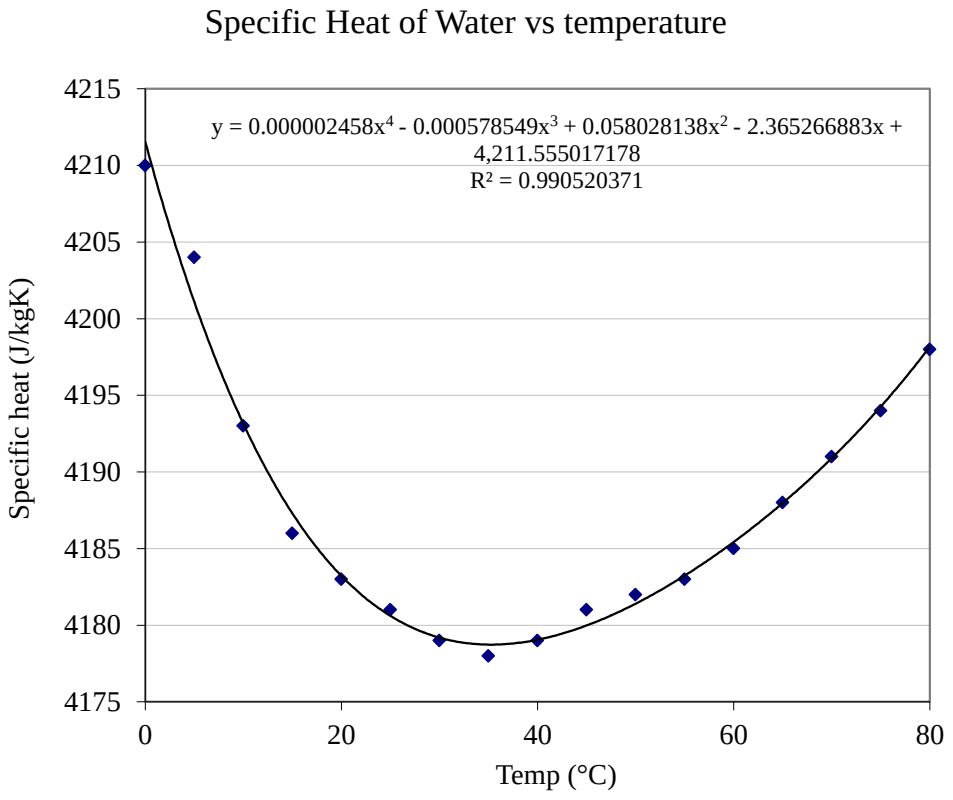

Figure 134: Variation of specific heat of water with temperature

Graph of enthalpy (h) vs Temperature for HFE7000

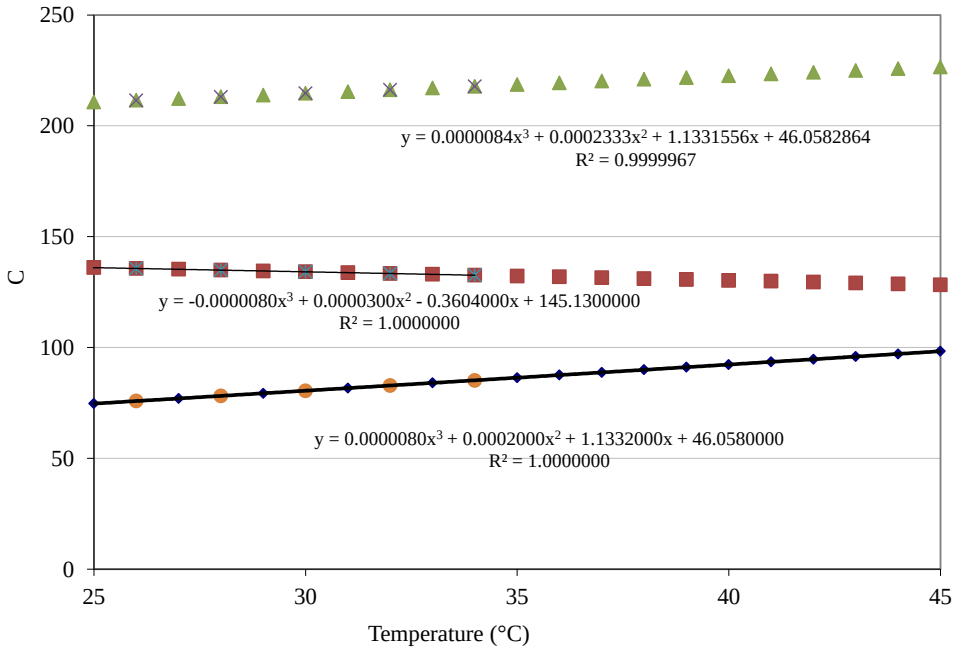

Figure 135: Enthalpy of HFE7000 versus temperature

Graph of enthalpy (h) vs Pressure for HFE7000

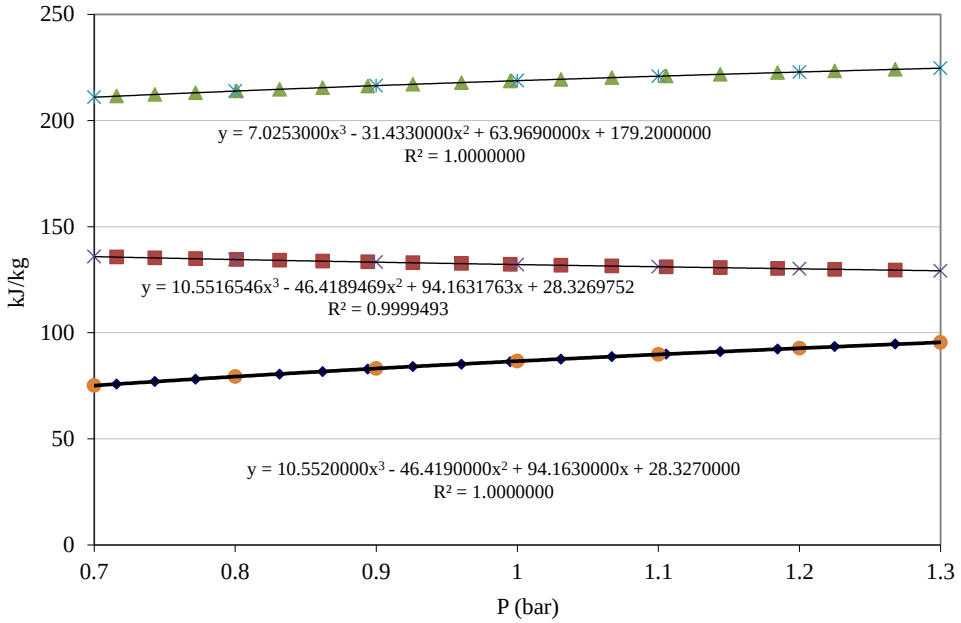

Figure 136: Enthalpy of HFE7000 versus pressure

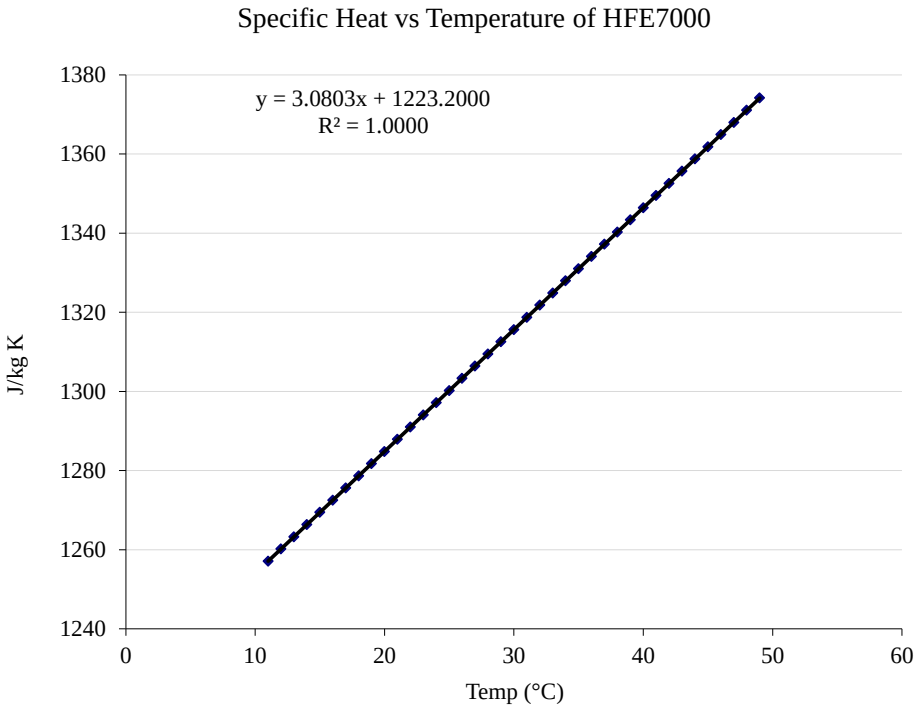

Figure 137: Variation of specific heat of HFE7000 with temperature

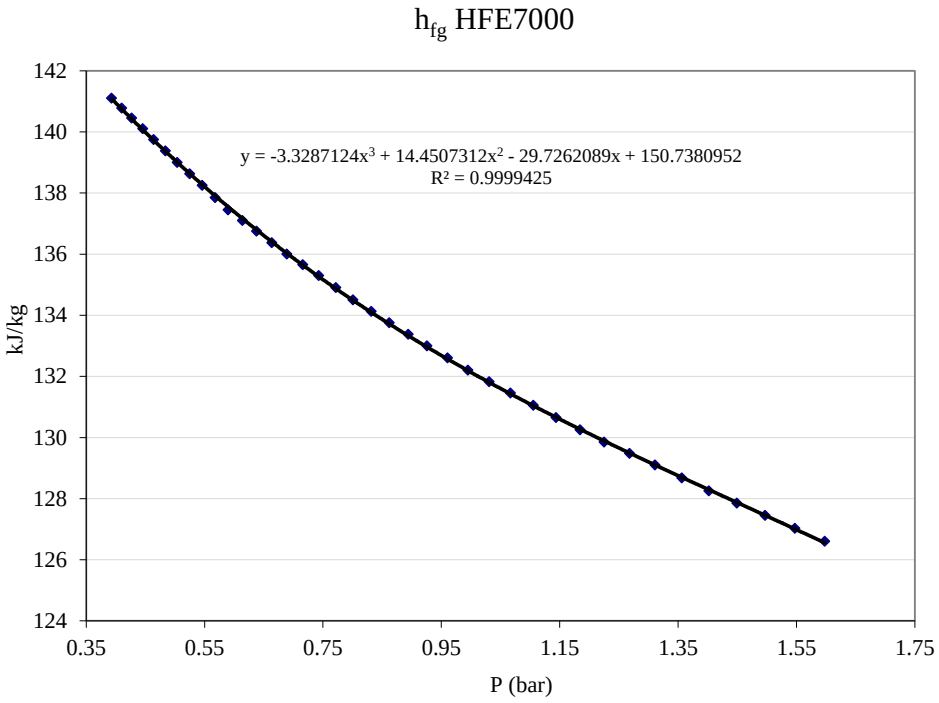

Figure 138:: Variation of latent heat of vapourisation of HFE7000 with temperature

Appendix C: Selection of Material for use as Sapphire Tube Supports

The material used for the pieces to support the sapphire tube had to possess adequate structural strength, high electrical insulation and chemical resistance to HFE7000. It also had to have good long-term resistance to hot water. The following table details a range of engineering polymers investigated. Several were suitable, of which the most economic was found to be polypropylene.

Material	*Comment*
Acrylic	Clear, usable up to 80°C, susceptible to cracking/crazing
Polycarbonate	Not resistant to hot water
Polypropylene	low water absorption, resistant to hot water, cheap, good insulator
Polyurethane	Low water absorption, water immersion good, Softens above ambient temp
PTFE	Poor adhesion, expensive.
PEEK	High temp resistance, resistant to hot water, low water absorption, expensive,
Acetyl (Delrin)	Black, difficult to bond, limited resistance to hot water, not insulating
Nylon	Attacked by water, absorption a problem
PPS	Not electrically insulating
PVC	Low glass transition temperature (70°C) 60°C max service temp, cheap, low water absorption, easy to bond
PVDF	Difficult to bond – HFE7000
Polyester	Easy to bond and weld , not good long term with water over 60°C
Polyethylene	Low water absorption, poor with hot water, 80°C difficult to bond,
Tufnol	Low voltage only, medium water absorption rate
ABS	Good in all respects but not resistant to hot water/washing

Appendix D: Local Heat transfer Coefficients in the Electrically Heated Test Section with Uncertainties

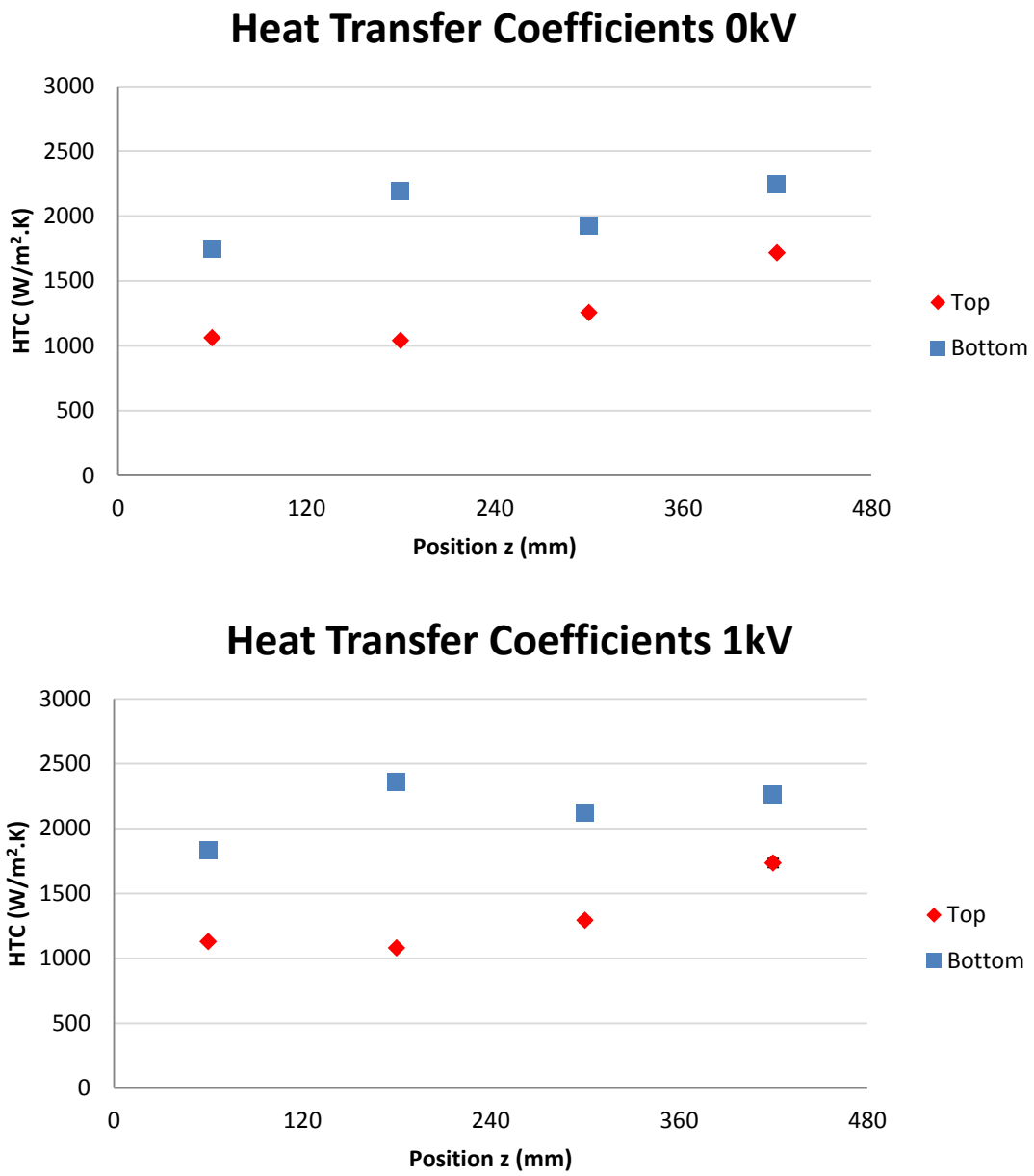

Figure 139: Local heat transfer coefficients in test section B, 0 kV and 1 kV

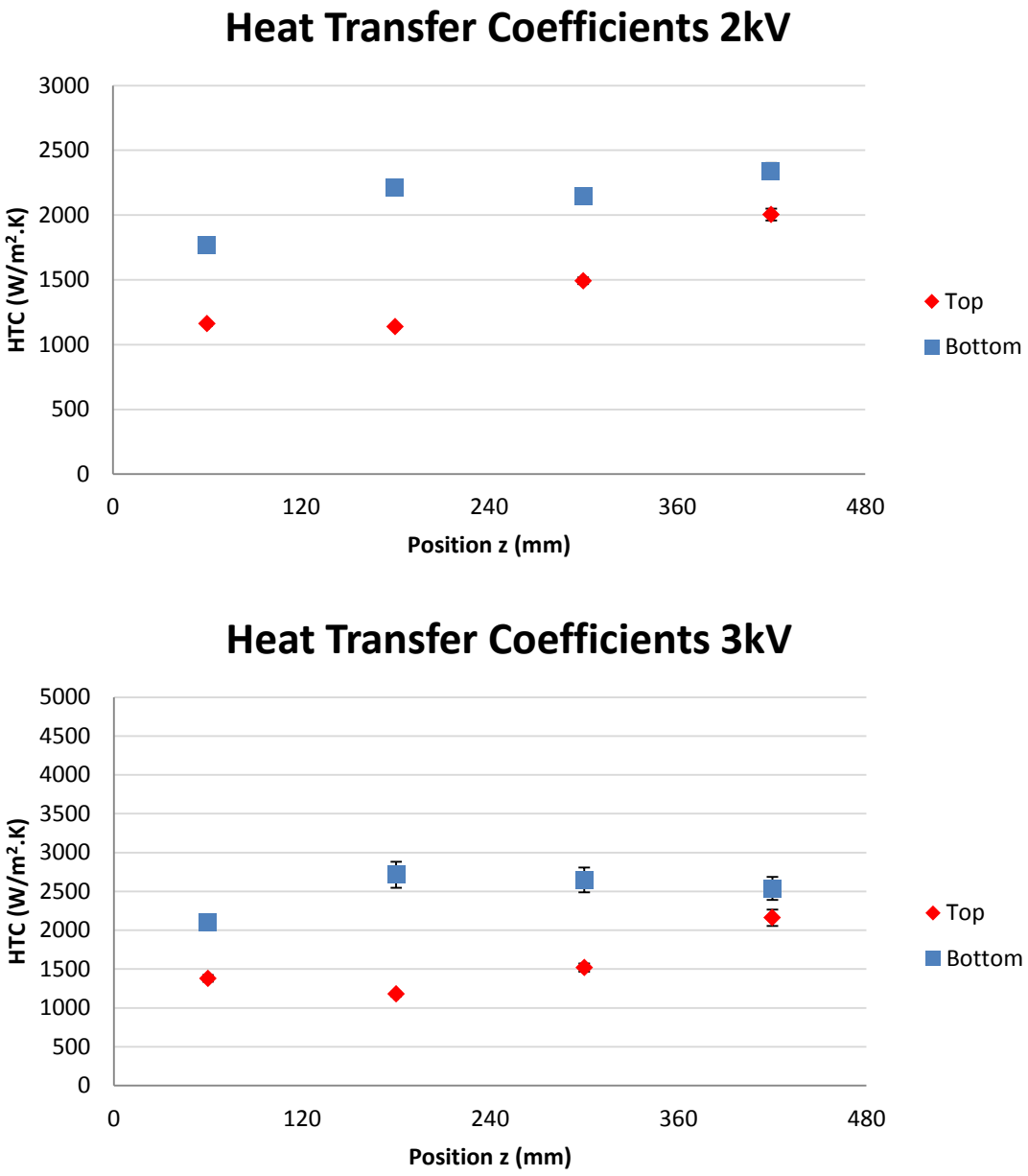

Figure 140: Local heat transfer coefficients in test section B, 2 kV and 3 kV

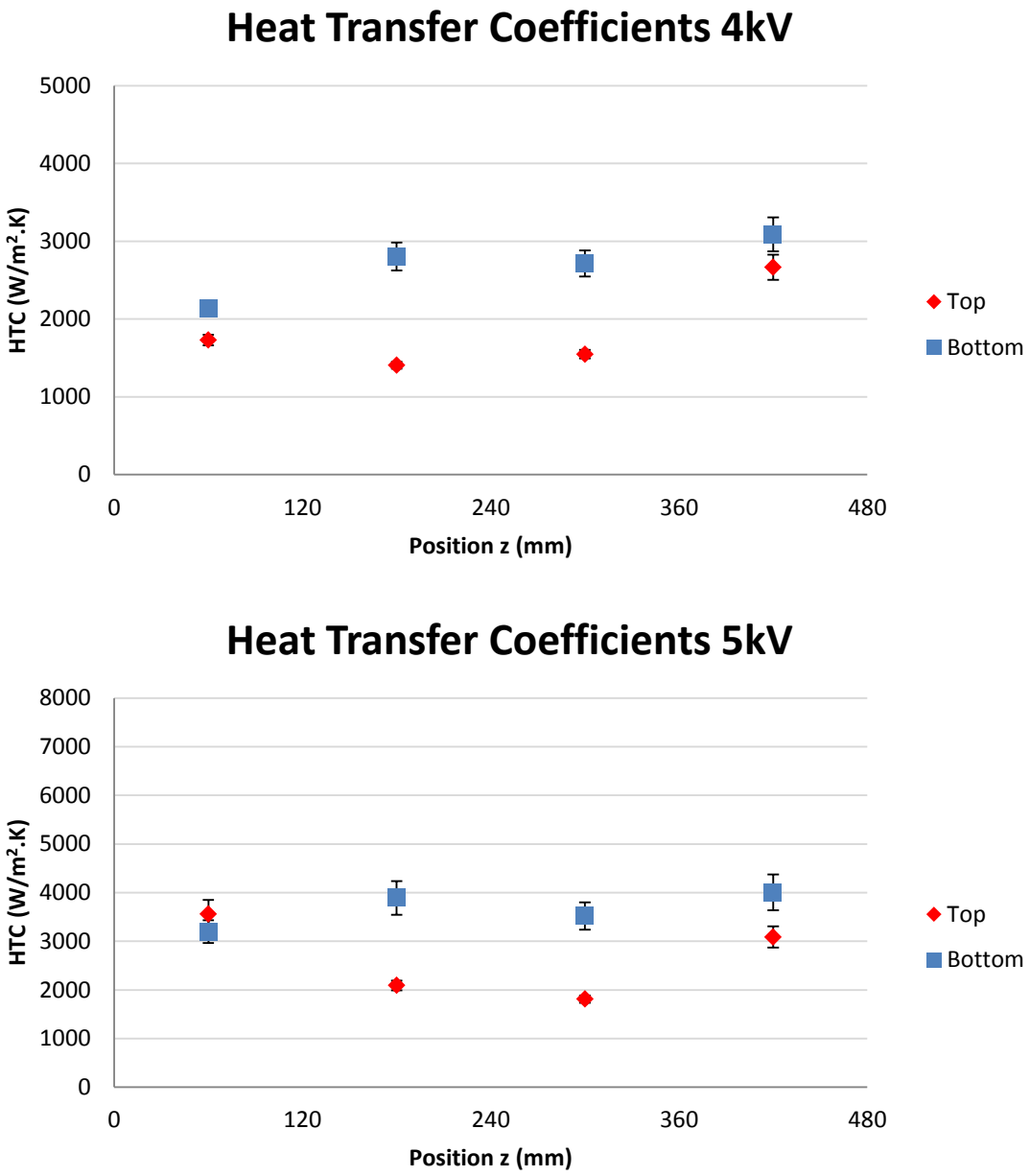

Figure 141: Local heat transfer coefficients in test section B, 4 kV and 5 kV

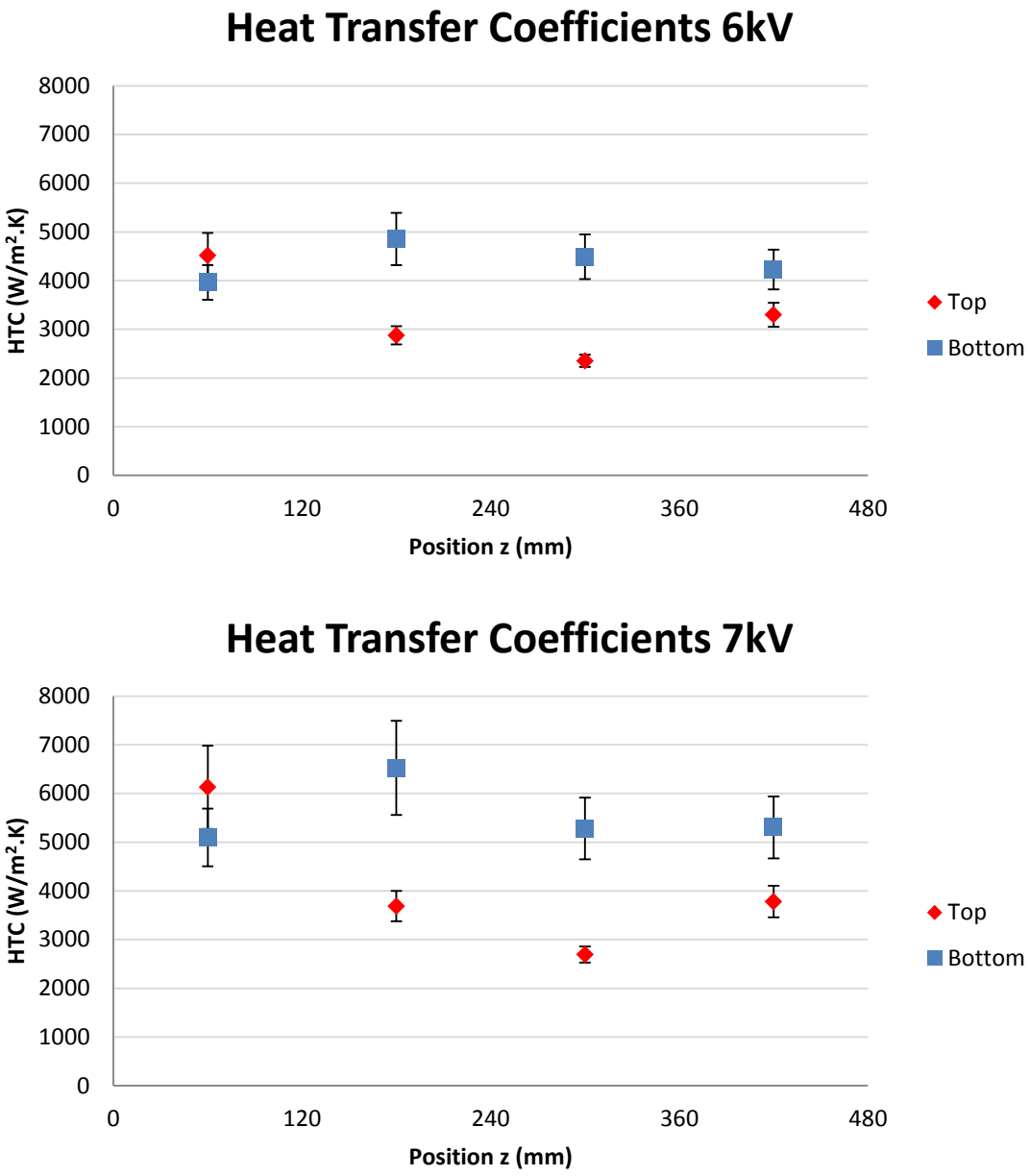

Figure 142 : Local heat transfer coefficients in test section B, 6 kV and 7 kV

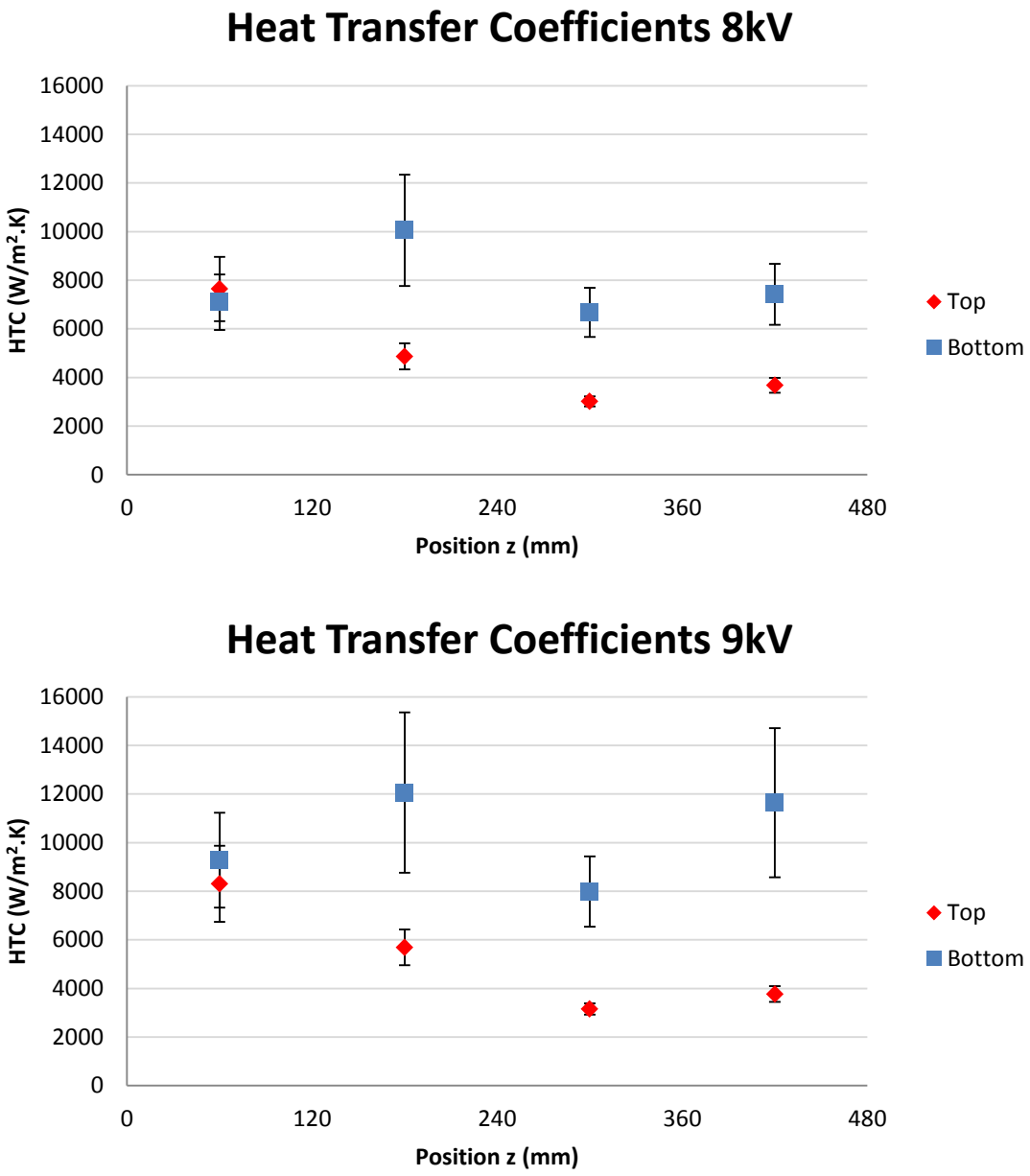

Figure 143 : Local heat transfer coefficients in test section B, 8 kV and 9 kV

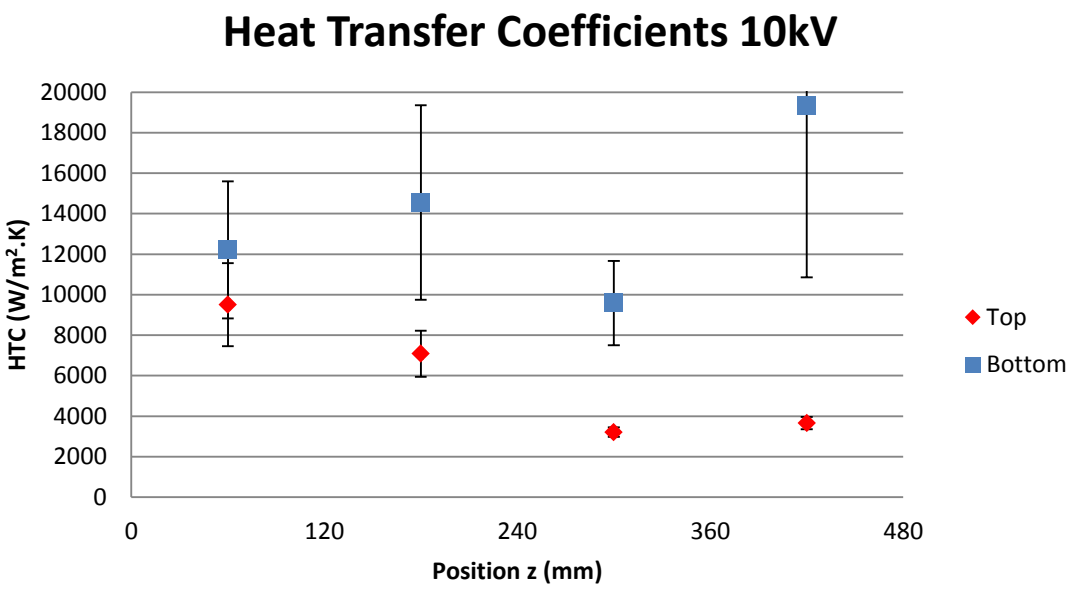

Figure 144 : Local heat transfer coefficients in test section B, 10 kV

Appendix E: Rouhani-Axelson Void Fraction Calculation

A plot of the inlet quality versus void fraction is shown in Figure 145. This curve was of assistance in cross checking the amounts of vapour present in the test section, especially at lower inlet qualities.

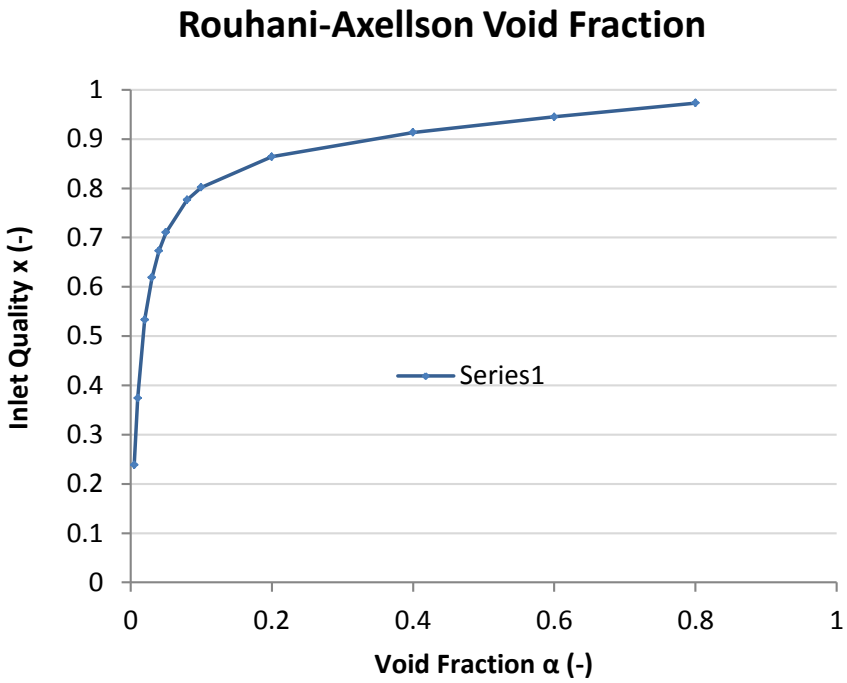

Figure 145: Rouhani-Axelson void fraction calculation graph

Appendix F*:* Combined convective and radiative losses from Test Section B

Combined convection and radiation losses are calculated by averaging the wall temperatures along the tube which permits estimation of the heat transfer coefficient. The tube is suspended in free air, but as the conditions in the laboratory during experiments were not quiescent, the losses cannot be estimated as due to pure natural convection. The sapphire tube is electrically heated and no fluid is flowing within the tube so as to eliminate internal heat exchange. The heat transferred by convection to the environment depends only on T_{wall} and T_{∞} which are measured by thermocouples. The heat transferred by radiation also depends on the surface temperature and on the emissivity of the sapphire tube and ITO coating. The results of the losses calculation are presented in Figure 146.

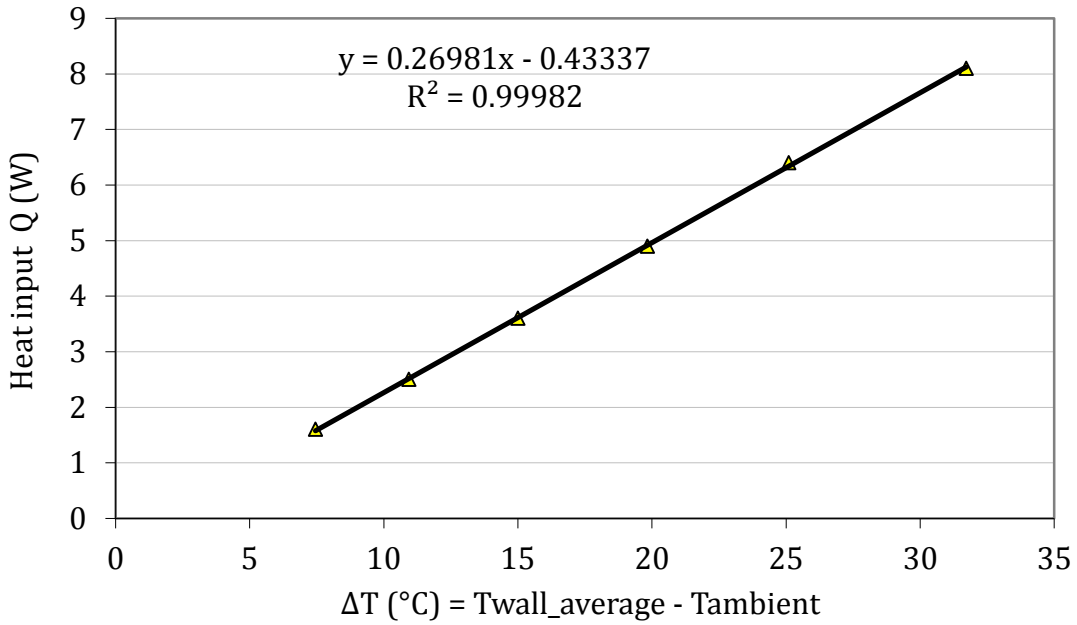

Figure 146: Heat input and wall temperatures for the determination of h_0.

The equation of the trendline gives h_0 as 17.9W/m^{2}K. At a steady state the energy balance leads to

$$q_{total} = V \times I \tag{122}$$

$$q_{total} = h_0 S_0 (T_{wall} - T_{\infty}) \tag{123}$$

Where the only unknown is h_0. After h_0 had been determined, it is easy to find q_{total} and then subtract this from the electrical power to determine the heat q received by the working fluid. In the working range of experimentation, losses due to combined convection and radiation were around 4-5W.

To contrast this with natural convection and radiative losses for a heated cylinder the following comparisons were made.
For radiation, the heat lost, q, can be calculated from

$$q = \varepsilon\sigma(T_h^4 - T_c^4)A \qquad (124)$$

where
σ is the Stefan-Boltzmann Constant (5.6703 x 10^{-8} W/m^{2}K^4)
ε is the emissivity which can range from 0.47 to 0.9 as reported by Biswas et al [94]
A is the surface area of the tube

Finding a precise value for the emissivity is difficult but assuming a worst case emissivity of 0.97, the radiative losses can be shown to be around 3W, while if ε is assumed to be 0.5, then losses are around 1.5W.

Natural convection calculations give a heat transfer coefficient of between 9 to 11 W/m^{2}K along the heated tube which equates to around 2.5 W of heat lost. Thus the calculations show that total natural convection and radiative losses can range between 4 to 5.5W. This is in line with that found by our measurements and graph shown in Figure 146.